**UNIVERSIDAD DE CHILE**
**FACULTAD DE CIENCIAS FÍSICAS Y MATEMÁTICAS**
**DEPARTAMENTO DE GEOLOGÍA**

# NEOTECTONICS AND SEISMIC SOURCE CHARACTERISATION IN THE CENTRAL HIGH ANDES, NEAR CHILE'S CAPITAL SANTIAGO

TESIS PARA OPTAR AL GRADO DE
MAGÍSTER EN CIENCIAS, MENCIÓN GEOLOGÍA

**JOSÉ ANTONIO ARAYA ZULETA**

PROFESOR GUÍA:
GREGORY DE PASCALE

PROFESOR CO-GUÍA
SERGIO SEPÚLVEDA VALENZUELA

COMISIÓN
GABRIEL EASTON VARGAS

SANTIAGO DE CHILE
2020

**RESUMEN DE LA MEMORIA PARA OPTAR AL TITULO**
**DE:** Magíster en Ciencias, Mención Geología.
**POR:** José Antonio Araya Zuleta
**FECHA:** 22/10/2020
**PROFESOR GUÍA:** Gregory Paul De Pascale

# NEOTECTÓNICA Y CARACTERIZACIÓN DE FUENTES SÍSMICAS EN LOS ALTOS ANDES CENTRALES, CERCA DE SANTIAGO, CAPITAL DE CHILE


La región metropolitana de Santiago contiene una población de más de 7 millones de habitantes, siendo el área más poblada de Chile. En este segmento del orógeno Andino, importante sismicidad cortical y evidencias de fallamiento Cuaternario han sido reportadas. En la Cordillera Principal, la falla San Ramón junto a la falla San José de Maipo son las únicas 2 fuentes de amenazas sísmicas conocidas. Esto muestra la falta de conocimiento sobre la neotectónica en la zona más poblada de Chile, uno de los países más sísmicos del mundo. Esta tesis busca aumentar el conocimiento sobre las fuentes sísmicas que están ubicadas en la Cordillera Principal cerca de la región Metropolitana, mediante un estudio neotectónico basado en técnicas de estudio remoto, mapeo en terreno y análisis de datos.

Fue posible caracterizar 3 fallas geológicas. Primero, la falla El Arrayan. Falla de rumbo siniestral de ~ 13 km de largo orientada ONO-ESE, evidenciada por escarpes de falla, portezuelos y ríos desviados, ubicados sobre depósitos Cuaternarios, además de exposición de rocas de falla. Aceleraciones máximas horizontales (PGA) de hasta 0.7 g son obtenidas a menos de 500 m de la traza en superficie de la falla El Arrayan para un escenario de ruptura sísmica con Mw 6.4, basado en el largo de la ruptura, lo que indica importante peligro sísmico. Segundo, a 40 km al SE de Santiago, en el Estero Coyanco, se evidencia una falla inversa vergente al este la cual será llamada falla Estero Coyanco. Esta es una zona de falla de 30 m de ancho, de orientación NNO-SSE y manteo al oeste, con tres núcleos de falla, donde dos de estos núcleos de falla están cortando depósitos Cuaternarios. Tercero, en el área de Baños Morales en el Río Volcán, la caracterización detalla a nivel de afloramiento, revelan la presencia de bandas de deformación dúctil y bandas de deformación frágil en la zona de falla El Diablo. La deformación frágil en la Falla El Diablo es compatible con transpresión dextral en una zona de falla orientada N-S. Las 3 fallas estudiadas evidencian direcciones de acortamiento E-O a NE-SO, las cuales son consistente con la dirección de convergencia de las Placas Tectónicas, campos de velocidad derivados de GPS y mecanismos focales de sismicidad.

## Abstract

Chile´s Santiago Metropolitan region holds a population over 7 million, been the most populated area of Chile. In this segment of the Andean orogen, important crustal seismicity and evidence of Quaternary faulting was reported. The San Ramon Fault and the San José de Maipo Fault, are the only two known seismic sources. This shows the lack of knowledge on neotectonics in the most populated area of Chile, one of the most seismic countries in the world. The aim of this thesis is to contribute in increase the knowledge of seismic sources located in the Principal Cordillera near the Metropolitan region, though a neotectonic approach based on remote sensing techniques, field work mapping and data analysis.

Three geological faults has been characterized. First, the El Arrayan Fault (EAF). A WNW-ESE orientated, ~ 13 km length, mainly left-lateral strike-slip fault, evidenced by aligned fault scarps, saddles and deflected streams channels over Quaternary deposits, and also fault rock exposure. Peak ground accelerations up to 0.7 g less than 500 m from the EAF fault trace at surface are obtained for the EAF rupture scenario, using a Mw 6.4 for the characteristic earthquake based on length of fault rupture, which indicates important seismic hazard in the near-field of the EAF. Second, 40 km SE of Santiago, in the Estero Coyanco, a east-vergent reverse fault is observed and will be called the Estero Coyanco Fault. This is a 30 m wide fault zone in a NNW-SSE orientation, comprising three fault cores, in which two of them are cutting Quaternary deposits. Third, at the Baños Morales area, in the Volcán River, outcrop-level detailed characterization, reveals the presence of ductile shear bands and brittle deformation at the El Diablo Fault area. The brittle deformation in the El Diablo Fault its compatible with dextral transpression in a N-S orientated fault zone. The three studied faults evidences E-W to NE-SW shortening directions, consistent with the Tectonic Plate convergence direction, GPS derived velocity fields and seismic focal mechanism.

## Agradecimientos

Quisiera agradecer a todas las personas que estuvieron presentes durante el desarrollo de esta tesis. En especial quisiera agradecer a mi profesor guía, Gregory, un excelente profesor, excelente guía y sobre todo excelente persona, la cual me ayudó y aconsejó durante toda la tesis. También quisiera agradecer a mi profesor co-guía, Sergio Sepúlveda, por la ayuda brindada y la confianza entregada. También agradecer al profesor Gabriel por acceder a ser parte de la comisión. Al proyecto NERC (Newton Fund) project NE/N000315/1 "Seismically-induced landslides in Chile: New tools for hazard assessment and disaster prevention", en el cual está inserto este proyecto de Magíster.

A todos los funcionarios del departamento de geología, a los profesores y también a los alumnos que he tenido el gusto de hacerles clases.

Agradecer profundamente a los integrantes del laboratorio de tectónica por hacer los días más agradables. También agradecer a mi familia por el apoyo brindado y sobre todo a Catalina por estar siempre a mi lado apoyándome.

## Table of contents

# Index of figures

## Index of tables

# Chapter 1: Introduction

## 1.1 Motivation

The South Central Andes between 33°-34°S it is one of the highest active growing orogens on Earth, with shallow and abundant seismicity and with high summits reaching elevations up to 6 km coincident with the volcanic arc. Here, crustal deformation is accommodated by displacement along fault zones, allowing shortening and uplift in addition to translation materials along strike slip faults. When crustal faults rupture an earthquake occurs; releasing accumulated elastic strain energy that generates seismic waves. Chile is one of the most seismically active countries in the world. The most recurrent and higher in Mw are the subduction earthquakes, along the tectonic plate interface (eg. Mw 9.5 Valdivia in 1962; Mw 8.8 Maule in 2010), however, seismic events of moderate to large Mw, also occur in the main Andes at shallow depth (eg. Mw 6.3 Las Melosas in 1958 and Mw 6.5 Curicó in 2004).

Santiago Metropolitan Region of Chile holds approximately the 40% of Chile´s population and it's characterized by presenting shallow seismicity in its surroundings. With the fast tectonic deformation rates and high elevations of the Central Andes, it is important to understand these seismic events, because they can cause potentially destructive earthquakes, resulting in major economic and social impact for the nation. In order to better understand and prepare for these natural disasters, the need to characterize the earthquake potential of individual crustal faults is important, in particular near populated centers.

The Center of Neotectonics Studies at the University of Nevada, Reno, defines neotectonics as "the study of geologically recent motions of the Earth´s crust, particularly those produced by earthquakes, with the goal to understanding the physics of earthquake recurrence, the growth of mountains, and the seismic hazard embodied in this processes". Studies of this discipline along both sides of the Andes attempt to understand the behavior of different seismic sources and their associated coseismic geohazards.

Along the eastern flank of the Central Andes, recent deformation is fairly well constrained. Numerous studies have been develop in the Puna (Cortés et al., 1987; Marrett et al., 1994; Hermanns et al., 2001); in the Pampean Ranges (Costa et al., 1999; Massabie et al.,2003; Casa et al., 2010), in the Precordillera (Cortes et al., 2006; Ahumada & Costa, 2009; Perucca et al., 2011; Perucca et al., 2013), and also in the broken foreland south of 35-36°S (Folguera et al., 2004). Related to this, a complete database of Quaternary faults in Argentina, with locations, age and activity rate of earthquake-related is found in Costa et al., (2000). However, along the western flank of the Andes, in Chile less attention has been focus on

neotectonics of crustal structures. In the late Cenozoic, at northern Chile, deformation and uplift in the coastal cordillera is related directly to the interplate seismic zone (Armijo & Thiele 1990; Allmendinger et al., 2005; Gonzales et al., 2003; Riquelme et al., 2003; Marquardt et al., 2004; Carrizo et al., 2008). Further to the east, Audin et al., (2003) reported Plio-Quaternary folding and faulting in the Cordillera de Domeyko. A more detail description of the main known Neogene active structures in Chile it's in the compilation work of Lavenu (2006).

Recently, a lot of attention focused on improving the knowledge about the seismic potential of the geological structures close to Santiago, the capital and most populated city in Chile with over 7 Million in habitants and located along the western flank of the main range. The Metropolitan Region in Chile exhibits numerous crustal faults that could be potential seismic sources (Fig. 1.1). Most of these structures are late Cenozoic structural systems related to the development of the Abanico basin (Charrier et al., 2002; Charrier et al., 2007) and the Aconcagua fold and thrust belt (Ramos et al., 1996; Giambiagi et al.,. 2003). Recent neotectonic studies identified active crustal faults close to Santiago, like the San Ramon fault, a N-S striking, west-vergent reverse fault which produce a prominent fault scarp at the foothills of the western flank of the Principal Cordillera (Rauld, 2002; Armijo et al., 2010; Rauld 2011; Vargas et al., 2014), and also the San José de Maipo fault inside the Maipo Valley, constituted by metric south-vergent reverse faults and drag folds deforming a high fluvial terrace (Lavenu et al., 1994; Lavenu et al., 2000; Lavenu, 2006; Lavenu & Cembrano, 2008). Almost 80 km north of Santiago, the Cariño Botado fault, N-S striking west-vergent reverse fault located just to the east of San Felipe – Los Andes, was reported as active by morphometric analysis, fault scarps and faulted Quaternary deposits (Troncoso, 2014; Medina, 2018). Nevertheless, besides these three faults it is unknown what other regional crustal faults may be active. Farias et al., (2006) prosed that the El Diablo Fault, due to the shallow seismicity, should be active, but no further studies have been done. In a bigger scale, the WAT (West Andean Thrust) is a first-order tectonic model proposed by Armijo et al., (2010) in which now a days the Andes at the 33.5°S is a primary west-vergent orogen, evolving to a double vergent configuration. The San Ramon Fault and the Cariño Botado Fault represents part of the active west vergent main structures of the WAT.

In order to better understand the relationship within seismic sources and their consequences, Leyton et al., (2010) applied probabilistic methodologies of seismic hazard and adapt them to central Chile incorporating intraplate, medium deep, and shallow seismicity as seismic sources, coming through with maps showing maximum horizontal acceleration (PGA) for a certain probability in a defined time spam. Their results shows that the most important expected PGA is in the coast in base of the high interplate seismicity (up to 0.83 g), but in the Santiago

Metropolitan area, by the influence of intermediate-depth and shallow earthquakes PGA values of 0.55 to 0.72 g are expected . Pérez et al., (2014) and Estay et al., (2016) explored ground motion generated by a San Ramon fault rupture, estimating peak ground accelerations (PGA) by using a kinematic fractal k-2 composite source model and empirical equations of Chiou and Youngs (2014) for crustal faults respectably. Their results yield that the Metropolitan region is exposed to PGA up to 0.7-0.8 g in the hangingwall of the fault.

On the other hand, regarding an important coseismic geohazard, Antinao & Gosse (2009) compared "rockslides" occurrence patterns with lithology, geological structures, timing and seismicity in the southern Central Andes of Chile. They suggest a causative relationship between active tectonics in Late Cenozoic structures of the western Cordillera Principal and large landslides, proposing that shallow seismicity is the main trigger mechanism. However, Moreiras & Sepulveda (2014) indicated that seismic tremors have been widely suggested as the main triggering mechanism in Chilean collapses, but paleoclimatic conditions are considered as the main cause of Argentinean giant landslides. These different approaches denote the lack of multidisciplinary studies focused on the controversy about seismic or climate trigger mechanisms for landslides in the Central Andes.

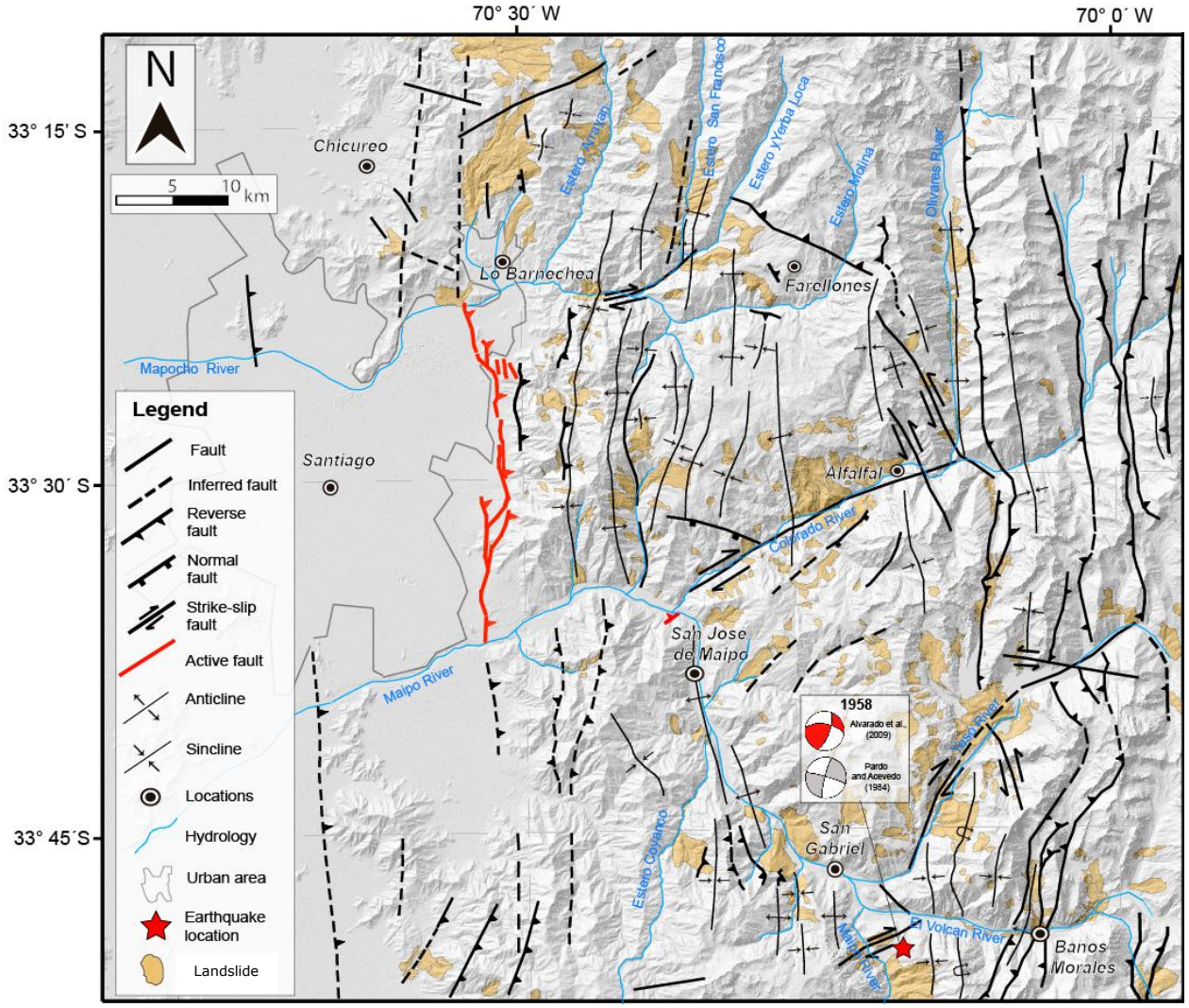


Figure 1.1 Compiled structural map of the Principal Cordillera of the central Chilean Andes between 33°-34°S, near Santiago Chile´s capital. The main structures at regional scale are shown. Active fault are marked by a red line. The Las Melosas 1958 Mw 6.3 earthquake epicenter it is shown by a red star. Faults and structures compiled from: Thiele (1980), Wall et al., (1999), Selles & Gana (2001), SERNAGEOMIN (2003), Giambiagi et al., (2003), Fock (2005), Calderon (2008), Lavenu & Cembrano (2008), Rauld (2011), Armijo et al., (2010), Deckart et al., (2013), Quiroga (2013), Castro (2012), Villela (2014) and Piquer et al., (2016). Landslides compiled from Antinao & Gosse (2009).

## 1.2 First order open ended scientific questions about seismic hazard in Central Chile

Thus there are a number of open-ended first order scientific questions related to the seismic hazard in Central Chile. Specifically, the following questions arise:

A) Are there other active crustal faults near Santiago that are possible seismic sources?

B) What´s the seismic hazard implications related to these faults?

C) What is the relation of these faults to first order Andean structural systems?

## 1.3 Goals of the thesis

The goal of this thesis is to address the above questions in order to update the knowledge about faults as crustal sources and the seismic hazard implications in the most populated region in Chile.

### 1.3.1 Working Hypothesis and Objectives

The work hypothesis is that the Central Andes at 33°S it is an active orogen. This mountain chain growth is, in part, produced by the ongoing activity of crustal faults. Thus, these crustal faults should be visible in the surface and they are seismic sources capable of producing shallow earthquakes with associated strong ground motions, and so important sources of seismic hazard.

### 1.3.2 The main objective of this thesis

The main objective of this thesis is to update the crustal seismic hazard model, by exploring crustal faults in the Metropolitan Region of Chile.

### 1.3.3 The specific objectives of this Thesis

A) Compile a database of potentially active structures from the existing literature.

B) Explore the potential presence of unrecognized crustal faults through remote sensing mapping, and field mapping.

D) Define the Quaternary behavior of the "new" crustal faults.

E) Evaluate seismic hazard implications of the structures.

## 1.4 Central Andes geological settings

The Central Andes from 33°S to 34°S is characterized by the ongoing subduction of the Nazca Plate beneath the South American Plate since the Jurassic (ca. 190 Ma) (Coira et al., 1982; Jordan et al., 1983; Allmendinger, 1986; Isacks, 1988; Mpodozis and Ramos, 1989, Charrier et al., 2007). It is situated immediately south of the flat-slab segment of the subducted oceanic Nazca Plate (28-33°S) (Cahill & Isacks, 1992; Yañez et al., 2002). Current absolute plate motion relative to hot spots for the South American and Nazca Plates are 4.8 and 3.2 cm/year, respectively and oriented N78°E (Fig.1.2a; Gripp & Gordon, 2002). Convergence rate of 8 cm/year in a N78°E direction was proposed by DeMets et al., (1994). According to Angermann et al., (1996), present-day plate convergence direction is N77°E and convergence rate is of 65 mm/year.

Near 33°S is the southern limit of the Pampean flat slab segment (Barazangi & Isacks 1976, 1979; Ramos et al., 2002), south of there, there are a few important first order geological features to highlight, such as the reappearance of volcanic chain and Central Depression, and the curve of the continental margin from N-S to the north, to NNE-SSW to the south, known as the Maipo Orocline (Arriagada et al., 2013). Between 33°-34°S, the first order morphotectonic units are from west to east, Coastal Cordillera, Central Depression, Principal Cordillera, Frontal Cordillera and Precordillera (Fig. 1.2b). The Coastal Cordillera is made up of late Paleozoic-Triassic basement along its western flank and east dipping Mesozoic sequences along its eastern flank (Thomas, 1958). The Central Depression is filled with alluvial deposits of Pleistocene to Holocene age (Thiele, 1980; Wall et al., 1999; Rauld, 2002). The Principal Cordillera approaches 6.000 m above sea level (a.s.l.), it can be divided into 2 parts, the western Principal Cordillera composed mainly by volcanic and sedimentary Cenozoic rocks of Abanico and Farellones Formation, related to the Abanico Basin domain (Charrier et al.,

2002, 2005), and the eastern Principal Cordillera constituted by Mesozoic mostly sedimentary rocks related to the Aconcagua fold and thrust belt domain (Ramos et al., 1996; Giambiagi et al., 2003).

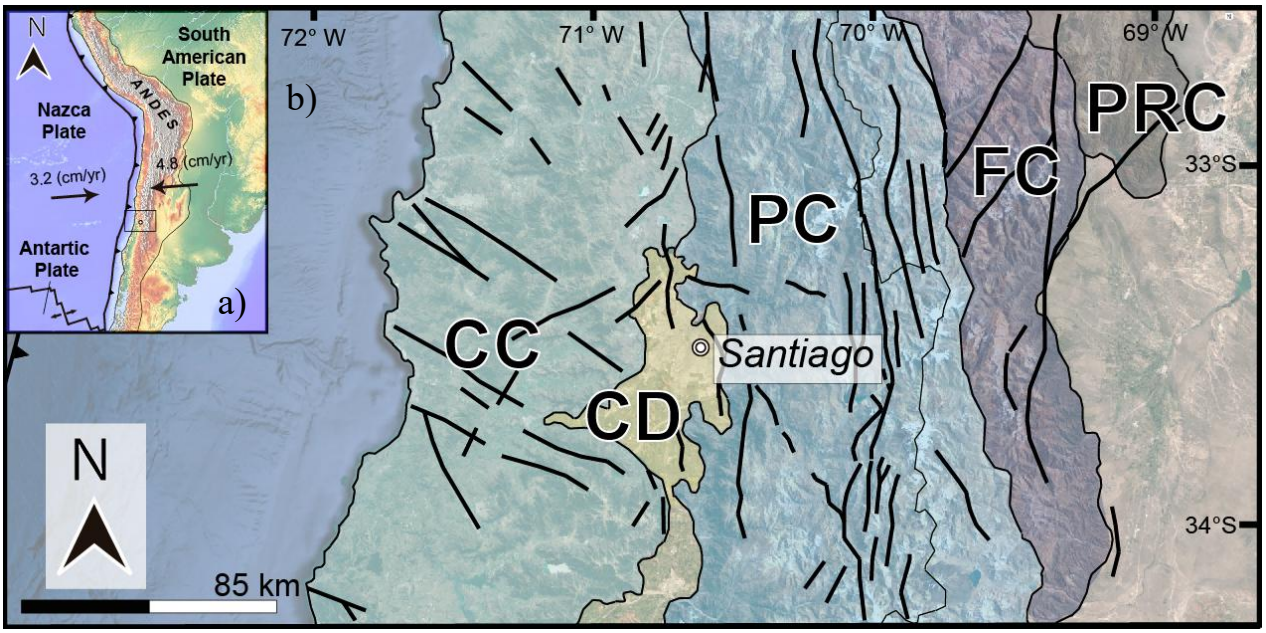


Figure 1.2 a) Tectonic configuration of the western border of South America, black arrows shows current absolute plate motion relative to hot spots frame for the South American and Nazca plates (Gripp & Gordon, 2002). Black box shows the position of Fig 1.2b. b) Main morphotectonic units of Central Andes between 33°-34°S. CC: Coastal Cordillera; CD: Central Depression; PC: Principal Cordillera; FC: Frontal Cordillera; PRC: Precordillera.

GPS velocity field by Brooks et al., (2003) for the South Central Andes, shows between 33° - 35°S, velocities of 19.5 -22.5 mm/yr directed to the ENE in the Andean forearc, and 12 mm/yr directed to the ENE at the Andean backarc (Fig. 1.3). Mateo et al., (2009) obtained GPS station data in the Aconcagua Mountain at the Central Andes between 2006 and 2008, estimating average horizontal velocity of 23 mm/yr toward NE.

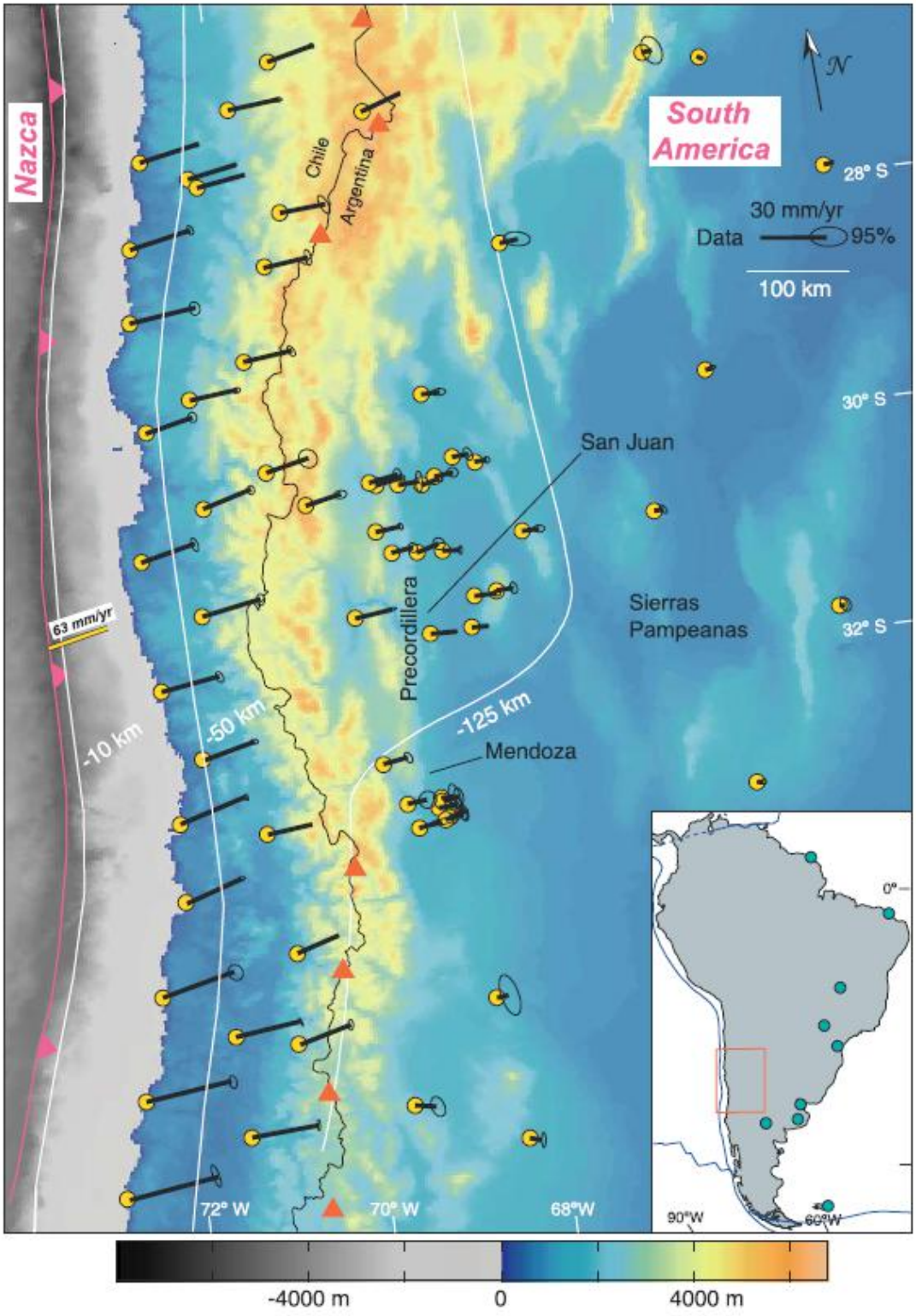


Figure 1.3 GPS velocity field superimposed on Andean topography. Inset shows map of South America with the study area highlighted (red box) and stations used to define the reference frame (blue circles). Extracted from Brooks et al., (2003).

## 1.5 Southern Central Andes Cenozoic tectonic evolution

During the late Eocene to late Oligocene (37-16 Ma) from 27°S to 39°S a NNE volcanic continental intrarc basin developed (i.e. the Abanico basin) were the Abanico Formation and Farellones Formation were deposited (Charrier et al., 2002, 2005). The dimension of the basin, more than 1000 km long, 70 km wide and approximately 3000 m of thickness make this a first order tectono-paleogeographic feature (Charrier et al., 2009).

In a first stage, extensional setting dominates and the Abanico Formation (mainly volcanic and sedimentary) was deposited. The extension was accompanied with crustal thinning, strong subsidence, normal faults (Los Angeles-Infiernillo, Pocuro-San Ramon, El Diablo-El Fierro; Fock 2005; Charrier et al., 2009), high thermal flux and an intense and wide magmatic arc (Charrier et al., 2002; Nystrӧm et al., 2003; Charrier et al., 2005).

Between the Oligocene to Early Miocene (20-15 Ma), some of the previous extensional structures reactivate changing the motion sense, causing a partial tectonic inversion of the basin (Godoy y Lara, 1994; Charrier et al., 2002, 2005, 2007; Fock, 2005; Jara y Charrier, 2014), originated due to the change from extensional to a regional compressive setting by the break of the Farallon Plate into two plates, which increased the convergence rate and reduced the obliquity of the convergence angle (Pardo – Casas and Molnar, 1987). Synchronously with this compressive setting, the younger Farellones Formation (mostly volcanic) was deposited in the central part of the basin. The Farellones Formation is gently folded except in its edges where is strongly deformed (Fock, 2005). Along the basin boundaries, Farellones Formation overlays uncoformably the Abanico Formation or shows grow strata in its lower part (Charrier et al., 2002; Fock, 2005). This compressive event was accompanied by crustal thickening, intense volcanic activity and also the emplacement of different plutonic bodies intruding both Formations (Charrier et al., 2002; Kay et al., 2005; Muñoz et al., 2009).

After 16 Ma, compressive deformation migrated toward the eastern Principal Cordillera, constituted predominantly by Mesozoic sedimentary sequences (Thiele, 1980). Most of the shortening in this region was accommodated between 16 and 8.5 Ma during the develop of the Aconcagua fold and thrust belt (Giambiagi et al., 2003). After 8.5 Ma, the inversion of rift related high angle normal faults as reverse faults uplifted the Proterozoic-Lower Triassic rocks that constitute the Frontal Cordillera just to the east of the Principal Cordillera (Giambiagi et al., 2003). In this period, some out of sequence fault deformed the Abanico Basin (Giambiagi et al., 2003; Fock, 2005; Charrier et al., 2009), and also the Andean orogen experiences a tilt to the west (Charrier et al., 2009; Farias et al., 2010). Figure 1.4 summarizes the previous mentioned tectonic evolution.

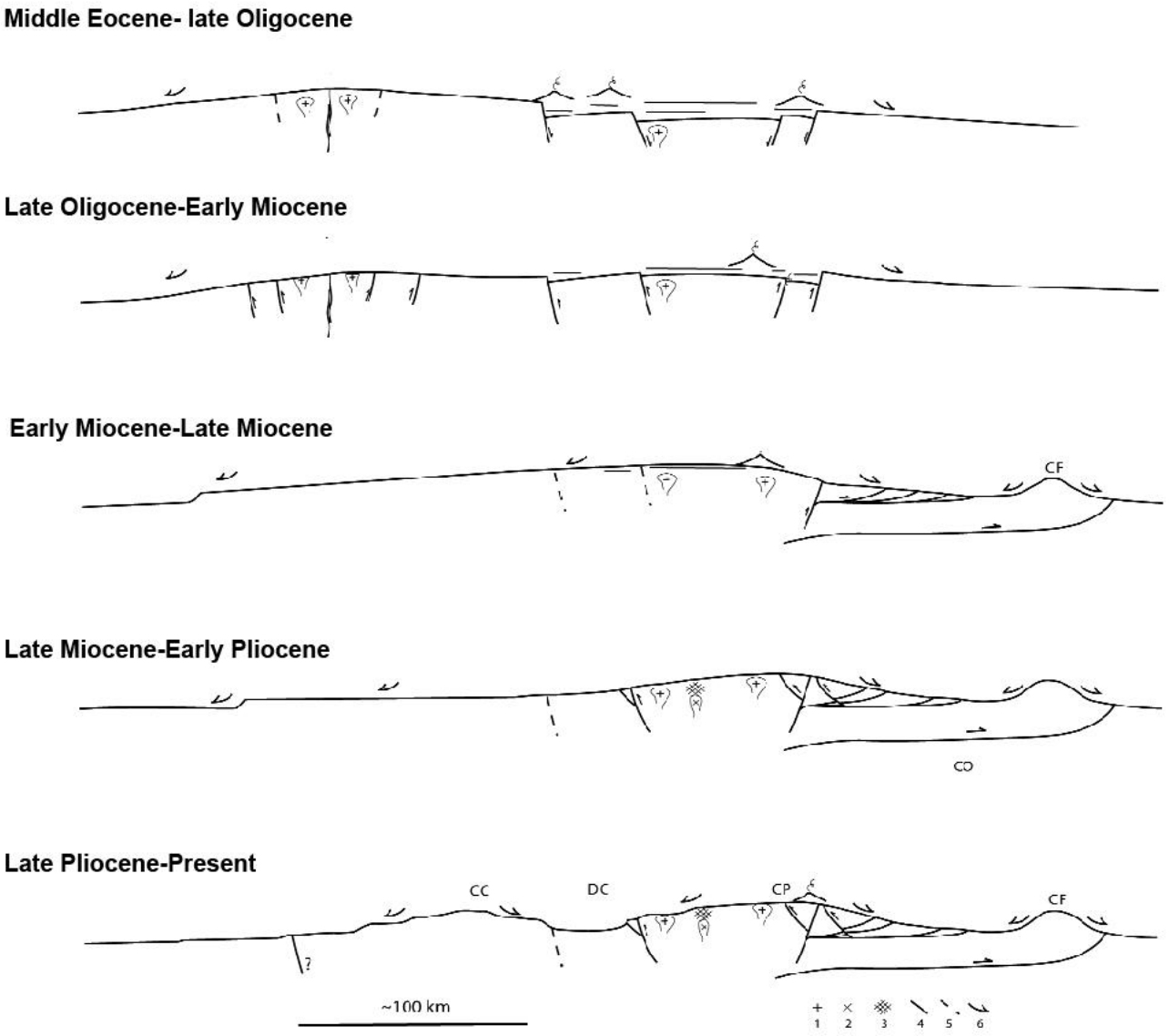


Figure 1.4 Schematic profiles of the Andean orogeny showing the tectonic and paleogeographic during Cenozoic south of the 27°S. a) Middle Eocene-Late Oligocene; b) Late Oligocene-Early Miocene; c) Early Miocene-Late Miocene; d) Late Miocene-Early Pliocene; e) Late Pliocene-Present. CC, coastal Cordillera; CF, Frontal Cordillera; CP, Principal Cordillera; DC, Central Depression; 1, Intrusive; 2, Subvolcanic intrusive; 3, Hydrothermal alteration; 4, Active faults; 5, Inactive faults; 6, Sediment transport direction. Figure extracted from Charrier et al., (2009).

## 1.6 Main structures between 33°-34°S

In this section the most relevant regional structures in the study area reported by previous authors are shown and described (Fig. 1.5). They will be described from west to east.

### 1.6.1 Eastern flank of the Coastal Cordillera and the western limit of the Central Depression

Infiernillo fault: The Infiernillo fault outcrops in the cuesta de Chacabuco area and was interpreted as a west dipping normal fault by assuming the nature of the Central Depression as a graben (Aguirre, 1957; Aguirre, 1960). Fuentes et al., (2002) also interpreted it as a normal fault. Fock (2005) reports a 010°/80°E fault, evidencing dip-slip kinematic indicators, overthrusting of the oriental block over the occidental block, and also drag folds. This fault has a regional influence and would have an equivalent more to the south with the Cerro de Renca Fault (Fock, 2005).

Cerro de Renca fault: In Renca area, north side of urban Santiago, the Cerro de Renca Fault was described by Sellés (1999) as a previously normal and after inverted west-vergent reverse fault, which overthrust the Cenozoic Abanico Formation over the Mesozoic Lo Valle Formation.

Portezuelo de Chada fault: In the Portezuelo de Chada, between Challay hill and Negro de Chada hill, Sellés y Gana (2001) reported a west dipping normal fault. Instead, Fock (2005) propose a west-vergent reverse fault in base of old Abanico Formation rocks overthrusting young Abanico Formation rocks.

### 1.6.2 Western flank of the Principal Cordillera

San Ramon fault: The San Ramon fault strikes N-S and is located between the Central Depression and the Principal Cordillera, particularly at the foothills of the mountain front. This fault was interpreted as a normal fault by Bruggen (1950) and Thiele (1980) acting as the eastern limit of an extensional graben. More recently, it was interpreted as a west-vergent reverse fault, in base of the prominent fault scarps at the foothills of the Ramon range mountain front (Rauld, 2002). Armijo et al., (2010) propose

that the San Ramon fault constitute part of the WAT (West Andean Thrust), a first-order tectonic model regarding the architecture of the orogen, in which the San Ramon fault is an active west-vergent thrust ramp at a the front of a basal detachment controlling the present days Andean uplift and deformation between 33°-34°S. However, Farias et al., (2010) proposed that the San Ramon fault acts as a backthrust of a main east-vergent ramp-detachment crustal scale structural Andean model. Topographic analysis in young scarps indicates plausible seismic event up to Mw 7.4 (Armijo et al., 2010). Paleoseismic analysis shows recurrent faulting with slip of 5 m in Quaternary deposits, 17-19 k.y. and 8 k.y. ago, estimating Mw up to 7.5 (Vargas et al., 2014). Slip rate of 0.4 mm/yr was calculated by Armijo et al., (2010). This information shows that this fault it's an important seismic source.

Barrientos et al., (2004) show shallow seismicity (<20 km) underneath the western flank of the Principal Cordillera. Pérez et al., (2014) defines a N-S seismicity band spatially correlated with the mountain front, located between 10-15 km depth, and compressive focal mechanism. No historical earthquake had reported for the San Ramon fault, neither historical surface ruptures.

Pocuro fault: The potential continuation and likely connection of the San Ramon fault to the north is the Pocuro fault in Los Andes-San Felipe. This fault was defined by Aguirre (1960) in Los Andes area, as a N-S band of mylonite rocks of tens of meters wide. It was interpreted as a normal fault bounding the central depression to the east (Aguirre, 1960; Carter y Aguirre, 1965; Aubouin et al., 1973) similar as the San Ramon fault in Santiago. Authors like Charrier et al., (2002), Fuentes (2004), Jara et al., (2013) and Jara & Charrier (2014), propose that this fault has 2 different periods of activity; first as a normal fault related to the Abanico basin development, and second, as a strike-slip reverse fault during the Abanico basin inversion. More recently Troncoso (2014) reported the Cariño Botado fault, a west-vergent reverse fault with Quaternary activity in the same location of previous defined Pocuro fault. Geomorphological analysis and fault rock outcrop evidence the recent motion of this fault, estimating plausible seismic events of Mw 6.0-6.5 (Troncoso, 2014). Campbell (2005) proposed that the Pocuro fault is the northern prolongations of the San Ramon fault. Between Santiago and Los Andes, Thiele (1980) reports 2 parallel N-S normal faults in the Estero Colina and north of it, and inferred a south prolongation to Cerro Manquehue and Lo Barnechea. After, Gana & Wall (1997) reported a "Pocuro Fault Zone", in the Estero Colina, evidenced by alienated discrete hydrothermal alteration related to Oligocene-Miocene minor intrusive bodies and N-S trending fault traces, but no south or north prolongation was propose. On the other hand, Wall et al., (1999) also report two nearly N-S no kinematics fault traces at the "Pocuro Fault Zone" (previously defines by Gana & Wall 1997), but they continuous the fault to the south, deflecting it

to the west acquiring a NE direction and then again taking a N-S trending but now as a west dipping normal fault ending in the Chicureo Valley.

### 1.6.3 Main Principal Cordillera

El Coroinal fault: El Coroinal fault is a N-S trending west-vergent reverse fault located in the Olivares River defined by Ramos et al., (1991) and after observed and mapped by Castro (2012) and Quiroga (2013). This fault overthrust the Colimapu Formation over the younger Abanico Formation, creating a syncline to the east of the Rio Olivares.

Laguna Negra fault: The Laguna Negra fault is a N-S trending west-vergent reverse fault (Fock 2005; Deckart et al., 2013) that goes from the Laguna Negra in the Yeso River, to the Plutón La Gloria at the Colorado River to the north. Fock (2005) proposed that this fault continuous to the north connecting with the Coroinal fault. To the south of Yeso River the fault trace disappears but an overturned anticline with west vergence is observed and can be related to this fault (Fock, 2005). The epicenter of the 1958 Las Melosas earthquake it is in the prolongation of this fault to the south of the Volcan River.

Chacayes Yesillo fault: The Chacayes-Yesillo fault was described as a high angle west-vergent reverse fault, which puts in contact the Cenozoic Abanico Formation to the west with the Mesozoic Colimapu Formation to the east (Baeza, 1999; Bustamante, 2001; Charrier et al., 2002). Bustamante (2001), evidence slickensides, slickenlines, high fractured rocks and minor decametric folding in the fault surroundings. Fock (2005) reports a 020°/80°E fault, from the Estero Morales to the High Maipo River, and propose that this fault is related with a tie anticline in the Colimapu Formation to the east of the fault, and a syncline with its oriental flank overturned to the west, to the west of the fault.

El Diablo fault: The El Diablo fault was defined in the Volcan River valley and Yeso River valley. This is mostly a nearly vertical N-S east-vergent reverse fault (Charrier et al., 2002; Fock et al., 2005; Farias et al., 2010). It is characterized by thrusting the Cenozoic rocks over the Mesozoic sequences (Fock 2005; Charrier et al., 2002, 2005). It marks a change between the Abanico basin domain to the west and the Aconcagua fold and thrust belt to the east. The south prolongations of this fault forms the El Fierro fault system (Charrier et al., 2009; Farias et al., 2010) received different names depending on the areas in which this fault system was studied, from the Yeso

River (Fock, 2005) to the Maule River (Astaburuaga, 2012). It is called the El Diablo fault at 34°S in the Maipo River (Fock, 2005); Las Leñas-Espiñoza fault at 34°S in the Cachapoal River (Charrier et al., 2002); El Fierro fault at 35°S in the Tinguiririca River (Davidson and Vicente, 1973). Barrientos et al., (2004) shows seismicity underneath the El Diablo fault trace, with hypocenters between 0-10 km depths. Perez et al., (2014) present a N-S seismicity band spatially correlated with the El Diablo fault and Chacayes-Yesillo fault, located at 5-15 km depth, very disperse but uniformly distributed on it, reflexing the complex structural style in the zone (Perez et al., 2014). Barrientos et al., (2004), Farias et al., (2010) and Pérez et al., (2014), agrees that most of the seismic activity is located near the Chile-Argentina boundary, particularly alienated with the El Diablo fault and it south prolongation. Farias et al., (2006) reported a NNE-SSW compression in a N-S fault plane as solution for focal mechanism for the Mw 6.5, 2004 august 28 earthquakes in the Teno River, at the southern prolongation of the El Diablo fault.

Besides this mentioned regional-scale N-S striking basin margin faults that dominated the western and eastern flank of the Abanico basin, Piquer et al., (2016) reported numerous mappable arc-oblique NW-SE and NE-SW Cenozoic faults that reflects the architecture of the pre-Andean basement (Fig. 1.6).

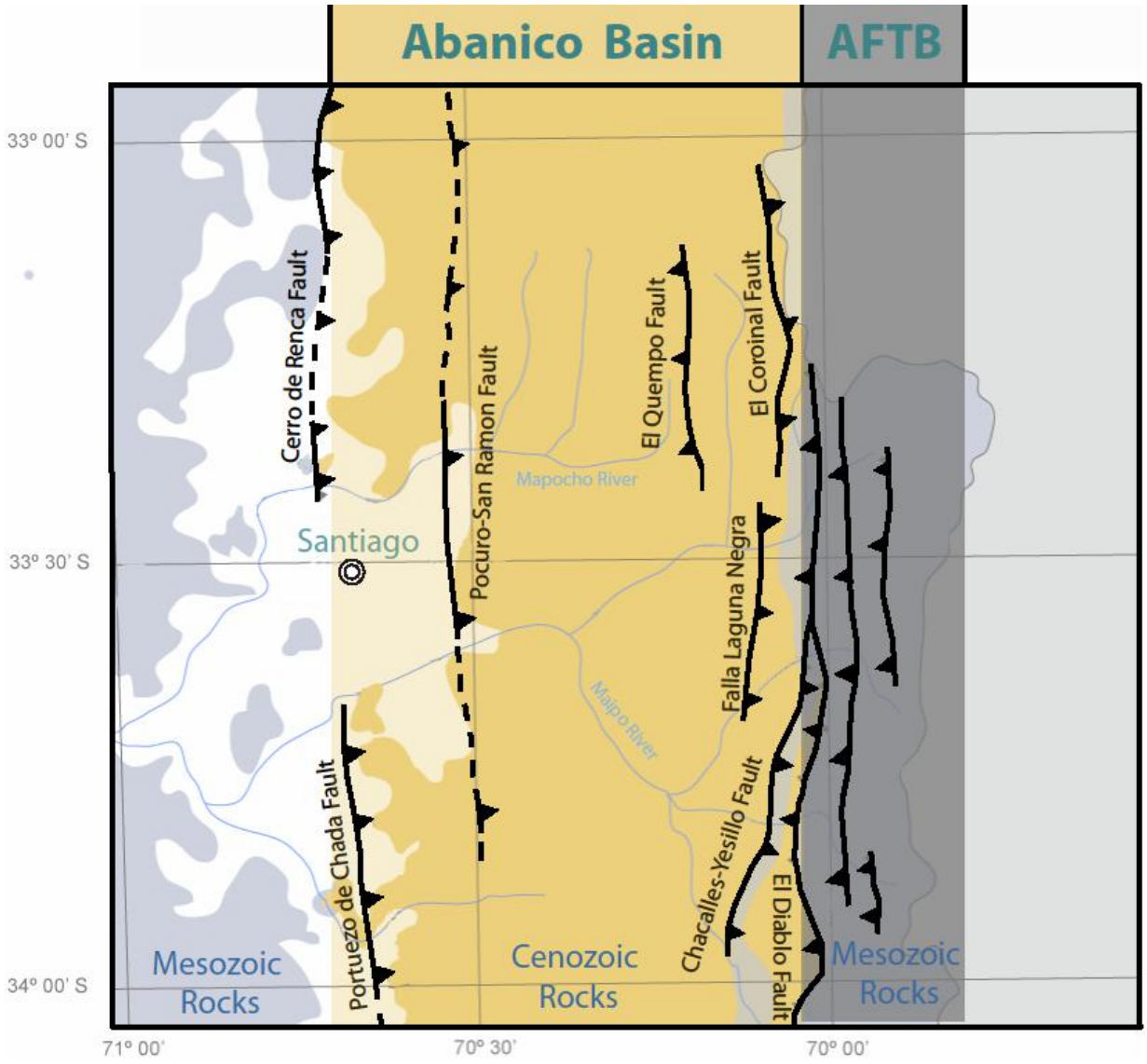


Figure 1.5 Simplified geological map of the Central Andes between 33°-34°S. Main structures are highlighted in thick black lines. Abanico basin and AFTB (Aconcagua fold and thrust belt) structural domains are indicated. Modified from Fock (2005) and Quiroga (2013).

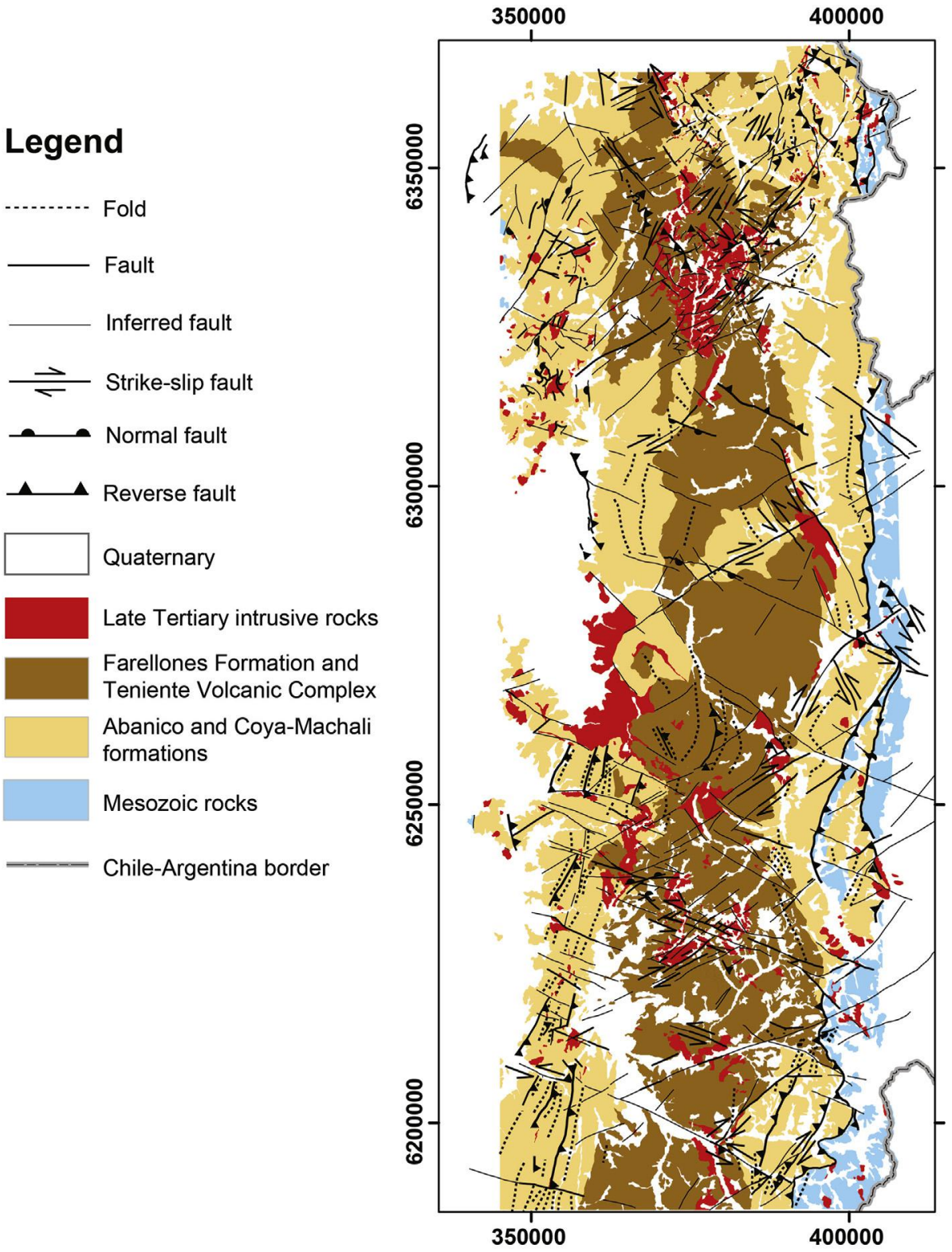


Figure 1.6 Simplified geological map of the Andes of central Chile. Extracted from Piquer et al., (2016)

## 1.7 Seismicity

### 1.7.1 Seismotectonic regionalization

To evaluate seismic hazard, authors all around the world, like Phuong (1991), Kebede (1996), Mirzaei et al., (1998) and Assinovskaya et al., (2014) have subdivided geological regions into geological sub regions seismically homogeneous called "seismic sources". This is a terrestrial zoning related with the seismic frequency and the local earth crust structure. This means that parameters of the Gutenberg and Richter relationship, i.e. the relationship between the magnitude and the frequency of earthquakes of at least that magnitude, remain fixed and can be attributed to the tectonic characteristics of that subregion. Such subdivision is called seismotectonic regionalization. Gregori & Christiansen (2018) subdivided the Andes between 28°-36°S in five main seismic sources or tectonic subregions (Fig. 1.7), in base of the morphostructural units and the neotectonic studies; (1) Basement of the Cuyana Basin: a widely distributed shallow seismicity concentrates in the southern end of the Precordillera morphostructural unit south of 32°, around Mendoza city (Argentina), related to inherited structures from the Cuayana basement; (2) Precordillera: to the west of the San Juan city (Argentina), where shallow seismicity is distributed in N-S lineaments alienated with regional structures of Precordillera morphotectonic unit; (3) San Juan: The surrounding of the San Juan city (Argentina) it's defined as a sismotectonic region included in the Precordillera tectonic subregion, because of the location and concentration of historical large Mw earthquakes (Mw>6.8); (4) Western Sierras Pampeanas: To the east of San Juan city, in the Andean foreland, shallow seismicity it's densely concentrated in the Sierra de Pie de Palo, related to the Sierras Pampeanas west-vergent structures; (5) Cordillera Principal: below the western side of the Andes, between 33°-35°S, shallow seismicity it's evidenced in the Principal Cordillera, related to the present day crustal deformation underneath the orogen. Part of Santiago Metropolitan Region locates in the Principal Cordillera seismotectonic region.

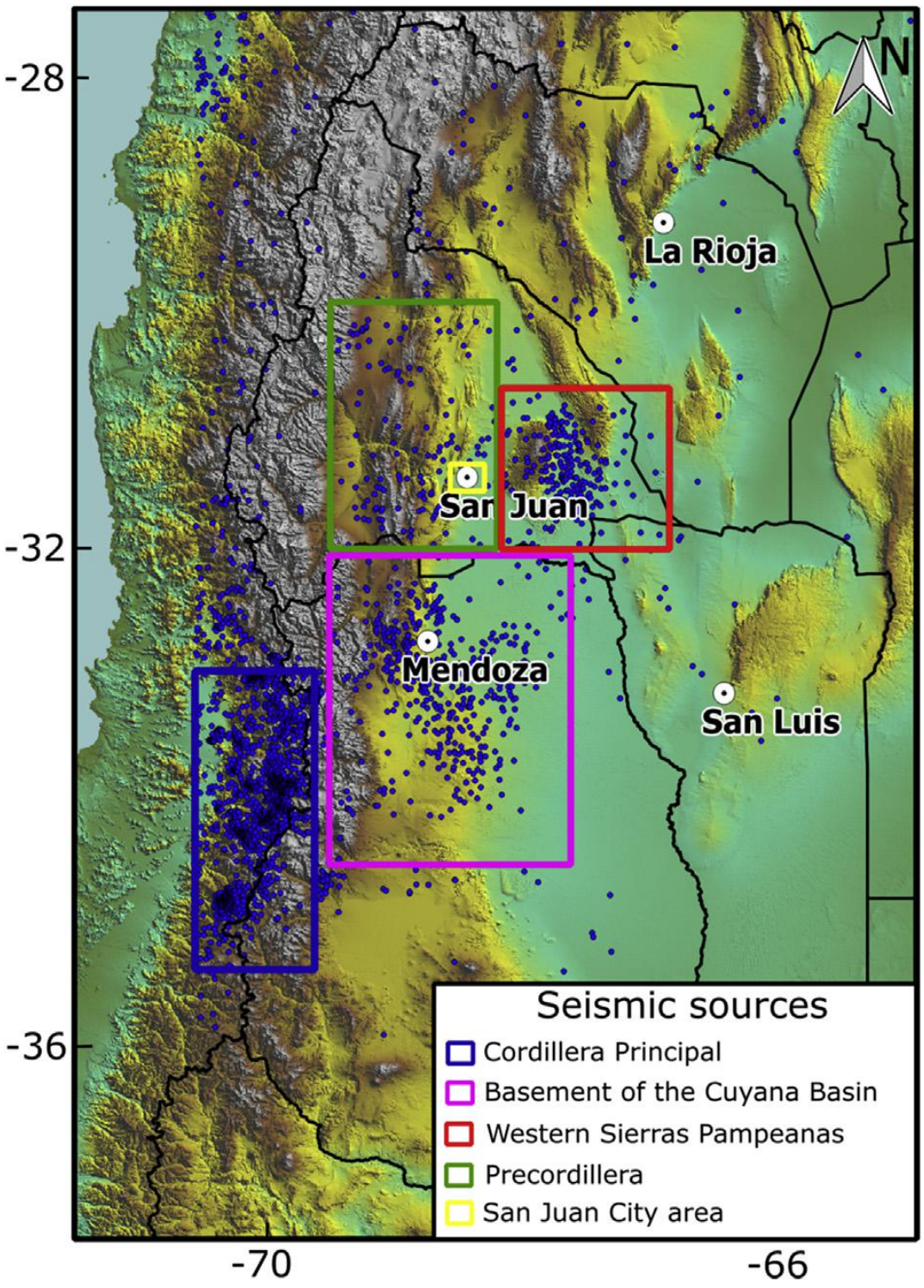


Figure 1.7 Seismic records of the Central Andes in Chile and Argentina. Seismic sources are indicated. Extracted from Gregori & Christiansen (2018).

### 1.7.2 Seismicity in Central Chile

In central Chile, at orogen scale, it is well known that there are 4 seismogenic zones or seismogenic sources (Fig. 1.8): large, shallow (0-50 km) megathrust earthquakes below the coast along the Tectonic Plates contact (interplate); large deeper (50-200 km) tensional and compressional events within the subducting Nazca Plate (intermediate depth); very shallow (0-30 km) crustal seismicity within the South American Plate, mostly in the mountain region of central Chile (intraplate); and moderate magnitude event occurring approximately 150 km from the coast to the west, due to the flexure of the Nazca Plate previous to the subduction (outer-rise) (Barrientos et al., 2004; Leyton et al., 2010). The shallow intraplate seismicity in the transition zone between a subhorizontal subduction to a more steeply dipping subduction, concentrates mainly along the western flank of the Andean mountain chain (Barrientos et al., 2004). This activity is likely the surface consequence of the dip angle change in the subducting Nazca Plate (Gutscher et al., 2000). This shallow seismicity is related to the released energy in crustal faults, caused by the tectonic stress transferred to the mountain zone. Very shallow (<30 km) seismicity characterize the Santiago Metropolitan region (Barrientos et al., 2004; Pérez et al., 2014)

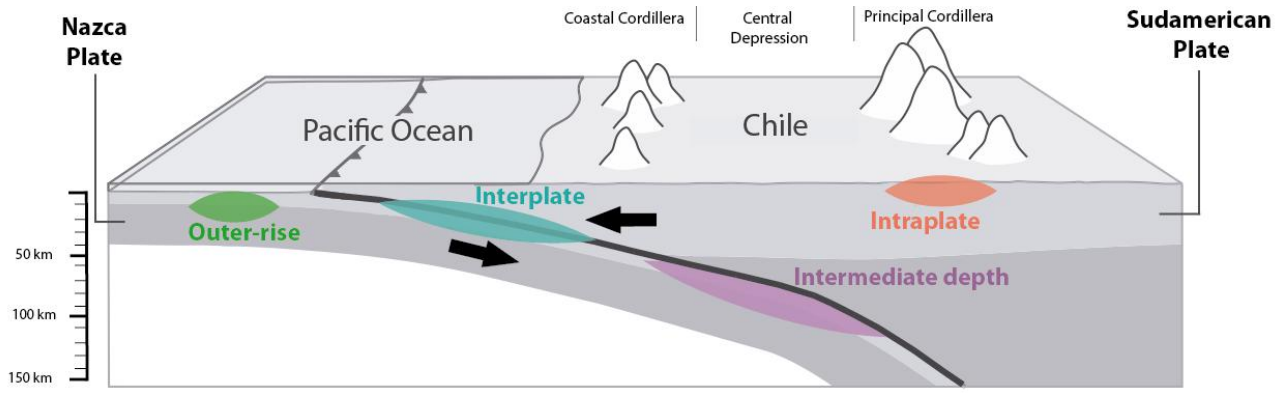


Figure 1.8 Schematic representation of the different seismogenic zones in Central Chile. Modified from Cisternas (2012).

### 1.7.3 Seismicity near Santiago

Historically shallow earthquakes in central Chile have occurred. The largest event occurred in the high Maipo River, the September 4, 1958, sited in Las Melosas (Fig. 1.9a and 1.10). According to Lomnitz (1961) and Piderit, (1961) Ms 6.9 was estimated. Alvarado et al., (2009), using modern body-wave modelling techniques, estimates Mw 6.3 for this event. These seismic events cause important damage on hydroelectric power plants and water supply infrastructure; the Queltehues power plant was suspended for 180 days (Sepúlveda et al., 2008). Figure 1.19b compile the intensities, which show peak values of VIII–IX in the epicentral area with a quick attenuation pattern, being reduced from IX to VI over a distance of just 40 km. At least two landslides were triggered by the 1958 earthquakes (Casas et al., 2005; Sepúlveda et al., 2008): (1) Las Cortaderas Landslide: a ca. 15-20 X $10^6$ $m^3$ landslide was triggered within an ancient mega-landslide on the eastern flank of the Yeso Valley (Flores et al., 1960). This landslide blocked the Yeso River for a few years creating a small lake (Borde., 1966); and (2) El Manzanito Landslide: a smaller ca. 4 x $10^6$ $m^3$ landslide was triggered on the eastern side of the Maipo Valley south of las Melosas locality on August 1958. This landslide did not reach the river but partially covered a fluvial terrace and destroyed a hydroelectric channel which supplies the Queltehues power station (Flores et al., 1960). Left-lateral strike-slip type on a steep north-south trending fault-plane solution has been suggested for the 1958 Las Melosas earthquake (Lomnitz, 1961; Piderit, 1961; Pardo and Acevedo, 1984; Alvarado et al., 2009; see Fig. 1.9a).

Others seismic events of lower magnitude were rerecorded. The September 13, 1987, in upper Cachapoal River (Fig. 1.9a and 1.11b) with Mw 5.9 according to Barrientos and Eisenberg (1988), and August 30, 2004, in Curico with Mw 6.5 according to Farias et al., (2006). A NNE-SSW dextral strike-slip fault plane is a possible solution of the focal mechanism for the 2004 earthquakes in the Teno River (Farias et al., 2006). Between 33°-34°S, immediately to the east of the Chile-Argentina border, the seismicity in the Andean Range drastically decrease (Barrientos et., 2004; Farias et al., 2010), except for the Mendoza, Cuyania and San Juan areas, where important shallow seismicity is recorded (Gregori & Christiansen, 2018) (See Fig. 1.7).

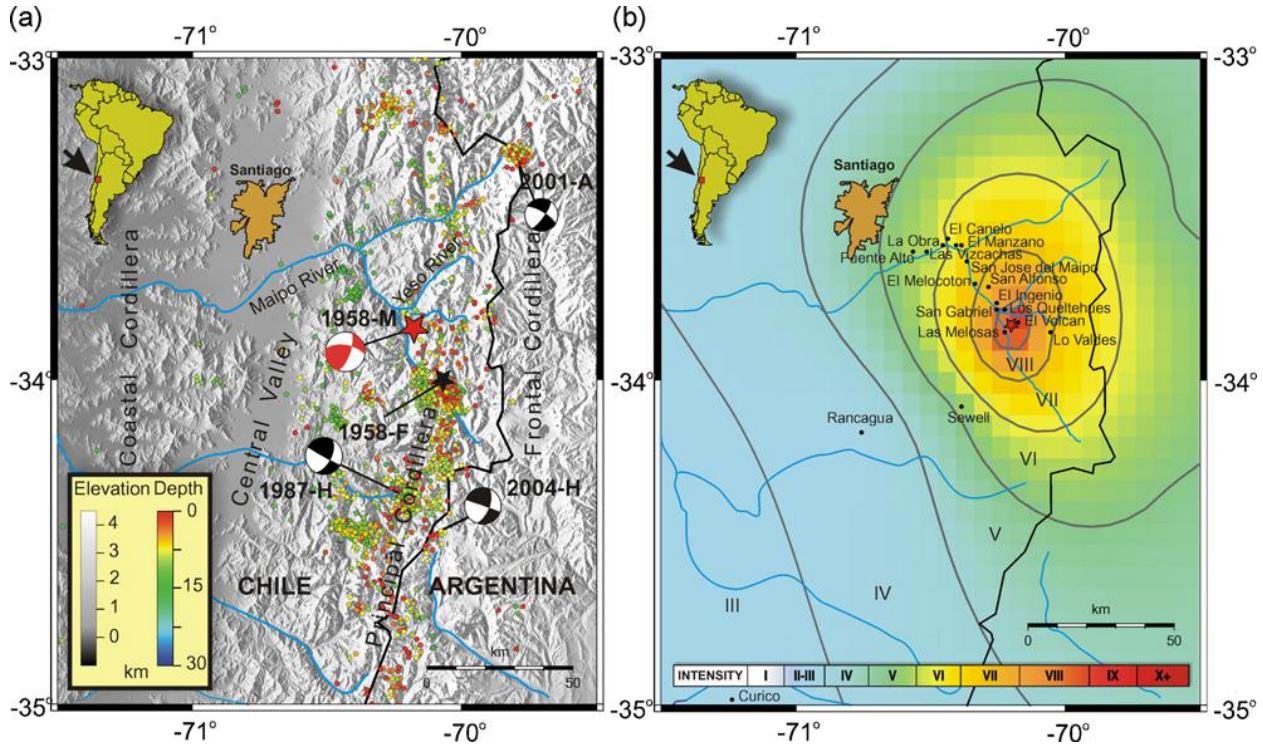


Figure 1.9 a) Relocated seismicity between 1995 and 2005 from Barrientos et al., (2004). Focal mechanism are shown for the 1958 Las Melosas earthquake, 2001 earthquake in Tupungato cluster, 1987 Cachapoal earthauqke, and 2004 Curico earthquake. b) Map of the MSK seismic intensities listed in Table 2 recalculated by Sepúlveda et al. (2008) for the Las Melosas crustal earthquake on 4 September 1958. Extracted from Alvarado et al., (2009).

Different authors (Barrientos et al., 2004; Farias et al., 2010; Pérez et al., 2014; Estay et al., 2016) have instrumentally studied the seismicity underneath the Chile most populated city and capital. The main type of seismicity is the shallow (<30 km depth) intraplate, located to the east of the Central Depression in the mountain area (Fig. 1.9a and 1.10). Here the seismicity is not uniformly distributed; the highest activity concentrated cluster of seismic events is in the upper reaches of the Maipo River and in lesser intensity in the region of the San José volcano (Figure 1.9a; Barrientos et al., 2004). Two clear morphological lineaments also seen related to seismicity activity, the southern extend of the Pocuro fault and the Olivares River (Fig. 1.9a; Barrientos et al., 2004).

Pérez et al., (2014) re-localize shallow seismic events at 32.5-34.5°S between 2000-2009 using data from the SSN (National Seismological Service or Servicio Sismológico Nacional in Spanish), they found two semi-parallel N-S lineaments of crustal seismicity (Fig. 1.10). A well-organized western band with sources between 10-15 km deep, just beneath the western edge of the

wester Principal Cordillera; and an eastern, wider and more diffuse band, located in the central part of the Principal Cordillera, at the contact between Cenozoic and Mesozoic rocks, with shallower (0-10 km depth) seismic events concentrated in the upper reaches of Maipo River (Fig. 1.10). The western band shows compressive mechanism (Pérez et al., 2014) meanwhile the eastern band shows strike-slip mechanism (Lomnitz, 1961; Alvarado et al., 2009) but also normal and reverse as well (Perez et al., 2014). Seismicity cluster are observed, like the Santa Rosa Cluster in the southern central part of the Santiago basin, Tupungatito cluster in the Tupungatito volcanic center, Andina-Los Bronces cluster and El Teniente cluster, although, last 2 are seismic clusters related to mining industry (Fig. 1.9a and 1.10, Barrientos et al., 2004, Pérez et al., 2014).

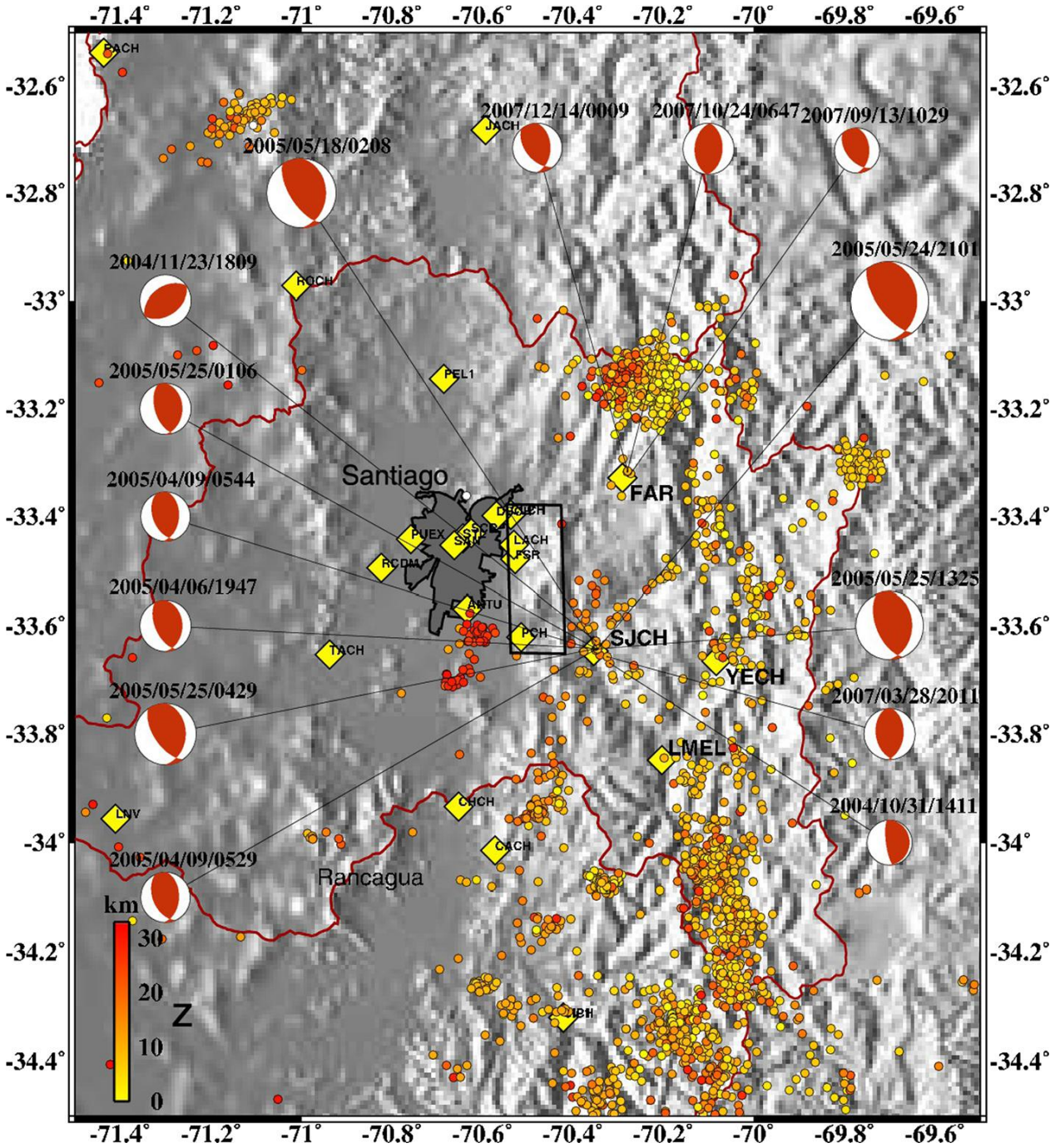


Figure 1.10 Hypocenter location of crustal seismicity (<30 km) recorded by SSN between 2000-2011. Extracted from Pérez et al., (2014).

## 1.8 Landslides Central Chile

Due to the geomorphological, climatic, and tectonic conditions there are many landslides of all sizes in the Central Andes. The most common type of landslide are debris and mud flows coming from the mountain range foothills mostly triggered by strong rainfalls, like the events in the San Ramon Ravine, Macul Ravine and Maipo River (Naranjo & Varela, 1996; Sepúlveda et al., 2008; Lara et al., 2010; Sepúlveda et al., 2015). Landslides in Central Andes are important source of direct and indirect hazard (Sepulveda & Moreiras, 2013). In spite of the controversy about the main trigger mechanism of these events, rock slides, rock fall and also large-landslides have been reported in the high Andes whit a triggering seismic source (Antinao & Gosse, 2009; Sepúlveda and Moreiras, 2013; Deckart et al., 2013).

Antinao & Gosse (2009), developed a comprehensive inventory of the landslides in the Central Andes between 32° and 34.5°S. They identify 378 landslides in an area of 15,000 $km^2$. They found a correlation between large landslides, seismicity and fault systems (Fig. 1.11), such as with the Pocuro-San Ramon Fault Zone (SRFZ, Rivano and Sepúlveda, 1986; Rauld, 2002) and in the Olivares River. Holocene landslides are concentrated along the western limit of the Abanico Formation, in the lower parts of the Colorado River and also in the northern part of the Pocuro-San Ramon Fault system. Rocks of the Abanico Formation are about a third of the total study area but it comprises almost 85% of all the landslides material. Landslides clustered near the boundary between the western and eastern Principal Cordillera. Finally, Antinao & Gosse (2009) propose that landslides are linked with Late Cenozoic structures and present-day shallow seismicity (< 30 km deep), suggesting a causative relationship between active tectonics in the western Cordillera Principal and large landslides. If the seismic events are the main trigger for large landslides, it is important to locate the seismic source and it behaviour, to be capable to predict hazardous landslides.

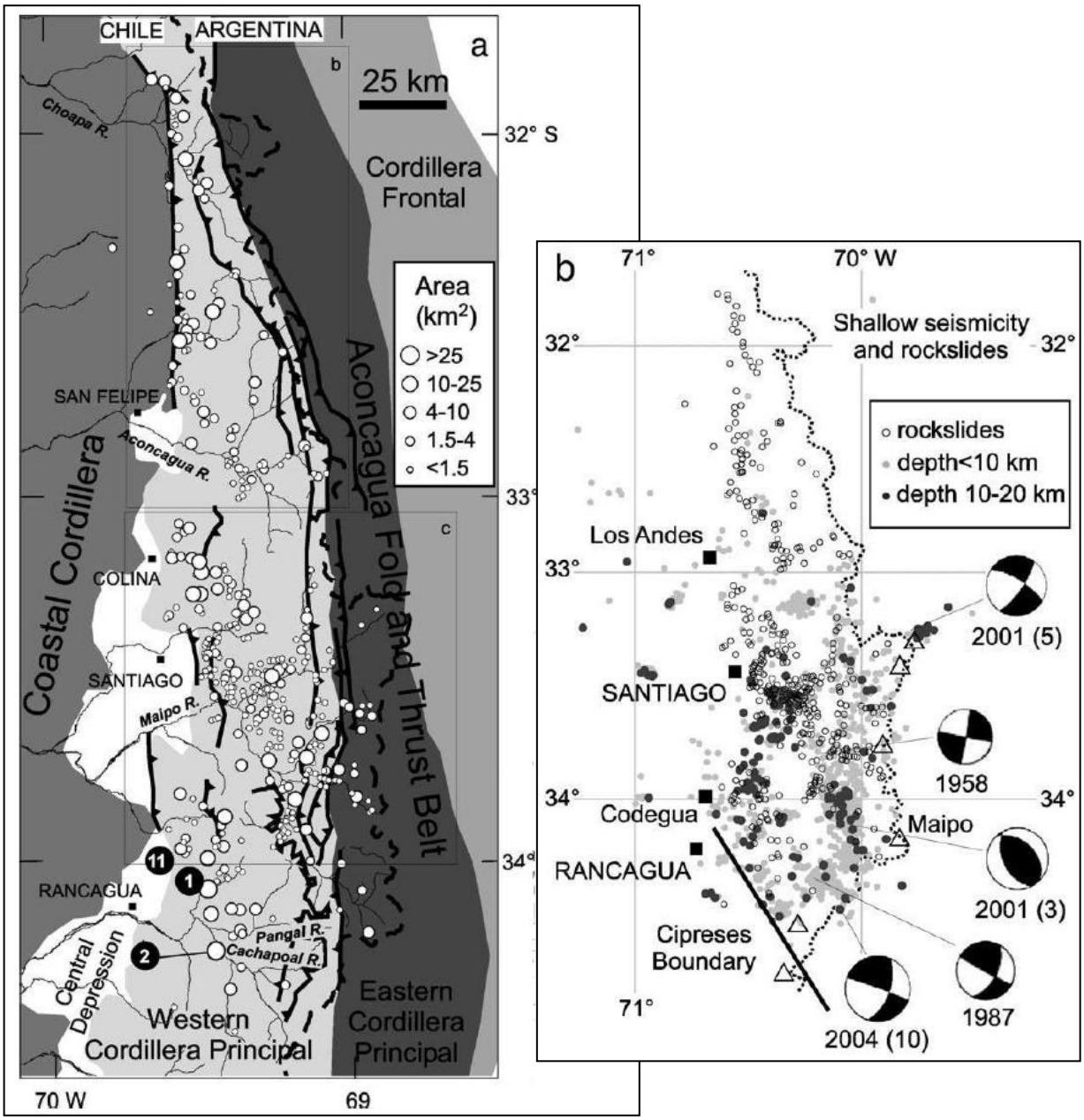


Figure 1.11 Spatial distribution of landslides between 32°-34.5°S. a) Relation between landslides, morphoestructural units and late Cenozoic faults; White circles indicated the locations of landslides; size of circles indicates area of the landslides. b) Relation between landslides and shallow seismicity epicenters, depth and published fault plane solutions for the area. Extracted from Antinao & Gosse, (2009).

## 1.9 Neotectonics in Central Chile

Lavenu & Cembrano (1999), by kinematic analysis in fault-slip data from central and southern Chile, identified two late Cenozoic deformation events. The first was an E-W compressional event of Pliocene age. During the second event, which is of Quaternary age, deformation was partitioned into two different stress states. NNE-SSW directed compression was registered for the present day fore-arc between 33°-37°S at the Central Depression and the Main Cordillera, but NE-SW directed transpressional stress state for the intra-arc zone near the Liquiñe-ofqui fault zone between 37°-42°S (Fig. 1.12).

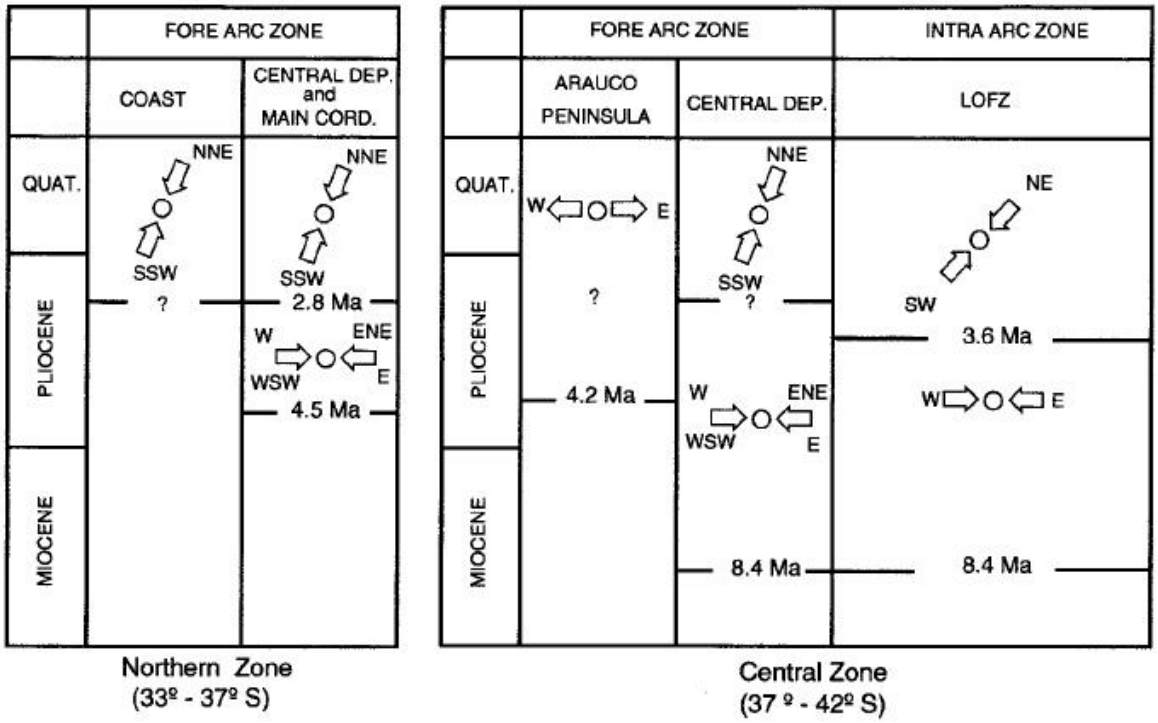


Figure 1.12 Chronology and strike of different tectonic regimes obtained by Kinematic analysis of fault slip data. Extracted from Lavenu & Cembrano (1999).

Rauld (2002), Armijo et al., (2010) and Rauld (2011) reported fault scarps related to a west-vergent reverse fault at the foothills of the Ramon range (Fig. 1.13), which cuts and tilt Quaternary fluvial deposits to the east. Rauld (2002) was the first in propose that the San Ramon fault has a Quaternary activity. After that, Armijo et al., (2010), presents a characterization of the crustal deformation and the seismic hazard of the San Ramon fault. He report fault scarps of about 3-200m, by morphostratigraphic correlations in fluvial terraces, also a maximum age of 45 ky by cosmogenic

isotopes ($^{36}Cl$) to the most recent fault scarp. Average long-term slip rate of 0.2-0.4 mm/yr is reported across the piedmont in base of the shortening (10 km) accommodated by the San Ramon fault in the last 25 Ma. Vertical throw measured across the youngest scarp suggests the occurrence of earthquakes with average slips of 1- 4 m, yielding Mw 6.9 - 7.4, with recurrence of 2500 to 10000 years. Rauld (2011) in his PhD thesis report, among other analysis, the result presents by Armijo et al., (2010), they work together in the "Millennium Science Nucleus of Seismotectonics and Seismic Hazard" project.

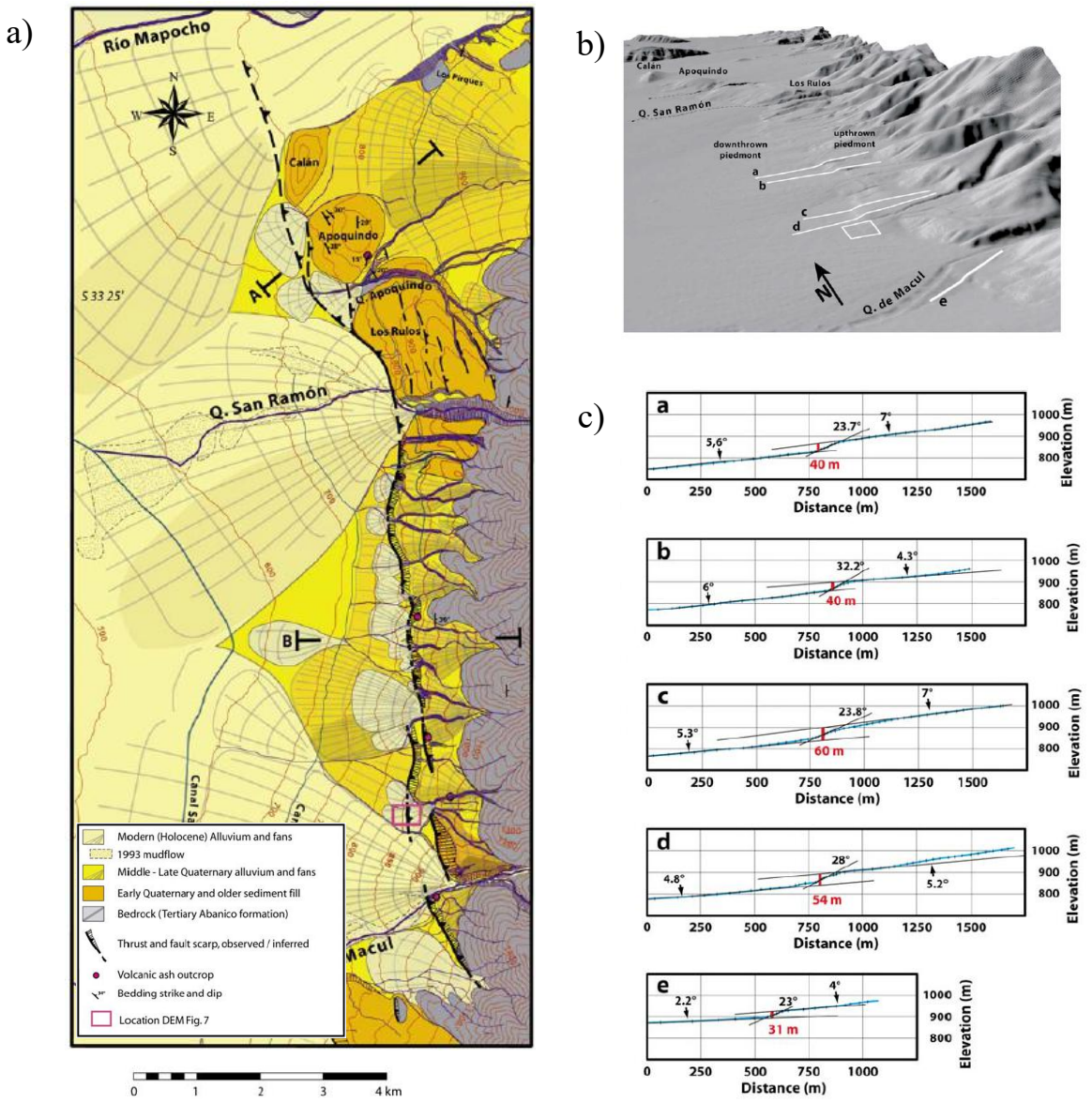


Figure 1.13 a) Simplified geological map of the foothills of the Ramon range, indicating the location of the San Ramon fault. b) Oblique view of the DEM that shows the morphology of the Ramon range foothills. c) Topographic profiles across piedmont scarp. Extracted from Armijo et al., (2010).

Only one paleoseismology study exists in Central Chile based on a trench across the San Ramon fault near Quebrada de Macul (Vargas et al., 2014). Using field observations, OSL and $^{14}C$ dating, Vargas et al., (2014) present evidence of recurrence faulting events of 5 m displacement, and two large paleoearthquakes ruptures within the past 17-19 ky, and the last event occurring 8 ky ago (Fig. 1.14b). They proposed that the fault is prepared to generate another Mw 7.5 earthquake in base of 5 m as the maximum surface displacement for the Wells and Coppersmith (1994) earthquake key parameter.

a)

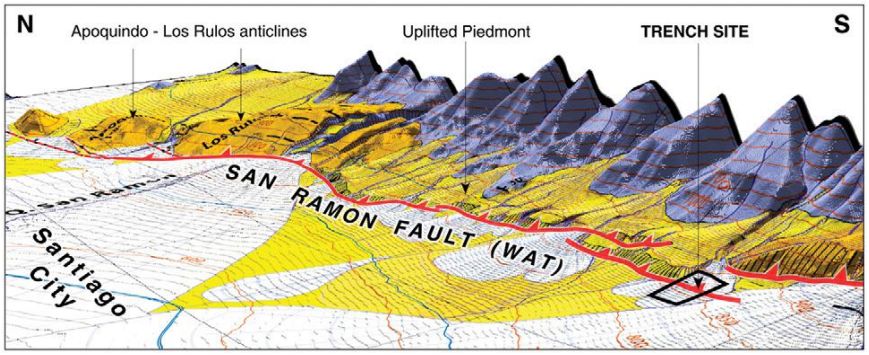


b)

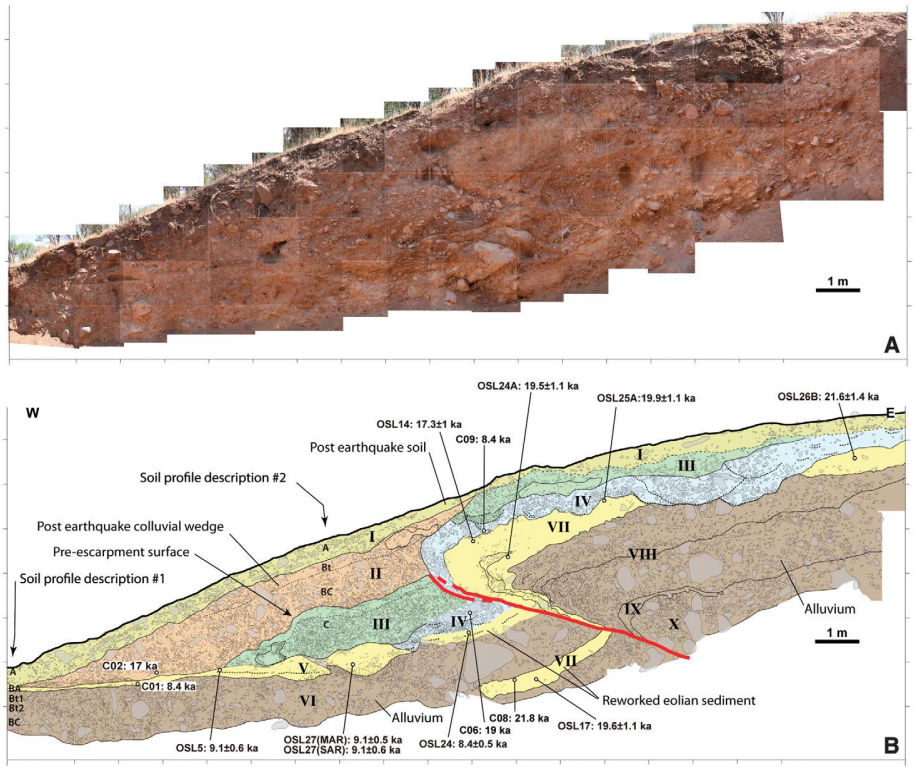


Figure 1.14 a) Oblique view to simplified geological map of the foothills of the Ramon range, showing San Ramon Fault and fault scarps. b) Trench log of the San Ramon fault. A: Photomosaic of the northern wall of the trench. B: Interpretation of the trenching, indicating geological units and dating. Extracted from Vargas et al., (2014).

Lavenu & Cembrano (2008) develop a neotectonic study in the Cajon del Maipo, 30 km south-east of Santiago, at the confluence of the Maipo River and the Colorado River. They acquire a datum of faults and kinematic indicator from three sites with the goal of reveal the stress state of the most recent deformations. Faults and folds in Middle-Pleistocene alluvial terrace of the Maipo River and minor structures in Abanico Formation bedrock, shows Quaternary compressive deformation with principal stress direction trending mostly NNW-SSE (N338°E) (Fig. 1.15). They also report a Neogene deformation event (post 9 Ma) whit E-W shortening direction.

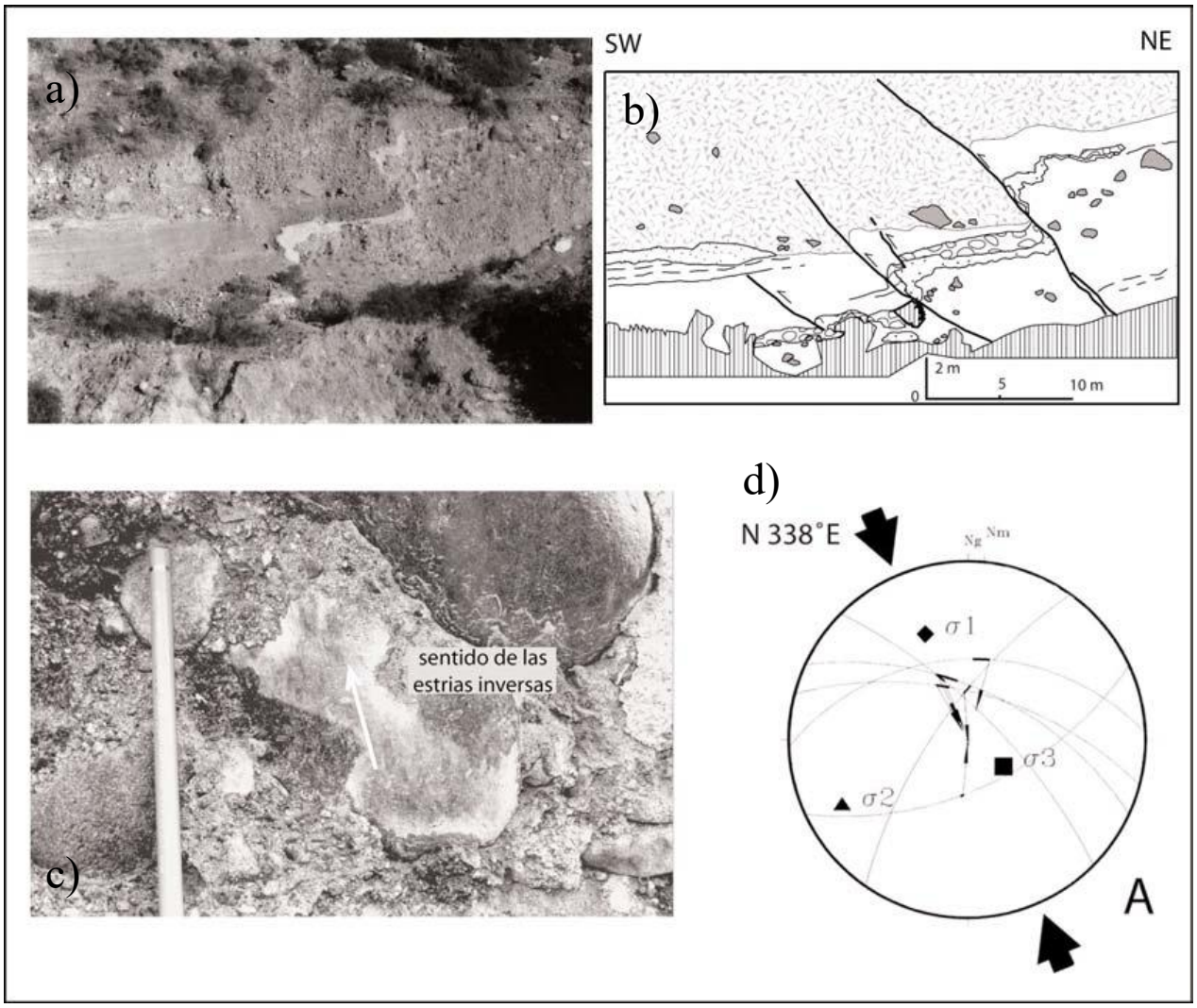


Figure 1.15 a) Faulted fluvial terrace of the Maipo River b) Faulting is evidenced by subparallel fault planes and drag folds. c) Grooves in rounded clast. d) Kinematic fault-slip analysis yielding N338°E shortening direction. Extracted from Lavenu & Cembrano (2008).

Further to the north, near Los Andes-San Felipe, neotectonic activity was evidence by morphometric analysis in the drainage pattern related to the Cariño Botado fault (Troncoso, 2014). Sinuosity index, knickzones and rocks of the Abanico Formation overthrusting alluvial deposits, reveals the recent activity (Fig. 1.16). Medina (2018) extends the fault trace of the Cariño north of the Estero San Francisco. By scaling laws of Wells and Copersmith (1994), Troncoso (2014) estimated potentially Mw 6.0-6.5 seismic events for the Cariño Botado fault. This last author also proposes another west-vergent reverse fault, named San Esteban fault, to the west of the Cariño botado fault, in base of a depression in the San Esteban locality.

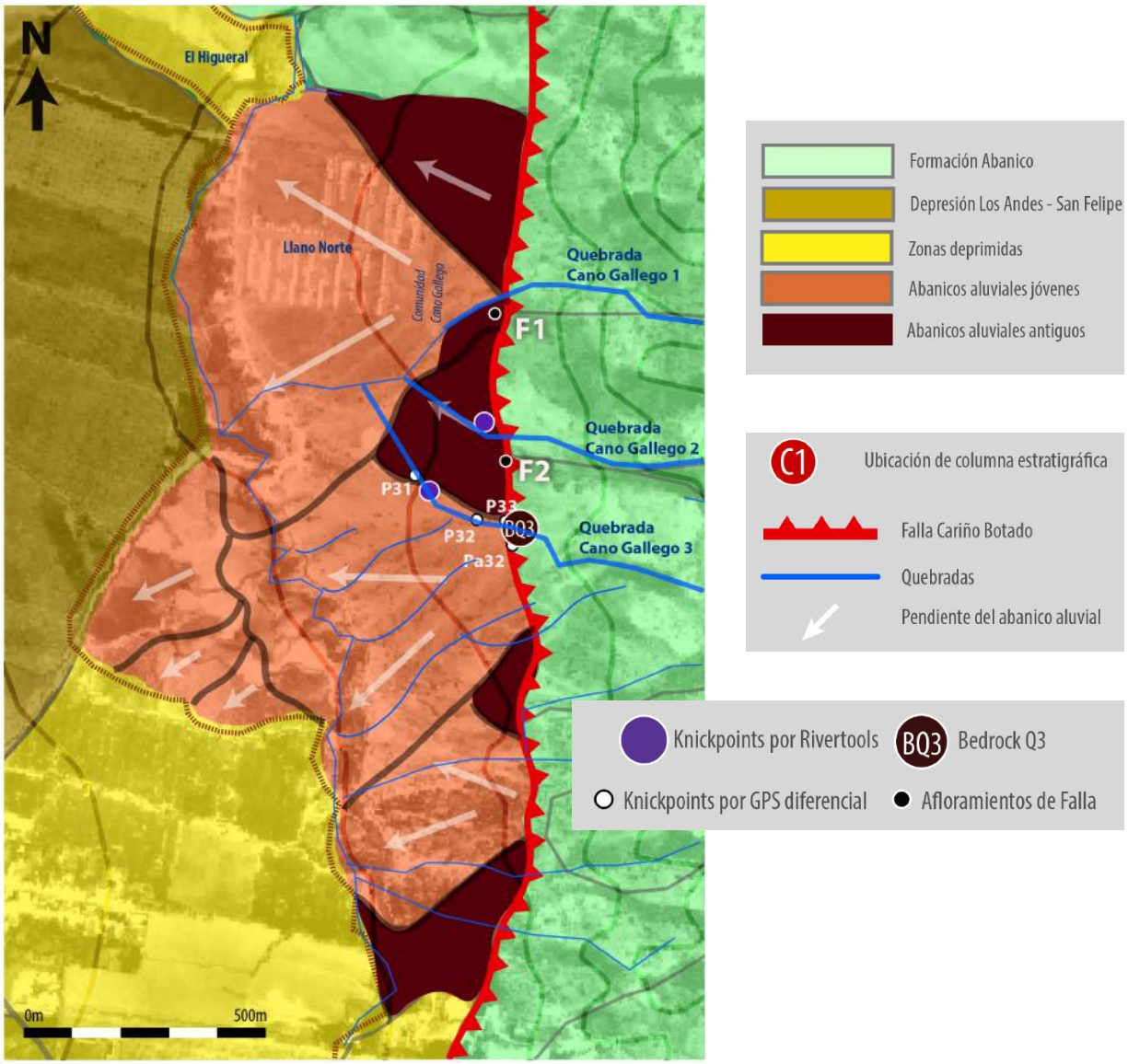


Figure 1.16 Geomorphological map of the eastern flank of the Central Depression at the latitudes of San Felipe-Los Andes. Knickpoints and fault outcrops represent the Cariño Botado fault. Extracted from Troncoso (2014).

## 1.10 A review of faults zones

Because of the complex variations in fault expression, is not easy to come up with a simple and general description of a fault. They are not simply planar features; they are zones of complex and heterogeneous strain distribution. Fault evolution understanding based on fault geometric component description, is helpful for seismic hazard assessment. Many authors have shown positive correlation between fault displacement and fault rock thickness (Robertson, 1983; Hull, 1988; Marrett and Allmendinger, 1990; Childs et al., 2009), sometimes being used to infer fault displacements (Marrett and Allmendinger, 1990; Little, 1995). Figure 1.17 shows a compilation of empirical relationship between fault rock thickness and fault displacement for different fault modes and different lithologies.

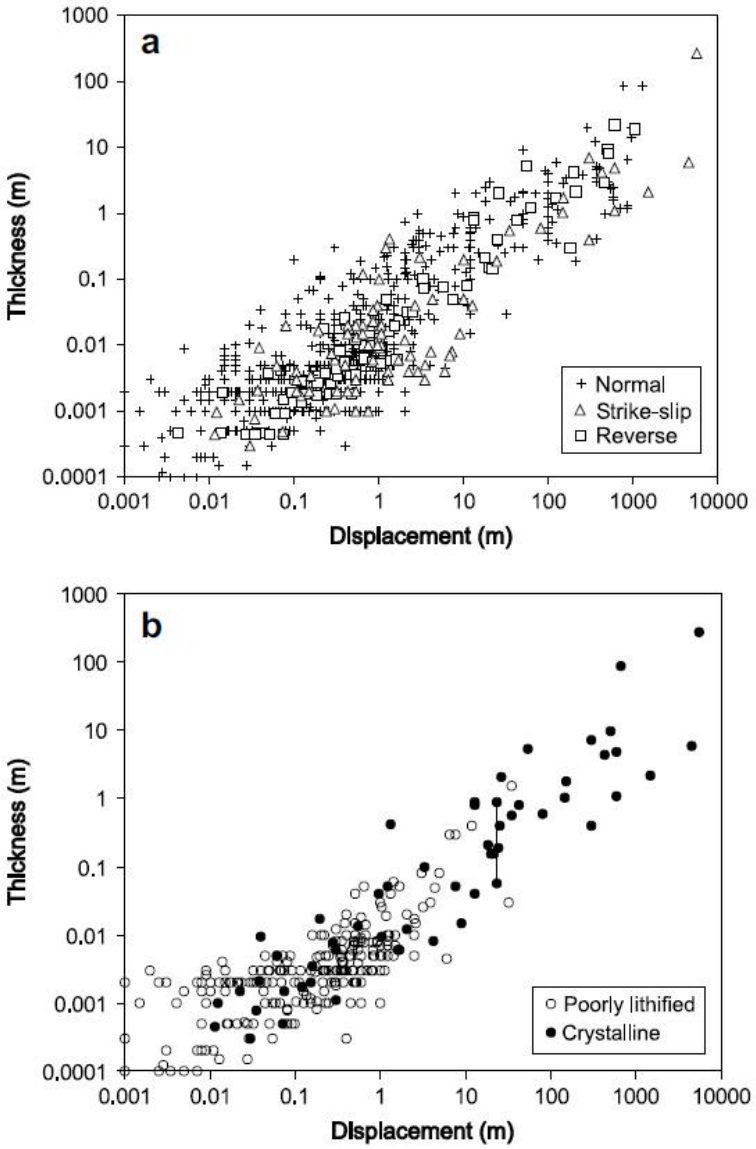


Figure 1.17 Plot of fault rock thickness versus displacement for (a) different modes of faulting (b) different lithologies. Extracted from Childs et al., (2009).

Lots of different definitions have been used for terms like fault rock, fault zone and damage zone, obstructing a correct development of knowledge on this topic. Fault zones are composed of distinct components: a fault core where most of the displacement is accommodated, and an associated damage zone that is mechanically related to the growth of the fault zone (Chester & Logan 1986; Chester et al., 1993; Caine et al., 1996). Some fault zones may have one distinct principal slip zone surrounded by a commonly asymmetric, substantially thicker, highly fractured, damage zone (Chester & Chester, 1998), while other faults comprise numerous anastomosing thin slip zones surrounding lenses of fractured protolith (Faulkner et al., 2003). In this work we use the terminology of "fault rocks" to refer to gouge, breccia and cataclasite. Also, we use "fault zone" as comprising a "fault core" containing fault rocks and slip surfaces, and "damage zone" comprising a network of subsidiary minor structures bounding the fault core, including small faults, veins, fractures and minor folds (Sibson, 1977; Chester and Logan 1986; Chester et al., 1993; Caine et al., 1996). Figure 1.18 shows a conceptual model of a fault zone based on Caine et al., (1996).

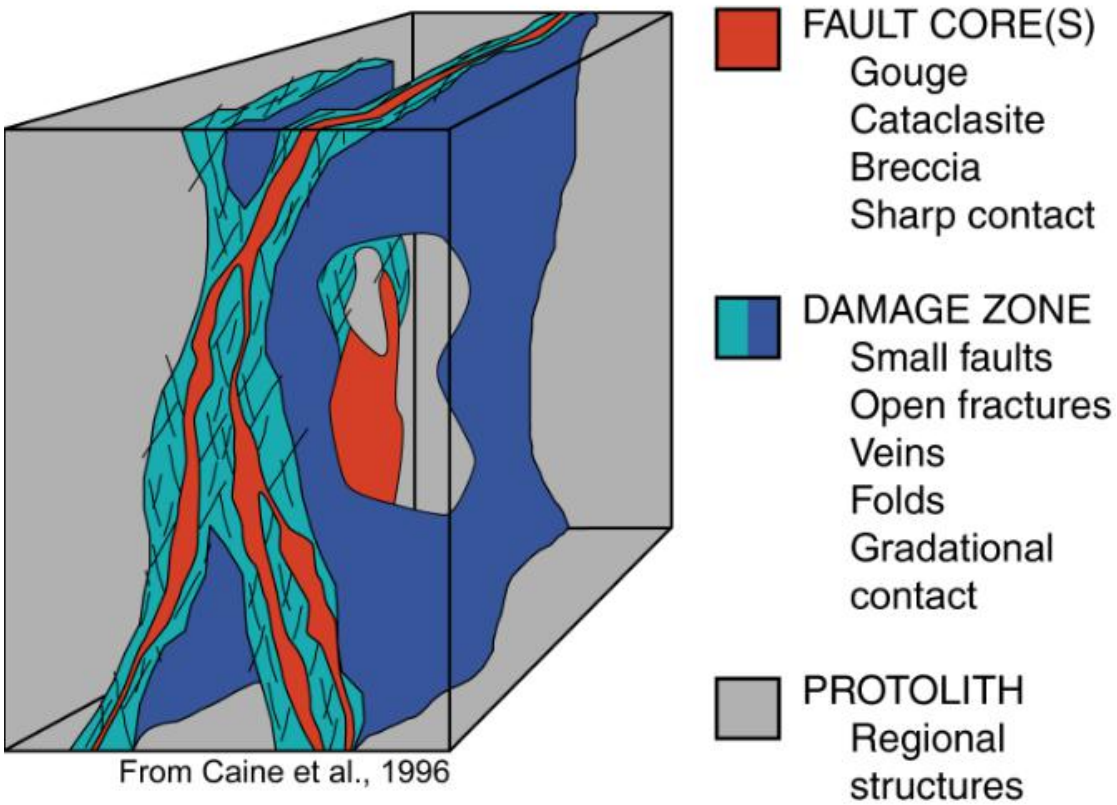


Figure 1.18 Generic fault zone conceptual models based on Caine et al., 1996. Extracted from Caine et al., (2017).

Earthquakes arise from frictional 'stick–slip' instabilities as elastic strain is released by shear failure, almost always on a pre-existing fault. How the faulted rock responds to applied shear stress depends on its composition, environmental conditions (such as temperature and pressure), fluid presence and strain rate. These geological and physical variables determine the shear strength and frictional stability of a fault, and the dominant mineral deformation mechanism. To differing degrees, these effects ultimately control the partitioning between seismic and aseismic deformation, and are recorded by fault rock textures. A complete conceptual fault model, incorporating geological features, deformation mechanisms, frictional stability, seismic behavior, crustal strength and depth were summarized by Fagereng & Toy (2011), based on the previous works of Sibson (1983) and Scholz (1988, 2002) (Fig. 1.19).

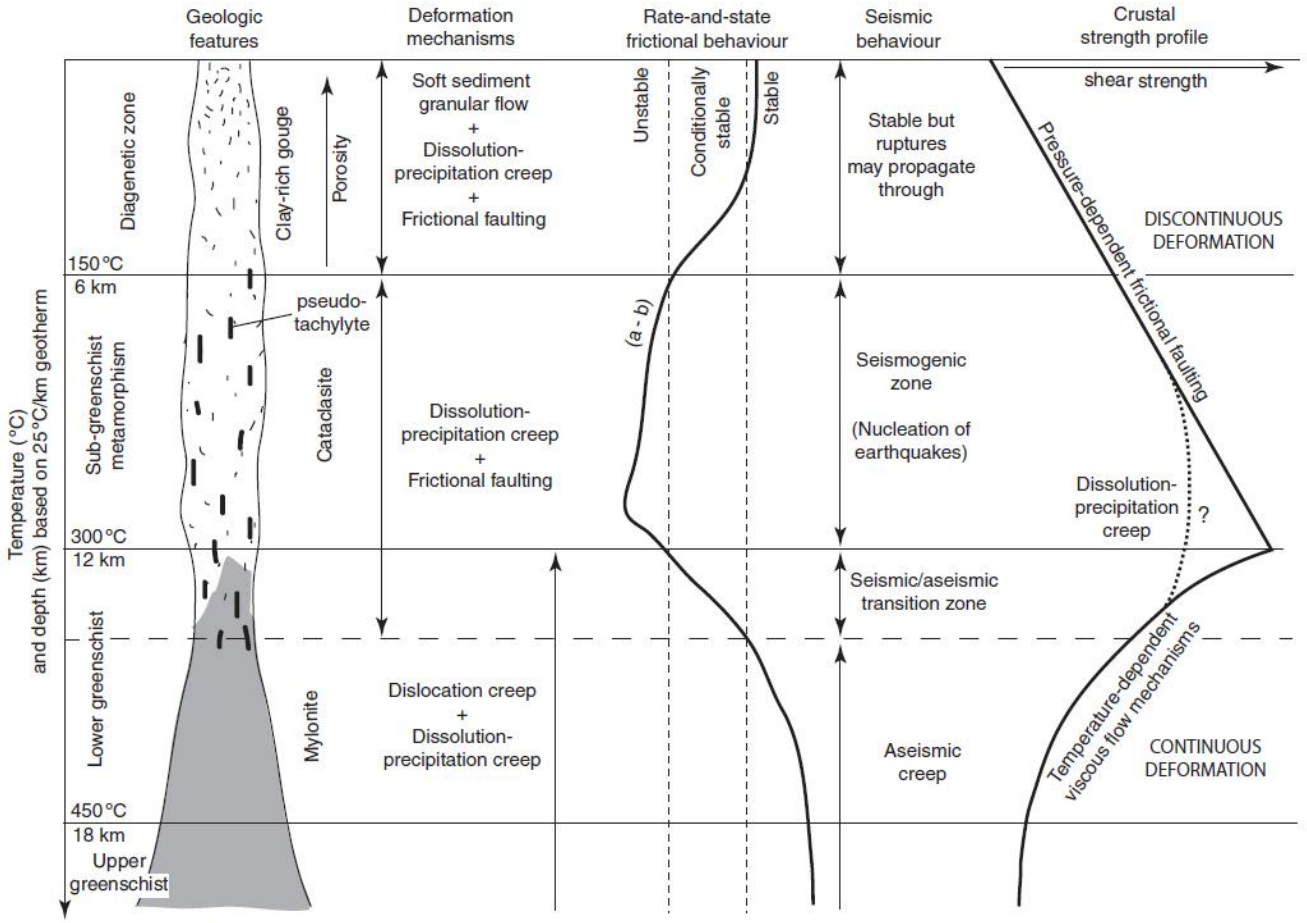


Figure 1.19 Conceptual fault-zone model, based on Sibson (1983) and Scholz (1988, 2002). Extracted from Fagereng & Toy (2011).

## 1.11 Summary of work to date (to September 2018) on neotectonics in Central Chile

The following table outlines the state of knowledge prior to the start of this thesis.

Table 1.1 Summary of knowledge on notectonics in Central Chile.

| Question | Answer |
|---|---|
| Is the Central High Andes of Chile active? | The high elevation, seismicity and active faults reported in the High Central Andes suggest that this is a growing orogen |
| How is the **seismicity** under the high central Andes? | I can be observed crustal seismicity (shallower than 30 km) characterized mostly by 2 N-S bands. The western band located under the western flank of the western Principal Cordillera, hypocenters within 10-15 km depth and compressive focal mechanism. The eastern band located in the boundary within the eastern and western Principal Cordillera, shows hypocenter centers between 0-10 km depth, strike-slip, reverse and normal focal mechanism, and a distribution wider than the western band, suggesting more complex structural framework. (Barrientos et a., 2004; Pérez et al., 2014;Ammirati et a., 2019; USGS seismic catalog) |
| Which is the **uplift rate** of the High Central Andes? | Rauld (2002) by ash level difference elevations estimates uplift rates between 0,16 and 0,1 mm/yr. |
| How many **crustal structures** are near Santiago de Chile? | We document at least 63 mapped (1:50000-1:100000) crustal structures between 33°-34°S in the Principal Cordillera (See Chapter 6) |
| How many of the structures had **Quaternay activity**? | Only 2 structures evidence Quaternary activity between 33°-34°S: (1) The San Ramon fault system at the foothills of the mountain range (Rauld 2002; Armijo et al., 2010; Rauld 2011; Vargas et al., 2014); (2) The San Jose de Maipo fault located in the conjunction of the Maipo and Colorado Rivers (Lavenu & Cembrano, 2008). Additionally between 32°-33°S, less than 80 km from Santiago, the Cariño Botado fault located at the foothills of the western flank of the main range also presents Quaternary activity (Troncoso 2014; Medina 2018). |

| | |
|---|---|
| What **paleoseismological data** are in the area? | Vargas et al., (2014) dug a trench across the youngest scarp of the San Ramon fault, near Quebrada de Macul, and they found clear evidence of the fault in subsurface, reporting 2 earthquakes with mean displacement of 5 m, dated by OLS and $^{14}C$ yielding ages of 8 k.y B.P. and 17-19 ky B.P. |
| Are there any **slip-rate** estimates for these structures? | For the San Ramon fault, Armijo et al., (2010) suggest slip rates in order of 0.2 - 0.4 mm/yr. Long term slip rates of 0.4 mm/year and minimum 0.2 mm/year are reported across the piedmont by morphostratigraphic correlations in fluvial terraces (Rauld, 2011). Later slip rates of 0.5 mm/yr were estimated by paleosismology trenching and dating (Vargas et al., 2014). |
| Which is the **stress field** for the structures with Quaternary activity? | Lavenu & Cembrano (1999) suggest nearly NNE-SSW shortening for Central Chile forearc in Central Depression and Main Cordillera. For the San José de Maipo fault a N338°E direction of shortening was calculated (Lavenu & Cembrano, 2008). For the San Ramon fault, in base of its orientation and kinematics, a nearly E-W shortening direction can be inferred. |
| Can we relate crustal structures with the **crustal seismicity**? | For the Las Melosas Earthquake a N13°E/77°W siniestral subvertical fault plane solution was calculated, unfortunately no surface rupture could be observe (Lomnitz, 1961). However, Alvarado et al., (2009) propose E-W north dipping fault plane which accommodates differences in shortening from north to south as the probable rupture plane for the Las Melosas earthquake. Barrientos et al., (2004), Charrier et al., (2005) and Perez et al., (2014) suggest that most of the seismic activity is located near the Chile-Argentina boundary, which is aligned with the El Fierro Fault system, but again, no surface rupture was observed. Microseismic study reveals seismic events spatially associated with the San Ramon faults less than 25 km depth (Estay et al., 2016). |
| Are these structures related with the **landslides** in the Central Andes? | Antinao & Gosse (2009) suggest a causative relationship between active tectonics in Late Cenozoic structures of the western Principal Cordillera and large landslides, proposing that shallow seismicity is the main trigger mechanism. However, whereas seismic tremors have been widely suggested as the main |

| | |
|---|---|
| | triggering mechanism in Chilean collapses, palaeoclimatic conditions are considered as the main cause of Argentinean giant landslides (Sepúlveda & Moreiras, 2013). These different approaches denote the lack of multidisciplinary studies focused on the controversy about seismic or climate trigger mechanisms. |
| Does anyone **estimate expected PGA values** in the High Central Andes? | Leyton et al., (2010) applies probabilistic methodologies of seismic hazard and adapt them to central Chile, obtaining PGA values of 0.55 to 0.72 g for Santiago urban area. Pérez et al., (2014), Estay et al., (2016) and Ammirati et al., (2019) quantifies the seismic hazard with empirical equations of peak ground acceleration (PGA), but only for the San Ramon fault as a seismic source, yielding PGA values of 0.7-0.8 near the fault. |
| What **Mw** have been calculated for the seismic sources? | For the San Ramon fault: Armijo et al., (2010) and Rauld (2011) estimates Mw 6,9 - 7,4; Vargas et al., (2014) and Ammirati et al., (2019) estimates Mw up to 7.5. These estimation where based on scarp geomorphology (Armijo et al., 2010; Rauld, 2011), fault slip (Vargas et al., 2014) and Wellls and Coppersmith (1994) equations. |

## 1.12 Organization of the Thesis

Chapter 1 it is the introduction to this work. Motivation and research questions are presents, as well as a brief review of the most important geological aspects of the study area for this investigation.

Chapter 2 outlines the methodologies that were developed to address the objectives of this thesis. It outlines the different types of remote sensing techniques (i.e. desktop mapping) and which tools and data where used, as well as which field work campaigns were made and the area covered by them.

Chapter 3 is a case study of the El Arrayan fault in north eastern Santiago. This is a previously un-identified fault in the Lo Barnechea area. This chapter is written in manuscript style so there is some repetition

between some of the information in the introduction and methods chapters in this manuscript.

Chapter 4 is the second study case. It describes the outcrop of a newly-discovered fault zone revealed by field campaigns. Its shows, at the Estero Coyanco in Maipo Valley, bedrock and Quaternary alluvial deposit faulted by at least 3 structures.

Chapter 5 is the third study case. Fault rock characterization was done in a gully close to Baños Morales, where the fault has been previously mapped but not detailed characterized. It provides new information about the kinematics of the fault and reinforces the suggested previous idea of been active.

Chapter 6 is where the seismic potential is evaluated for all the regional faults near Santiago. This chapter takes in account the structures reported by previous authors and the ones reported in this work. Moment of Magnitud (Mw) where estimates using Wells and Coppersmith (1994) earthquake parameters scaling laws, and the related seismic hazard implications are discussed. PGA was estimated for the EAF in base of Sadight et al., 1997 ground motion attenuation equations.

Chapter 7 is the discussion and conclusion chapter. Here we coupled the new information provide by this work (Chapters 3-6) with the one already published and discuss the implications of the new reported structures, present days structural style, kinematics and stress field in the Principal Cordillera in the Central Andes and related seismic hazards. Recommendations for future works in this topic are also shown.

Chapter 8 is Bibliography. Here a complete list of references used in this work it’s presented.

Chapter 9 is Appendant. The participation on conferences directly related to this thesis are shown. A list of digital element attached to the thesis it’s delivered.

## Chapter 2: Methodologies

To be able to fulfill the objectives proposed in this work, different methodologies where used. First a bibliographic compilation was done with the goal of outlining with the research problem and the geology of the area. Second, field work was developed to identify the main structural features and data collect. Third, the data collected were analyzed in order to characterize the crustal faults, their behavior and related seismic hazard. Here I describe the main source information, the geological data acquisition, and finally the methodology for the data analysis.

### 2.1 Source information

2.1.1 Geological maps

The first step was to collect and study geological information of the area of interest, with special attention in structural data.

1. Public regional Chilean basic geological cartography. Figure 2.1 shows the main source of information and the area that they cover:

    a. Hoja Santiago; Thiele (1980) at 1:250.000.
    b. Hoja Til-Til; Wall et al., (1999) at 1:100.000.
    c. Hoja Talagante-San Francisco de Mostazal; Selles & Gana (2001) at 1:100.000
    d. Mapa Geológico de Chile; SERNAGEOMIN (2003) at 1:1.000.000

2. Publications in scientific journals in which geological maps exhibit important structural information. Figure 2.2 shows the main source of information and the area that they cover:
3. 
    a. Giambiagi et al., (2003); Geological map at 1:50000. This study aims to integrate previous data with new structural data to analyze the style, distribution and timing of deformation of the Andes between 33° and 34° S.
    b. Armijo et al., (2010); Geological map at 1:25000. Purpose of the study was to analyze the active fault propagation fold system in the Andean cover behind the San Ramon fault and the related seismic hazard.
    c. Deckart et al., (2013); Geological map at 1:25000. A study in which the goal was to present new insights in the origin of the Meson alto deposit in the Yeso River valley.
    d. Piquer et al., (2016); Geological map at 1:250000. This study aim to discuss the role of arc-oblique fault systems in the

Cenozoic structural evolution and metallogenesis of the Andes of central Chile.

4. Thesis of undergraduate geology students, as well as, from MSc and PhD students in which structural information is shown. Figure 2.3 shows the main source of information and the area that they cover:

    a. Fock (2005), MSc thesis; Geological map at 1:500000. Purpose of the study was to analyze the Neogene tectonic exhumation and chronology of Central Andes between 33°-34°S.
    b. Calderon (2008), Geology thesis; Geological map at 1:25000. Purpose of the study was to develop a metamorphic analysis of the rocks in Rio Volcán, to establish a buried and metamorphic history.
    c. Rauld (2011), PhD thesis; Geological Map at 1:50000. Purpose of the thesis was to study the crustal deformation and the seismic hazard related to the San Ramon fault.
    d. Quiroga (2013), Geology thesis; Geological map at 1:100000. Purpose of the study was to establish a structural model for the Mapocho River area, based on stratigraphy, cross sections and it's respectively restoration.
    e. Castro (2012), Geology thesis; Geological map at 1:50000. A study in which the goal was to analyze the structural style of the deformed Mesozoic and Cenozoic deposits in the Colorado River valley.
    f. Villela (2014), Geology thesis, Geological map at 1:40000. Purpose of the study was to develop a structural model for the El Ingenio area, in the Maipo river valley, regarding the geometry and kinematic of the structural system.

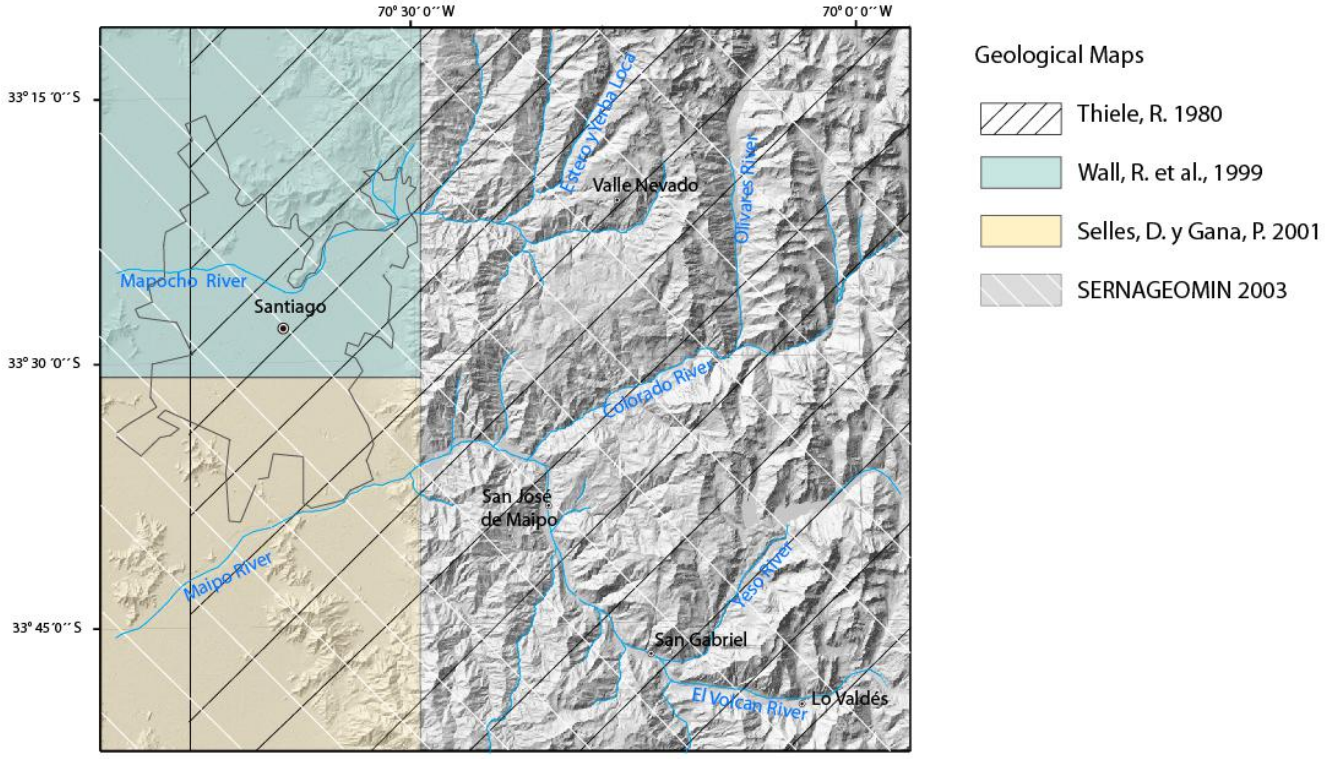


Figure 2.1 Map showing the area covered by public regional Chilean basic geological cartography.

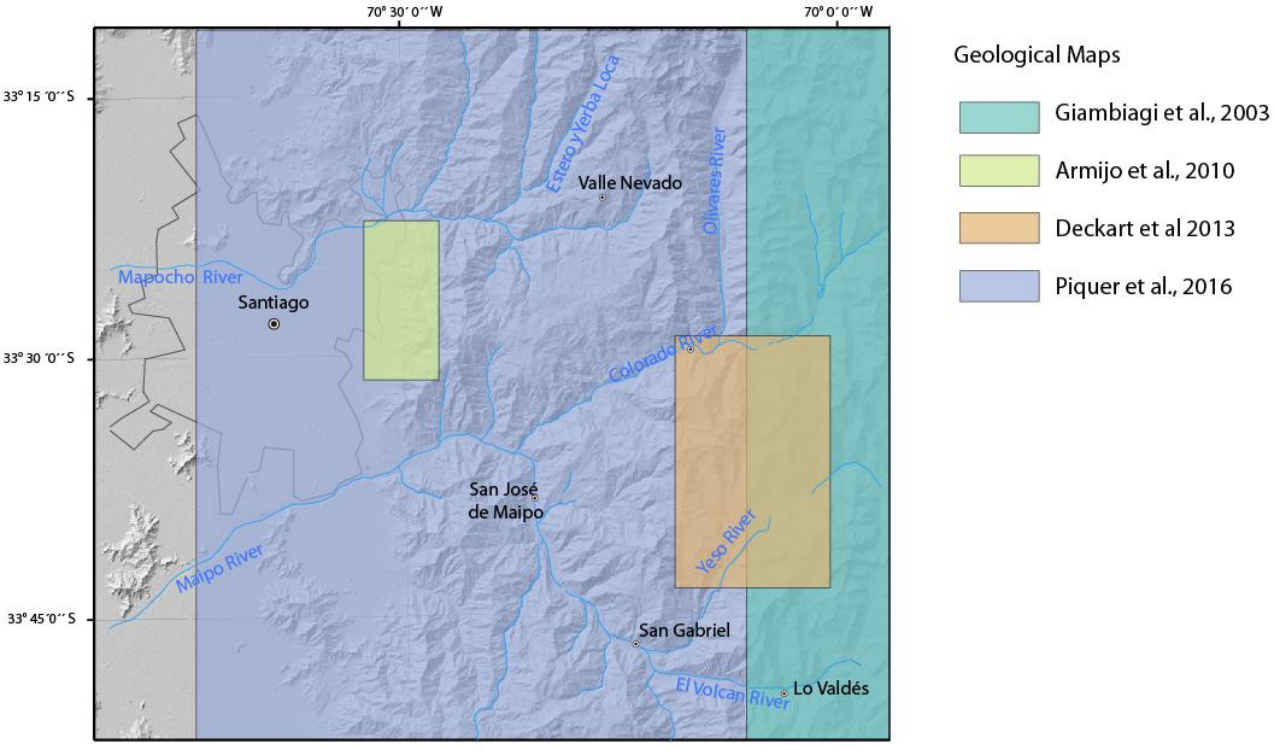


Figure 2.2 Map showing the area covered by publications in scientific journals in which geological maps exhibit important structural information.

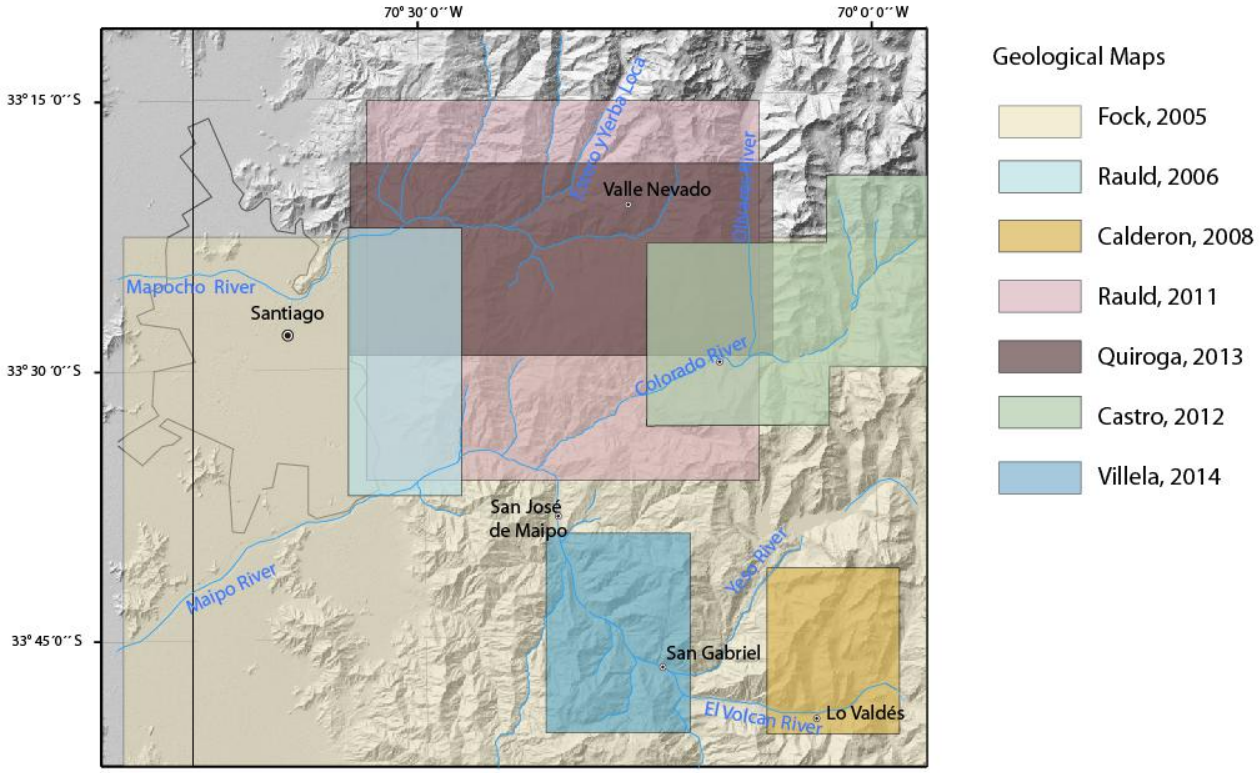


Figure 2.3 Map showing the area covered by thesis of undergraduate geology students, as well as, from MSc and PhD students.

### 2.1.2 Topographic data

The topographic information is extracted from two sources. First, open-access digital elevation models (DEM) from ALOS PALSAR covering the whole Metropolitan area. Second, DEMs derived from photographs, generated by photogravimetric techniques.

1. DEM from ALOS (Land observing Satellite) PALSAR (Phased Array type L-band Synthetic Aperture Radar): Open-access 12 m spatial resolution radiometric terrain corrected DEMs in GeoTIFF formats are directly extracted from The Alaska Satellite Facility (ASF) web page (https://vertex.daac.asf.alaska.edu/). The acquire DEMs are;
   1) ALPSRP273874290, acquire by the satellite on 2011-03-16.
   2) ALPSRP273874300, acquire by the satellite on 2011-03-16.
   3) ALPSRP270016510, acquire by the satellite on 2011-02-18.
   4) ALPSRP270016500, acquire by the satellite on 2011-02-18.
   This topographic information is processed in QGIS 3.10 . An example of the ALOS PALSAR DEM is shown in Figure 2.4a.

2. DEM from photogravimetry: These DEMs are constructed by Structural from Motion (SfM), which is a photogrammetry technique that allows the reconstruction of a three-dimensional (3D) scene from a series of 2-dimensional (2D) images. The 3D models were created by aligning spatially a group of photos with Agisoft 1.3.2 software and identifying points in common. Then a point cloud model is build, where each point represent a common pixel between images and also has depth calculated from the estimate position of the cameras. Finally a 3D model can be obtained after constructing a polygonal mesh model on grounds of the point cloud. Additionally a texture can be attributed to the model, showing the superficial features. For model (1) 136 images where taken by Drone, and then used to construct the DEM, which has a 26.3 cm/pix spatial resolution, with a coverage area of 1.24 $km^2$ and a point density of 14.5 point/$m^2$. The second is a 79.3 cm/pix spatial resolution DEM generated in base of 125 images, with a coverage area of 4.03 $km^2$ and a 1.59 points/$m^2$ point density. Technical reports of the DEM are in Chapter 9 (appendant). An example of the photogravimetry derive DEM is shown in Figure 2.4b.

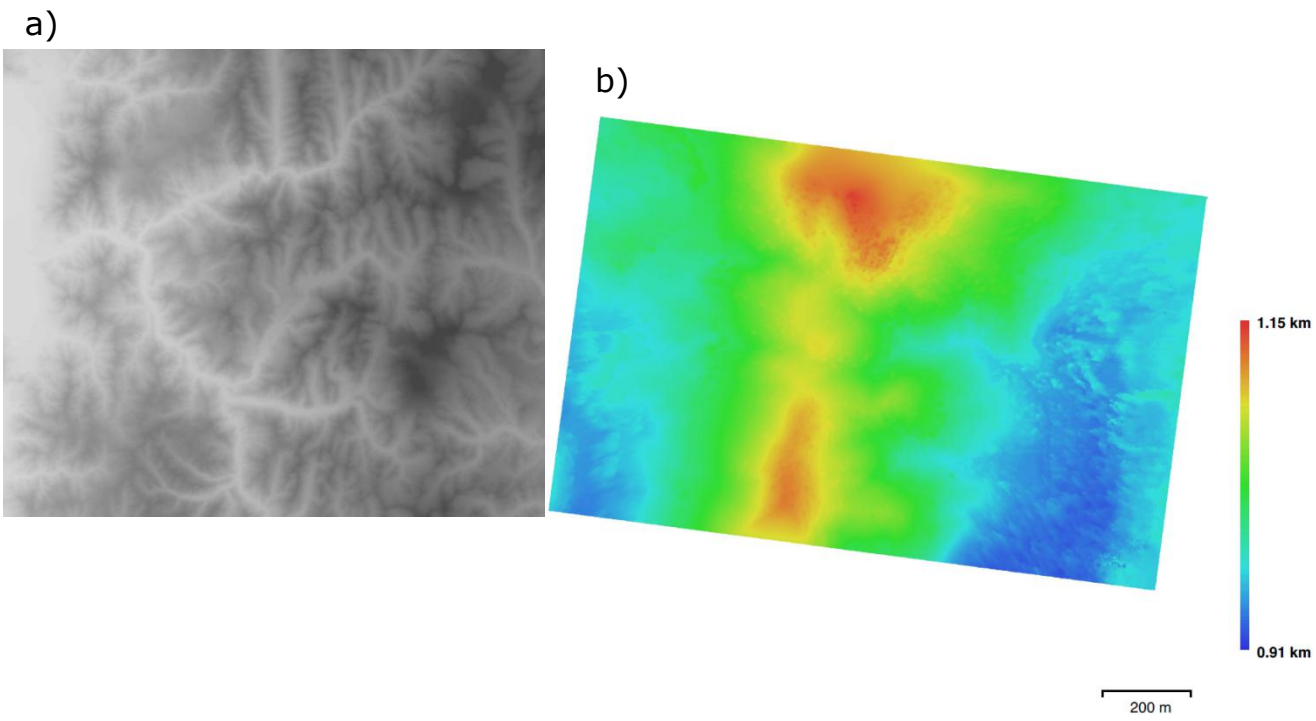


Figure 2.4 Digital elevation models used in this thesis. a) ALOSPALSAR DEM elevation in grey scale, and b) Photogravimetry derived DEM indicating elevation values in colors.

2.1.3 Satellite Images:

In this work I use Sentinel images, because they are open-access and 10 m/pixel spatial resolution. This is an European radar imaging satellite part of the European Union´s Copernicus program on earth observation.

Satellite Image from Sentinel-2B: Four multi-spectral 100 km x 100 km images in TIFF format are obtained from The Alaska Satellite Facility (ASF) web page:

(1) 2B_IW_RAW__0SDV_20170428T095444_20170428T095516_005359_009652_DC4E obtained by the satellite on 2017-04-28.
(2) S2B_IW_RAW__0SDV_20170421T100326_20170421T100358_005257_009353_23BC obtained by the satellite on 2017-04-21.
(3) S2B_IW_RAW__0SDV_20180505T095450_20180505T095523_010784_013B63_1FA9 obtained by the satellite on 2018-05-05.
(4) S2B_IW_RAW__0SDV_20180505T095515_20180505T095548_010784_013B63_3E4E obtained by the satellite on 2018-05-05.

An example of the satellite image used is shown in Figure 2.5.

Figure 2.5 Example of Sentinel-2B satellite image used in this thesis, showing the NE corner of urban Santiago

2.1.4 Geological data:

Lithology, structural data, geomorphology and general observations were documented during field work campaigns. Activities as rock sampling, rock description, strike and slip measurements, kinematic indicator detection and photo shooting were develop. This information is presented in geological maps and tables further in the text. Important information like geochronology, structural data sets, lithology identification where also extracted from the text related to the maps described in section 2.1.1.

2.1.5 Seismological data

Most of the seismic data is extracted from published scientific works like Barrientos et al., (2004), Alvarado et al., (2009), Pérez et al., (2014), Estay et al., (2016) and Ammirati et al., (2019). The seismic data comprises location of epicenter, depth of seismic events, magnitude (Mw) and in some cases focal mechanism. USGS seismic catalog was also used to extract seismic data as earthquake epicenter, Mw, depth and date.

## 2.2 Data analysis methodologies

2.2.1 Compile a structure database

A compilation of the previous works in the area (mentioned in 2.1.1) was done, resulting in a regional structural map of the Principal Cordillera near Santiago de Chile (Fig.1.1), which shows the topography and sum up all the recognized structures in the area. The author's recognize different structures and they propose different fault traces with varied degree of certainty. These characteristics had to be compared between the maps and integrated with the remote sensing data, using QGIS and Illustrator software, to come up with a coherent and complete regional structure 1:50.0000 scale map.

2.2.2 Explore the potentially presence of unrecognized crustal faults

New potentially structures are recognized by two different complementary mapping methodologies. The mapping was done in a 1:10.000 scale.

1. Remote sensing mapping: With the aerial images and the topographic information it was possible to develop first-order geological features recognition. All the remote sensing info was compiled in QGIS 3.10 software creating:

a. Slope maps: Maps that shows the inclination angle (in degrees) of a certain surface. The angle of slope is represented by a color map that represents flat surfaces as green, low slopes as yellow, moderate slopes as light orange and steep slopes as red (Fig. 2.6a).

b. Hillshade maps: Maps that shows the hypothetical illumination of a certain surface, determination the illumination parameters for each cell in a raster file. The illumination and shades are represented in gray colors. The main parameters to create a hillshade map are the location of the sun in the sky, defined by azimuth and altitude. The Azimuth and altitude used are 315° and 45° respectably (Fig. 2.6b).

c. Contour lines: They are curves that joint point of equal elevation value. The contour interval used varies from 15 to 100 m. They are useful to visualize the topography in detail (Fig. 2.6c).

d. Topographic profiles: Vertical profiles showing the topography related to some surficial traces. Vertical scale could by exaggerated to highlight some features. Flat areas and steep surfaces can be recognized (Fig. 2.6d).

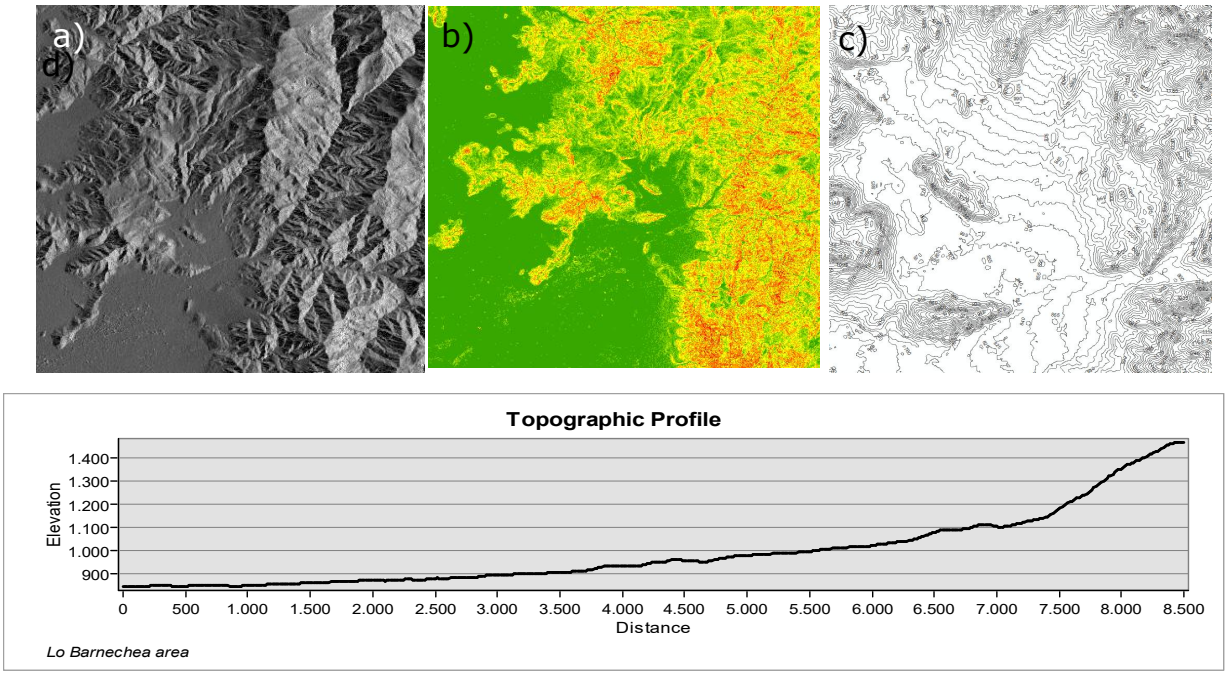


Figure 2.6 Example of DEM derived products develop by Spatial analysis in QGIS software. a) Slope maps, b) Hillshade maps, c) Topographic profiles and d) Contour lines.

2. Field work mapping: Field work was crucial to validate the remote sensing information and collect direct and solid geological data. Days in the field by Campo I and Campo II (Field School I and II), Proyecto 1 (Personal Project I), Fundamentals of Structural Geology classes, Newton Found field trip, and personal outdoor trips were useful to collect the regional and local information to develop this thesis project. Recognition campaign were done in the Maipo and Mapocho rivers, to familiarize with the study area and to identify the most important local areas and access (yellow boxes in Fig. 2.8). Special permission was needed to access to some urban areas, some other couldn't be possible to access because of well develop urbanization and the no-collaboration of some land owners. Three areas where more detailed mapped, Lo Barnechea district, in the NE corner of urban Santiago to the north of the Mapocho River; El Toyo locality in the Maipo River valley, more precisely in the Estero Coyanco; and the Baños Morales locality in Volcan River valley (White boxes in Figure 2.8). One helicopter flight was done (Fig. 2.7a), covering the Ramon range, Plateau de Farellones and Olivares River valley for recognition of the area (Fig. 2.9). Standard technics of field mapping were applied including lithological identification, structural measurements with classic "silva" compass, photographs of the studied outcrops with integrated camera of the

Android device SM-G532M, geomorphological observations, hand sample and fault rock characterization (Fig.2.7b and c). No GPS where used in the mapping thanks to the high-resolution mapping and the urban characteristics that are usefull for positioning and orientation.

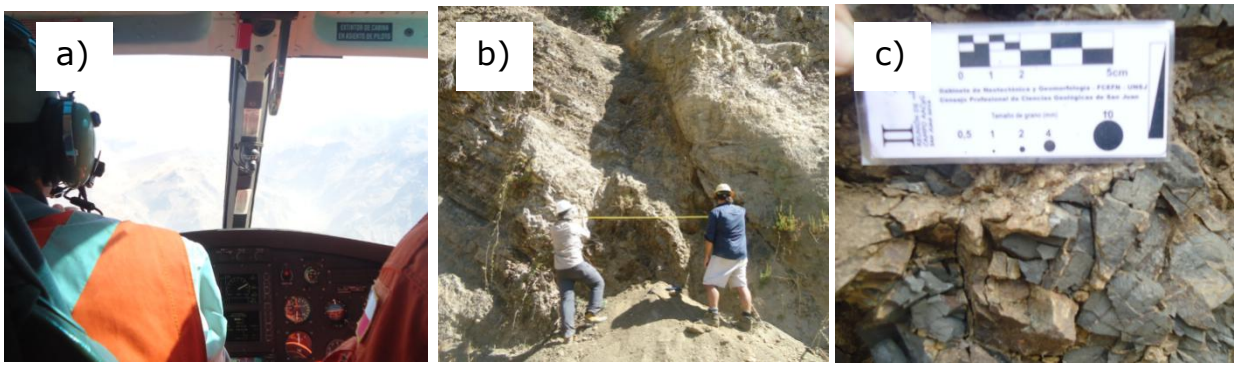


Figure 2.7 Field work photo examples. a) Helicopter flight, b) direct field measurement and c) rock sampling and photo shooting.

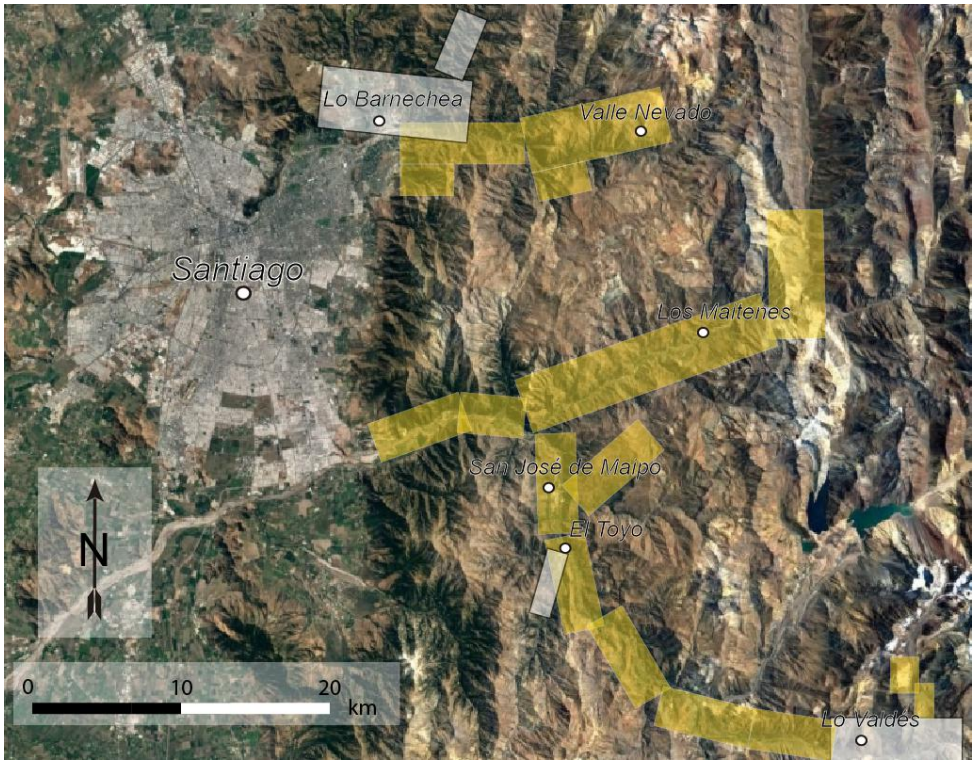


Figure 2.8 Map showing the area covered during field work campaigns. Yellow boxes indicated areas of general inspection. White boxes indicated areas of more detailed mapping.

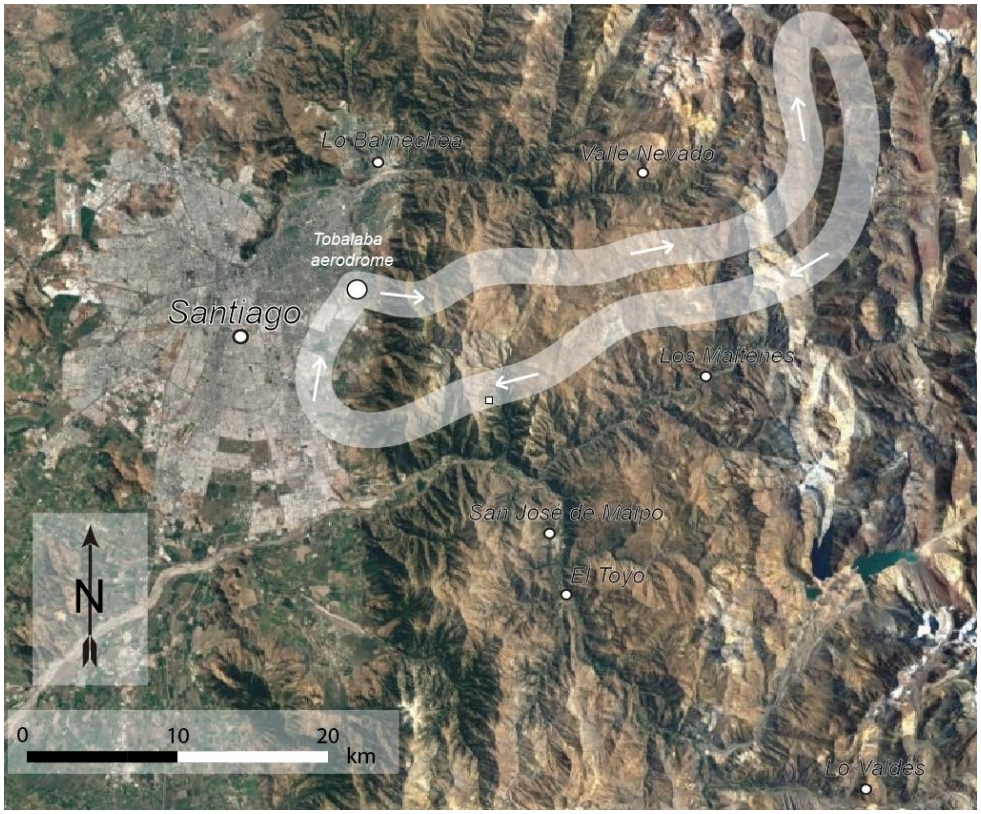


Figure 2.9 Map showing the area covered during helicopter flight.

### 2.2.3 Define the Quaternary behavior of the "new crustal faults"

Geomorphological markers as drainage pattern perturbations, scarps, shutter and pressure ridges among others, are analyzed in the remote sensing data and also in the field work validation to identify recent fault motion. These morphologies are related to tectonic activity, and its presence in the present day landscape indicates at least a Quaternary age of fault motion. Geometry and orientation of landforms are measured and analyzed. Observations of clearly faulted or deformed Quaternary deposits also indicate recent fault activity. In this work no age determination are made.

3D model are very useful at the moment of analyze the morphological features, because it can be used as a high resolution DEM. Structural from Motion is a photogrammetry technique that allows the reconstruction of a three-dimensional scene from a series of bi-dimensional images. 3D models where build with the Agisoft 1.3.2 with images toked from the field work. This software aligns spatially a group of photos, identifying point in common. Then a point cloud model is build, where each point represent a common pixel between images and also has depth calculated from the estimate position of the cameras. Finally a 3D model can be obtained after constructing a polygonal mesh model on grounds of the point cloud.

Additionally a texture can be attributed to the model, showing the superficial features. Figure 2.10 summaries the previous mentioned Sfm procedure.

Kinematic analysis in FaultKinTM software (Marret and Allmendinger, 1990; Allmendinger et al., 2012) which utilizes the right dihedra geometrical method of Angelier and Mechler (1977) and Pfiffner and Burkhard (1987), was used to calculate the orientation of the compression and tension axes for individual fault planes and also for fault populations. If these represent infinitesimal strain (i.e. small-offset faults that have not been subsequently rotated) the strain axes should be representative of paleo-stress principal axes.

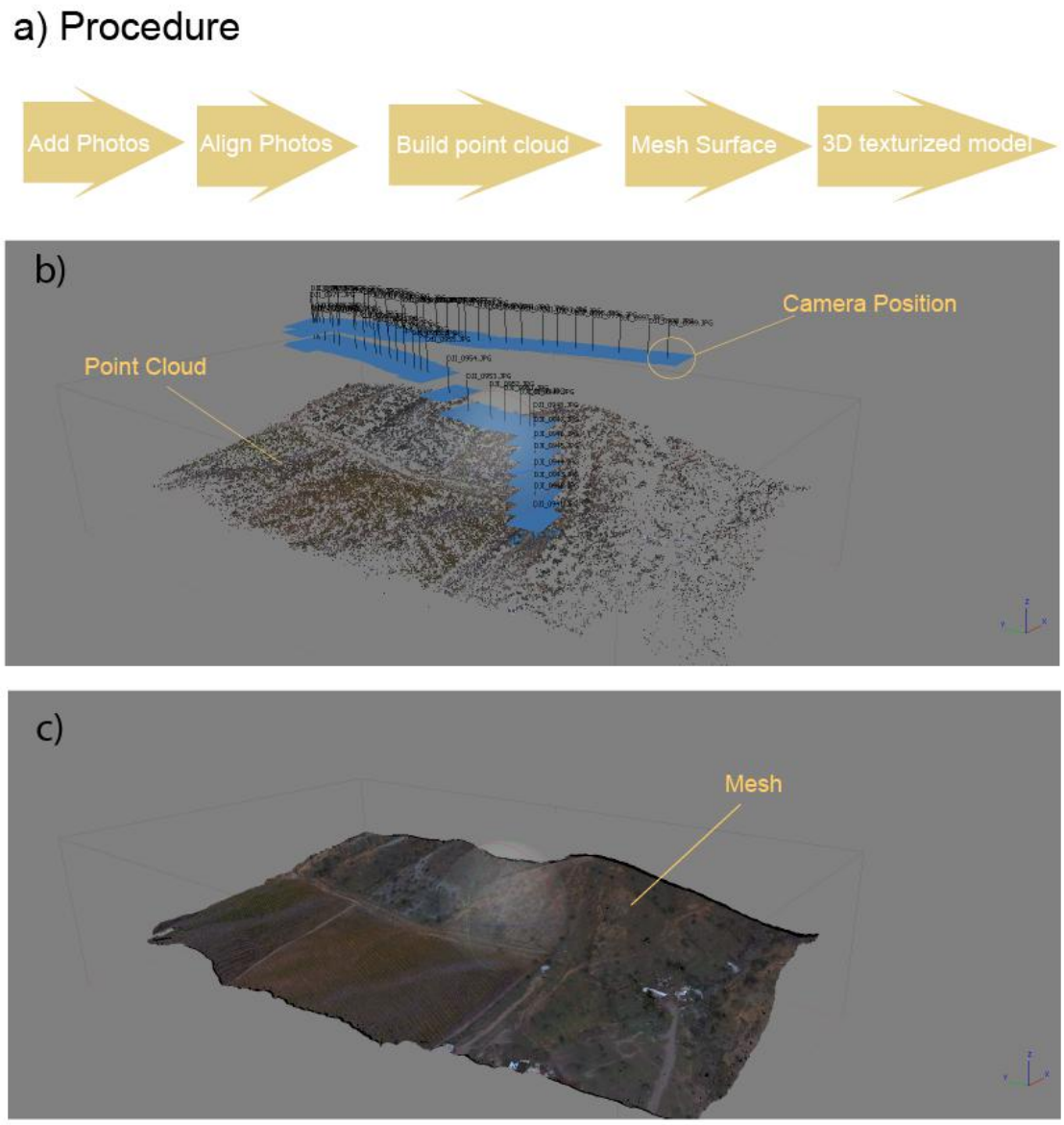


Figure 2.10 Structural from Motion (SfM) 3D model building workflow. a) Procedure. b) Spatially aligned group of photos, identifying point in common. c) 3D model obtained after constructing a polygonal mesh model on grounds of the point cloud.

### 2.2.4 Evaluate the potential seismic hazard of the structures

For all the crustal faults, the ones reported by previous authors and the ones described in this work, the related seismic hazard will be evaluated. First a complete compilations of all the mapped structures is develop. Data as strike, dip, kinematics, length, seismic depth, plausible area of rupture plane and degree of certainty (observed or inferred) is collected in base of reported information by previous authors and the data collected in this work. Second, as a worst case scenario, all the faults will be assume as active, and then using Wells and Coppersmith (1994) fault parameters scaling laws, different Mw will be calculated for each fault depending on the fault parameter used and different rupture scenarios. The results will be presented in tables and also in maps in Chapter 6. This different scenario ruptures will be compared to identify the areas were higher Moment Magnitud (Mw) are expected, and thus, present more hazardous zones. The spatial relation between Mw and populated areas is also analyzed to identify the areas that could be more affected by the earthquakes. Additionally, the faults expected Mw are also compared with landslide distribution in order to identify the possibility of this faults as potentially seismic sources that could trigger coseismic landslides.

## Chapter 3: Case study of the El Arrayan fault

This chapter presents a case study of the El Arrayan fault. It is written as a manuscript for eventual publication and thus has distinct abstract, literature review, methods, results, and summary section.

## The Likely Quaternary Active El Arrayan Fault, Santiago, Chile

### 3.1 Abstract

Understanding the location and nature of Quaternary active crustal faults is critical to the reduction of both fault rupture and strong ground motions hazards in built environments. Recent work along the San Ramon Fault (SRF) demonstrates that crustal seismic sources are important hazards within the Santiago Metropolitan region of Chile. In this paper we present the evidence of a second likely Quaternary active fault (the El Arrayan Fault, EAF) that runs through the northeastern part of Santiago, in Lo Barnechea. The EAF is a strike-slip fault zone at least 13 km-long, has a steep dip (mean dip 77º NNE), and a WNW-ESE general trend (~ 110º) that cuts across folded rocks of the Abanico Formation. Sequences of meter-wide fault rocks in El Arrayan can be tied to the tectonic geomorphology of the EAF, with fault scarps, deflected streams, saddles, "island hills", sag ponds and linear valleys in the La Dehesa area coincident with fault strike from the bedrock exposures. Although direct dating is not yet available, fault exposures tied to fault-related tectonic and geomorphic features cutting Late-Quaternary morphologies and deposits (including landslides and alluvial fans), provides strong evidence that the EAF is a Quaternary active and seismogenic crustal fault. Sinistral slickensides and left-lateral deflected streams indicates a left-lateral kinematics (with slight up to the north reverse motion) for the EAF. Due to the location, geometry, kinematics and likely Quaternary activity of the EAF, this structure could be interpreted as an arc-oblique transfer zone of the WAT (West Andean Thrust). If the EAF has stick-slip behaviour, it is potentially an important source of fault rupture and strong ground motions and could be responsible for earthquakes up to Mw 6.4 based on earthquake scaling laws and microseismic surveys in and around Santiago. The in-existence of fault zone avoidance criteria (i.e. do not build in and around active faults) in Chilean law, requires immediate enhanced fault mapping, legislation and the implementation of active fault rupture avoidance areas to reduce the risk associated with active crustal structures in the built environment.

### 3.2 Introduction

The Andes of Central Chile and Argentina is one of the highest active orogens on Earth with peaks reaching up to 7,000 m high (e.g. Mt Aconcagua, Tupungato volcano), partially controlled by a rapid (6-8 cm/year) tectonic plate convergence (Fig. 3.1a; Pardo-Casas and Molnar, 1987; DeMets et al., 1994; Gripp & Gordon, 2002). Santiago is the Capital City of Chile (with ~7 Million inhabitants) and is located at approximately 500 m above sea level immediately

to the west of the Central High Andes (Fig. 3.1a). Although hazards associated with great to giant earthquakes along the plate boundary here are well-known (e.g. Dura et al., 2015; Candia et al., 2017), the seismic hazard associated with crustal faults is less known. According to historical seismicity record, in September 1958 a strike-slip related moment magnitude (Mw) 6.3 earthquake occurred at a depth of 8 km at Las Melosas , ~60 km to the southeast of Santiago (Fig. 3.1b; Alvarado et al., 2009). This earthquake caused significant damage to hydroelectric plants, a water-supply aqueduct, and there were also extensive landslides and rock falls in the region (Sepulveda et al., 2008). In spite of the impressive manifestations of strong ground motion from this event, no surface rupture was found. This event demonstrates the importance of shallow crustal earthquakes (from the rupture of crustal faults) as sources of seismic hazards in the Principal Cordillera and around Santiago. Instrumentally registered earthquakes over the past few decades indicate that the shallow seismicity in the Andes concentrates along two N-S lineaments exposed along the western flank of the Principal Cordillera (~15 km depth) and within the Principal Cordillera (~10 km depth; Fig. 3.1b; Barrientos et al., 2004; Pérez et al., 2014; Ammirati et al., 2019). However, it should be noted that along many Quaternary active faults, the seismic recurrence may occur over time periods of hundreds to tens of thousands of years, something that cannot be captured from relatively short-duration seismic networks records (e.g. Schwartz and Coppersmith, 1984). Thus, geological investigations focussed on mapping and active fault characterization remains as a major goal in seismic hazard assessments.

Numerous geological faults were mapped in the Central Andes around Santiago (Fig. 3.1b; Thiele, 1980; Wall et al., 1999; Selles & Gana 2001; Giambiagi et al., 2003; SERNAGEOMIN, 2003; Fock 2005; Armijo et al., 2010; Piquer et al., 2016; 2019; Riesner et al., 2017), however there is incomplete discussion on how these faults appear in the field (e.g. fault rocks, sense of motion), or recency of activity. Most of these structures are Late-Cenozoic in age and are related with the development and later inversion of the Abanico Basin (Charrier et al., 2002; Charrier et al., 2007). The classic version of the development of the Abanico Basin is as follows. The Abanico Basin is a former Cenozoic intra-arc extensional basin which is now inverted where the mostly volcanic, volcaniclastic and also sedimentary Abanico Formation and Farellones Formation were deposited. This deposition occurred between the Oligocene and Miocene (Charrier et al., 2002, 2007; Giambiagi et al., 2003; Fock, 2005) based on stratigraphic relationships, fossil occurrence, and radioisotopic ages. The tectonic extension of the basin was related to the activity of N-S high-angle regional scale normal faults such as the Los Angeles-Infiernillo, San Ramon, and El Diablo faults mainly located at the edges of the basin during Oligocene (Charrier et al., 2002, 2007; Fock et al. 2006; Farías et al. 2008). These N-S striking regional fault systems also controlled a tectonic basin inversion and exhumation during the Early to Middle Miocene (Giambiagi et al., 2003), in which the Abanico Formation was deformed and the Farellones Formation was deposited (Charrier et al., 1996, 2002, 2007). The now inverted N-S regional scale reverse

structures are part of large tectonic unit like the east-vergent Aconcagua Fold and Thrust Belt (Fig. 3.1b; Giambiagi et al., 2003) and the west-vergent West Andean Thrust (Fig. 3.1b; Armijo et al., 2010). In the internal part of the basin conjugate NW-SE and NE-SW orientated strike-slip structural trends were interpreted based on direct structural observations, regional-scale gravimetry, seismic and magnetic data (Piquer et al., 2016, 2019). Early to Middle Miocene faulting is likely for the main compressive deformation of the Abanico Basin during its inversion (Charrier et al., 2005).

To further complicate the previously accepted history of the Abanico Formation outlined above, new dating and fieldwork (Mosolf et al., 2018) from southeast of Santiago (~35°S) provides a robust and older chronostratigraphic framework spanning c. 75-11 Ma. Thus this new work shows the Abanico basin is much older than previously recognized, with Late-Cretaceous to Late Eocene intra-arc sedimentation and volcanism which deposited the Abanico Formation, followed by Late Eocene to Late Miocene strike slip dextral shearing within the volcanic arc. Mosolf et al. (2018) separate the Abanico into upper and lower Abanico, with 37 Ma being the limit between these two divisions. Based on accumulation rates, and other data, they suggest that instead of a fault-bounded basin, the Abanico Formation slowly accumulated in a intermontane basin bounded by a volcano. Importantly, based on their field mapping and age control (Mosolf et al., 2018), they also show NW-striking sinistral strike-slip faulting that appear to be younger than all other structures in regionally based on cross-cutting relationships.

Additionally, Middle Miocene – Early Pliocene faulting in the Abanico Basin is suggested by syn-tectonic hydrothermal mineral fibers on the NW-striking and NE-striking conjugated strike-slip faults system, under a transpressive regime with E- to ENE-directed shortening (Piquer et al., 2015, 2016). Late-Quaternary faulting in Santiago was documented along the San Ramon Fault (SRF). The SRF is a N-S to NNW-SSE striking, west-vergent reverse fault, that is part of the West Andean Thrust (Armijo et al., 2010), with a prominent fault scarp at the foothills of the western flank of the Principal Cordillera, within the limits of urban Santiago, that accommodates part of the compressional stress regime in this sector of the Central Andes (Rauld, 2002; Armijo et al., 2010; Rauld, 2011; Vargas et al., 2014; Estay et al., 2016). The fault is well mapped between the Mapocho and Maipo Rivers (Armijo et al., 2010; Rauld, 2011). The geometry of the northern part of the SRF is characterized by a string of three arch-shaped hills. These hills correspond to eroded remnants of a gentle NW-striking anticline structure which deforms the Abanico Formation bedrock and the Quaternary sediments (Armijo et al., 2010). This anticline, compared with the southern and more regular part of the SRF, is not located immediately to the west of the mountain front. The anticline instead may be indicative of some near-surface complexity in the process of fault propagation in this area (Armijo et al., 2010). Geophysical evidence of the SRF supports the presence of the structure at the subsurface (Diaz et al., 2014; Pérez et al., 2014; Estay et al., 2016, Ammirati et al., 2019).

Wells and Coppersmith's (1994) scaling relationships, allow to estimate a Mw 6.9 earthquake potential for the SRF, based on structural reconstructions (Armijo et al., 2010). However, paleo-seismic trenching (Vargas et al., 2014) provides a general first order potential Mw 7.5 earthquake. Some authors suggest that the fault continues to the north at the east of Chicureo, and continues to the south at the east of Pirque (Armijo et al., 2010; Vargas et al., 2014, Estay et al, 2016). Nevertheless, strong evidence of these northern and southern locations of the San Ramon Fault or related structures is not currently available.

The San José de Maipo fault, located 5 km north of San José de Maipo, in which reverse faults and drag folds, of unknown length, were described within Quaternary terraces (Lavenu et al., 1994; Lavenu, 2006; Lavenu & Cembrano, 2008). The fault does not have geomorphic expression in the landscape and a map trace length could not be determined (Lavenu & Cembrano, 2008). A NNW shortening direction was determined based on kinematic analysis of mesoscopic fault-slip data of the San Jose de Maipo fault (Lavenu & Cembrano, 2008). Nonetheless, apart from these 2 faults, the existence of other active crustal seismic sources in or around metropolitan Santiago are still poorly constrained.

Therefore, for developing an accurate seismic hazard assessment and for understanding fault rupture hazards of the most populated city in Chile, it is necessary to recognize and understand the active regional crustal seismic sources. This work, characterizes the El Arrayan Fault (EAF), that we discovered and mapped in northeastern Santiago.

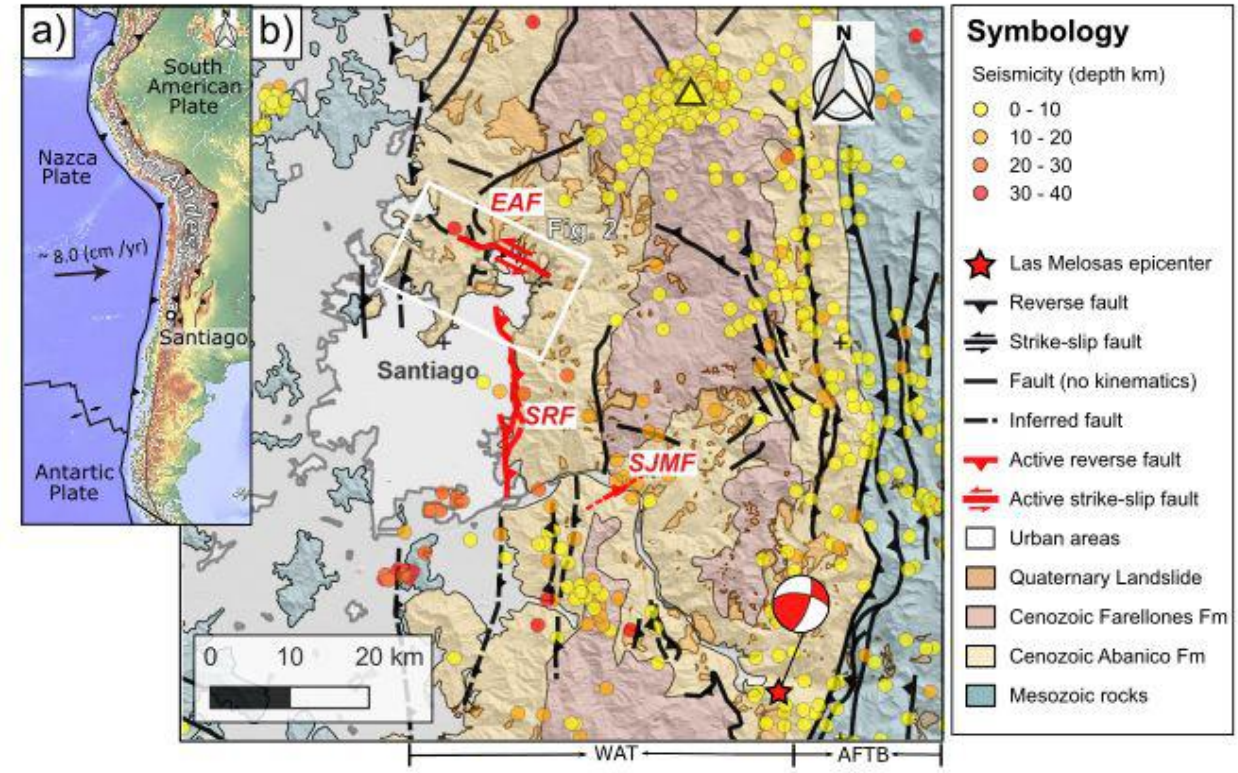


Fig. 3.1: a) Simplified tectonic framework of the subduction margin of the Andes. Black arrow shows tectonic plate convergence velocity (Gripp & Gordon, 2002). Location of the City of Santiago is shown. b) Geologic and seismic framework of Santiago and the Principal Cordillera between 33°-34°S and the locations of major known or suspected active faults from this study and other authors (see text). Major faults are shown with thick black lines. Seismicity from USGS, where small circles marks the epicenter locations. Red star shows the 1958 Mw 6.3 Las Melosas Earthquake location and focal mechanism is shown (Alvarado et al., 2009). White box shows location of Fig. 3.2. EAF: El Arrayan Fault; SRF: San Ramón Fault; SJMF: San José de Maipo Fault. WAT (West Andean Thrust); AFTB (Aconcagua Fold and Thrust Belt).

## 3.3 Methods

The EAF was discovered by the research team during field mapping in order to evaluate potential active faults within urban Santiago at the type section in the El Arrayan sector within the Municipality of Lo Barnechea. A combination of remote sensing and fieldwork was done in order to document and characterise the EAF there. Lithology, structural data, geomorphology and general observations were documented during fieldwork. Activities such as rock sampling and description, structural measurements, determination of kinematic indicators and photographic documentation allowed for the characterisation of the EAF. We later field mapped to track the tectonic geomorphology of the EAF westward from

El Arrayan where it crosses the basin of La Dehesa. Given that these sites are heavily urbanized (Fig. 3.2a) and crossed by roads, modern mapping is challenging due to severe human and construction-induced modifications. Also, as most of the property is private (and walled off) thus access is not always possible. Fault rocks were classified following the classification of Sibson (1977). A combination of remote sensing and field mapping was used to explore tectonic geomorphology and landforms such as deflected streams, saddles, sag ponds and scarps (McGill and Sieh, 1991; Burbank and Anderson, 2012) in order to determine the evidence fault surface expression.

Digital topographic data was obtained from two sources. Open-access digital elevation models (DEM) from ALOS (Land Observing Satellite) PALSAR (Phased Array type L-band Synthetic Aperture Radar), that covers the entire Santiago Metropolitan area, and DEMs derived from drone photographs, generated by photogrammetric techniques. The DEM obtained from ALOS PALSAR provides open-access 12 m resolution radiometric terrain corrected DEMs in GeoTIFF formats, which were used for mapping and spatial analysis in QGIS software. Site specific DEMs along the EAF were constructed with Structural from Motion (SfM) techniques (Förstner, 1986; Harris and Stephens, 1988). SfM is a photogrammetry technique that allows the reconstruction of a three-dimensional (3D) scene from a series of 2-dimensional (2D) images. The 3D visual models and DEMs were created with photographs collected with a Phantom 4 (DJI) drone (UAV) using the Argisoft 1.3.2 software to create DEMs and digital orthophotos.

A kinematic analysis with FaultKinTM software (Marret & Allmendinger, 1990; Allmendinger et al., 2012) based on field observations was performed. This software uses the right dihedral geometrical method of Angelier & Mechler (1977) and Pfiffner & Burkhard (1987) for calculating the orientation of the compressional and tensional axes of individual fault planes and fault populations on the basis of structural data.

The seismic hazard of the EAF was explored based on the distribution of fault rocks and geomorphological evidence, which was subsequently evaluated using Wells and Coppersmith (1994) fault parameter scaling laws.

## 3.4 Results

### 3.4.1 Geological fault observations

While screening for active faults and evidence of the San Ramon Fault in the Santiago region, we discovered the exposure of the EAF in El Arrayan. There we worked on the fault exposure outlined below and afterwards we conducted field mapping and further field investigations to the west of El Arrayan. Field mapping in the Lo Barnechea area shows volcanic and sedimentary rocks of the Abanico Formation (Fig. 3.2a and 3.2d). The strike and dip of the bedding within the Abanico Formation rocks in this area differs significantly from the rest of the

mountain front, especially in the San Ramon Range (and the eastern side of the El Arrayan Valley), where it is primarily east dipping (e.g. Riesner et al., 2017). The EAF cuts the stratification and post depositional folding in the Abanico formation and represents the youngest deformation within this formation.

### 3.4.2 Main fault zones

The main fault exposure is located in the El Arrayan neighbourhood, adjacent to the El Arrayan stream, a tributary to the Mapocho River in the Borough of Lo Barnechea, in the northeast of Santiago (Fig. 3.2d, Site A). The road cut on the west side of the "Camino Refugios del Arrayan" (between turn off to Camino el Estero and Camino Mallalil), exposes stratified andesites interbedded with dark-coloured fine-grained sedimentary rocks (siltstone/mudstone, 1-5 cm thick: Fig. 3.3c). The exposure is ~15 m high and ~30 m long. Dark-grey inclined and stratified beds (250-270/38-50°N) to the left (south) are in fault contact with relatively flat-lying (140/10-20°SW) volcanic and sedimentary layers to the north. Within this fault zone, a series of fault rocks are found (Fig. 3.3c and 3.3d).

The fault rocks constitute the core of the EAF (e.g. Caine et al., 1996). The fault core is a 3.5 to 4.0 m wide fault sequence with crush breccia, protocataclasites and fault gouge layers (Fig. 3.3d). The principal slip zone is characterized by gouge and the two sub-vertical gouge-lined planes (290/77°NE: Fig. 3.3c and 3.3d). Sub-horizontal fault grooves (i.e. slickenlines) along the two main slip planes shows slightly dipping rakes between 12° – 18°E, indicating mainly strike-slip kinematics (Fig. 3.3e). Unfortunately, no sense of movement could be determinated in situ, however a left-lateral deflection of the El Arrayan stream immediately adjacent to the site suggests a sinistral kinematics (Fig.3.3a and 3.3b). According to the rake angle and the left-lateral kinematics, using the method proposed by Marret & Allmendinger (1990), this fault likely accommodates mostly strike-slip motion and minor dip-slip (up to the north) with a shortening axis (P) of 062/03° (Fig. 3.3d). A subsidiary slip plane (106/82°S) displaces a brown volcanic lava bed, with a 1 m vertical throw (Fig. 3.3c). Altogether with the northern main slip plane they form a light-colored wedge shaped block of protocataclasite with abundant gypsum veins (Fig. 3.3c). The protocataclasite is curved, concave and close to the main slip zone (Fig. 3.3d), in a similar way to drag folds in a discrete reverse fault. The protocataclasite is also faulted with centimeter-scale displacements along by minor NE dipping reverse fault planes (Fig. 3.3d).

In addition to the type exposure of the EAF in El Arrayan, geomorphic mapping and field reconnaissance (outlined in the section below) allowed recognition of a second EAF exposure at the western limit of Lo Barnechea, where the Juan Pablo II road connects Lo Barnechea with Chicureo (Fig. 3.2d, Site D; in a road cut along the southern side of Juan Pablo II Road), which is ~11 km to the west of Site A in El Arrayan. In this locality massive porphiric dark red andesites of the Abanico Formation to the north are separated from massive porphiric light-

grey andesites to the south. Between both rock units is a 70 m-wide highly sheared fault zone. Numerous meter-wide fault rocks including breccias and protocataclasites were found (Fig. 3.4a, 3.4b, 3.4c and 3.4d), as well as sub vertical sharp individual fault planes in variable orientations (Fig. 3.4b). Along the NW side of the fault zone the most prominent structure (i.e. the master fault) was observed. This is a ~1.5 m wide, white colored, S-shape protocataclasite that presents numerous minor faults planes with S-C fabric and gypsum veins which suggest a reverse kinematics (Fig. 3.4a). Flanking the S-shape protocataclasite to the NW, subhorizontal (5°-15°) slickensides with left-lateral kinematics were reported from a 110/83°SW orientated fault plane. This 110/83°SW fault plane is very similar orientation to the 106/82°SW main fault planes reported at Site A. Due to the width of the fault zone, 65 individual fault planes, veins and fractures were measured. From these measured structures, 18 had likely kinematic indicators (Fig. 3.4b). Based on field data, a mean compression axis (P) 213/30° (Fig. 3.4b was obtained for the fault population using FaultKinTm (Marret &Allmendinger, 1990; Allmendinger et al., 2012). An W-E structural trend with left-lateral strike-slip kinematics is clearly visible in the stereonet plot (Fig. 3.4b). Also at site D, poorly-consolidated and a presumably Quaternary alluvium deposit was observed. (Fig 3.4b). This alluvium deposit is characterized by an orange silt to fine grain sand matrix and semi-rounded fractured volcanic clast ranging sizes from 50 cm to a tens of millimeters and no clear sedimentary structure. A 210/60°W orientated, 10-30 cm wide protocataclasite juxtaposes volcanic dark-reddish massive andesite in the hangingwall with this alluvium in the footwall (Fig 3.4c). Additionally, an 185/40°W orientated, also ~10-30 cm wide protocataclasite, juxtaposes the alluvium in the hangingwall with a ~7 m wide fault breccia in the footwall. Finally, the fault breccia is bounded to the SW by a 180/75°W fault plane, juxtaposing it against a massive light-grey andesite (Fig. 3.4d).

In addition, two other field sites were found in this highly-urbanised zone (Fig. 3.2d, Site B and C). Site B is a 6 m wide fault zone in between massive porphyric andesites (Fig. 3.5a; Yellow star). Here, cataclasite, breccia and gouge has a W-E to WNW-ESE strike with sub-vertical dips to the north (Fig. 3.5c). No kinematics indicators were found in the fault zone, however a possible left-lateral stream deflection (Las Hualtatas stream), immediately adjacent to the site, is suggestive of sinistral kinematics (Fig. 3.5a and 3.5b). To the west of the fault outcrop, a NW-oriented saddle is found (Fig. 3.5a). On the western side of the saddle, at the "Santa Martina" road, another fault zone is found (Fig. 3.5a; Orange star). Here, massive purple and grey andesites are cut by 3 subvertical 5-30 cm wide fault rocks (breccia and cataclasite) and associated fault planes. Figure 5d shows the exposed cataclasite. These fault planes vary from 330° to 350° and unfortunately no kinematic indicators were found. At Site C, in grey aphanitic volcanic rocks with sub-horizontal fractures, a 4 m-wide deformation zone is shown. It is characterized by 6 subvertical minor fault planes with subhorizontal grooves that shows a dextral sense of motion with a mean 065° strike. A 10-20 cm wide fault breccia was observed immediately adjacent to a

065/80°SE fault plane (Fig. 3.4e) with a 30° rake groove with Riedel fractures that indicates a left-lateral strike-slip kinematics (Fig. 3.4f). Based on field data, a mean compression axis (P) 019/28° (Fig. 3.4f) was obtained for the fault plane and grooves FaultKinTm (Marret &Allmendinger, 1990; Allmendinger et al., 2012).

Additionally, a NW-plunging anticline is recognized in the study area (Fig. 3.2d). This anticline topographically correlates with a NW orientated hill (Fig. 3.2b and 3.2c). Another structure is the study area is the NNW-SSE striking reverse fault previously mapped by Wall et al., (1999) in the Cerro el Zorro (Fig. 3.2d).

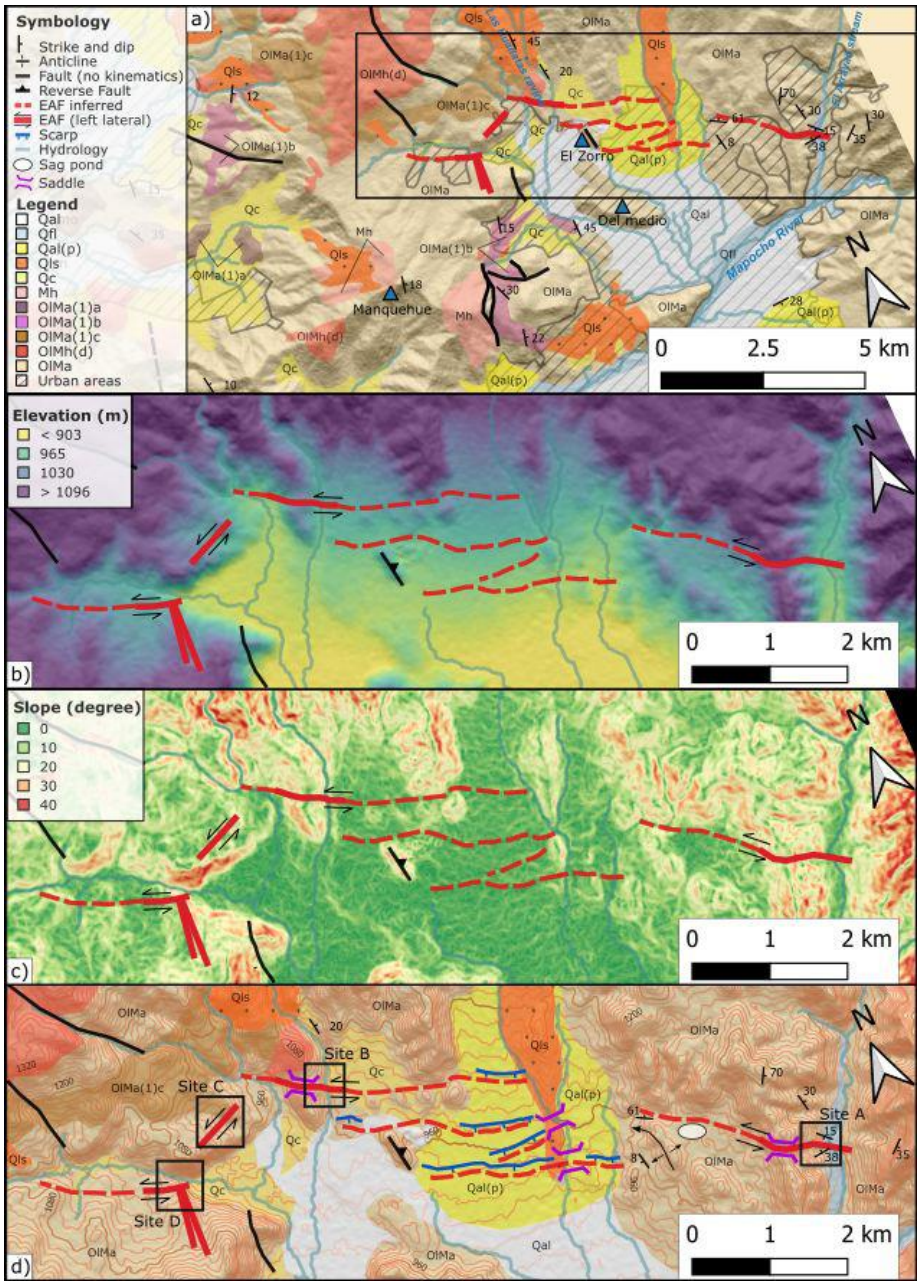


Fig. 3.2: a) Simplified geological map of study area. The map shows topography, lithology, Quaternary deposits and mayor structures but no kinematics for simplicity. Hydrology, hills including "island hills" (in blue triangle) are also indicated. Black box shows the locations of Figure 3.2b, 3.2c and 3.2d. Qal: Quaternary alluvial deposits; Qal(p): Quaternary alluvial piedemont deposit; Qls: Quaternary landslides; Qc: Quaternary colluvial deposits; Qfl: Quaternary Maipo River fluvial deposits; Mh: Subvolcanic andesites and dacites; OlMa: Oligo-Miocene Abanico Formation constituted by andesitic to basaltic lavas interbedded by tuffs and continental sedimentary rocks; OlMa1(a): Dacitic to rhyolitic to welded tuffs; OlMa1(b): Sedimentary intercalation of fluvial conglomerates, sandstones and shales. OlMa1(c): Acid cineritic tuffs. OlMh: Stocks of basaltic andesites to dacites; Geology compiled from Thiele (1980), Wall et al., (1999) and this work. b) DEM of study area colored by elevation. Hydrology is also shown. The EAF is indicated. c) Slope map of the study area. The EAF is indicated d) Detailed geological map of the study area. Black boxed show the study sites. Legend is the same as the Figure 3.2a.

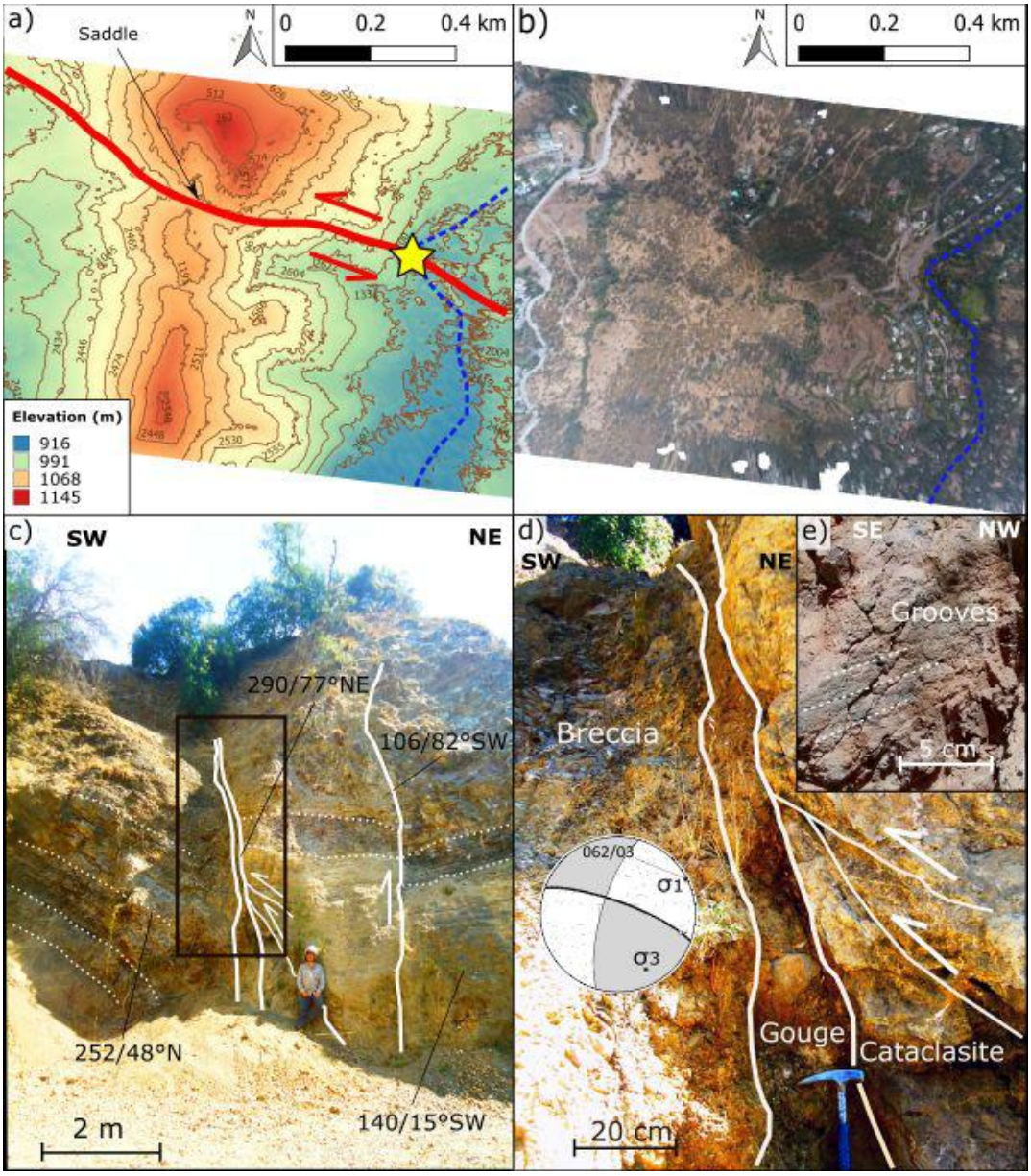


Fig. 3.3: a) SfM DEM from Site A. Yellow star shows the location of the fault outcrop in Fig. 3.3c). Dotted blue line shows the El Arrayan stream. Red line shows the aproximated location and kinematics of the EAF. B) Orthophoto derived from SfM. Dotted blue line shows the El Arrayan stream. c) Field photo of EAF at Site A in El Arrayan. Black box shows the locations of Figure 3.3d. d) Field photographs showing fault rocks within the EAF fault core. Stereonet shows the shortening axis (P) of 062/03° obtained in Site A. Note minor reverse fault in cataclasite. e) Grooves on SW main slip plane

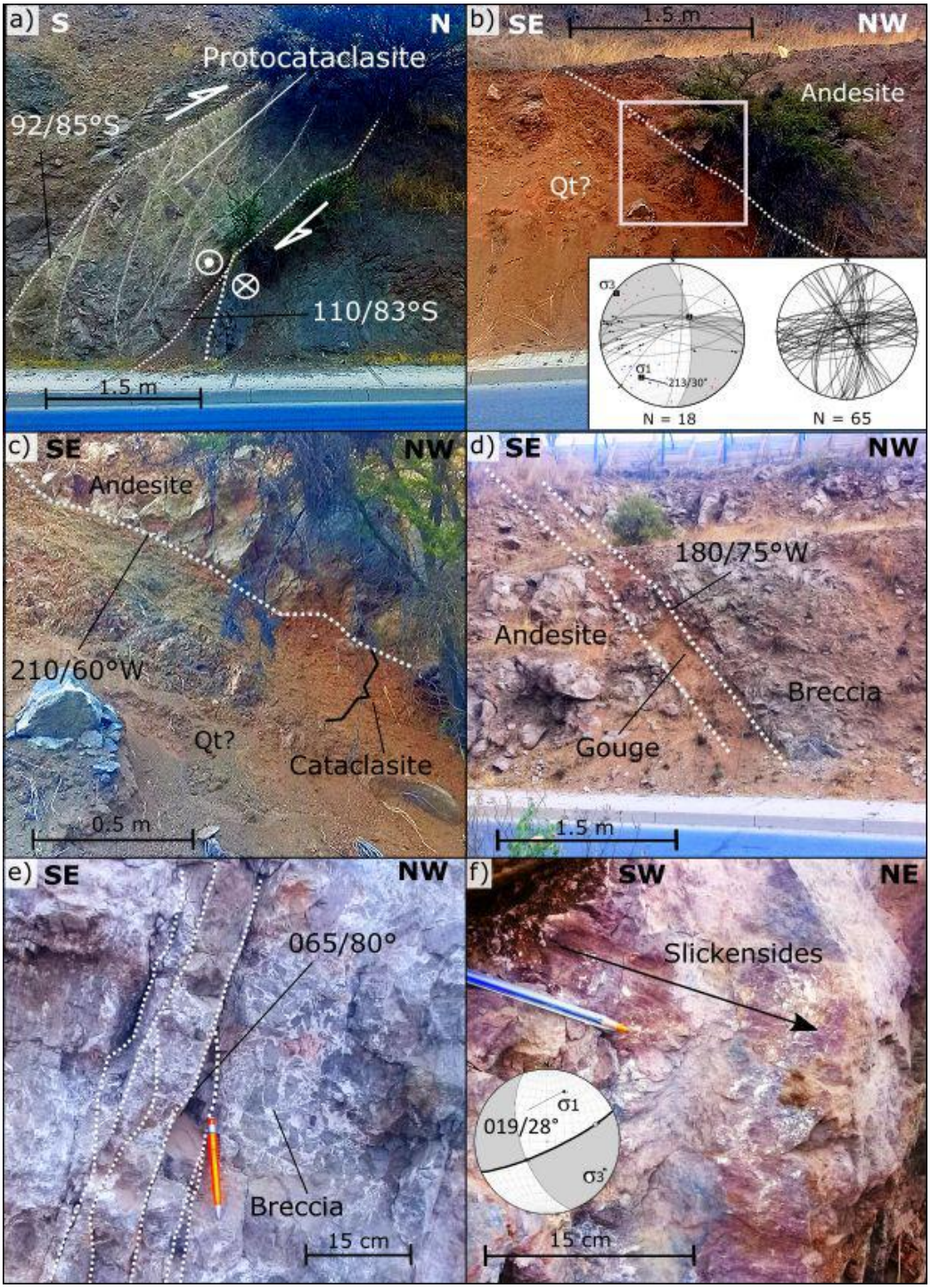


Fig.3.4: a) Field photo of EAF outcrop with WNW-ESE orientation at Site D. Dotted withe line shows fault surfaces.b) Field photo of the EAF minor ~N-S fault at Site D. White box shows location of Fig. 3.4c. Stereonets show the structural data obtained in Site D. c) Closer view of the fault outcrop shown in Fig. 3.4b. d) Field photo of the EAF minor N-S fault at Site D. e) Field photo of the EAF ENE-WSW minor fault at Site C. f) Field photo of subhorizontal slickenlines and grooves at Site C. Stereo net shows the shortening axis (P) of 019/28° obtained in Site C.

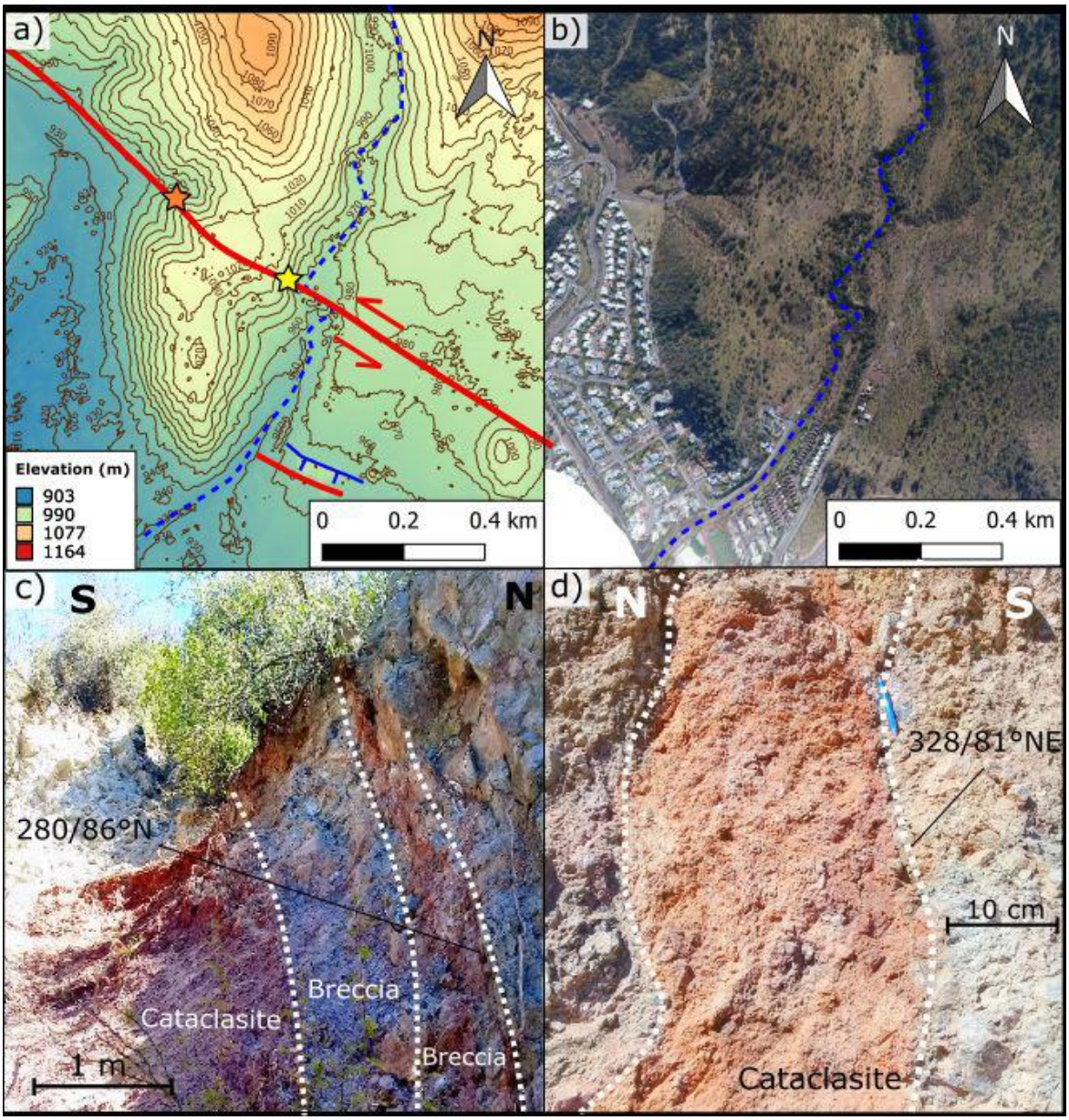


Fig. 3.5: a) SfM DEM from Site B. Yellow star shows the location of fault outcrop of Fig 3.5c. Orange star shows the location of fault outcrop of Fig. 3.5d. Red lines shows the aproximated location and kinematics of the EAF. Dotted blue line shows the location of the Hualtatas stream. Solid blue line shows a fault scarp, short blue line indicated down side. b) Ortophoto derived from SfM of Site B. Dotted blue line shows location of the Hualtatas stream. c) Field photo of the EAF in the Hualtatas stream at Site B. d) Field photo of the EAF at "Santa Martina" road in Site B.

### 3.4.3 Remote Sensing and Geomorphic observations

Finding the exposure of the EAF led us to target the tectonic geomorphology from El Arrayan and westward through La Dehesa. Within the study area, in Lo Barnechea, there are conspicuous low areas with respect to the surrounding elevations, within the foothills of the Principal Cordillera, north of the Mapocho River and east of the Manquehue Hill (Fig. 3.2a). These low areas were infilled by Mapocho River sediments (Quaternary alluvium) in addition to piedmont Quaternary alluvial material and colluvium from the surrounding hills (Fig. 3.2a). Urban development is concentrated in these low-lying areas (e.g. La Dehesa) at an average elevation of 850 m (Fig. 3.2b). Quaternary alluvium deposits with fan morphologies are well exposed (Fig. 3.2d), with a drainage running from NNE to SSW (Fig. 3.2b and 3.2c). Isolated hills (almost island hills) disrupt the average south-west facing 3°- 4° slopes (Fig. 3.2c) reaching elevation up to 970 m in the Medio and El Zorro Hills which have a NNW to NW elongation, and are composed of sedimentary Abanico Formation rocks (Fig. 3.2a). North of El Zorro Hill, three en echelon left-stepping NNW-elongated hills are aligned in a WNW-ESE orientation (Fig. 3.2b, 3.2c and 3.2d). The eastern limit of the depression of La Dehesa has an irregular morphology composed by numerous hills, some with an WNW to NW elongation (Fig 3.2b and 3.2c). Quaternary mass movement (i.e. landslide) deposits are found within this area, which exhibit long and narrow shapes, orientated in N-S to NNE-SSW directions, and with numerous saddles along them (Fig. 3.2d).

Slope maps in conjunction with topographic profiles, when combined with the observations from the fault exposures and field observations show the existence of discontinuous, but aligned, tectonic landforms such as sag ponds, drainage pattern perturbations, saddles and also topographic steps, or breaks in the slopes of these fans (~10-14° and between 3-14 m in elevation). These topographic steps are semi-parallel, and have crests that strike E-W to NW-SE (Fig. 3.2d), contrasting with the NNE to SSW drainage pattern (Fig. 3.2c). These topographic steps are coincident with the island hills that disrupt the low-lying basin around the La Dehesa area.

At Site A (in El Arrayan), a left-lateral displacement of the El Arrayan stream (immediately to the east of the fault outcrop) suggests left-lateral strike-slip kinematics for the EAF. (Fig. 3.3a and 3.3b). However, landslides or slope deposits from the valley side to the east may be responsible for an apparent deflection. A NW-oriented saddle in the main ridge between El Arrayan and La Dehesa immediately to the west and along strike from the fault exposure (Site A) is noteworthy (Fig 3.3a). This ridge has higher elevations to the north on the hangingwall of the fault, which is suggestive of long-term up to the north dip slip motion in addition to the dominant strike-slip motion there (Fig. 3.3a). Further to the west, aligned with the saddle and the fault zone, a potential sag pond (Lo Barnechea lagoon) in relative flat area between irregular hills is found (Fig. 3.2d).

Noting again that this area is densely populated and altered, between Sites A and B, due to geomorphic observations, possible fault strands of the EAF are found based on topographic scarps found in the Quaternary alluvium within La Dehesa (Fig. 3.2d). The southern strand is inferred by a ~150 m length, WNW-ENE oriented, SSW-facing topographic scarp of ~12 m high and ~12° dip between surfaces (Fig. 3.6, P5). This scarp is aligned with a saddle on an irregular Quaternary alluvial deposits (Fig. 3.2d). To the west of the saddle a ~1.5 km length, WNW-ESE orientated topographic scarp can be recognized on a Quaternary alluvial deposit with an average ~10° dip and ~ 9 m high in its central part (Fig. 3.6, P4). These semicontinuous aligned scarps and saddles suggest the presence of a WNW-ENE fault with up to the north sense of motion (i.e. coincident with observations from Site A). Unfortunately, no in-situ structural data could be collected to validate the geomorphological observation and to better constrain geometry and kinematics of the inferred fault. Further north, the next strand is inferred by the presence of a ~ 600 m length, WNW-ENE oriented, SSW-facing topographic scarp which is ~11 m high and has a 14° dip between surfaces along the Quaternary alluvial deposit (Fig. 3.6, P3). The western part of the strand is represented by ~ 200 m length, WNW-ESE, SSW-facing topographic scarp of ~ 3 m and ~12° dip in Quaternary colluvial deposit (Fig. 3.6, P1). Between both of the aforementioned scarps, the continuity of the strand is associated with three en echelon left-stepping NNW-elongated hills aligned in a WNW-ESE orientation (Fig. 3.2b, 3.2c and 3.2d). These landforms are commonly observed between parallel left-lateral right stepping strike-slip faults (Wilcox, 1973; Sylvester, 1988 and references therein). Interestingly, the retrospective analysis of recent 2019 Ridgecrest California earthquakes (which involved two different faults), demonstrated that the 2019 Mw 6.4 sinistral strike slip and ~17 km-long rupture (along a previously unknown fault) had subtle geomorphic evidence for previous surface ruptures with scarps, deflected drainages, aligned hills (Thompson Jobe et al., 2020), many observations that are similar to what we see along the EAF. Unfortunately, no in-situ structural data could be collected to validate these geomorphological observations and to better constrain geometry and kinematics of the inferred fault strand because this area is heavily urbanized. However due to the aligned morpohotectonic features that connect the two key fault exposures in the east and west, we inferred the presence of a WNW-ESE left-lateral strike-slip with minor uplift along the northern side of the fault. Between both previous mentioned strands, a W-E trending scarps are found (Fig. 3.6, P6). This scarp is ~0.7 km in length, faces to the south, dips 10° and is ~14 m high. To the east, this scarp is aligned with a prominent saddle in between a Quaternary landslide (Fig. 3.2d). The presence of this scarp could allow an inference of an W-E striking fault. The northern strand between Sites A and B is inferred by the presence of a WNW-ESE oriented, ~600 m length, SSW-facing topographic scarp of ~11 m high and 10° dip in Quaternary alluvial deposit (Fig 3.6, P2). The strand is aligned to the west with the northern termination of the three NNW-elongated hills, and also the displaced stream adjacent to the fault outcrop at Site B (Fig. 3.2b and 3.2c).

To the western side of the study area, a WNW-ESE linear valley suggest that this fault zone continues from WNW-ESE striking fault exposure at Site D to the west (Fig. 3.2b and 3.2c) and is a structure that is at least 13 km long. The road here is along strike with the fault zone (with associated urbanization along the road) and no other collected field data or observations to define the western limit of the fault zone were possible.

### 3.4.4 Geometric and kinematic analysis

Geometrically, Riedel shear structures are characterized by a series of fractures, compression textures, and/or sub-faults, oriented at particular angles to the general trend of the shear zone (called the Principal Displacement Zone or PDZ). An idealized Riedel shear zone is composed generally of six principal elements: R and R’ conjugate shears, T tension fractures, P and X shears, and Y shear faults, but also extensional and compressive structures (Fig. 3.7b; Tachalenko, 1970; Wilcox et al., 1973; Sylvester 1988; Dooley et al., 2012). Due to the orientation, geometry and kinematics, some of the structures reported in this work are consistent with a Riedel shear pattern in a WNW-ESE oriented left-lateral strike-slip fault system with a principal stress direction of ENE-WSW (Fig. 3.7b). The PDZ is represented by the WNW-ESE main faults at Site A, B and D. Synthetic Y-shear are represented by WNW-ESE minor left-lateral strike slip faults in Site A and Site D (Fig. 3.3c and Fig. 3.7a). In a counterclockwise 20-30° rotation from the PDZ synthetic R-shear faults are represented by E-W to ENE-WSW left-lateral strike-slip faults in Site C and Site D (Fig. 3.4e and Fig. 3.7a). Compressive structures, which are formed nearly perpendicular to the principal stress direction, are represented by the NW-SE oriented anticline (Fig. 3.2d), the NNW-SSE reverse fault in the El Zorro Hill (Fig. 3.2d), and the ~N-S faults at Site A (Fig. 3.4c and 3.4d). No R’,T, P, X shears nor normal faults were identified at the field however considering the heavily-urbanized nature of this area, these may be obscured by the built environment.

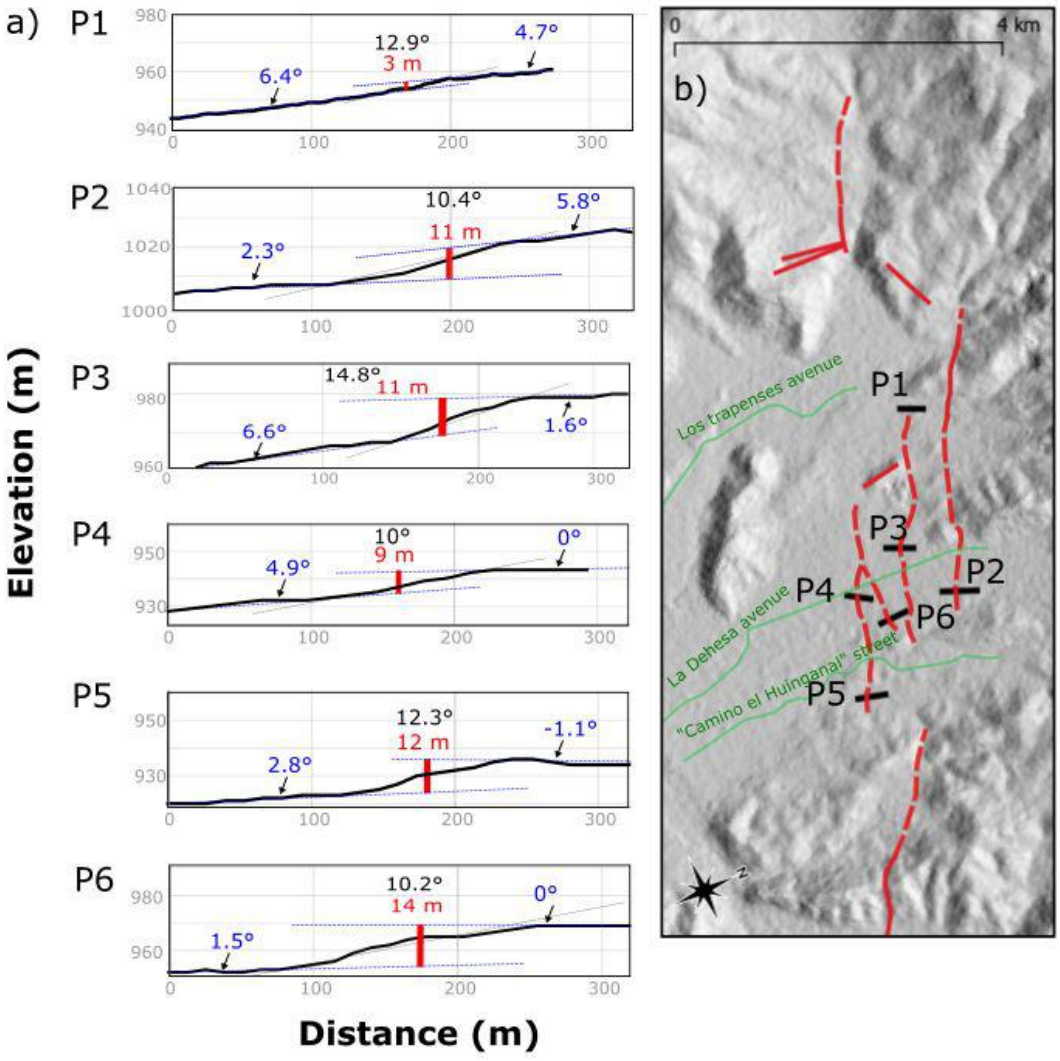


Fig. 3.6: a) Topographic profiles of the study area. P1 extracted from SfM DEM. P2-P6 are extracted from ALOS-PALSAR DEM. b) Location of Topographic profiles of the study area. Solid red lines shows locations of observed EAF traces, dashed red lines shows the locations of inferred EAF strand. Green lines shows the main roads of the study area within the La Dehesa area of Lo Barnechea.

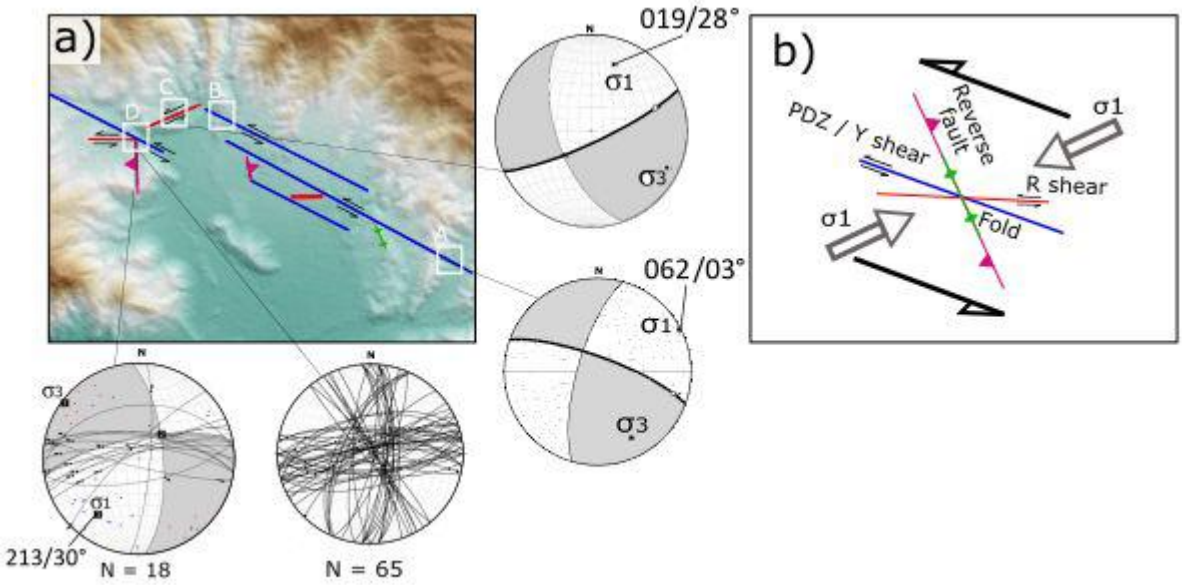


Fig. 3.7: Field DEM with colored elevations of the study area. Colored lines are mapped structures. Colors correlate with Riedel model structures from Fig. 3.7b. Stereonets and structures from study sites are shown. Kinematic analysis with FaultKinTM software (Marret & Allmendinger, 1990; Allmendinger et al., 2012) was performed and principal stress directions are obtained. White boxes show the study sites. b) Idealized Riedel model adapted to the EAF mapped structures. Principal stress direction (σ1) is derived from the Riedel Model.

## 3.5. Discussion

### 3.5.1 Geometry and kinematics

Based on classic field techniques, such as exposure characterisation, field mapping and remote sensing, it was possible to discover and document the occurrence of a previously undocumented brittle upper crustal strike slip fault zone with associated fault rocks within the City of Santiago that we call the El Arrayan Fault (EAF; Fig. 3.1b and 3.2a). The internal architecture of the EAF is characterized by a network of semicontinuous at the surface (and likely continuous but obscured due to urbanization) subparallel and also oblique faults with variable kinematics (Fig. 3.2). This semicontinuous assemblage is compatible with strike-slip fault system geometry (Fig. 3.7b; Naylor et al., 1986; Woodcock and Fischer, 1986, Sylvester, 1988). In this study, the intense urbanization (Fig. 3.2a) and private properties limits the opportunity to collect more data, and therefore, possibly hiding an important number of structural and geomorphic data and the possibility of further analysis. The EAF orientation and kinematics is in agreement with the internal structure of the Abanico Basin proposed by Piquer et al., (2016) being part of the NW-striking strike-slip fault system.

The main strike-slip kinematics of the EAF is clear in the morphology (Fig. 3.2d) and also in the in-situ structural data of the main segments (Fig. 3.7a). However vertical motion is also evidenced for some of the EAF main segment in oblique grooves at site A and D (Fig. 3.3e and Fig. 3.4f), discrete reverse fault planes (Fig. 3.3c), and also fault scarps with the north side up (Fig. 3.2d), and consistent with the higher topography to the north of the EAF versus south of the fault. This suggests that WNW-ENE main segments of the EAF not only accommodates strike-slip faulting, but also N-S shortening. Therefore, the stress regime of the EAF is transpressional (i.e. sinistral-reverse – up to the north). The only normal component of faulting evidenced is limited to minor faulting reported in Site D with orientations varying from WNW-ESE to ENE-WSW (Fig. 3.4b). This normal component of faulting can be attributed local extension on joints of main EAF strands, however there is no clear joint of the western strand of the EAF to the east with another fault strand. Other explanation for this normal component of faulting is that some of the faults are closely parallel to the ENE-WSW principal stress direction, and may be accommodating part of the created local extension in the strike slip fault system or perhaps that there is a stepover to the east.

### 3.5.2 Potential for Quaternary Activity

So by considering at all of this evidence, is the EAF an active structure that may be responsible for earthquakes and surface rupture hazards from active faulting within northeastern Santiago? In this section we explore this question in detail. Here we document for the first time the youngest brittle bedrock deformation (i.e. faulting along the EAF over at least 13 km within Urban Santiago) that cuts the folded stratigraphy, and the dominantly N-S striking axial traces of folds within the Abanico Formation within and adjacent to urban Santiago. In addition to these fault traces being much younger than the folding of the Abanico Formation, the Late-Quaternary geomorphology provides insight into recency of activity along this structure. In this section we will thus explore the timing of Abanico Formation deposition and deformation, and explore insight from other similar structures in order to provide analogues and insight as to if the EAF is Quaternary active.

The timing of Abanico Formation deposition and deformation is important for understanding the timing of the EAF. As outlined in the introduction, the deposition perhaps occurred between the Oligocene and Miocene (~34 to 5 Ma; Charrier et al., 2002, 2007; Giambiagi et al., 2003; Fock, 2005). However, new dating and fieldwork (Mosolf et al., 2018) from southeast of Santiago (~35°S) provides a robust and much older chronostratigraphic framework spanning c. 75-11 Ma. Thus if the Abanico basin is much older than previously recognized, with Late-Cretaceous to Late Eocene intra-arc sedimentation and volcanism which deposited the Abanico Formation, followed by Late Eocene to Late Miocene strike-slip dextral shearing within the volcanic arc, then the strike slip faulting may have started from the Eocene onwards. If that is the case, then the EAF could be older

exhumed faults and not Quaternary active. However, other recent work suggests that the internal conjugate strike-slip fault systems in the Abanico Formation (Piquer et al., 2019) have Middle Miocene – Early Pliocene activity, but also proposed that some structures of the system are still being reactivated under the current stress regime, based on seismicity and distribution of active volcanic centers. Also, Piquer et al. (2019) propose that fault reactivation is inferred based on regional scale first-order observations instead of more in-situ active faulting evidence, they present the possibility of ongoing arc-oblique strike-slip faulting on the Abanico Basin based the current stress regime. The present day ENE-WSW (N77°-78°E) plate tectonic convergence direction (DeMets et al., 1994; Gripp & Gordon, 2002) and the GPS ENE-WSW (N72°E) velocity field directions (Brooks et al., 2003) is consistent with the ENE-WSE (Az 65°) principal stress direction inferred for the EAF based on a Riedel model (Fig. 3.7b). In support of this, the principle stress orientation (σ1) derived from kinematic analysis from fault plane data are similar and compatible. The difference of the σ1 orientation obtained (Fig. 3.7a) can be caused by local reorientation of stress in local structures, which can be slightly different from the main structures. On the other hand, regional stress inversion results by Pérez et al. (2014) underneath the San Ramon Fault and seismicity analysis by Ammirati et al. (2019) along the western flank of the Andes, suggests that the seismicity along the western side of the Central Andes is accommodating NE-SW compressional stress, and thus also consistent with our EAF results. This indicates that the EAF orientation and kinematics is compatible with the modern ongoing first-order tectonic compressional setting. In conclusion, without considering the geomorphology, the seismicity and regional stress data support the current activity along the EAF, however no local dating of the rocks provide ambiguous results regarding activity.

The geomorphology of the EAF provides strong evidence for Quaternary activity that complements the implications from the rock record. The EAF cuts bedrock (e.g. the ridge between El Arrayan and La Dehesa and Late-Quaternary deposits, i.e. those in the La Dehesa area). Neotectonic lineaments, inflection points and likely strike slip fault scarps in Late-Quaternary fans, deflected streams, displacements of the main ridge between El Arrayan and La Dehesa, pop up “island hills” in the La Dehesa basin coincident with bedrock exposures of the EAF provides strong evidence for Late-Quaternary activity. Additionally, the occurrence of large landslides on the hanging wall of the EAF constitutes additional supporting evidence for activity, with landslides tending to occur on the hangingwall of faults with a vertical component (Fig. 3.1b; e.g. Serey et al., 2020). So the tectonic geomorphology is there, but in the absence of direct dating (a goal the we suggest should be pursued soon), what else can we refer to? Other faults in the Santiago area and faults globally is a good place to start.

Other Quaternary faults reported in the Andes of Central Chile are the SRF (Rauld, 2002, Armijo et al., 2010; Rauld, 2011) and the San José de Maipo Fault (Lavenu & Cembrano, 2008) as previously mentioned. Due to the N-S to NNW-SSE orientation and present day reverse kinematics of the SRF, a E-W to ENE-

WSW principal stress direction can be attributed to the SRF (Rauld, 2011). This E-W to ENE-WSW principal stress direction of the SRF is similar and compatible with the EAF principal stress direction, and also the modern ongoing first-order tectonic compressional setting. On the other hand, Lavenu & Cembrano (2008) proposed a NNW-SSE directed principal stress direction. The San José de Maipo Fault is visible only very locally and no trace fault prolongation can be made at the surface, which can indicate that perhaps the fault is just a small structure accommodating local stress, and the derived principal stress direction from this fault does not represent the regional scale principal stress direction like the SRF and the EAF that are faults with several km in length and have a more clear geomorphological expression, and therefore, more regional representation.

A seismic sequence in California occurred in July 2019 that may provide insight to potential EAF activity. Two fault ruptures occurred in this sequence, a Mw 6.4 and Mw 7.1 rupture (e.g. Thompson Jobe et al., 2020). The sinistral rupture of the Salt Wells Valley fault zone (SWVFZ) during the Mw 6.4 event was ~21 km long, and occurred largely along a fault that was largely unmapped (only 37% of the fault zone that ruptured was mapped) prior to the rupture (Thompson Jobe et al., 2020). However, through careful mapping of pre-event imagery Thompson Jobe et al. (2020) established that at least 59% of the length of the fault had pre-existing features (e.g. scarps, deflected drainages, and lineaments, and contrast in topography or vegetation and ground colour) that later ruptured in 2019. These same authors stated that of the pre-rupture mappable features related to the fault, only 53% of the fault-related features were relatively "obvious", while 7% was "subtle". One of the authors of this paper (De Pascale) participated in post-earthquake reconnaissance along the Mw 6.4 Ridgecrest rupture and fault mapping and was struck by the low-lying hills popping up out of the flat landscape of southern California along the fault and how strikingly similar this appeared to the hills in La Dehesa along the EAF. Since about >60% of the along-strike trace of the EAF (between sites A to west of site B) or about 14 km, with similar neotectonic features (i.e. scarps, deflected streams, lineaments), found in Late-Quaternary surfaces as found during the Ridgecrest earthquake Mw 6.4 rupture these non-so subtle features along the EAF suggest they were generated from Late-Quaternary fault ruptures along the EAF.

### 3.5.3 Tectonic implications

In a regional scale, the western flank of the Andes in Central Chile is characterized by the presence of the WAT (Armijo et al.,2010). The SRF is the most prominent expression of the WAT (Armijo et al., 2010; Rauld, 2011; Pérez et al., 2014; Vargas et al., 2014; Estay et al., 2016; Riesner et al., 2017), but its continuity to the north is not well established. On the other hand other faults to the north and south were proposed (Armijo et al., 2010; Estay et al. 2016; Riesner et al., 2017) but no clear evidence yet presented. In this sense, connection between segments WAT is unclear. Due to the location, orientation and kinematics of the EAF, and also its Quaternary recent activity, the EAF could be

interpreted as transfer system between thrusts in the WAT, connecting the SRF to the west with other N-S striking reverse faults part of the WAT further north of Santiago. The abrupt mountain front morphology change of the Principal Cordillera to the north of the Mapocho River, and the near-surface complexity in the process of fault propagation at the north part of the SRF, evidenced by a gentle NW striking anticline forming along the group of three arch-shaped "island" hills, is consistent with the hypothesis of deformation being transferred to the west by the EAF towards the Central Depression.

### 3.5.4 Potential EAF Seismic hazard

If the EAF is an active Quaternary crustal structure that fails in stick-slip behaviour, then by assuming a surface rupture of at least 13 km (and perhaps longer) with a seismogenic thickness of the upper crust of at least 15 km (supported by the recent microseismicity data of the Santiago area by Ammirati et al. 2019), suggests a seismic potential of at least Mw 6.4 using the earthquake scaling relations of Wells and Coppersmith (1984). If the fault length is longer and/or the seismogenic zone is thicker (Ammirati et al. 2019 reported earthquakes up to 25 km in the upper crust within the study area), then Mw 6.4 is an under estimate. To put the EAF in perspective, another recent event, the February 2011 Mw 6.3 earthquake along the blind Port Hills fault (e.g. Li et al., 2014), which was responsible for $30 Billion New Zealand Dollars of damage to the City of Christchurch, did not even rupture to the surface. Thus, a well expressed fault zone like the EAF with fault rocks and exposures tied with tectonic geomorphology suggests ruptures of up to Mw 6.4 are possible if it fails. If the EAF ruptures with the SRF, something that the recent Kaikoura earthquakes in New Zealand demonstrated is a possibility, then the pre-existing estimates for seismic hazard along the SRF (Mw 7.5 e.g. Vargas et al., 2014) may be an underestimate.

## 3.6 Conclusions

Remote sensing and fieldwork allowed us to discover, characterize and map the previously unreported El Arrayan fault (EAF) found within the northeastern edge of urban Santiago. The fault presents upper crustal fault rocks (e.g. Sibson, 1977) of gouge, cataclasite, and breccia and cuts Abanico Formation folded bedding (which means the EAF formed after the formation of folds within the Abanico Fm). This represents, to our knowledge, the first documentation of fault rocks (e.g. Sibson, 1977) at the surface within the City of Santiago. The EAF strikes 110° (WNW-ESE), subvertical, and is slighly northward dipping and has strike-slip left-lateral kinematics. The EAF has semicontinous major fault strands in addition to minor strike-slip and reverse faults. The EAF location from exposures and strike is coincident and aligned with deflected streams, a displaced ridgecrest, fault scarps, lineaments, sag pond and a linear valley. The present day ENE-WSW (N77°-78°E) plate tectonic convergence direction (DeMets et al., 1994; Gripp & Gordon, 2002) and the GPS ENE-WSW (072°) velocity field directions

(Brooks et al., 2003) is consistent with the σ1 derived from the kinematic analysis with fault slip planes and the ENE-WSW (065°) principal stress direction inferred for the EAF based on the Riedel model (Fig. 3.7b).

The occurrence of large landslides on the hanging wall at the northern extension of the fault constitutes additional supporting evidence for activity. The geomorphic evidence, that coincides with well exposed fault trace and fault rocks cutting the Abanico Formation rocks and Quaternary sediments, provides evidence that the EAF is a likely a Quaternary structure that is accommodating tectonic deformation in the upper crust, and as such it has a surface rupture potential and associated seismic hazard of at least up to Mw 6.4. We suggest that further work is immediately required to determine how recent the last rupture occurred along the EAF (i.e. fault trenching and geophysics tied with Quaternary dating) and to better define connections with active structures to the north and south of the EAF. Needless to say, the presence of an important crustal fault within a highly populated and quickly urbanizing part of Santiago constitutes a potential risk, particularly given the lack of fault rupture avoidance-surveys and legislation. A rupture of the EAF in the densely-populated La Dehesa would indeed have severe consequences.

Crustal faults require more attention in Chile in order to reduce fault rupture, strong ground motions, and co-seismic geohazards (see De Pascale, In Press). Legislation in areas of seismic risk should include a mandatory fault construction avoidance zone around active faults, and special regulations, to be included on the building code, for constructions in areas with potential shallow ground motions (Sepulveda et al., 2008). Because no active faults were known in Santiago until 2002, further work may demonstrate the existence of other neotectonic active faults that are an additional source of seismic hazard. Future work along both the EAF and SRF, will provide more detail on key earthquake behaviour to better understand implications for the Santiago area. As building of residential and commercial infrastructure is in progress along the San Ramon and El Arrayan faults traces and scarps it is important to rapidly develop an appropriate legislation for conditioning the construction across or around active faults, in a similar way to legislations in places such as California, New Zealand, or Japan. This documentation of a likely Late-Quaternary active strike-slip structure (the El Arrayan Fault: EAF) in the Chilean Central Andes raises a question to conclude with: “where are the other active strike-slip faults in the Metropolitan Region of Chile and Central Chile?”, because n = 1 is highly unlikely.

## Chapter 4: Case of study Estero Coyanco fault

This chapter presents a case study of the Estero Coyanco fault. It is written as a manuscript for eventual publication and thus has distinct abstract, literature review, methods, results, and summary section.

## East-vergent compressive Quaternary faulting in the western Principal cordillera, south of San José de Maipo, Chilean Central Andes.

### 4.1 Abstract

Active deformation at the western flank of Principal Cordillera in Central Andes between 33°-34°S has been documented and characterized by shallow seismicity with compressive focal mechanism and also by west-vergent active faults. Based on field observations and structural data acquisition in a natural rock exposure at the Estero Coyanco 40 km SE of Santiago, this work present solid evidence for an un-previously recognized east-vergent reverse that will be named the Estero Coyanco fault (ECF). This is a 30 m wide NNW-SSE striking west-dipping fault zone, comprising bedrock damage zone, which is bounded by three fault cores. Two of this fault cores are cutting and displacing Neogene volcanic bedrock and Quaternary alluvial deposits. Remote sensing techniques reveal a knickpoint next to fault zone outcrop, validated on the field by a 2 m waterfall. The geometry and kinematics of the Estero Coyanco fault are consistent with a E-W to NE-SW shortening direction, which is also compatible with the orientation and kinematics of the active San Ramon fault and the fault plane solutions of the focal mechanism recorded by the San José de Maipo seismic station, present-day GPS derived velocity fields and Tectonic Plate convergence direction; this supports the hypothesis of the Estero Coyanco fault as an active fault. Using 1-2 m as the maximum surface displacement, scaling laws (Wells and Coppersmith 1994) predicts seismic events with Mw 6.7-6.9.

### 4.2 Introduction

Central Chile is part of the central segment of the Andes orogenic belt. Since 25-15 Ma the Andean orogeny has been actively deforming by compressive setting, caused by the subduction of the Nazca Plate underneath the South American Plate (Coira et al., 1982; Jordan et al., 1983). Shallow crustal seismicity (Barrientos et al., 2004; Pérez et al., 2014, Ammirati et al., 2019) and Quaternary faulting in the main range (Rauld 2002; Lavenu and Cembrano 2008; Armijo et al., 2010; Rauld, 2011; Vargas et al., 2014) evidences the active deformation between 33°-34°°S in the orogen.

The western flank of the Principal Cordillera is characterized by a prominent mountain front which limits the Central Depression to the east. West-vergent active faults located at the foothills of the mountain front are proposed to control the morphology of this first order geographic feature, like the San Ramon fault in Santiago (Rauld, 2002; Armijo et al., 2010; Rauld, 2011; Vargas et al., 2014) and the Cariño Botado fault in Los Andes (Troncoso, 2014; Medina, 2018). On the other hand, a short length (1.3 km) south-vergent Quaternary faulting was reported in a fluvial terrace at the confluence of the Colorado River and the Maipo River, 30 km SE of Santiago, inside the western Principal Cordillera. Unfortunately, these are the only three active fault reported in the Principal Cordillera, which clearly reflect a lack of active tectonics data essential to understand the present day orogen-scale deformation. This work presents, by classic field work techniques, structural and geomorphological observations, evidence for a newly active un-previously recognized fault at the Estero Coyanco, a tributary of the Maipo River, 15 km south of San José de Maipo.

## 4.3 Geological setting

The Central Andes from 33°S to 34°S is characterized by the ongoing subduction of the Nazca Plate beneath the South American Plate since the Jurassic (190 Ma) (Coira et al., 1982; Jordan et al., 1983; Allmendinger, 1986; Isacks, 1988; Mpodozis and Ramos, 1989, Charrier et al., 2007). It is situated immediately south of the flat-slab segment of the subducted oceanic Nazca Plate (28-33°S) (Cahill & Isacks, 1992; Yañez et al., 2002). Current Tectonic Plates convergence vector with N77°-78°E direction and rates between 6-8 cm/yr are reported (Fig. 4.1a; DeMets et al., 1994; Gripp & Gordon, 2002). ENE-WSW orientated velocity field in the range of 19.5 -22.5 mm/yr, derived from GPS where obtained by Brooks et al., (2003). At this latitude the first order Chilean morphotectonic units are from west to east, Coastal Cordillera, Central Depression, Principal Cordillera, Frontal Cordillera and Precordillera (Fig. 4.1b).

The western Principal Cordillera comprises the Abanico basin, a Cenozoic (31-15 Ma) extensional intra-arc basin developed in Central Chile, where the mainly volcanic and also sedimentary Abanico Formation and Farellones Formation where deposited (Charrier et al., 2002; Fock 2005). This basin was tectonically inverted and exhumed during the Early to Middle Miocene (Giambiagi et al., 2003). On the other hand, the eastern Principal Cordillera located immediately to the east of the Abanico basin, is constituted by the Aconcagua fold and thrust belt, where Mesozoic continental and marine sedimentary rocks of the Lo Valdes Formation, Rio Damas Formation and Rio Colina Formations where highly deformed during the Middle to Late Miocene Andean compressional tectonic event (Giambiagi et al., 2003). Finally, the central Principal Cordillera is a structural domain between the eastern and

western Principal Cordillera; it comprises Cenozoic deposits, as well as the western Principal Cordillera, bounded to the east by nearly N-S striking east verging fault that puts in contact the Abanico Formation over the Mesozoic sequences of the eastern Principal Cordillera (Charrier et al., 2002; Farias et al., 2010).

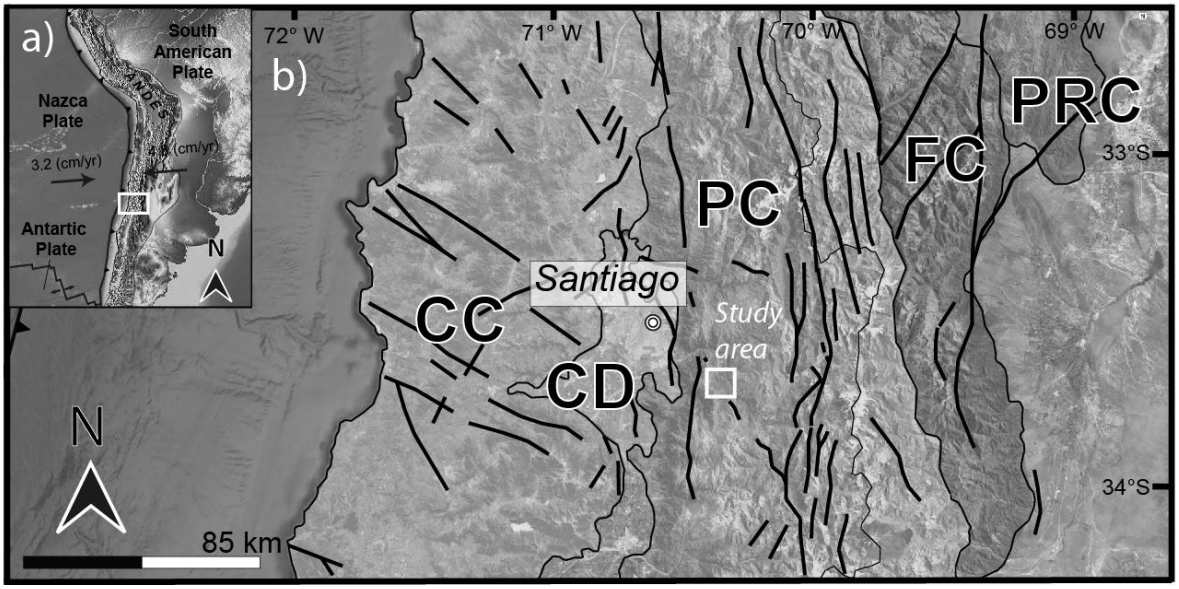


Figure 4.1 a) Continental plate tectonic setting. Black arrows indicate convergence rates of tectonic plates from Gripp & Gordon, (2002). White box indicate location of b). b) Chilean Central Andes morphotectonic units and mayor structures. CC: Coastal Cordillera; CD: Central Depression; PC: Principal Cordillera; FC: Frontal Cordillera; PRC: Precordillera. Thick black lines are the main regional-scale faults (extracted from SERNAGEOMIN 2003). White box shows the study area.

The most important known structure in the western flank of the Principal Cordillera is the previously mentioned San Ramon fault, a ca. 30 km long active thrust fault related to a prominent fault scarp at the foothills of the western flank of the Principal Cordillera (Rauld, 2002; Armijo et al., 2010; Rauld, 2001). Paleoseismological investigations provide evidence two large earthquake ruptures of ~5m slip; the most recent event occurred ~8 k.y. ago and the previous within 17-19 ka (Vargas et al., 2014). Wells and Coppersmith (1994) scaling laws applied on the San Ramon fault yield Mw estimates up to 7.5. Lavenu and Cembrano (2008) reports in the western side of the Principal Cordillera, 30 km to the SE of Santiago, reverse faults cutting alluvium deposits, naming this as the San José de Maipo Fault. This structures dips to the north, have centimetric to metric vertical slip, and cuts a Maipo´s river fluvial terrace of estimated middle Plesitocene age. Kinematic analysis in the San Jose de Maipo fault yielded compression axis σ1 = N338°E (Lavenu & Cembrano 2008). Up to day these are the only two

reported active structures in the western Principal Cordillera between 33°-34° (Fig. 4.2a).

Historically shallow earthquakes in central Chile between 33°-34°S have occurred. The largest event occurred in the high Maipo River, the September 4, 1958, sited in Las Melosas (Ms 6.9; Lomnitz, 1961; Piderit, 1961), located close to 60 to the SE of Santiago. Alvarado et al., (2009), using modern body-wave modelling techniques, estimates Mw of 6.3 and a hypocenter located 8 km depth for this event. The main type of seismicity instrumentally recorded, is shallow intraplate, located between the eastern side of the Central Depression and western flank of the Andean mountain, but also near the border between Chile and Argentina (Barrientos et al., 2004; Pérez et al 2014, Ammirati et al., 2019). According to Pérez et al., (2014) by relocalization of shallow seismic events at 32.5-34.5°S between 2000-2009 using data from the CSN (National Seismological Service or Centro Sismológico Nacional in Spanish), they found two semi-parallel N-S lineaments of crustal seismicity. A well-organized western lineament with sources between 10-15 km deep, just beneath the western edge of the western Principal Cordillera; and an eastern, wider and more diffuse band, located in the Central Principal Cordillera, at the contact between Cenozoic and Mesozoic rocks, with shallower seismic events (0-10 km depth) concentrated in the upper reaches of Maipo River. The western band shows compressive mechanism (Pérez et al., 2014) meanwhile the eastern band shows normal, reverse and strike-slip mechanism (Lomnitz, 1961; Alvarado et al., 2009; Pérez et al., 2014). Figure 4.2b shows de Pérez et al., (2014) seismic record.

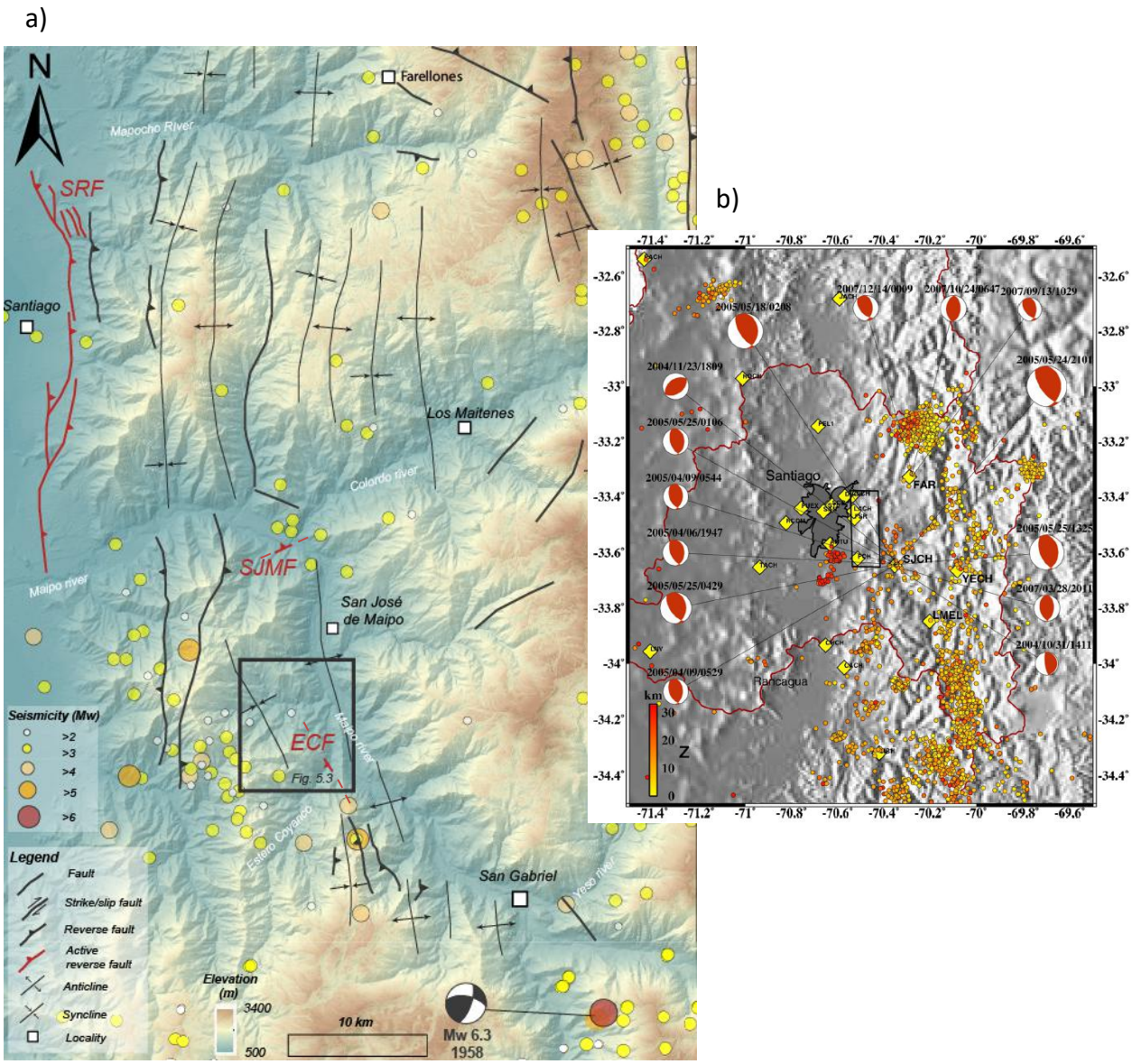


Figure 4.2 a) Simplified geological map of the western Principal Cordillera. Based on Thiele (1980), SERNAGEOMIN (2002) Villella, (2014), Armijo et al., (2010), Piquer et al., (2016) and this work. Main regional structures and seismicity (<50 km depth) from USGS catalog recorded between September 1950 and September 2018 are showed. SRF: San Ramón fault; SJMF; San José de Maipo fault; ECF: Estero Coyanco fault. 1958 Las Melosas earthquake epicenter and focal mechanism are indicated. b) Seismic record of Pérez et al., (2014). Colored points indicate hypocenter locations and depth. Yellow diamonds are seismological stations from the SSN. The closed dark gray polygon represents the city of Santiago.

## 4.4 Methodology

With the purpose of identify and characterize active faulting in the western Principal Cordillera, field mapping were undertake south of San José de Maipo. While mapping, a fault zone was explored in a E-W segment of the overall N-S orientated Estero Coyanco (Fig. 5.3a and 5.4). Rock sampling and hand sample description, combined with structural observations were undertaken to characterize the fault zone. Morphological observations were taken to complement the structural data.

Fault zone is described in base of a fault core and a damage zone (Chester & Logan 1986; Chester et al., 1993; Caine et al., 1996). The fault core is defined here by the presence of fault rocks as mylonite, breccia, plastic-gouge and cataclasite; and the damage zone is defined as the area that presents secondary and minor structures, like folds, fractures and veins, related to the main structure (Sibson, 1977; Chester & Logan 1986; Goddard & Evans, 1995; Caine et al., 1996).

Slope map derived from ALOSPALSAR 12 m spatial resolution, is develop in QGIS software for topographic analysis.

Due to the lack of slickenside, first order kinematic analysis is develop in base of fault orientation an sense of motion, inferring a general shortening direction which must be mechanically coherent with geometry and kinematics of the faults.

## 4.5 Results

At the Estero Coyanco, west dipping volcanic and sedimentary beds, corresponding to the top of the Abanico Formation are exposed, constituting part of the western limb of the Maipo Anticline (Thiele, 1980; Charrier, 2002; Fock, 2005). At the northern area of the Estero, near the confluence of the Estero Coyanco and Maipo River, beds are NW to N-S orientated and steeply dipping reaching almost 85°, meanwhile at upstream areas, the beds start to decrease their dipping, reaching almost 40-50° dip 4 km inside the Estero Coyanco (Fig. 4.3).

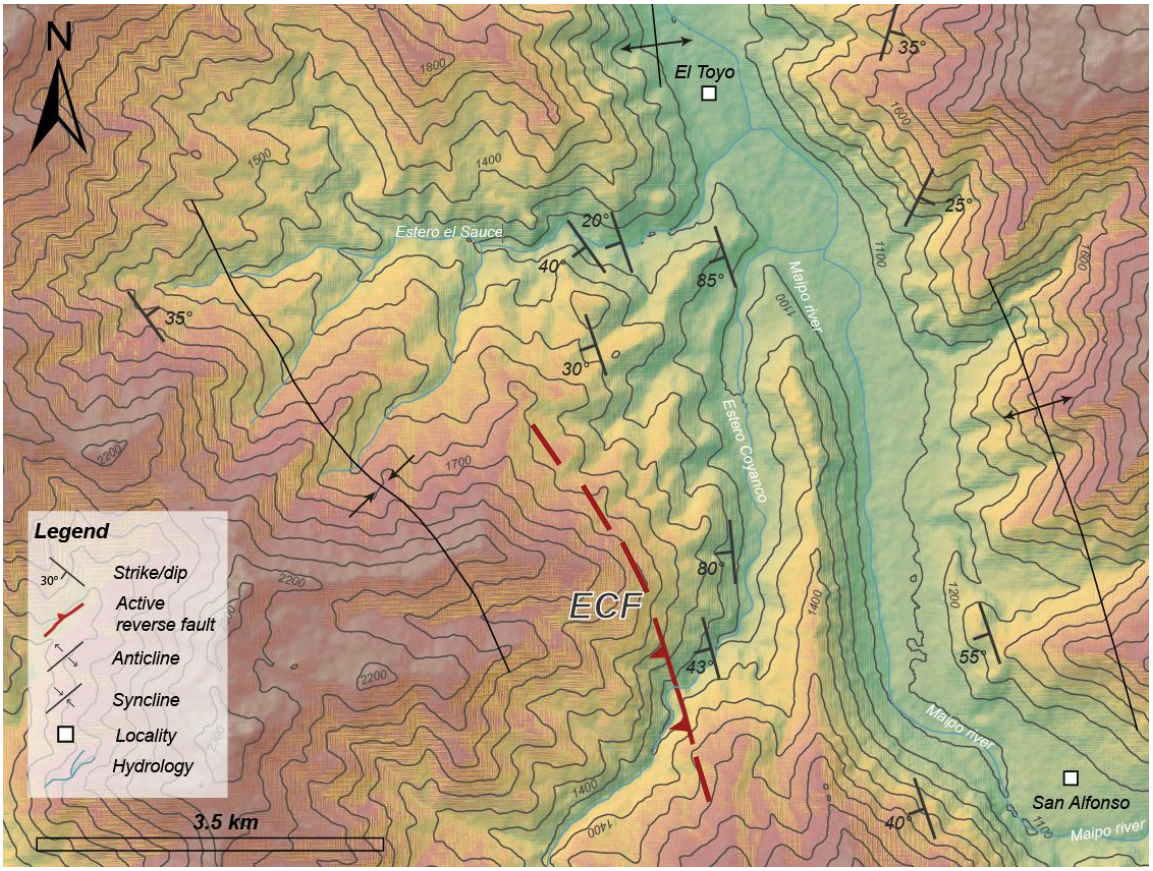


Figure 4.3 Simplified geological map of the Estero Coyanco and Estero el Sauce area. Structural data compiled from Thiele (1980), Villela (2014) and this work. ECF: Estero Coyanco fault.

In an E-W segment of the Estero Coyanco, almost 4 km inside the Estero from its confluence with Maipo River, a 30 m wide fault zone can be observed. The fault zone comprises damage zone bedrock, bounding by three fault cores (Fig. 4.4).

The damage zone is characterized by highly fractured massive volcanic rock and minor stratified beds with NNW-SSE orientation and dipping 45° to the west (Fig. 4.4). No folding can be observed in this area. The different fault cores are identified by the presence of fault rocks. They will be described from west to east, been the FC1 the western and FC3 the eastern.

FC1 is the wider fault core, reaching almost 8 m wide. It separates a grey massive andesite block from orange-grey massive and subtly stratified volcanic rocks (Fig. 4.4). It comprises one clear slip surface which strikes 170° and dips 50° to the west (Fig. 4.5a and 4.5b), one gouge band adjacent to the fault plane, and two breccia cataclastic bands (Fig. 4.5c and 4.5d). The gouge band is 1-1.3 cm wide and presents orange color. The western breccia band its 1.1–1.5 m wide and present angular 1-7 cm clast

immerse in an orange scarce matrix of milimitric clast size (Fig. 4.5c). The eastern breccia (Fig.4.5d) is 0.7-1.5 m wide and grey-purple colored with orange bands related to mineral alteration. This breccia presents angular clast up to 15 cm. On top of FC1, massive alluvial wed shape deposit of suppose Quaternary age can be observed (Fig. 4.4, 4.5e). The deposit is clearly cut by the fault, where massive volcanic rock overthrust the alluvial deposit, showing evidence of recent activity (Figure 4.5f).

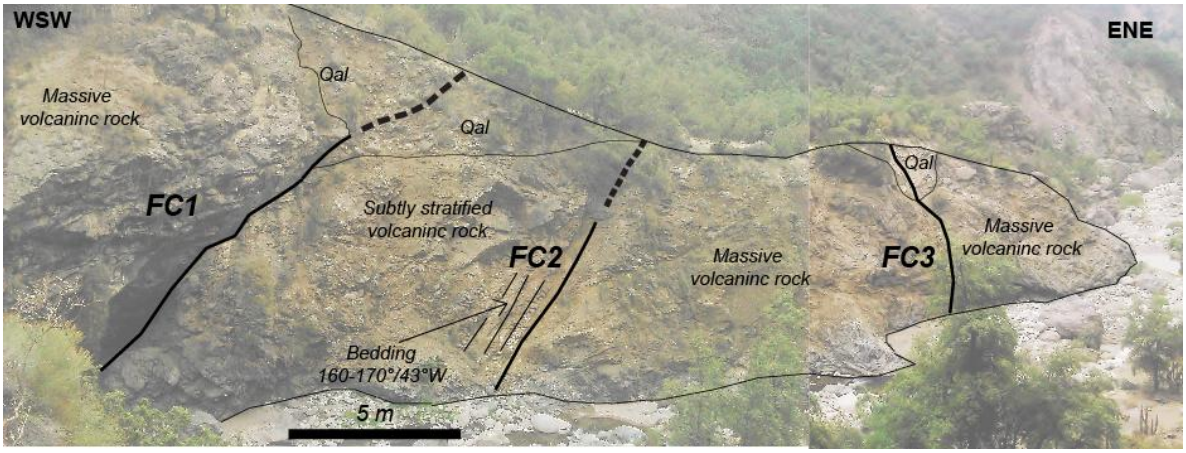


Figure 4.4 Panoramic view of the fault zone, comprising three fault cores (FC) bounding the damage zones.

FC2 strikes 160-170° and dips 60° to the west; it is 0.5 m wide, comprising a 0.45 breccia and a 5 cm orange gouge layer (Fig. 4.6). The breccia contains angular clast with sized up to 20 cm. The alluvial deposit which is on top of FC1, reach just to the top of FC2. No faulted Quaternary deposit was observed related to FC2.

FC3 is 1-2 m wide, strikes 160°-180° and dips 60° to the west. It separates 2 massive blocks of volcanic bedrock with different fracture patterns (Fig. 4.7). It is constituted mainly of a breccia, where greenish angular clasts up to 8 cm are surrounded by orange plastic gouge material (Fig. 4.8). Over the bedrock, a fluvial deposit constituted by fine grain sediment layer interbedded with coarse well-rounded gravel levels can be observed (Fig 4.4 and Fig 4.7). On top of the footwall of FC3, massive alluvial deposit can be observed, characterized by subangular clast of sizes up to 1 m. The contact between these two different Quaternary deposits is clear and straight (Fig. 4.7). Additionally the difference on elevation of the top of the bedrock, which is higher to the west of the FC3, suggest that the fault extends to the Quaternary deposits as a reverse fault elevating the western block and producing the sharp contrast between the two different deposits.

Topographic variations are observed at the top of each of these fault cores, where the hangingwall is always at higher elevations than the footwall (Fig 4.4). Slope map shows an important topographic anomaly at the Estero Coyanco adjacent to the reported fault zone, where a topographic step revealed by a high (>28°) slope that cross the Estero Coyanco (Fig. 4.9). Field work let us identify a waterfall adjacent to the fault zone to the west (Fig. 4.9). Thus, I assigned this topographic anomaly as a knickpoint.

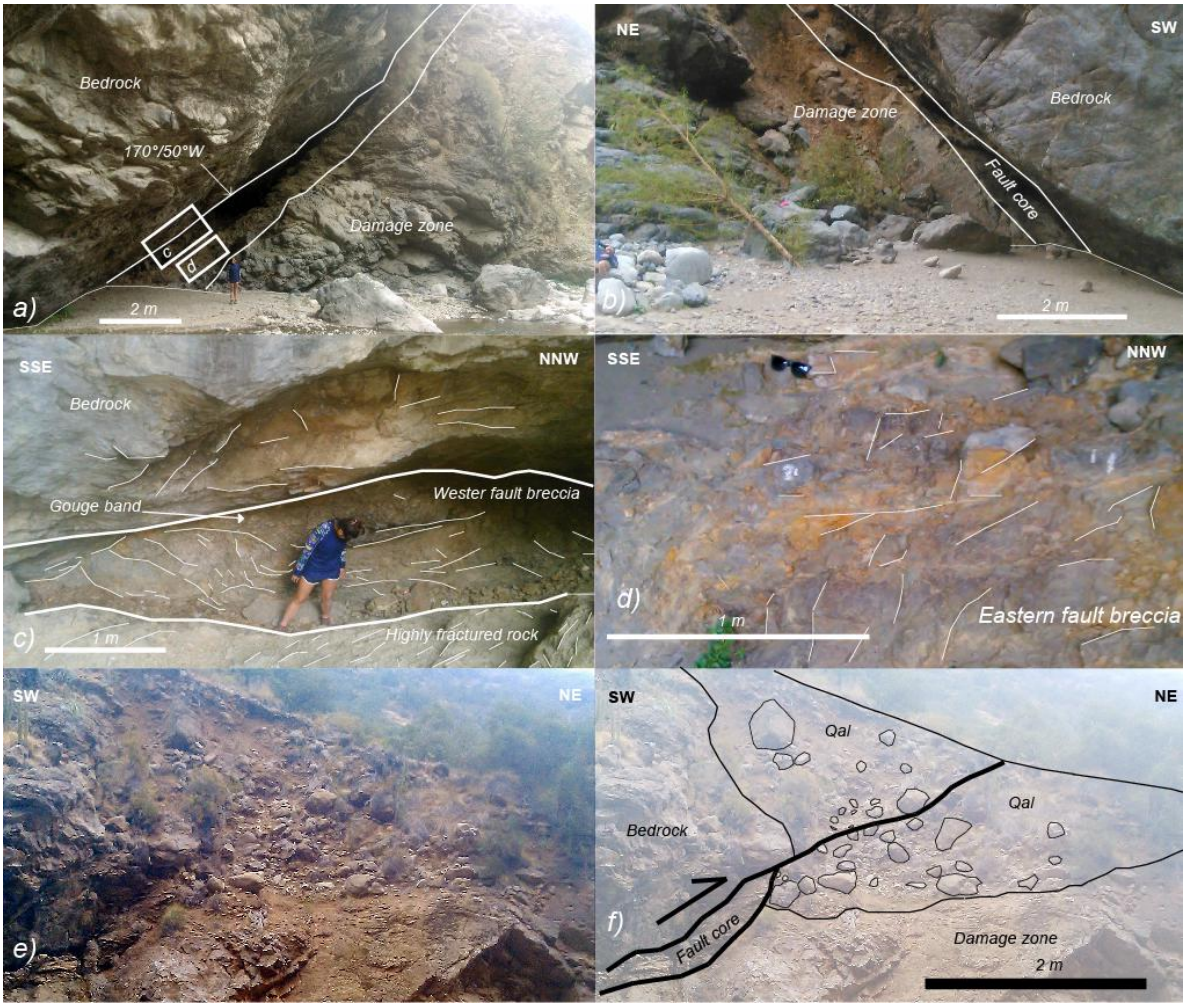


Figure 4.5 FC1 features. a) Panoramic view north side of the Estero showing bedrock, fault core and damage zone. b) Panoramic view south side of the Estero. c) Closer view to western breccia. Thin white lines are fractures. d) Closer view to eastern breccia. Thin white lines area fractures. e) Photo of alluvial deposit on top of FC1. F) Interpretation of e) showing cut alluvial deposit.

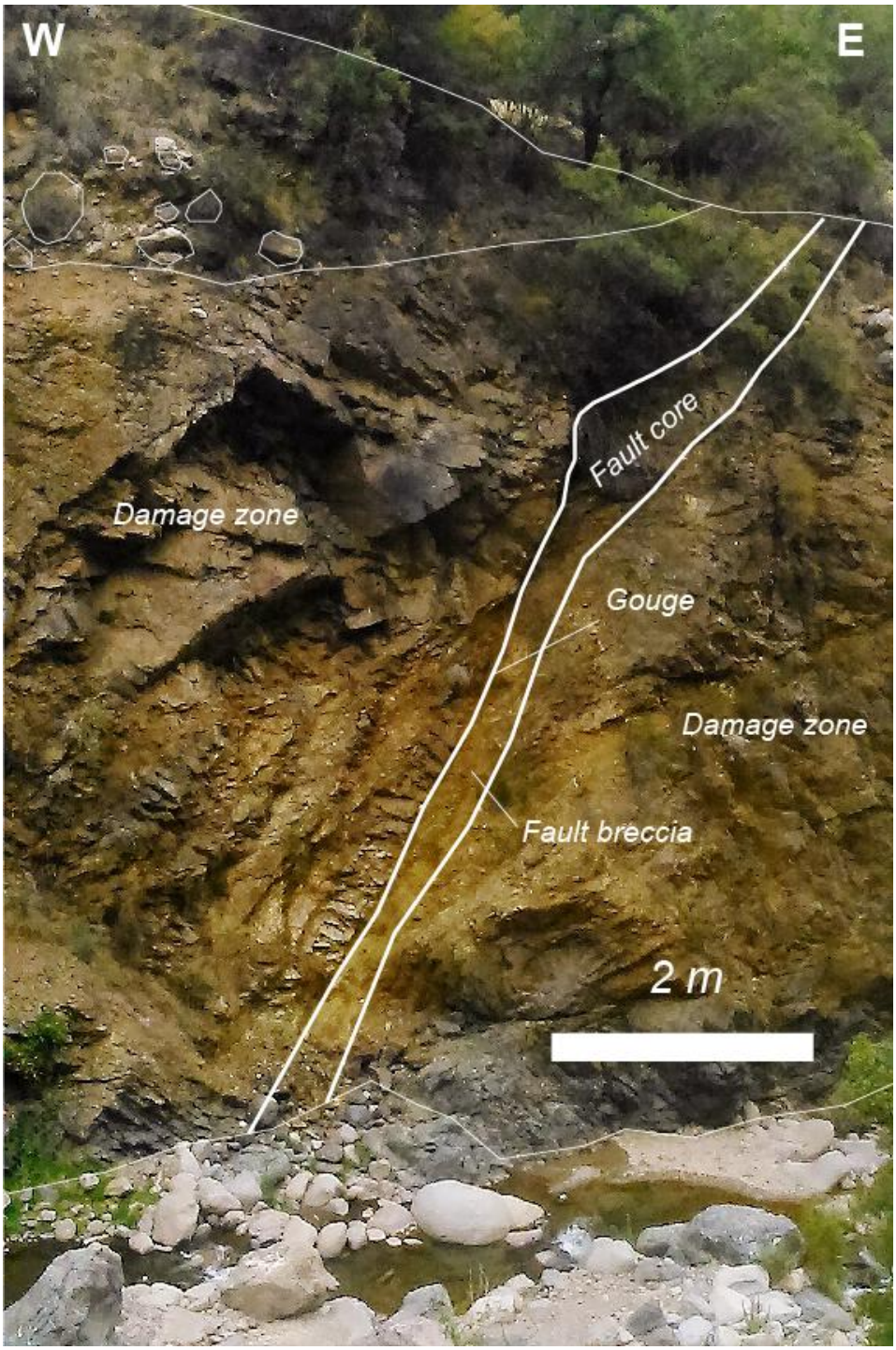


Figure 4.6 FC2 configuration indicating fault rocks, damage zones and Qal deposit.


Figure 4.7 FC3 configuration indicating fault core damage zone and Quaternary deposits.

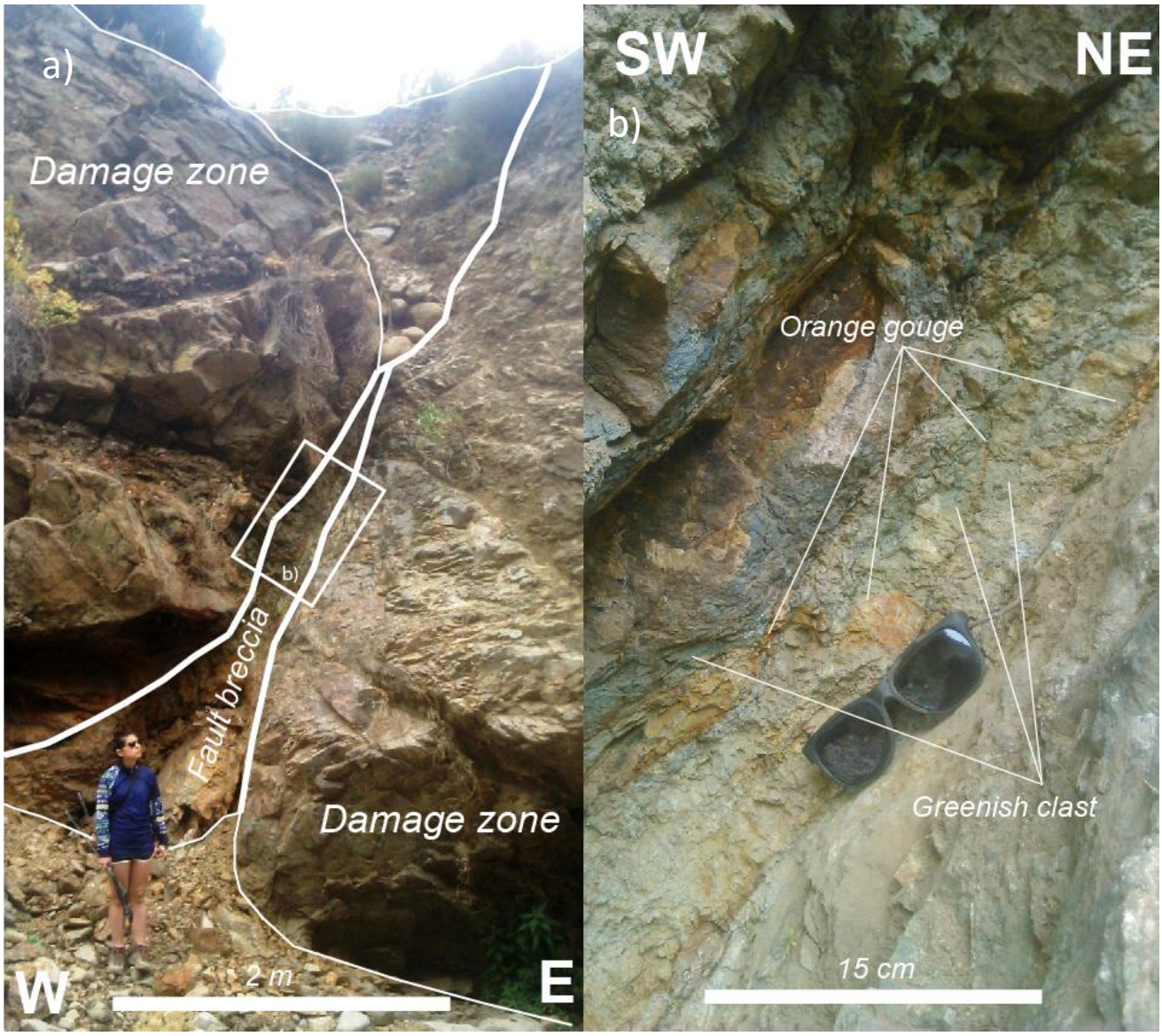


Figure 4.8 a) Closer view to FC3. White box shows location of b). b) Zoom of fault rocks in FC3.

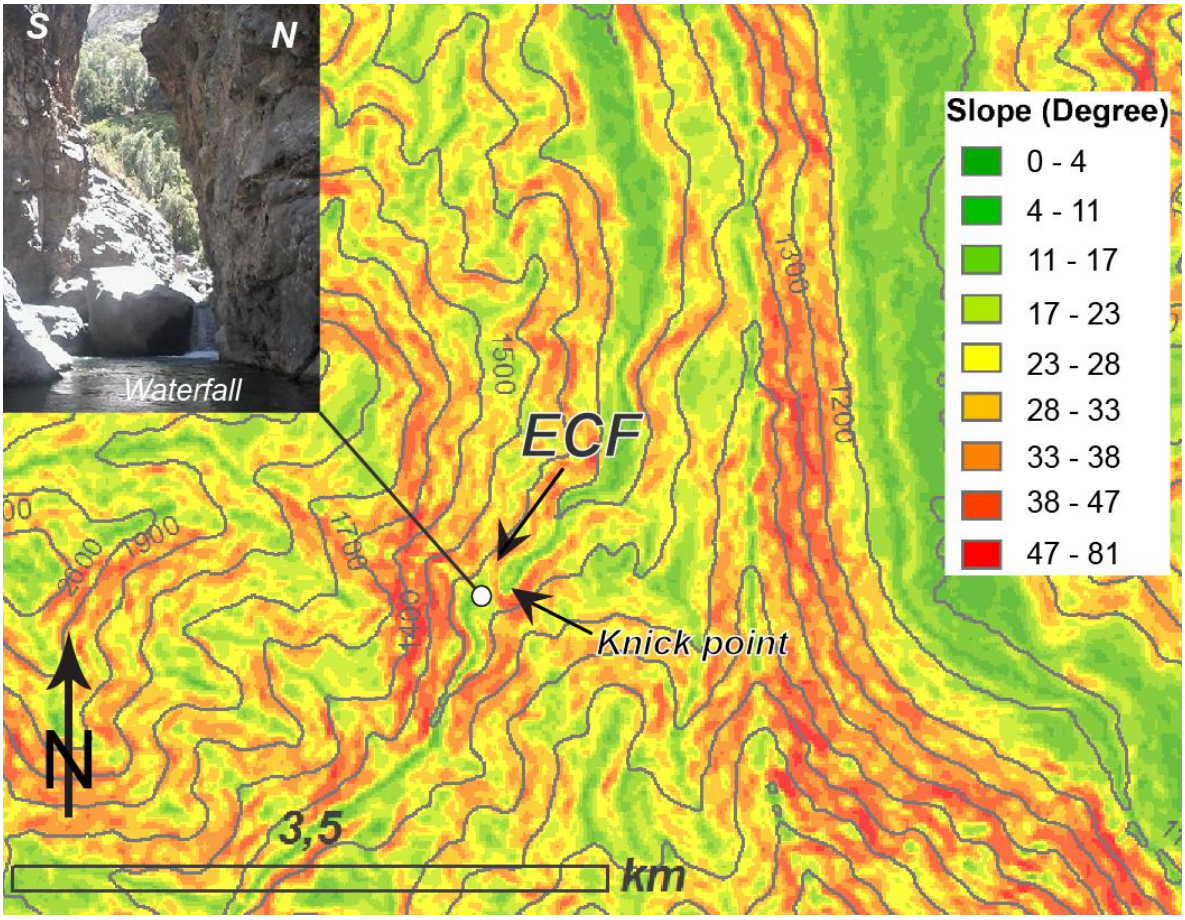


Figure 4.9 Slope map of the study area. Estero Coyanco fault (ECF) outcrop location, knickpoint location and waterfall location area are also indicated.

## 4.6 Discussion

### 4.6.1 Fault extend

The ECF is well characterized at the Estero Coyanco because the water erosion exposes more than 8 m of the fault in vertical. However, this is a mountainous area and the flanks of the Estero are very steep and therefore further field recognition couldn´t be done, additionally the densely vegetation of the area also difficult the surface exploration. In base of the topographic analysis, the reported knickpoint is a clear anomaly in the average slope of the stream channel, but away from the water channel, in the mountainous area, the slopes present less contrast, so the topographic anomaly is not clear. Therefore the fault has been just mapped at the Estero area. Further studies must be done regarding the fault extends.

### 4.6.2 Fault kinematics

Overthusting of massive volcanic rock over Quaternary alluvial deposit on top of FC1 clearly indicates a reverse sense of motion in a NNW-SSE orientated fault plane. The higher elevation of the top of bedrock at the hangingwall of FC3 compared with the footwall of FC3 also indicates a reverse sense of motion. Another evidence of reverse sense of motion is the east-facing observed waterfall where water runs from W to E. Unfortunately no kinematic indicators as slickenside o secondary structures could be observed at the fault cores to corroborate the inferred kinematics.

### 4.6.3 Fault temporality

The FC1 and FC3 are deforming bedrock as well as alluvial and fluvial deposit. In spite of no age constrains in this deposits, a general Quaternary age can be attributable doe to general observations. Thus, I propose that this fault zone have present at least Quaternary age, and therefore, classified as active.

### 4.6.4 Fault displacement

In base of the empirical relationship between fault rock thickness and fault displacement of Child et al., (2009), the 8 m wide of the FC1 suggest that that this fault core have accommodated tens of meters of displacement. However, on top of FC1 the base of the faulted alluvial deposits presents an offset of approximately 1 m. Thus, this suggests that the FC1 have been accommodating fault displacement before the deposition of the Quaternary alluvial deposits.

FC2 and FC3 present thinner fault rock thickness, and thus, I assume less fault displacement accommodation, however, on top of FC3, the top of the volcanic bedrock has been offset at least 2 m. This indicates that the FC1 is the area that has accommodated more displacement of the fault zone, although for Quaternary times the FC3 is the area where more displacement has occurs. Observational data from field studies of faults as well as theoretical studies of seismic moment suggest that earthquake magnitude should correlate with the amount of displacement along the causative fault (Wells and Coppersmith, 1994). Assuming the worst case scenario, using 1-2 m as the maximum surface displacement in one rupture event, scaling laws (Wells and Coppersmith 1994) predicts seismic events with Mw 6.6-6.9.

### 4.6.5 Regional kinematics

The NNW-SSE orientation of the fault zone, combined with the inferred reverse sense of motion, is compatible with E-W to NE-SW shortening direction. Because the reverse kinematic was inferred in base of the offset of the Quaternary deposits on top of FC1 and FC3, the E-W to NE-SW shortening direction is attributable to Quaternary times. This stress state is also in agreement with the San Ramon fault kinematics and orientation, but not for the San José de Maipo fault. The fault plane solutions for the focal mechanisms of the seismic events reported by Pérez et al., (2014) in the San Jose de Maipo seismic station are mostly N-S to NNW-SSE orientated with a compressional axis in a nearly E-W direction (Fig 4.2b). This fault planes solutions and compressional axis are well suited with the geometry and kinematics of the Estero Coyanco fault. Moreover, the obtained shortening directions is also similar to the present-day ENE-WSW GPS derived velocity fields (Brooks et al., 2003) and the N°77-78° Tectonic plate convergence direction. Thus, the Estero Coyanco fault most recent discernible activity is similar to present day deformation derived from seismicity and geodesic data. This supports the hypothesis of the Estero Coyanco fault as an active fault.

## 4.7 Conclusion

The Estero Coyanco fault is a newly-discovered NNW-SSE striking west dipping reverse fault. This fault zone comprises three fault cores faulting volcanic bedrock of the Abanico Formation, and two of them are faulting Quaternary deposits. The fault cores evidence total acumulate displacement of 1-2 m for Quaternary times. The geometry and kinematics of the ECF are consistent with a E-W to NE-SW shortening direction, which is also compatible with the orientation and sense of motion of the active San Ramon fault, seismic data recorded by the San José de Maipo seismic station, geodesic GPS velocity fields and Tectonic Plate convergence, which supports the hypothesis of the Estero Coyanco fault as an active fault. Using 1-2 m as the maximum surface displacement, scaling laws (Wells and Coppersmith 1994) predicts Mw 6.7-6.9.

## Chapter 5: Case of study El Diablo fault

This chapter presents a case of study of the El Diablo fault. It is written as a manuscript for eventual publication and thus has distinct abstract, literature review, methods, results, and summary section.

## Multiple kinematics for the El Diablo fault, revealed by local structural data, Chilean Central Andes.

### 5.1 Abstract

A high angle west-dipping fault named El Diablo fault (EDF) located in the core of the Chilean Central High Andes, in the Volcan River east of Santiago, is closely related to the development of the Andes orogen. Structural data has been examined at outcrop scale in Baños Morales area of Volcan River. Fault rock characterization combined with kinematics analysis in fault outcrop, reveals the presence of ductile shear bans and a brittle fault zone. The ductile deformation is evidenced by tabular mylonite shear bands whit subvertical foliation and tight folding. The brittle regime is overprinting the ductile deformation, and is characterized by cataclastic belts, including breccia, plastic gouge, veins and fractures. For the ductile deformation event, left lateral strike-slip motion is inferred by σ-porphyroclasts and S-C fabrics in mylonites. For the brittle regime, two different kinematic are inferred. First, a mainly right lateral strike-slip motion is revealed by the geometry of structural features and kinematic indicators in Riedel fracture assemblage (slicken fiber steps and veins offset); and second, a reverse motion for this fault is revealed by S-C fractures in fault breccia. The brittle deformation is compatible with dextral transpression along N-S fault zones, which is consistent with present day Plate Tectonics convergence direction, GPS velocity fields and focal mechanism seismicity. This study provides detailed geometric and kinematic data that allow us to better understand the nature of the regional scale El Diablo fault which is an ancient structure that have been exhumed at least 12 km, and incorporate at least 3 different deformation events.

## 5.2 Introduction

The Cenozoic deformation in Chilean Central Andes, is controlled by the interaction between the subduction oceanic Nazca Plate and the overriding continental South American Plate (Fig.5.1a, Coira et al., 1982; Jordan et al., 1983). At these latitudes the main mountain chain comprises the Principal Cordillera and the Frontal Cordillera (Fig. 5.1a). The Principal Cordillera can be separated in 3 domains (Fig. 5.1a and Fig.5.1d). The western Principal Cordillera, made up by the Abanico basin, a Cenozoic (31-15 Ma) intra-arc basin developed in central Chile, where the mainly volcanic and also sedimentary Abanico Formation and Farellones Formation where deposited (Charrier et al., 2002; Fock 2005). This basin was tectonically inverted and exhumed during the Early to Middle Miocene (Giambiagi et al., 2003). On the other hand, the eastern Principal Cordillera is made up by the Aconcagua fold and thrust belt, located immediately to the east of the Abanico basin, where Mesozoic continental and marine sedimentary rocks of the Lo Valdes Formation, Rio Damas Formation and Rio Colina Formations where highly deformed during the Middle to Late Miocene Andean compressional tectonic event, and now a days have a nearly N-S trending and subvertically dipping disposition (Giambiagi et al., 2003). Finally, the central Principal Cordillera is a structural domain between the eastern and western Principal Cordillera; it comprises Cenozoic deposits, as well as the western Principal cordillera, bounded to the east by nearly N-S striking east-verging fault that puts in contact the Abanico Formation over the Mesozoic sequences of the eastern Principal Cordillera (Charrier et al., 2002; Farias et al., 2010).

N-S striking fault systems separates the Cenozoic rocks units from the Mesozoic rock units (Fig. 5.2), and had been interpreted as the inverted previously normal faulted boundaries of the Abanico basin (Charrier et al., 2002; Fock et al., 2005; Farias et al., 2010). While the Infiernillo fault, Cerro de Renca fault, Portezuelo de Chada fault and the San Ramon fault are east dipping reverse faults constituting the western limit of the western Principal Cordillera, a nearly vertical west dipping reverse fault located in the central Principal Cordillera, the El Diablo fault (EDF here and after) and its southern continuations (Las Leñas-Espinoza fault and el Fierro fault), constitute the eastern edge of the Abanico basin (Fig 5.1b, 5.1c and 5.2; Charrier et al., 2002, 2005; Fock 2005; Farias et al., 2010). In this context, the three previously described N-S striking east-vergent regional-scale faults were grouped and constitute the El Fierro Fault System, a ~ 300 km long fault zone composed of a suite of faults that were grouped because of its similar position, strike and kinematics (Fig. 5.1a, Charrier et al., 2005; Farias et al., 2010). Figure 5.1a shows the main faults of this system which received different names according to the latitude in which where described: El Diablo fault at 33°45'S (Thiele 1980; Fock 2005), Las Leñas–Espinoza fault at 34°30'S (Charrier et al., 2002), and El Fierro fault at approximately 35°S (Davidson, 1971; Davidson and Vicente, 1973).

Tholeiitic geochemical characteristics of volcanic rocks of the Abanico Formation support an extensional intra-arc setting for this basin (Nystrom et al., 2003; Charrier et al., 2005). Fock (2005) proposed that the ca. 3000 m thickness of the Abanico formation in the Volcan River area could be favored by tectonic subsidence related to the El Diablo fault during Abanico basin extensional settings (Charrier et al., 2002; Nyström et al., 2003). Synchronic deformation, evidenced by grow strata in the upper part of the Abanico Formation and the lower part of the Farellones Formation, has been interpreted as evidence of the reactivation and inversion of previously normal faults (Charrier et al., 2002, Fock, 2005). Charrier et al., (2002) report that most of the N-S striking faults in the Abanico Formation present folding related to thrust faults, show subvertical disposition, put younger over older rocks, and therefore, probably correspond with inverted normal faults. Fock (2005) and Farias et al., (2010) propose a tectonic inversion of the Mesozoic and Cenozoic extensional basins in base of the geometry of folds and related faults observed in the eastern limit of the Abanico basin near the Volcan River (Fig. 5.1c). However, there is limited field data to evaluate the fault itself and history of deformation. This study provides for first time, detailed geometric and kinematic data from a newly-discovered field exposure in the Volcan River that allows new insight into the regional scale EDF.

Near the Volcan River, a tributary of the Maipo River (red star in Fig. 5.1b), Thiele (1980) in the geological map Santiago (1:250000 scale) reported the EDF as a normal fault. Fock (2005) and Farias et al., (2010) documented the EDF, also in the Volcan River Valley, as a high-angle reverse fault that was previously active as a normal fault, because of the grow strata identification immediately to the west of the EDF and complex deformation in the area let them propose a deformational style dominated by tectonic inversion. In the Las Leñas River, a tributary of the Cachapoal River (yellow star in Fig. 5.1d) Charrier et al., (2002) because of the irregular folding style of Abanico Formation, with highly variable amplitude, tightness, and both east and west vergency, propose that Las Leñas- Espinoza Fault is an inverted normal fault that is currently operating as a reverse fault (Fig 5.1d). In the Tingiririca River, the N-S orientated El Fierro thrust was reported as an east-vergent steep dipping fault, owing to stratigraphic correlations and cross-cutting relationship (Zapata 1994; Charrier et al., 1996). The coincident strike and position, similar structural style (tectonic inversion), same east-vergence of the EDF, Las Leñas fault and El Fierro fault, permitted propose that a regional-scale extensional structure (El Fierro fault System) originated along the eastern flank of the Abanico basin during Eocene to late Oligocene (Charrier et al., 2002) which were reactivated and inverted during Early to Middle Miocene (Giambiagi et al., 2003). However, in spite of this regional scale stratigraphic and structural correlations (Charrier et al, 2002, 2005; Fock, 2005; Farias et al., 2010) and geochemical features (Nystrom et al., 2003; Charrier et al., 2005) that supports a extensional basin in which the EDF acted as a normal fault and after inverted as a reverse fault, due to

the difficulties to outcrop access, local detailed kinematic data of the EDF has not been presented. To better constrain the kinematics of the EDF, I have studied a fault zone outcrop in Baños Morales locality to better characterize this structure.

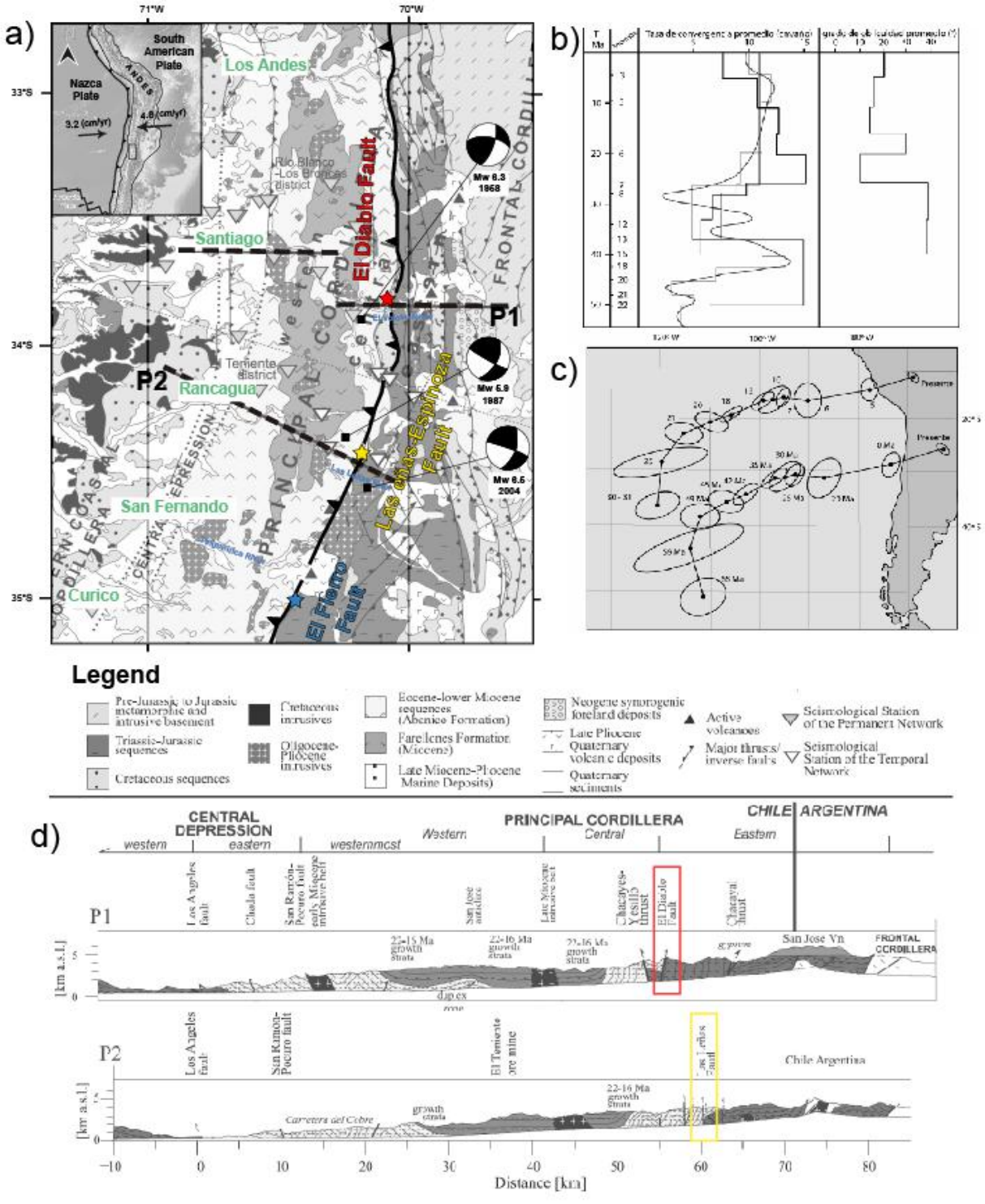
a)
71°W
70°W
33°S
34°S
35°S
South American Plate
Nazca Plate
3.2 (cm/yr)
4.8 (cm/yr)
Los Andes
Río Blanco -Los Bronces district
El Diablo Fault
Mw 6.3 1968
Santiago
P1
P2
Teniente district
Rancagua
Mw 6.9 1987
Las Chacs-Espinoza Fault
Mw 8.5 2004
San Fernando
Curico
El Fierro Fault
FRONTAL CORDILLERA
PRINCIPAL CORDILLERA
CENTRAL DEPRESSION
COASTAL CORDILLERA
b)
c)
Legend
Pre-Jurassic to Jurassic metamorphic and intrusive basement
Triassic-Jurassic sequences
Cretaceous sequences
Cretaceous intrusives
Oligocene-Pliocene intrusives
Eocene-lower Miocene sequences (Abanico Formation)
Farellones Formation (Miocene)
Late Miocene-Pliocene Marine Deposits)
Neogene synorogenic foreland deposits
Late Pliocene Quaternary volcanic deposits
Quaternary sediments
Active volcanoes
Major thrusts/ inverse faults
Seismological Station of the Permanent Network
Seismological Station of the Temporal Network
d)
CENTRAL DEPRESSION
western
eastern
westernmost
Western
PRINCIPAL CORDILLERA
Central
Eastern
CHILE
ARGENTINA
P1
Los Angeles fault
Chada fault
San Ramón-Pocuro Fault
early Miocene intrusive belt
San José anticline
Late Miocene intrusive belt
Chacayes-Yesillo thrust
El Diablo Fault
Chacaval thrust
22-15 Ma growth strata
22-16 Ma growth strata
22-16 Ma growth strata
San José Vn
FRONTAL CORDILLERA
[km a.s.l.]
P2
Los Angeles fault
San Ramón-Pocuro fault
El Teniente ore mine
Las Chacs fault
Chile Argentina
Carretera del Cobre
growth strata
22-16 Ma growth strata
[km a.s.l.]
Distance [km]

Figure 5.1 a) Small box show tectonic configuration of the western border of South America, black arrows shows current absolute plate motion relative to hot spots frame for the South American and Nazca plates (Gripp & Gordon, 2002). Simplified geological map of the Chilean Central Andes, between 33°-35°S. El Fierro Fault System is highlighted with a thick black line and colored stars show the type location and the name of the different segments of the fault system. Focal mechanism for the highest Mw shallow seismicity it is presented. Focal mechanism are extracted from Barrientos et al., (2004), Farias et al., (2006), Alvarado et al., (2009), and references therein. Modified from Farias et a., (2010). b) Compiled average convergence rate and obliquity between Nazca and South American Plates, based on Pilger et al., (1983), Pardo-Casas y Molnar (1987), Soler and Bonhomme (1990), extracted from Fock (2005). c) Kinematic reconstruction of Nazca Plate since Cretaceous until present from Pardo-Casas and Molnar, (1987). d) Simplified cross-section of the main Andean Range in Central Chile. Red and yellow boxes indicated the location of the El Fierro Fault System. Modified from Farias et al., (2010).

## 5.3 Geological Setting

The Central Andes from 33°S to 34°S (Fig. 5.1b) is characterized by the ongoing subduction of the Nazca plate beneath the South American Plate since the Jurassic (ca. 191 Ma) (Coira et al., 1982; Jordan et al., 1983; Allmendinger, 1986; Isacks, 1988; Mpodozis and Ramos, 1989, Charrier et al., 2007). Locations of magnetic anomalies and calibration of the Cenozoic Magnetic Polarity Time Scale (Pardo-Casas and Molnar, 1987; Somoza, 1998), suggest that the subduction rate and obliquity has strong variations since the Cretaceous (Fig. 5.1c). Authors postulate different Plate tectonics convergence rates in the order of 6-8 cm/yr in a N°-77-78°E direction (Figure 5.1a; DeMets et al., 1994; Gripp & Gordon, 2002).

During the late Eocene to late Oligocene (37-23 Ma), a NNE elongated continental extensional intra-arc basin was developed, and the Abanico Formation was deposited (i.e. the Abanico basin) from 27°S to 39°S (Charrier et al., 2002, 2005, 2007). The dimension of the basin, more than 1000 km long, 70 km wide and > 3 km thick make this a first order tectono-paleogeographic feature (Charrier et al., 2007). This formed in an extensional setting accompanied by crustal thinning based on geochemical tholeiitic signatures of the volcanic deposits of the Abanico Formation (Nystrom et al., 2003; Charrier et al., 2005).

Around 28-25 Ma, due to the broke of the Farallon Plate into the Nazca and Cocos Plates, an increase in the convergence rate to 14.9 cm/yr at 25 Ma, and a reduction of the convergence angle obliquity to 10° occurred (Fig.5.1c and 5.1d; Pardo-Casas and Molnar, 1987), changing the generalized extensional setting to a regional compressive setting. This caused partial tectonic inversion of the basin, reactivating some of the previous extensional structures as reverse faults (Godoy y Lara, 1994; Charrier et al., 2002; Fock, 2005). During the Early and Middle Miocene (23-16) the younger Farellones Formation was deposited in the central part of the basin (Charrier et al., 2002). A compressional setting accompanied by crustal thickening was proposed for this period (23-16 Ma) on the basis of grow strata in the lower layers of Farellones Formations (Farias et al., 2010), some local unconformably contact between Abanico and Farellones Formations, and the calcalkaline geochemical signatures of the Farellones Formation (Charrier et al., 2002, 2005).

High-magnitude historic shallow crustal earthquakes were recorded in central Chile. The largest event occurred in the upper Maipo River, the ~ 10 km depth September 4, 1958, Ms 6.9 earthquake in Las Melosas (see location in Fig. 5.1a and Fig. 5.2; Lomnitz, 1961; Piderit, 1961). More recently Alvarado et al., (2009), using modern body-wave modelling techniques, estimates Mw of 6.3 for this event at 8 km depth. Left-lateral strike-slip on a steep north-south trending fault-plane, or right-lateral strike-slip on east-west striking fault plane, are the solution suggested for the 1958

Las Melosas earthquake focal mechanism (Fig. 5.1a; Lomnitz, 1960; Piderit, 1961; Pardo and Acevedo, 1984; Alvarado et al., 2009). Farias et al., (2006) shows a NNE-SSW dextral strike-slip focal mechanism solution for the <15 depth Mw 6.5, 28 august, 2004 earthquake near Curico, calculated from CMT Harvard catalog, in the Teno River, close to the El Fierro fault (Fig 5.1a). For the <10 km depth Mw 5.9, September 13, 1987 seismic event (Barrientos and Eisenberg, 1988), located in the Cachapoal River, near the Las Leñas-Espinoza fault trace, the focal mechanism solution from CMT Harvard catalogue indicates a dextral strike-slip motion in a nearly N-S subvertical fault plane (Fig. 5.1a).

Barrientos et al., (2004), Pérez et al., (2014) and Ammitati et al., (2019) present N-S seismicity lineaments in central Principal Cordillera, spatially correlated with the EDF and Chacayes-Yesillo fault, located at 0-10 km depth, very disperse but uniformly distributed on it. USGS seismic catalog (Fig. 5.2) also shows that most of the seismic activity is located near the Chile-Argentina boundary, particularly aligned with the EDF and its south prolongation (Fig. 5.2). Seismic clusters are observed in the Tupungato Volcano, and also the Rio-Blanco Los Bronces mining district (Barrientos et al., 2004; USGS seismic catalog); however the last cluster is an anthropogenic product.

## 5.4 Fault rock background

In terms of fault rock formation process, "cataclasis", is the process which involves the brittle fragmentation of mineral grains with rotation of grain fragments accompanied by frictional grain boundary sliding and dilatancy (Sibson, 1977). This process generates fault breccia, gouge and cataclasite; minor recrystallization and neomineralization can also occur in the groundmass (Sibson, 1977). Although Sibson (1977) classified cataclasites as containing only random fabrics, it has been demonstrated that cataclasites may also develop a foliation defined by alignment of elongate grains (Chester et al., 1985). In contrast, "mylonitization" is a ductile process involving grain size reduction by the dynamic recovery and recrystallization of highly strained grains which have undergone intense intra-crystalline plastic deformation (Bell & Etheridge, 1973; White, 1973). The seismogenic frictional slip regime in which cataclastic process occurs overlies an aseismically quasi-plastic regime where mylonitization occurs. The transition between these two regimes depends on material properties, temperature, effective normal stress and strain rate, and thus occurring at different depths. The shear resistance increase with depth reaching the highest values in the base of the frictional slip regime favoring the cataclastic process, meanwhile the quasy-plastic regime develops underneath the frictional slip regime, favored by a low shear resistance originate mylonites. Major transition zones appear to occur at temperatures of approximately 300

°C, corresponding to depths 12 km, assuming a typical continental geothermal gradient of 25 °C /km (Sibson, 1983).

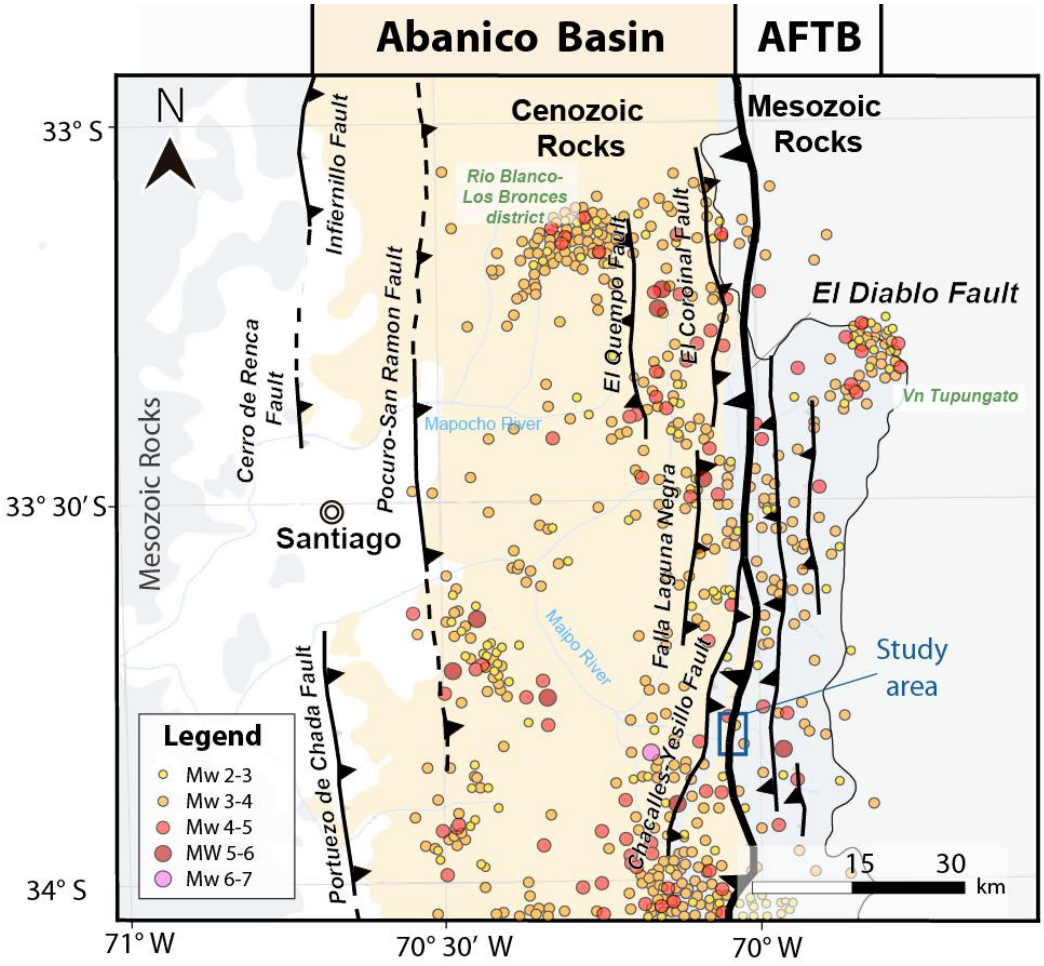


Figure 5.2 Structural framework of the Principal Cordillera between 33°-34°S, main regional-scale fault and structural domains are shown. Mw>2 shallow seismicity (<40 km depth) between 1900 and 2018 USGS catalog is presented. The El Diablo Fault (EDF) is marked by a thick black line. Blue box shows the study area at El Volcan River close to Baños Morales Locality. In green letters the Tupungato volcano and the Rio-Los Bronces mining district are shown. Thin black line represents the Chile-Argentina border.

## 5.5 Methodologies

To be able to constrain the kinematics of the EDF, field mapping were done in the Baños Morales. While mapping, a fault zone was explored in a NNE striking gully at the northern side of the Volcan River Valley (Fig. 5.3a and 5.4). This gully was identified as part of the fault trace previously by Thiele (1980) and Fock (2005). Rock sampling and hand sample description, combined with structural observations were undertaken to characterize the fault zone architecture. Orientation of the principal fault planes, subsidiary planes, slickenlines and foliations where measured to constrain the kinematics.

Fault zone is described in base of a fault core and a damage zone (Sibson, 1977; Chester & Logan 1986). The fault core is defined here by the presence of fault rocks as mylonite, breccia, plastic-gouge and cataclasite; and the damage zone is defined as the area that presents secondary and minor structures, like folds, fractures and veins related to the main structure (Sibson, 1977; Chester & Logan 1986; Goddard & Evans, 1995; Caine et al., 1996).

Kinematic analysis in FaultKinTM software (Marret and Allmendinger, 1990; Allmendinger et al., 2012) was used to calculate the orientation of the compression and tension axes for individual fault planes and also for fault populations. Geometrical and kinematic data of the structural features are compared to the idealized "Riedel Shears" model (Hills, 1963) which refers to a specific fault geometry first created in clay cake models (Riedel, 1929). The pattern includes relatively short, in échelon fault segments that may link to form a through-going Principal Shear Zone (PSZ) (Skempton, 1966).

## 5.6 Results

### 5.6.1 Fault zone characterization

In a panoramic view, the fault passes through a narrow gully flanked by vertical walls, to the east of Baños Morales in the northern side of the river (Fig. 5.3a). This gully is a clear discontinuity between a massive greenish-grey porphyric andesitic rock with intense epidote alteration, corresponding to the Abanico Formation to the west (EoMa in Fig. 5.4; Thiele 1980; Fock 2005), from a dark-grey NNE-SSW subvertical stratified volcano-sedimentary sequence, comprising andesites, volcanic breccia, conglomerates and minor sandstones, corresponding to Lo Valdes Formation to the east (Klv(3) in Fig. 5.4; Thiele 1980; Fock, 2005). Topographically the block located to the west of the gully present minor elevations compared to the eastern block (Fig. 5.3a). At the southern side of the El Volcan River, a

light colored area of hydrothermal complicates the process of locate the fault trace (Fig. 5.3b). Although the light color clays of the hydrothermal alteration, suggest an approximate fault trace location, the scarce contrasting rock colors and no clear bedding difficult the process of identify the discontinuity observed in the north side of the valley, and thus, trace the southern continuation of the fault.

The gully is ~ 4 m wide. On the western vertical wall of the gully, a greenish-grey porphyric andesitic rock characterized by no clear stratification and notorious epidote infill in fracture planes is observed (Fig. 5.11a) On the eastern wall of the gully a reddish-dark porphyric andesitic rock with no clear stratification can be observed. Epidote alteration in fracture planes is notoriously less to the east than in the west side of the gully. Between the walls that limits the gully, a suite of NNE-SSW subvertical deformed rock bands can be observed.

The damage zone was determined by the presence of these fractures with epidote infill, reaching close to 200 m to the west of the creek, and almost 5 m to the east. Mm to cm scale slickenside steps, correlated with Crystal fibers (Doblas, 1998 and references therein) are frequently observed in fracture planes in the damage zone. No folding can be observed in the damage zone. In between the two andesitic blocks with distinguish color, a series of subvertical fault rock band are exposed representing the main fault core.

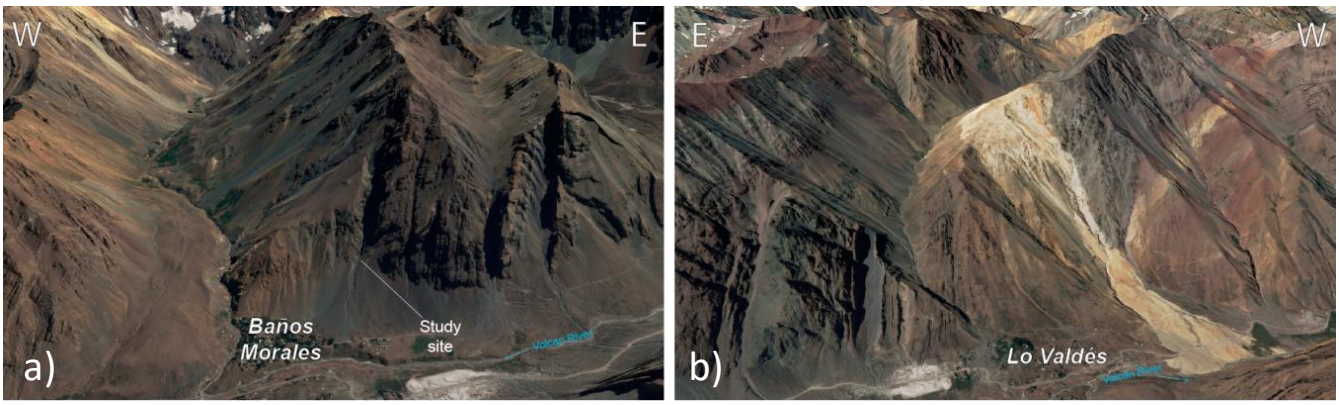


Figure 5.3 Panoramic view of the Volcan River valley. Lo Valdés and Baños Morales localities are shown. Blue arrow indicates the Volcan River flow direction. a) North side of the valley, the gully in which the study was done is indicated. b) South side of the valley. Images modified by Google Earth.

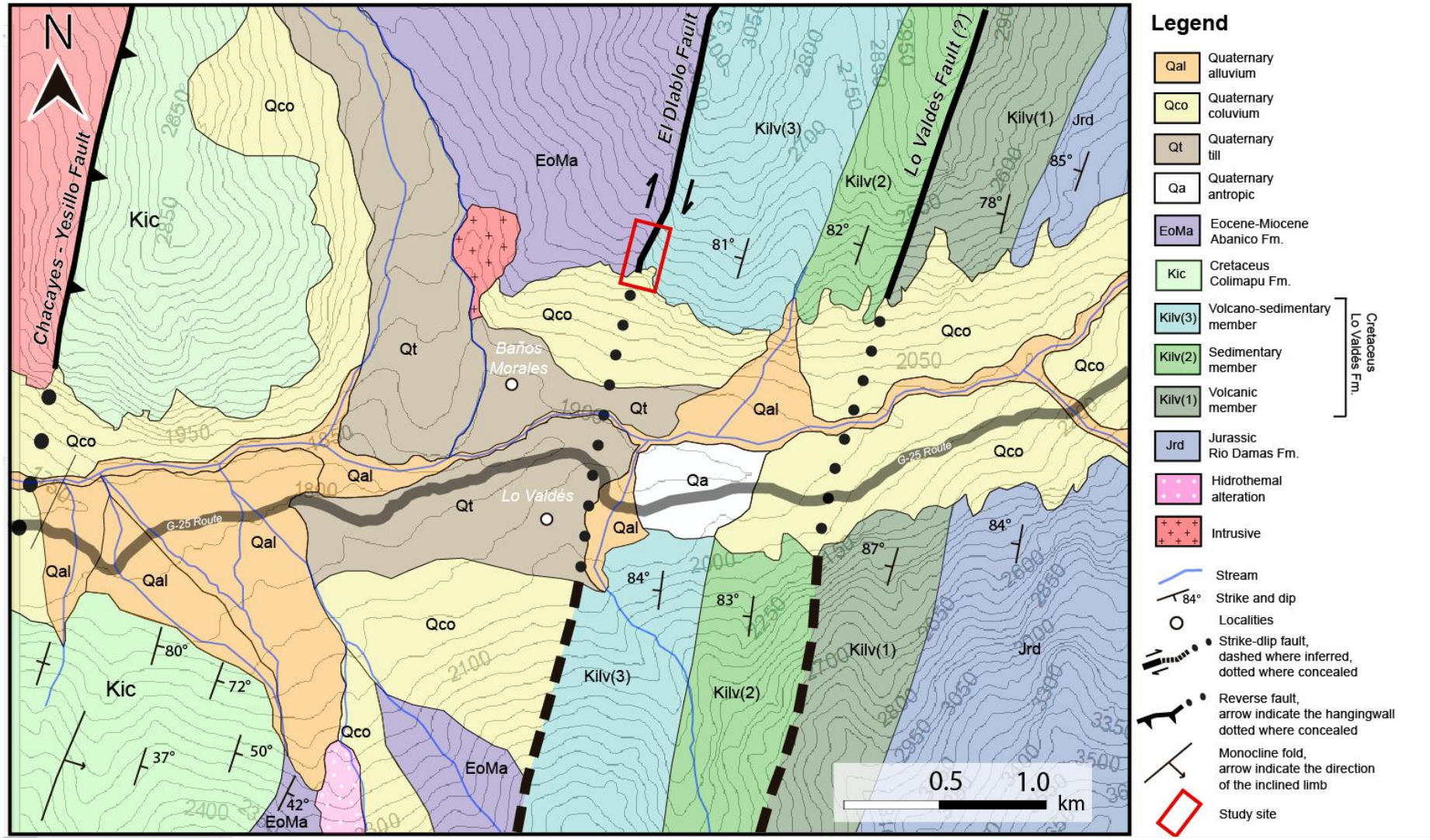


Figure 5.4. Geological map of the study area in Volcán River where Baños Morales and Lo Valdés localities are situated.

The fault core constitute the gully itself (Fig. 5.5), where the weak deformed rock where probably more easily to erode. Three NNE-SSW bands of foliated rocks with volcanic photolith can be observed (Fig. 5.6). From west to east: (1) 30-60 cm foliated grey mylonite band with S-C fabric (Fig. 5.7a); (2) 50-150 cm grey mylonite with vertical foliation and tightly cm-scale folds (Fig. 5.7b); (3) 1.5-2 m foliated reddish mylonite containing subvertical undulating elongated lenses of gray color, and asymmetric light gray porphyroclast (Fig. 5.7c)

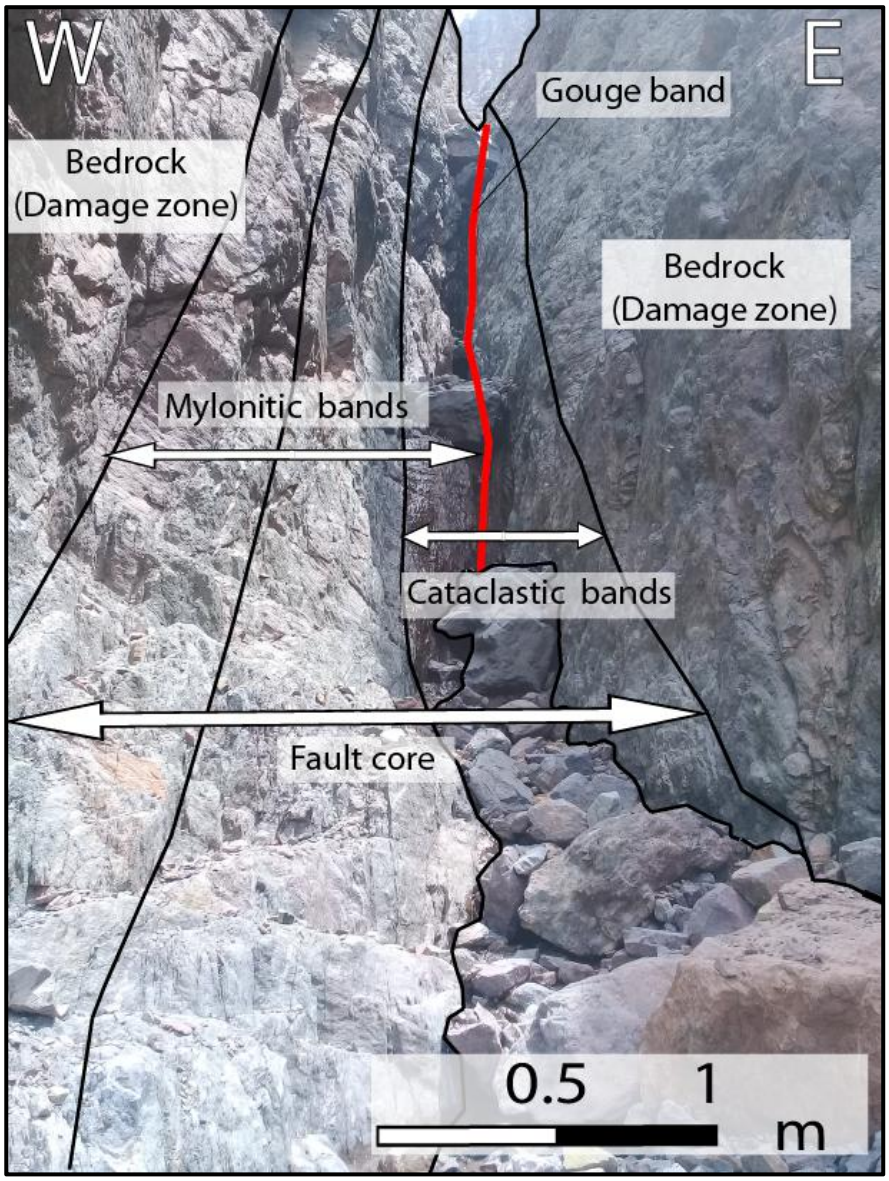


Figure 5.5 General view of the fault zone, indicating the mylonitic and cataclastic bands.

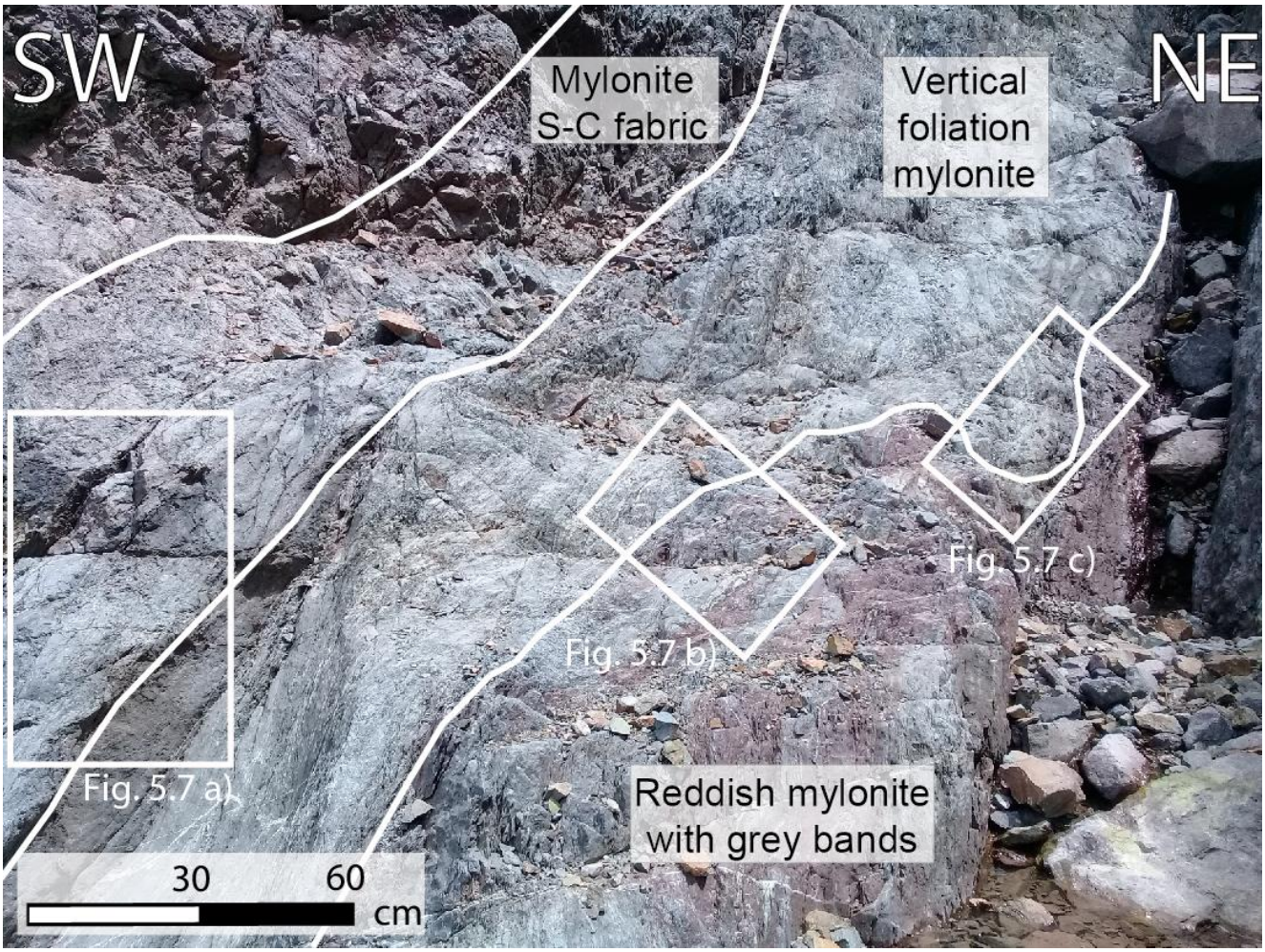


Figure 5.6 View of the three subvertical mylonitic bands observed in the study area. Black boxes show the locations of photos in Fig. 5.7.

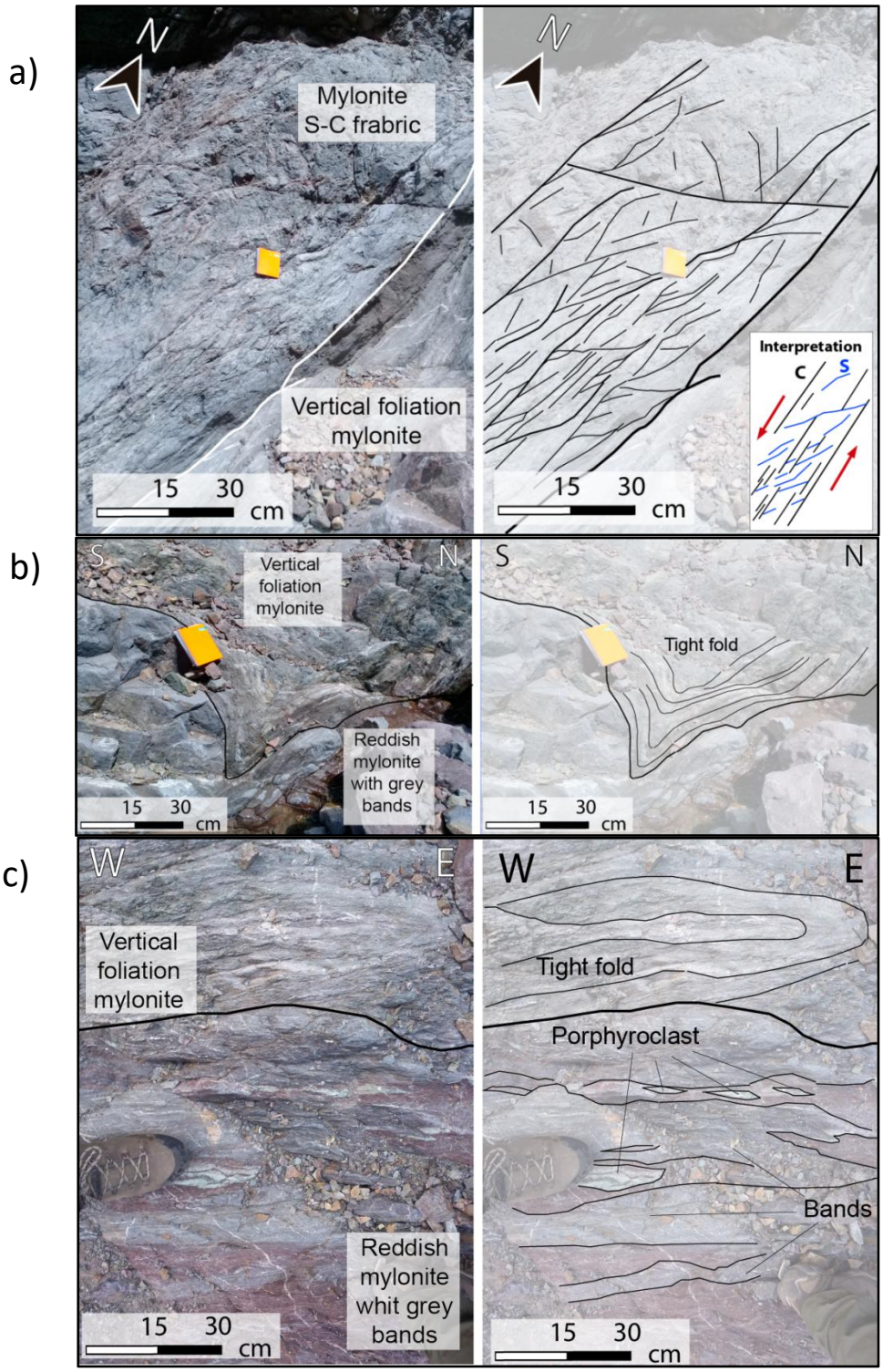


Figure 5.7 a) Closer look to the mylonite band with S-C fabric; and kinematic interpretation. b) Closer look to vertical foliation mylonite band, showing tight fold; and interpretation. c) Closer look to vertical foliation mylonite band with tight fold and reddish mylonite with grey bands and porphyroclast; interpretation is also shown. See photo location in Fig. 5.6.

Subvertical white curved calcite veins of 1-2 mm with a 040-070° azimuth direction are present cutting the 3 previously mentioned mylonite bands. This calcite veins are dextrally offset by NNE-SSW subvertical minor fault planes (Fig. 5.10).

At the core of the gully the mylonite bands are overprinted by two less than 1 m wide fault breccia and a 2 cm gouge band (Fig. 5.8a). The gouge band is uncemented and subvertical, constituted by two contrasting colors, a grey thin gouge layer surrounded by a reddish gouge (Fig. 5.8b). The gouge band is flanked by two main slip planes with 10-15°/76-85°W orientation (Fig. 5.8b). The orientation of the main slip planes determines the main fault zone orientation, which has an average of 012°/80°W. To the west of the gouge layer, a 1.5 m wide fault breccia containing clast ranging from 1-10 cm and S-C fractures can be observed (Fig. 5.9a). To the east of the gouge layer a second 50-60 cm fault breccia presenting S-C fractures, contains clast ranging from 1-30 cm (Fig. 5.9b).

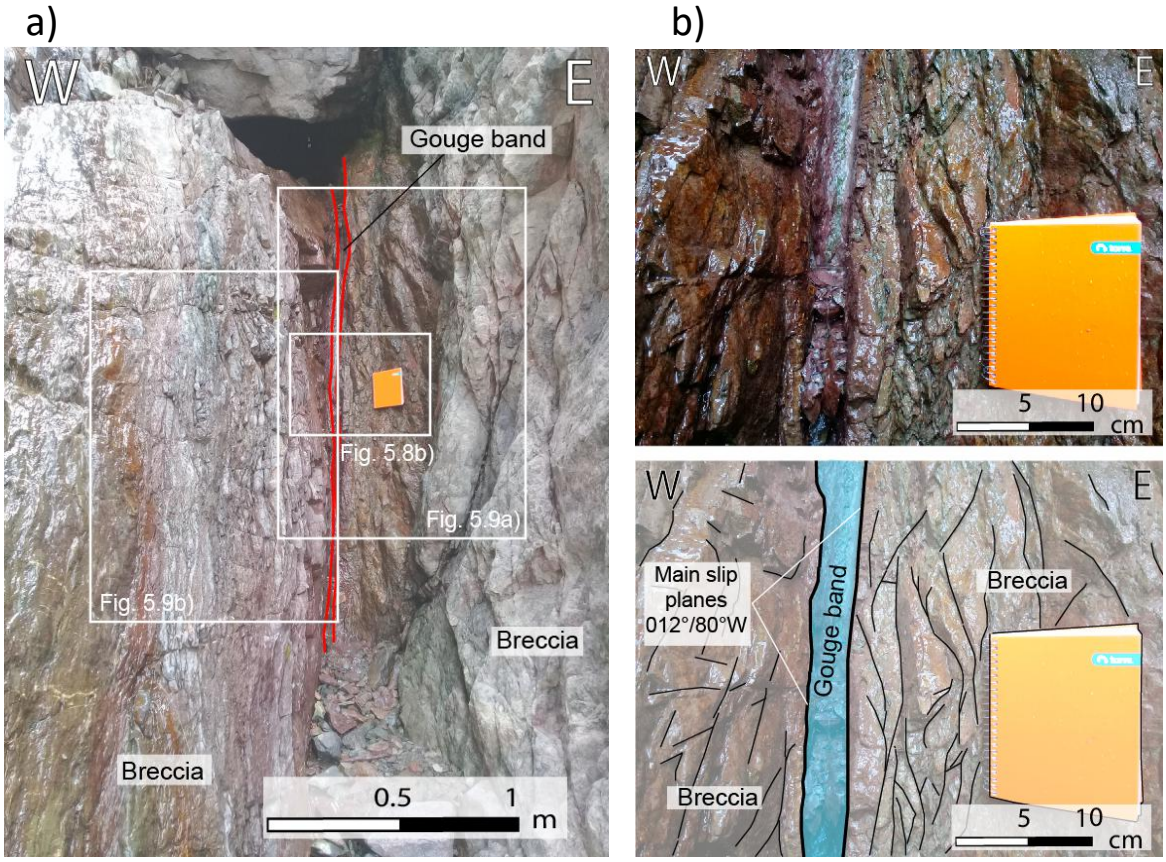


Figure 5.8 a) View of the cataclastic bands, at the core of the gully overprinting the mylonite bands. Black boxes show the locations of photos of Fig. 5.9a and 5.9b. b) Closer view of the axis of the gully, where it can be seen the reddish and grey plastic gouge band; and interpretation.

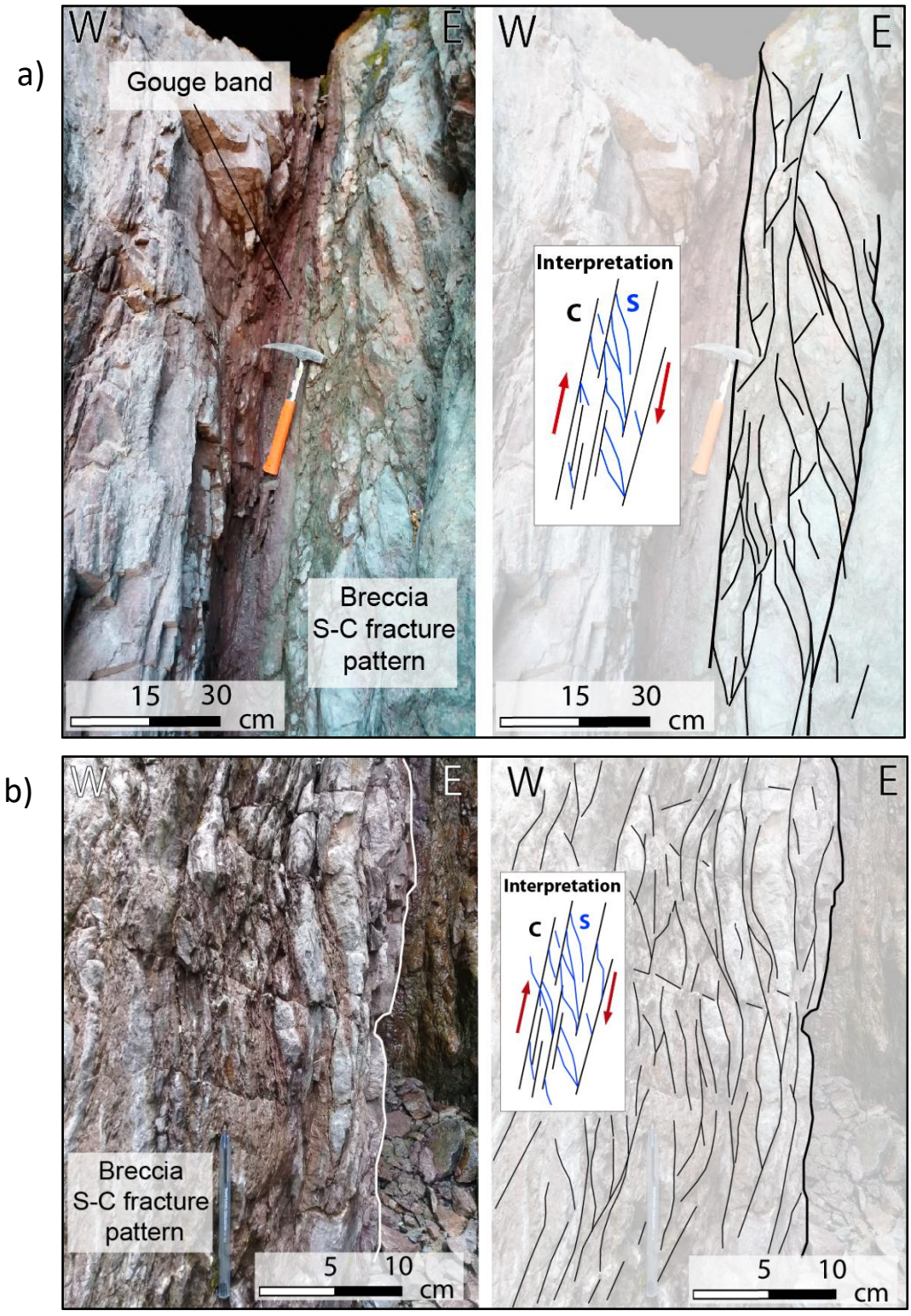


Figure 5.9 a) Closer look to the footwall fault breccia with S-C fractures; and interpretation. b) Closer look to hanginwall breccia with S-C fractures; and interpretation. See photo location in Fig 5.8a.

### 5.6.2 Kinematic analysis

The NNW-SSE orientation and vertical dispositions of the colored foliated shear bands, indicates a vertical plane of motions. Grey cm-scale σ porphyroclasts are observed at hand sample in the oriental foliated reddish mylonite, indicated a left-lateral sense of motion (Fig 5.10). S-C fabric in grey mylonites also indicates a left-lateral sense of motion (Fig. 5.7a).

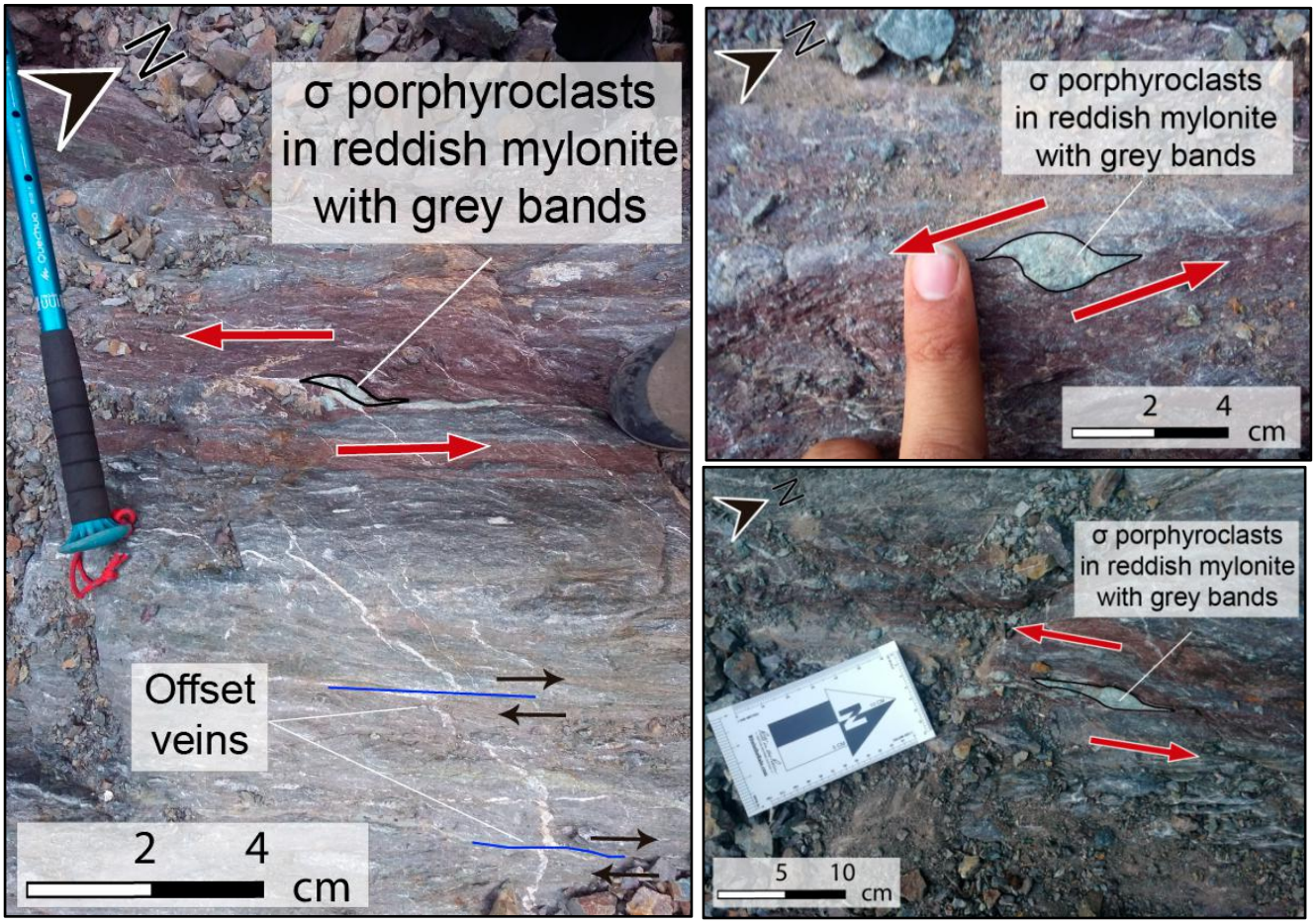


Figure 5.10 Grey centimetric asymmetric σ porphyroclasts in reddish mylonite with grey bands, indicating a left-lateral sense of motion. Photos in plant view.

In this work different kinematic indicator and analysis were develop to accurate constrain the EDF brittle kinematics. S-C fracture pattern in both fault breccias (Fig. 5.9a and 5.9b), strongly suggest a reverse sense of motion for this fault. The calcite veins offset, parallel to the main fault zone orientation, cut by subvertical minor fault surfaces, indicates a right lateral strike-slip kinematics (Fig. 5.10a). Additionally, striated fracture surfaces (ca. 040° azimuth) with mean rakes of about 20°, oblique to the main fault zone orientation (ca. 012° azimuth) presents slickenfiber and steps, evidencing a right lateral strike-slip kinematics (Fig. 5.11a). Kinematic analysis for individual striated minor fault surfaces (n=16) registered in the hangingwall

and footwall, yields shortening directions mainly between NE-SW to E-W. The kinematic analysis for the hole suit of striated surfaces grouped together yields an average of 085.5°/19° (trend/plunge) shortening direction (Fig. 5.11b).

Furthermore, if we compare the orientation of the striated minor surfaces at the damage zone, the white calcite veins, and the subvertical minor surfaces that dextrally offset the calcite veins, it can be seen that the assemblage is consistent with a Riedel arrangement shear zone with right-lateral sense of motion (Fig. 5.12). In this context, the principal shortening direction should be NE-SW.

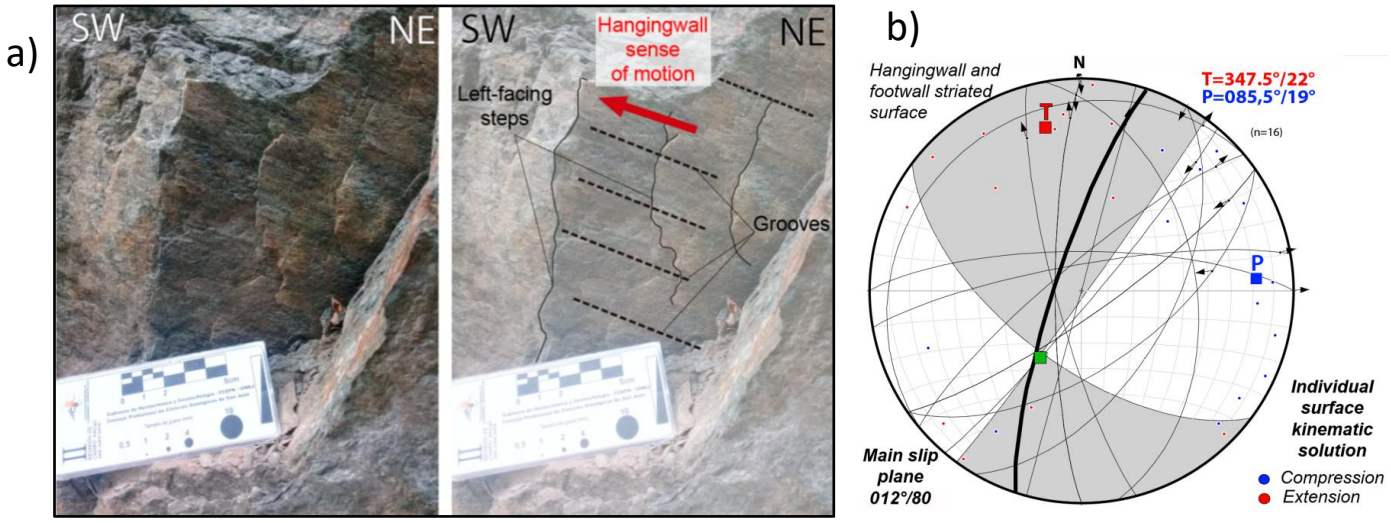


Figure 5.11 a) Photo of the striated surface of an oblique minor fault plane, showing slickenfibers and steps, indicating a mainly right lateral displacement. b) Kinematic analysis of 16 striated minor and small scale fault surfaces.

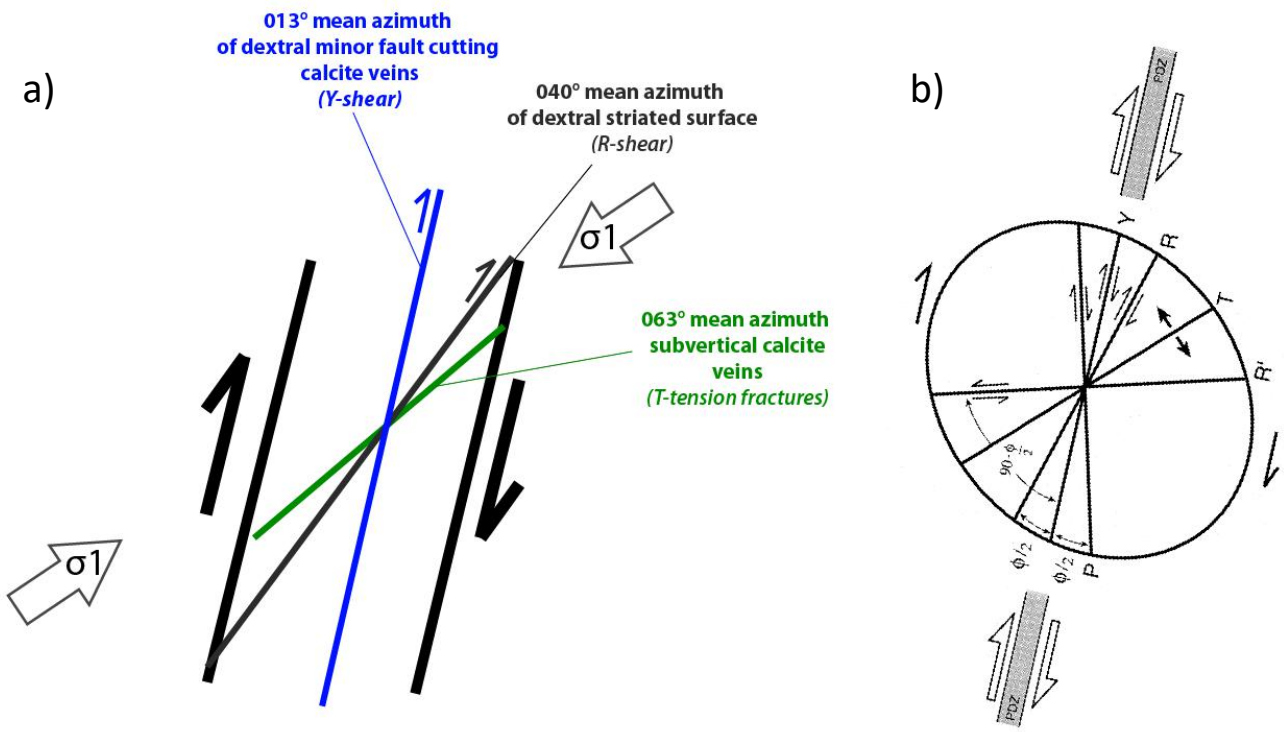


Figure 5.12 a) Sketch of the main brittle structural features in the EDF compared to Riedel arrangement idealized model. b) Riedel arrangement idealized model extracted from Davis et al., (2000).

## 5.7 Discussion

### 5.7.1 Multiple kinematics

The type of fault rocks on the trace of the EDF represents two different types deformation. The mylonite with S-C fabric, the grey mylonite with vertical foliations and tightly cm-scale folds, together with the reddish mylonite containing horizontally elongated bands of grey color, because of tight folding, porphyroclasts and the highly foliated texture, evidence a ductile deformation episode. Second, a brittle deformation episode is evidenced by fault breccia, gouge band, veins and fractures. The breccias and gouge, are direct evidence of cataclastic process in fragile regime.

Two different kinematic indicators, cm-scale σ-porphyroclasts as well as S-C fabric in mylonite bands indicate a left-lateral strike slip sense of

motion. The brittle deformation can be separated in two episodes; (1) a reverse motion of the fault directly derived by S-C fracture pattern observed in the breccias; and (2) a mainly dextral strike slip motion derived from the striated surfaces, the minor subvertical surfaces that cut the calcite veins and calcite veins geometrical and kinematic assemblage. Besides, a minor normal kinematic component is derived from the striated minor fault surfaces (Fig. 511b). Geometrically, an idealized Riedel shear zone consists of five principal elements (Davis et al., 2000): R and R' conjugate shears, T tension fractures, P shears, and Y shear faults, which are oriented at particular angles to the general trend of the shear zone, called the Principal Displacement Zone or PDZ. The geometric and kinematic analysis of the fracture assemblage, calcite vein and main slip planes orientation, reflects a Riedel´s right lateral strike-slip shear zone, where most of the minor striated surfaces with kinematic indicator correspond to R-shear, the minor fault surfaces cutting calcite veins are X-shear bands, calcite veins as T tensional fractures, and the orientation of the main fault planes as the PDZ (Fig. 5.12b). From the Riedel geometrical analysis, a NE-SW maximum shortening (σ1) is derived (Fig. 5.12a).

### 5.7.2 Timing of deformation

The relative timing of deformation can be deduced by the cross-cutting relationship between structural features. The ductile deformation should be originated at depths associated to temperature and pressure capable to produce dynamic recovery and recrystallization, however now we see them at surface, thus considerable time should pass to exhume these rocks. Also, a cataclastic band, constitute by the hangingwall breccia, its overprinting the reddish mylonite band, which is a clear indicator that the brecciation process occur after the mylonitization process. The white calcite veins are cutting the mylonite bands, which also indicates that the mylonitization occur before, however the veins are also cut by minor fault parallel to the principal displacement zone, indicating that the dextrally offset of the veins are originated after the veins precipitation. Nevertheless, as the calcite veins and the minor faults cutting the veins are related to the same kinematic deformation mechanism controlled by the Riedel shear fracture assemblage, the fact that minor fault surfaces are cutting the calcite veins can be caused by the sequentially develop of the brittle shear zone, where the X-shear bands parallel to the PDZ are the last to develop (Tchalenko, 1968; Bartlett et al., 1981). Unfortunately, no clear cross-cutting relationship can be observed between the vertical calcite veins and the breccia to infer if the strike slip or the reverse motion occurred first.

### 5.7.3 Kinematic model

The nearly E-W (striated surfaces analysis) to NE-SW (Riedel shear assemblage zone analysis) shortening direction for the dextral strike-slip deformation episode, it is partially in agreement with the Quaternary compressional NNE-SSW stress state derived from kinematic analysis in individual fault planes (Fig. 5.13a, Lavenu & Cembrano, 1999), the ENE-WSW Tectonic Plates convergence angle (DeMets et al., 1994; Gripp & Gordon, 2002) and GPS velocity field obtained by Brooks et al., (2003) (Fig. 5.13). According to Alvarado et al., (2009) and the Harvard CMT catalogue, larger crustal seismic events in the High Cordillera (1987 and 2004) indicate focal mechanisms with right-lateral strike-slip along fault-plane solutions of north-south trending (Fig. 5.1a and 5.13), which it is also in agreement whit the brittle dextral strike-slip episode shortening direction derived from this study. The coincident kinematics obtained for the brittle dextral strike-slip and the previous mentioned present-day geophysical and geological data indicates that the most recent documented deformation of the EDF is similar to present day deformation, suggesting that the EDF is a potentially active fault with an expected dextral strike-slip kinematics. Geomorphologically, the EDF trace pass through the Volcan River valley, which is covered by Quaternary deposits, unfortunately no clear evidence of fault displacement at surface can be observed. The lack of clear surface ruptures could be favored by low seismic recurrence time and the high erosional rates at this elevation of the Andean mountain belt, similar as proposed by Cox et al., (2012) near the Alpine fault.

The kinematics documented in this work, are not completely in agreement with the previous literature. For the EDF a first normal motion where inferred from grow strata, stratigraphic and structural relations (Fock 2005, Farias et al., 2010), however, a normal kinematics is inferred only for the mainly dextral strike-slip episode. The no observed initial normal kinematics could be caused because of the El Diablo Fault had a more relevant strike-slip motion in its origins than previously thought, or because of the repeated reactivation of this fault may overprint and erase the initial normal kinematic evidence. Reverse motion was inferred for the EDF, during the Early-Middle Miocene Abanico basin inversion, in base of the structural arrangement observed (Giambiagi et al., 2003; Fock 2005; Farias et al., 2010), which is consistent with the kinematics inferred from the S-C fracture pattern in the fault breccia. A dextral strike-slip sense of motion was proposed for the El Fierro Fault System by Farias et al., (2006) in base of focal mechanism of the 2004 Curicó earthquake, consistent with this work results.

If we compare the potentially active EDF with the San Ramon fault orientation and kinematics, the only regional scale active fault in the Principal Cordillera to the east of Santiago de Chile, we notice that in spite of have similar N-S orientation, the kinematics are quite different. The San Ramon

present a reverse kinematics (Armijo et al., 2010; Vargas et al., 2014), meanwhile I inferred a dextral strike-slip active kinematics for the EDF. However, both kinematics are compatible with shortening directions around NE-SW to E-W.

According to Pérez et al., (2014) and the 1958, 1987 and 2004 shallow earthquake seismic focal mechanism, reverse mechanism in N-S trending fault planes characterized the western flank of the Principal Cordillera (where the San Ramon fault locates), and variable kinematics with strike-slip predominance in N-S trending fault planes characterized the central Principal Cordillera (where de EDF locates). Both fault orientation and kinematics, together with available focal mechanism are compatible with a NE-SW shortening direction. Thus, this could reflect a strain partition in the stress transfer from the subduction zone with ENE-WSW convergence vector to the Principal Cordillera, in which the western flank accommodates E-W shortening parallel to the main Andean chain and the subduction trench though N-S orientated reverse fault (e.g. San Ramon Fault), meanwhile the central Principal Cordillera accommodates a more N-S shortening, parallel to the main Andean chain and the subduction trench thought NNE-SSW trending dextral strike slip structures (e.g EDF). Notice that NNE-SSW orientation of the EDF is less orthogonal to the Tectonic Plate convergence vector (ENE-WSE) than the N-S orientation of the San Ramon fault, which would favor a dextral strike slip movement for the EDF compared with the San Ramon fault. The location of the EDF, less than 10 km from the San José volcano could produce crustal weakening that combined with an inherited zone of weakness represented by the EDF, could favored the existence of a strike-slip margin parallel reginal scale fault zone in an oblique (10-20°) subduction context.

Thus, our results indicates at least three deformation events with different stress field condition, because we don´t have age absolute constrain we will assign relative deformation ages in base of the structural level of de deformation, the overprinting cross-cutting relationship and the correlations with available previous author´s data and interpretation. Thus, first, a depth ductile strike left-lateral slip motion evidence by foliated shear bands, possibly occurring during the initial state of the fault development in Eocene-Late Oligocene times, after that, a fragile deformation event with reverse kinematic is recorded in the fault breccia, this related to the Early-Middle Abanico basin inversion. Finally the brittle deformation shown by the Riedel´s fracture pattern indicates a dextral strike slip motion, which is compatible with the present day geological and geophysical data. The subsidiary normal component linked to the main dextral strike slip kinematic of the most recent brittle deformation event, can be the result of a strain partition in a highly structural complex area. This normal motion could be favored by the vertical disposition of the fault and, maybe, due to a

decoupling between the Abanico basin structural domain and the Aconcagua Fold and Thrust belt.

The mylonite bands are originated by dislocation creep and dissolution-precipitation creep mechanisms, which should occurred between 300° - 400°C in an aseismic zone (Sibson 1983; Fagereng, 2011). Considering a typical geothermal gradient of 25°C, the mylonits should be originated around 12-18 km depth. On the other hand, the frictional faulting mechanism responsible for the cataclastic bands must occurred under 300°C at the seismogenic zone which indicated less than 12 km depth. Particularly the clay-rich gouge band should originate at no more than 6 km depth associated with temperature less than 150°C (Sibson 1983; Fagereng 2011). The fact that we have at surface level mylonite bands indicates an exhumation of at least 12 km. The different types of cataclastic bands located one next to the other, some of them overprinting mylonite bands, combined with the different deformation episodes evidence with distinctive kinematic characteristics, suggest that the fault was active during different stress state, passing through different structural levels along the minimum 12 km exhumation. These are clear evidence and confirm that EDF fault is deep ancient structure that has accommodates significant deformation during its time life.

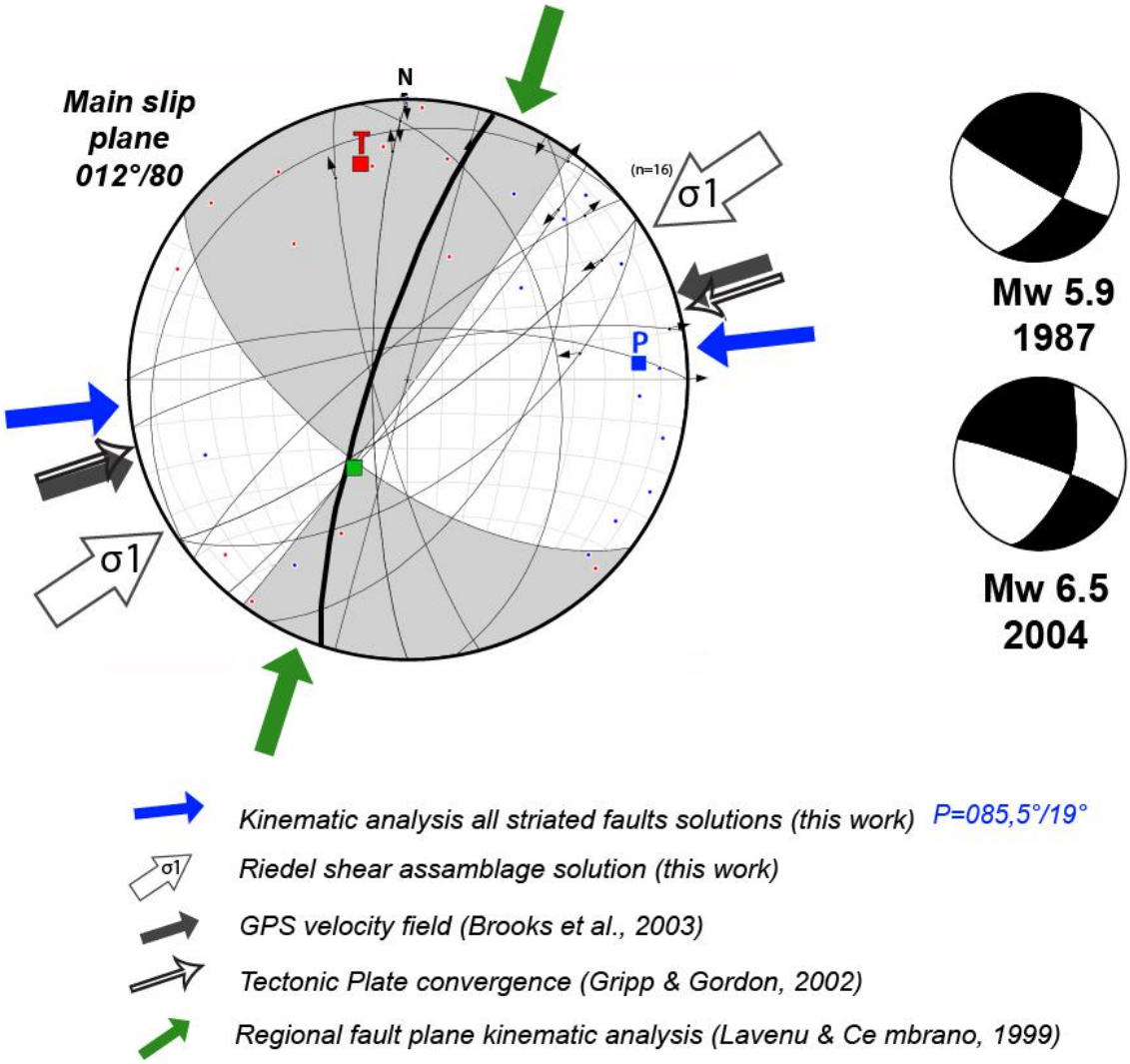


Figure 5.13 Comparison of horizontal shortening directions obtained in this study and geological, geodesic and seismic data presents by previous authors. Focal mechanisms are from Harvard CMT catalogue, extracted from Alvarado et al., (2009) and Farias et al., (2006).

## 5.8 Conclusions

This work presents solid structural data, at the outcrop scale of the steeply dipping EDF in the central High Andes of Chile. Here we see evidence for two different styles of deformation separated in one ductile and two fragile deformation episodes in an exposure of the EDF. First, a ca. 3 m wide zone of mylonites shows a ductile deformation event related to deeper crust levels. Left lateral strike-slip motion is evidenced by σ-porphyroclasts and S-C fabric for the ductile event. Second, 2 m wide zone of cataclasites including breccias, plastic gouge, veins and fractures, reflects a more fragile regime at shallow crustal levels. This fragile regime is separated in two different deformation events. One revealed by S-C structures in fault breccia indicating a reverse motion for this fault; and other deformation event revealed by the Riedel shear observed assemblage, which indicates a mainly right lateral but also a minor normal motion in a fragile deformation event. The dextral strike-slip motion on the NNE-SSW orientated EDF caused by a NE-SW to ENE-WSW shortening direction is in agreement with present seismic data, GPS derived velocity field and Tectonic Plates horizontal shortening direction, which suggest that the EDF is potential active fault, unfortunately no surfaces ruptures are observed. The difference between the San Ramon fault and the EDF kinematics, could evidence a strain partition from the subduction to shallow crust in the Principal Cordillera, where the western flank of the Principal Cordillera accommodates E-W margin perpendicular shortening and the central Principal Cordillera accommodates nearly N-S margin parallel shortening.

Geological data shows local arguments for an ancient structure that have been exhumed at least 12 km, and incorporate at least 3 different deformation events, which are in agreement with previous reverse and dextral strike-slip kinematics interpretations of this structure, but also report a new ancient left lateral strike-slip kinematics for the EDF.

# Chapter 6: Faults seismic potential

## 6.1 Introduction

Although Chile is one of the most seismically active countries on Earth, little is known about the seismic hazard related to crustal faults, in particular near the main populated centers including the Capital City of Santiago. To evaluate the seismic potential for the total population of known faults in the Principal Cordillera of the Central High Andes near Santiago, Chile, I compiled in both a map and database (Fig. 6.1-6.5 and Table 6.1) showing all the major structures mapped in previous works, including strike, dip, kinematics, length, seismic depth and certainty into a database indicated by the previous research. Afterwards earthquake parameters of each of the faults were used to define potential moment magnitudes (Mw) by Wells and Coppersmith (1994) empirical relation (see Table 6.1). Diverse structural maps with faults in colors indicating the range of earthquake Mw expected are shown (Fig. 6.2-6.5). A comparison between faults and landslides is developed to analyze the possibility of fault as source of coseimic landslides (Fig. 6.6). Until September 2018, and prior to this work, only two active faults are identified (N°20 San Ramon fault and the N°41 San José de Maipo fault: Rauld, 2002; Armijo et al., 2010; Rauld, 2011; and Lavenu & Cembrano, 2008, respectably). Two active faults are reported in this thesis in previous Chapters (N° 64 El Arrayan fault, and N°65 Estero Coyanco fault) and one reported as a potentially active fault (N°18 El Diablo fault). For the other faults there is no knowledge about recent motions or if these fault are currently active. For "potentially" seismic hazard analysis, I will assume all the faults as "active", which is based on the workflow of Cox et al., (2012) which used a similar methodology for poorly-characterized faults and areas of rapid erosion in the Southern Alps of New Zealand.

The data used to develop this fault compilation are detailed described in section 2.1.1 and are derived from the following research.

Thiele (1980); Wall et al., (1999); Selles & Gana (2001); SERNAGEOMIN (2003); Giambiagi et al., (2003); Fock (2005); Calderon (2008); Lavenu & Cembrano (2008); Rauld (2011); Castro (2012); Quiroga (2013); Villela (2014); Armijo et al., (2010); Deckart et al., (2013); Piquer et al., (2016).

Seismic depth data is obtained from USGS seismic catalog, Barrientos et al., (2004), Perez et al., (2014) and Ammirati et al., (2019). From the USGS catalog, the shallow (< 40 km depth) seismicity occurred between 1950 and present is obtained and analyzed in QGIS software. From

Barrientos et al., (2004), Perez et al., (2014) and Ammirati et al., (2019) seismic depth were directly obtained from the Figures showed in those works. All the databases indicate two seismic depths for the Principal Cordillera. First, the western flank presents an average seismic depth of 15 km and a maximum of 25 km. Second, the eastern side of the Principal Cordillera, near the Chile-Argentina border, presents average seismic depths of 5 km and a maximum of 15 km. Geometric fault parameters are not available for all faults; therefore, general dip values in base of style of faulting are used for first-order approximations. When no dip is available, for reverse faults values of 30° where used, for normal faults 60° was used, for strike-slip faults 80° was used, and for faults without kinematic a dip value of 45° was used.

Surface rupture length (SRL) and Rupture area (RA) are the main key parameter used to calculate the expected Mw, because those are the easiest data to collect. However, the fault N°65 Estero Coyanco fault, expected Mw are also calculated in base of Maximum displacement (MD) because is one of the acquired data (See Chapter 6). Unfortunately the Maximum displacement (MD) parameter is not available for the rest of the faults. This result is presented in Table 6.2.

## 6.2 Results

### 6.2.1 All Faults

The mapped compilation with all the faults is shown in Figure 6.1 and a full scale version is shown in Appendant (Chapter 9). This map illustrates the distribution, orientation and kinematics of the major known structures that can be mapped at scales up to 1:50.000 or 1:100.000 scales in the study area. Each fault it is assigned with a number which correlated with Table 6.1. The numbers increase from west to east and from north to south. The two newly reported active faults (N°64 and N°65) are entered at the end of the list. The landslide (Antinao & Gosse 2009) distribution is also shown on this map in orange-yellow polygons in order to better understand the relationship between crustal faults and coseismic landslides distribution.

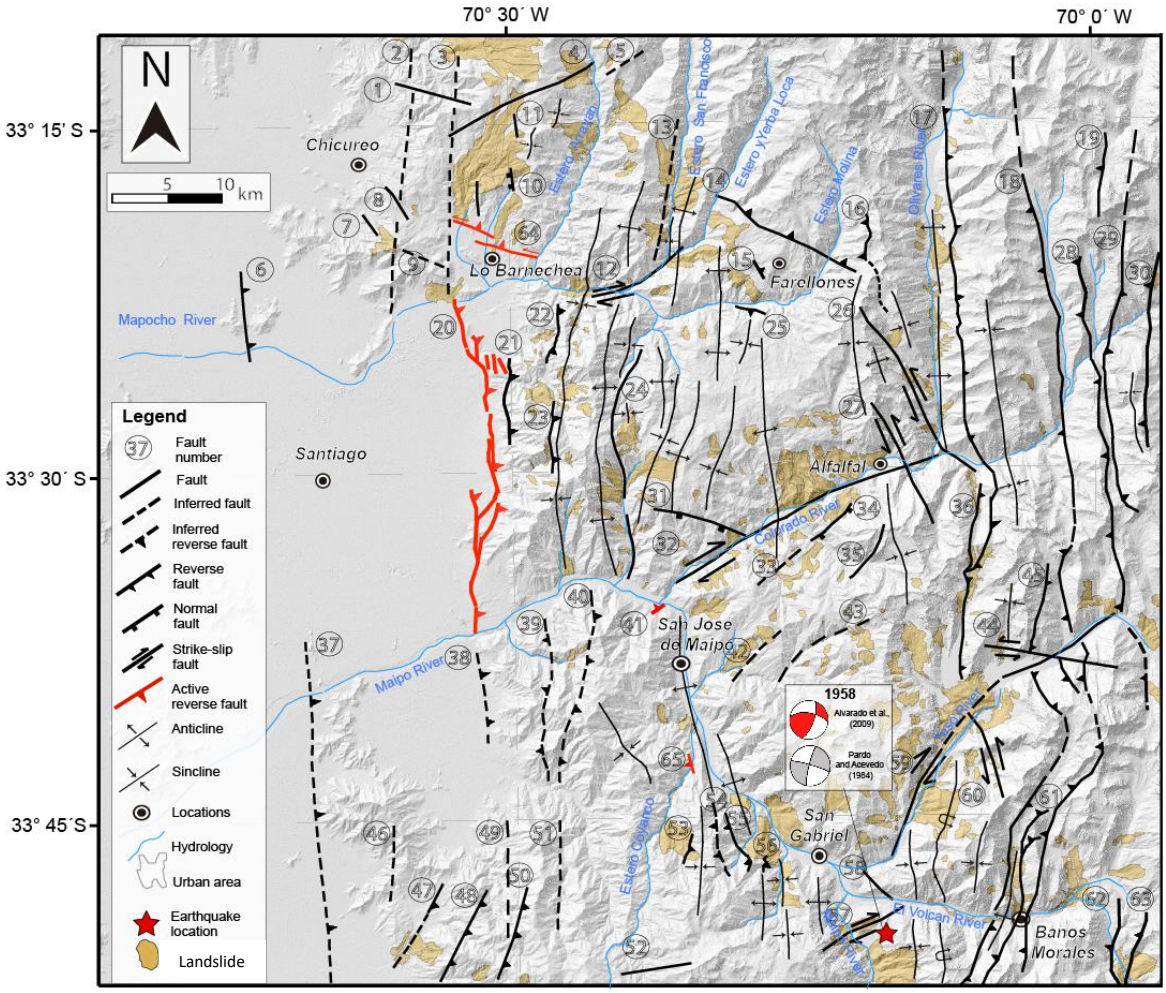


Figure 6.1 Structural map showing the compiled structural data for the Principal Cordillera near Metropolitan Region. Faults are indicates by number, which correlated with the ones in Table 6.1. Las Melosas earthquake location is marked by a red star, focal mechanism are also shown. Faults and structures compiled from: Thiele (1980), Wall et al., (1999), Selles & Gana (2001), SERNAGEOMIN (2003), Giambiagi et al., (2003), Fock (2005), Calderon (2008), Lavenu & Cembrano (2008), Rauld (2011), Armijo et al., (2010), Deckart et al., (2013), Quiroga (2013), Castro (2012), Villela (2014) and Piquer et al., (2016). Landslides compiled from Antinao & Gosse (2009).

Table 6.1 Table shows the main characteristics of the compiled structures. The kinematics and certainty are marked with different color, as well as the calculated Mw with the Wells and Coppersmith (1994) equations, in which the blue is for Mw: 4.5-5.5; yellow is for Mw: 5.6-6.0; orange for Mw: 6.1-6.5; red for Mw: 6.6-7.0; dark-red for Mw>7.0

| Fault number | Fault name | Strike | Kinematics | Lenght (km) | Dip(°) | Depth (Average) (km) | Depth (Max) (km) | Mw(L) | Mw (RA av) | Mx(RA max) | Certeza | Reference |
|---|---|---|---|---|---|---|---|---|---|---|---|---|
| 1 | T1 | N75°W | nd | 7 | 45 | 15 | 25 | 6,1 | 6,2 | 6,4 | Inferred | Thiele (1980) |
| 2 | T2 | N10°E | nd | 19 | 45 | 15 | 25 | 6,6 | 6,6 | 6,8 | Inferred | Thiele (1980); Wall et al., (1999) |
| 3 | T3 | N10°E | nd | 18 | 45 | 15 | 25 | 6,5 | 6,6 | 6,8 | Inferred | Thiele (1980) |
| 4 | P1 | N26°E | nd | 10 | 45 | 15 | 25 | 6,2 | 6,4 | 6,6 | Observed | Piquer et al., (2016) |
| 5 | T4 | N22°E | nd | 3,5 | 45 | 15 | 25 | 5,7 | 5,9 | 6,1 | Inferred | Thiele (1980) |
| 6 | Co. De Renca | N5°W | Reverse (W-vergent) | 8 | 30 | 15 | 25 | 6,1 | 6,4 | 6,6 | Observed | Selles (1999) |
| 7 | Co. Gordo W | N20°W | nd | 2,5 | 45 | 15 | 25 | 5,5 | 5,8 | 6,0 | Observed | Thiele (1980); Wall et al., (1999) |
| 8 | Co. Gordo E | N25°W | nd | 3 | 45 | 15 | 25 | 5,6 | 5,8 | 6,1 | Observed | Thiele (1980); Wall et al., (1999); Piquer et al., (2016) |
| 9 | Co. Manquehue | N40°W | nd | 3 | 45 | 15 | 25 | 5,6 | 5,8 | 6,1 | Inferred | Thiele (1980); Piquer et al., (2016) |
| 10 | Organillo | N5°W | Normal | 6 | 60 | 15 | 25 | 6,0 | 6,0 | 6,3 | Observed | Wall et a., (1999); SERNAGEOMIN (2003); Piquer et al., (2016) |
| 11 | T5 | N5°W | nd | 2,3 | 45 | 15 | 25 | 5,5 | 5,7 | 5,9 | Observed | Thiele (1980) |
| 12 | La Ermita | N40°E | Strike slip (right lateral) | 9 | 80 | 15 | 25 | 6,2 | 6,2 | 6,4 | Observed | Piquer et al., (2016) |
| 13 | T6 | N10°E | nd | 9 | 45 | 15 | 25 | 6,2 | 6,3 | 6,5 | Inferred | Thiele (1980) |
| 14 | Valle Nevado | N60°W | Reverse (SW-vergent) | 13,5 | 30 | 15 | 25 | 6,4 | 6,6 | 6,8 | Observed | Piquer et al., (2016) |
| 15 | Plaza de los Pumas | N23°W | Reverse (SW-vergent) | 0,8 | 30 | 15 | 25 | 5,0 | 5,4 | 5,6 | Observed | Quiroga (2013) |
| 16 | El Quempo | N5°-8°W | Reverse (E-vergent) | 3,5 | 30 | 5 | 15 | 5,7 | 5,6 | 6,1 | Observed | Quiroga (2013) |
| 17 | El Corinal | NS - N5°W | Reverse (W-vergent) | 30 | 30 | 5 | 15 | 6,8 | 6,5 | 7,0 | Observed | Theiele (1980); Fock (2005); Castro (2014) |
| 18 | El Diablo | NS | Reverse | 60 | 80 | 5 | 15 | 7,1 | 6,5 | 7,0 | Observed | Thiele (1980); SERNAGEOMIN (2003); Fock (2005); Deckart et al., (2013); Piquer et al., (2016); Mardones (2016); Calderon (2013) |
| 19 | High colorado | N5°E | Reverse (E-vergent) | 9 | 30 | 5 | 15 | 6,2 | 6,0 | 6,5 | Observed | Thiele (1980); SERNAGEOMIN (2003) |
| 20 | San Ramon | NNW-NS | Reverse (W-vergent) | 28 | 50 | 15 | 25 | 6,8 | 6,8 | 7,0 | Observed/Inferred | Thiele (1980); SERNAGEOMIN (2003); Fock (2005); Rauld (2006); Armijo et al., (2010); Rauld, (2011); Quiroga (2013); Piquer et al., (2016) |
| 21 | Aguas de Ramon | N5°E | Reverse (W-vergent) | 7 | 30 | 15 | 25 | 6,1 | 6,3 | 6,6 | Observed | Fock (2005); Quiroga (2013) |
| 22 | Co. Provincia | N5°E | Reverse (W-vergent) | 3 | 30 | 15 | 25 | 5,6 | 6,0 | 6,2 | Observed | Thiele (1980); SERNAGEOMIN (2003); Fock (2005) |
| 23 | Ramon | NS | Reverse | 3 | 30 | 15 | 25 | 5,6 | 6,0 | 6,2 | Observed | Fock (2005) |
| 24 | Covarrubias Manzano | N5°E | nd | 20 | 45 | 15 | 25 | 6,6 | 6,6 | 6,9 | Observed | Godoy et al., (1999); SERNAGEOMIN (2003) |
| 25 | Estero Molina | N77°W | Reverse (N-vergent) | 3,5 | 30 | 15 | 25 | 5,7 | 6,1 | 6,3 | Observed | Quiroga (2013) |
| 26 | El Alfalfal | N35°W | Strike slip (left lateral) | 18 | 80 | 5 | 15 | 6,5 | 6,0 | 6,5 | Observed | Thiele (1980); Piquer et al., (2016) |
| 27 | El Alfalfal 2 | N31°W | Strike slip (left lateral) | 14,5 | 80 | 5 | 15 | 6,4 | 5,9 | 6,4 | Observed | Piquer et al., (2016) |
| 28 | Las Yeseras | N5°W | Reverse (E-vergent) | 38 | 30 | 5 | 15 | 6,9 | 6,6 | 7,1 | Observed | Thiele (1980); Fock (2005); Castro (2014); Piquer et al., (2016) |
| 29 | Estero Rabicano | N5°E | Reverse (W-vergent) | 21 | 30 | 5 | 15 | 6,6 | 6,3 | 6,8 | Observed | Thiele (1980); Castro (2014); Fock (2005) |
| 30 | Estero del azufre | N10°E | Reverse (E-vergent) | 17 | 30 | 5 | 15 | 6,5 | 6,3 | 6,7 | Observed | Castro (2014); Fock (2005) |

Table 6.1 continuation.

| | | | | | | | | | | | | |
|---|---|---|---|---|---|---|---|---|---|---|---|---|
| 31 | Colorado bajo | N74°W | Normal | 9 | 60 | 15 | 25 | 6,2 | 6,2 | 6,4 | Observed | Piquer et al., (2016) |
| 32 | Colorado river | N25°E | strike slip (right lateral) | 25 | 80 | 15 | 25 | 6,7 | 6,6 | 6,8 | Inferred | Thiele (1980); Piquer et al., (2016) |
| 33 | Am1 | N40°E | nd | 6 | 45 | 15 | 25 | 6,0 | 6,1 | 6,4 | Inferred | Thiele (1980) |
| 34 | Am2 | N40°E | Normal | 5 | 60 | 15 | 25 | 5,9 | 6,0 | 6,2 | Observed | Thiele (1980) |
| 35 | Am3 | N30°E | nd | 6 | 45 | 15 | 25 | 6,0 | 6,1 | 6,4 | Observed | Thiele (1980); Piquer et al., (2016) |
| 36 | Laguna Negra | N6°E | Reverse (W-vergent) | 18 | 30 | 5 | 15 | 6,5 | 6,3 | 6,7 | Observed | Fock (2005); Castro (2014); Deckart (2013) |
| 37 | Portezuelo de Chada | N6°W | Reverse (W-vergent) | 28 | 30 | 25 | 30 | 6,8 | 7,2 | 7,2 | Inferred | Thiele (1980); Fock (2005) |
| 38 | Pirque | N5°W | Reverse | 7,5 | 30 | 15 | 25 | 6,1 | 6,4 | 6,6 | Inferred | Yañez et al., (2015) |
| 39 | San Roque Wester | N6°E | Reverse (E-vergent) | 15 | 30 | 15 | 25 | 6,4 | 6,7 | 6,9 | Inferred | Thiele (1980); SERNAGEOMIN (2002) |
| 40 | San Roque Eastern | N10°E | Reverse (W-vergent) | 18 | 30 | 15 | 25 | 6,5 | 6,7 | 7,0 | Inferred | Thiele (1980); SERNAGEOMIN (2003) |
| 41 | San José de Maipo | N35°E | Reverse (SE-vergent) | 0,3 | 30 | 15 | 25 | 4,5 | 5,0 | 5,2 | Observed | Lavenu & Cembrano (2008); Piquer et al., (2016) |
| 42 | Am4 | N42°E | nd | 5 | 45 | 15 | 25 | 5,9 | 6,1 | 6,3 | Inferred | Thiele (1980) |
| 43 | Am5 | N38°-50°E | nd | 13 | 45 | 10 | 25 | 6,4 | 6,3 | 6,7 | Inferred | Thiele (1980) |
| 44 | Oblique Yeso | N58°W | Strike slip (left lateral) | 11 | 80 | 5 | 15 | 6,3 | 5,8 | 6,2 | Observed/Inferred | Piquer et al., (2016) |
| 45 | Chacayes - Yesillo | N12°E | Reverse (W-vergent) | 40 | 80 | 5 | 15 | 6,9 | 6,3 | 6,8 | Observed/Inferred | Fock (2005); Deckart (2013); Calderon (2013); Mardones (2016); Piquer et al., (2016) |
| 46 | Co. Del principal | N5°E | nd | 6 | 45 | 15 | 25 | 6,0 | 6,1 | 6,4 | Inferred | Thiele (1980) |
| 47 | Huelquen Western | N31°E | Reverse (W-vergent) | 9 | 30 | 15 | 25 | 6,2 | 6,5 | 6,7 | Observed | Piquer et al., (2016) |
| 48 | Huelquen Center | N27°E | Reverse (W-vergent) | 9 | 30 | 15 | 25 | 6,2 | 6,5 | 6,7 | Observed | Piquer et al., (2016) |
| 49 | La Retamilla | NS | nd | 10 | 45 | 15 | 25 | 6,2 | 6,4 | 6,6 | Inferred | Piquer et al., (2016) |
| 50 | Huelquen Easterm | N18°E | Reverse (W-vergent) | 9 | 30 | 15 | 25 | 6,2 | 6,5 | 6,7 | Observed | Thiele (1980); Piquer et al., (2016) |
| 51 | Co Blanco | NS | nd | 8 | 45 | 15 | 25 | 6,1 | 6,3 | 6,5 | Inferred | Thiele (1980) |
| 52 | Co. Euskadi | N80°E | nd | 6,5 | 45 | 15 | 25 | 6,0 | 6,2 | 6,4 | Observed | Thiele (1980); Piquer et al., (2016) |
| 53 | Co Pangal Western | N17°E | Reverse (W-vergent) | 3 | 30 | 15 | 25 | 5,6 | 6,0 | 6,2 | Observed | Villela (2014); Piquer et al., (2016) |
| 54 | Co. Pangal Eastern | N14°W | Reverse (E-vergent) | 6 | 30 | 15 | 25 | 6,0 | 6,3 | 6,5 | Inferred | Fock (2005); Villela (2014) |
| 55 | El Ingenio Western | N15°W | Reverse (E-vergent) | 5 | 30 | 15 | 25 | 5,9 | 6,2 | 6,4 | Observed | Fock (2005); Villela (2014); Piquer et al., (2016) |
| 56 | El Ingenio Eastern | N5°E | Reverse (W-vergent) | 1 | 30 | 15 | 25 | 5,1 | 5,5 | 5,7 | Observed | Villela (2014); |
| 57 | Las Melosas | N61°E | Strike slip (right lateral) | 4 | 80 | 5 | 15 | 5,8 | 5,4 | 5,8 | Observed | Thiele (1980); Piquer et al., (2016) |
| 58 | San Gabriel | N44°W | nd | 2 | 45 | 5 | 15 | 5,4 | 5,2 | 5,7 | Observed | Thiele (1980); Piquer et al., (2016) |
| 59 | Yeso river | N30°-60°E | Right lateral | 30 | 80 | 5 | 15 | 6,8 | 6,2 | 6,7 | Observed/Inferred | Piquer et al., (2016) |
| 60 | Meson Alto | N22°W | Strike slip (left lateral) | 4 | 80 | 5 | 15 | 5,8 | 5,4 | 5,8 | Observed | Thiele (1980); Piquer et al., (2016) |
| 61 | Baños Morales | N21°E | Reverse (E-vergent) | 17 | 80 | 5 | 15 | 6,5 | 6,0 | 6,4 | Observed | Thiele (1980); Fock (2005); Piquer et al., (2016); Calderon et al., (2013) |
| 62 | Punta Zanzi | N15°E | Reverse (E-vergent) | 10 | 80 | 5 | 15 | 6,2 | 5,7 | 6,2 | Observed | Thiele (1980); Calderon (2013); Mardones (2016) |
| 63 | Baños Colina | N20°E | Reverse (E-vergent) | 18 | 80 | 5 | 15 | 6,5 | 6,0 | 6,5 | Observed | Thiele (1980); SERNAGEOMIN (2003); Fock (2005) |
| 64 | El Arrayan | N°70W | Strike slip (right lateral) / Reverse (SW-vergent) | 12 | 75 | 15 | 25 | 6,4 | 6,3 | 6,5 | Observed | This work |
| 65 | Estero Coyanco | N15°W | Reverse (E-vergent) | 0,15 | 65 | 15 | 25 | 4,1 | 4,5 | 4,7 | Observed | This work |

Table 6.2 Estero Coyanco fault expected Mw estimations in base of Wells and Coppersmith (1994) empirical equations using Maximum displacement (MD) as a key fault parameter. Two different cases are develop, with the minimum and the maximum displacement observed. Letters "a" and "b" are the Wells and Coppersmiths (1994) equations constants.

| Estero Coyanco fault | MD | a | b | Mw |
|---|---|---|---|---|
| Case 1 | 1 | 6,69 | 0,74 | 6,7 |
| Case 2 | 2 | 6,69 | 0,74 | 6,9 |

### 6.2.2 All faults no-segmentation / Surface rupture length as a key parameter

Every fault is considered as composed by only one segment. Faults composed by observed and inferred segment will count as only one fault with a length value as the sum of every segment. This scenario allows us to calculate a full length rupture scenario for each fault. The fault parameter used to estimate Mw is the "Surface rupture length (SRL)" in km. The used equation is for all type of faults (ie, normal, reverse, strike slip), because Wells and Coppersmith (1994) indicates that the regression for all slip type is the most appropriate. Legend is the same for the Figure 6.1. Kinematics are omitted to highlight the fault extend and the seismic potential. Figure 6.2 shows the calculated Mw for each fault.

The used Wells and Coppersmith (1994) equation is:

M = a + b*log (SRL); a=5.08; b=1.16; for fault with SRL range from 1.3 to 432.0 km.

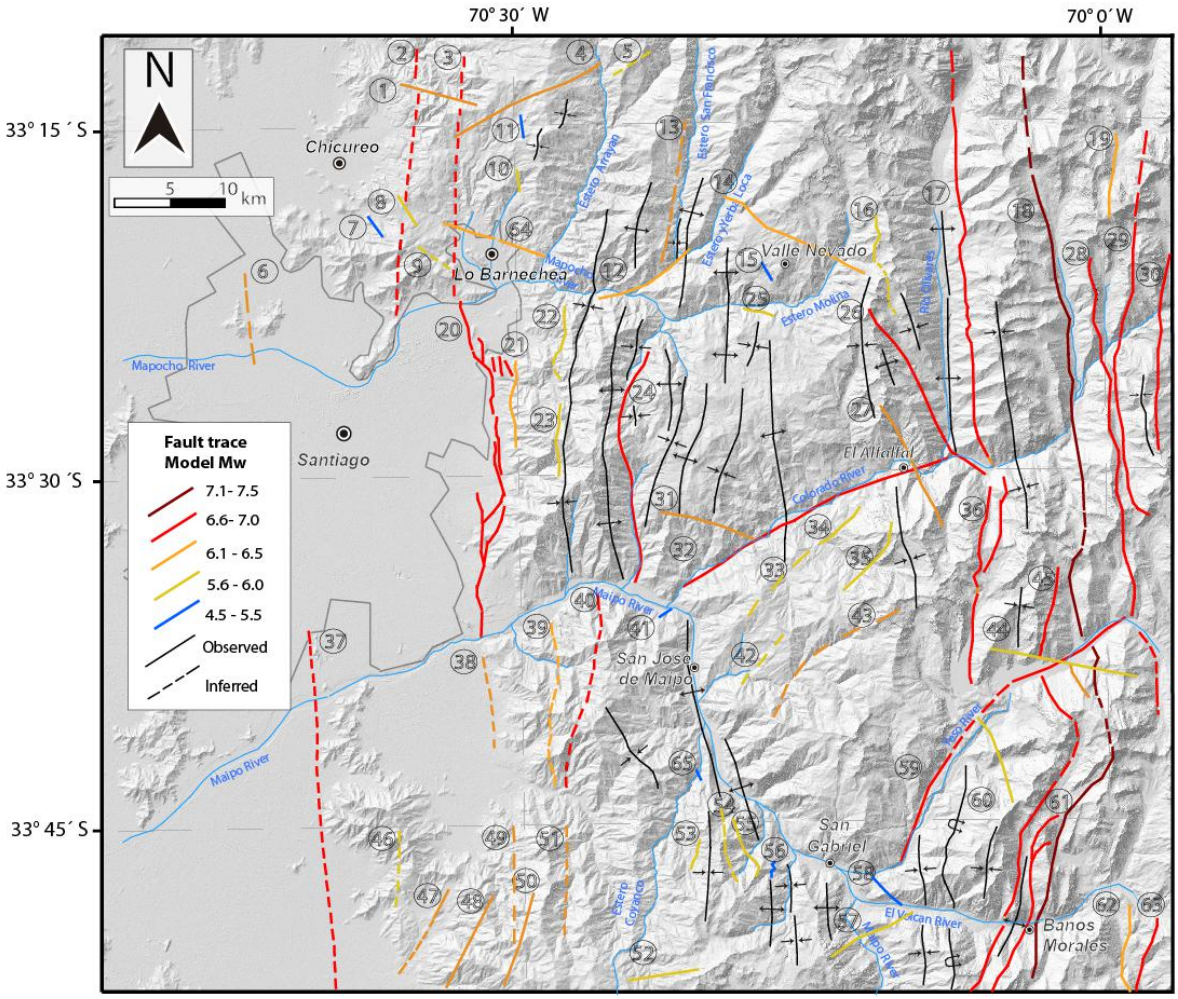


Figure 6.2 Structural map showing faults color coded which are assigned in base of expected Moment Magnitude (Mw) based on Wells and Coppersmith (1994). Faults are considered as composed by only one segment and "surface fault length" as a key parameter. Numbers and colors are the same for the Table 6.1.

### 6.2.3 All faults with segmentation / Surface rupture length as a key parameter

In this section, I will separate faults in segments of different confidence level. This scenario allows us to calculate an expected Mw for just each segment rupture and not a full length fault rupture. The fault parameter used to estimate Mw is the "Surface rupture length (SRL)". The used equation is for all type of faults (ie, normal, reverse, strike slip), because Wells and Coppersmith (1994) indicates that the regression for all slip type is the most appropriate. Legend is the same for the Figure 6.1. Kinematics are omitted to highlight the fault extend and the seismic potential. Figure 6.3 shows the calculated Mw for each fault.

The segmented faults are:

(1) N°17 El Coroinal fault, separated in two segments, one northern inferred and one southern observed.
(2) N°18 El Diablo Fault, separated in 3 observed segments separated by minor inferred segments;
(3) N°20 San Ramon Fault, separated in three segment defined by Armijo et al., (2010) and minor segments in Cerro los Rulos (to the west of fault N°21)
(4) N°28 Las Yeseras fault, separated in one northern observed segment and other southern inferred segment.
(5) N°29 Estero Rabicano fault, separated in two segments, one northern inferred segment and other observed southern segment.
(6) N°45 Chacayes-Yesillo fault, separated in three observed segments and one inferred.
(7) N°59 Yeso river fault, separated in two observed and one inferred segments.
(8) N°64, El Arrayan Fault, separated in two observed segment, the segmentation is not in base of degree of certain, instead is segment because of the nature and geometry of the fault (See Chapter 3 in this work)

The Wells and Coppersmith (1994) equation is:

$M = a + b*\log(SRL)$; with a=5.08; b=1.16

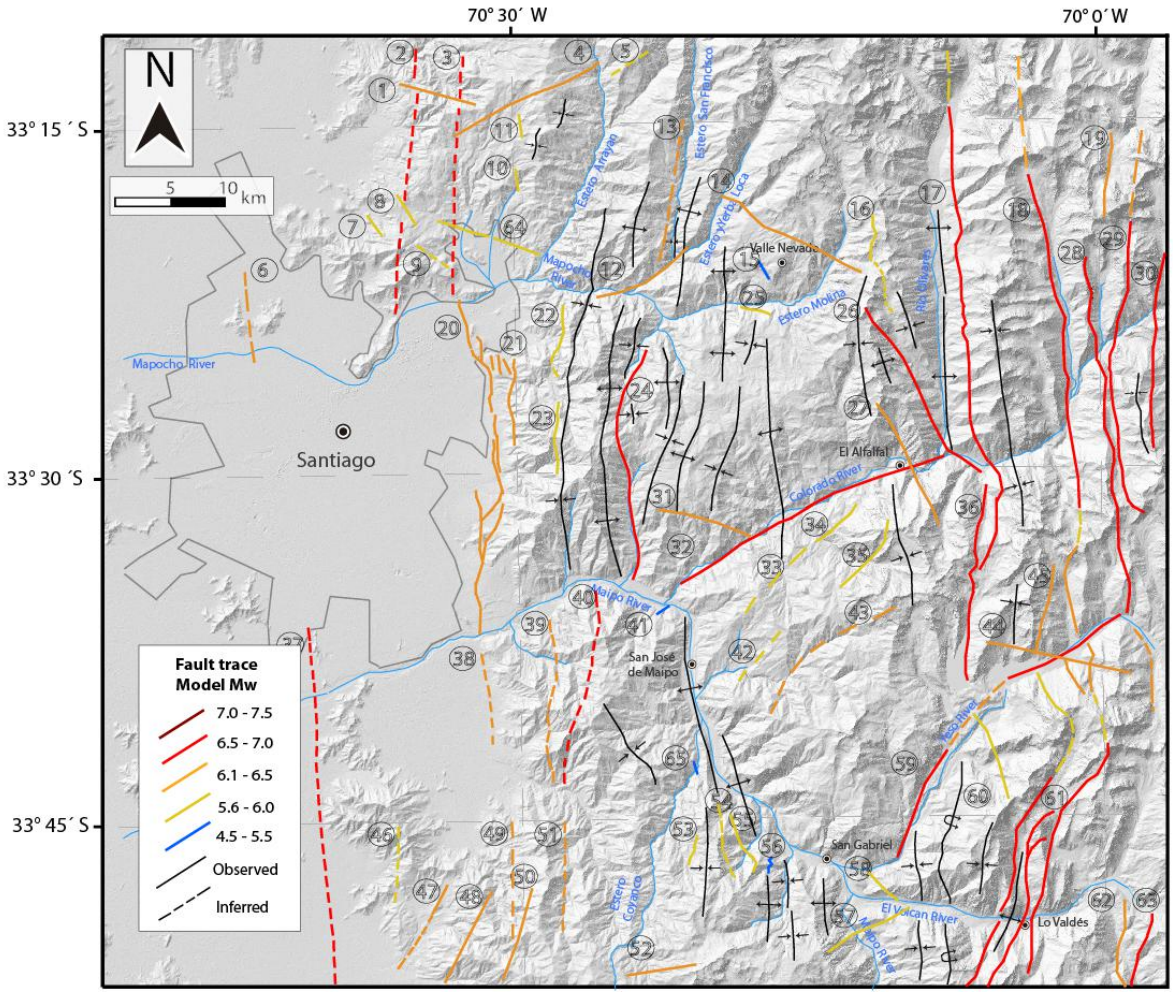


Figure 6.3 Structural map showing faults color coded which are assigned in base of expected Moment Magnitude (Mw) based on Wells and Coppersmith (1994). Fault are considered as composed by more than one segment (when it correspond) and "surface fault length" as a key parameter, thus overall Mw values are less than those in Fig.6.1. Numbers and colors are the same for the Table 6.1.

### 6.2.4 All faults no-segmentation / Rupture area as a key parameter / Average seismogenic depth

In this model, each fault is considered to be composed by only one segment. Faults composed by observed and inferred segment will count as only one fault with a length value being the sum of each segment. This scenario allows us to calculate a full length rupture scenario for each fault. The fault parameter used to estimate Mw is the "Rupture area (RA)" in $km^2$. The equation is for all type of faults (ie, normal, reverse, strike slip), because Wells and Coppersmith (1994) indicates that regression for all slip type. Legend is the same for the Figure 6.1. Kinematics are omitted to highlight the fault extend and the seismic potential. Figure 6.4 shows the calculated Mw for each fault.

The geometric parameter for the faults are extracted from the author´s work, like fault length, but fault dip is rarely reported in the text or in the maps used to make this compilation. The mapped fault trace intrinsically contain the dip of the fault, but unfortunately for scaling problems there is no good degree of certainty for the extracted data, thus when no dip data are obtained average 30° dip are assigned for reverse faults, 60° for normal faults, 80° for strike-slip faults and 45° for no-kinematics faults. Field work in the Rio Volcan, the El Diablo Fault (N°18), Chacalles-Yesillo Fault (N°45), the Baños Morales Fault (N°61), Punta Zanzi Fault (N°62) and the Baños Colina Fault (N°63), allow us to have better constrained dip data, which are all nearly vertical faults. The San Ramon Fault (N°22) has dip of 50° (Perez et al., 2014). Two seismic depths are used for each seismicity band defined by Perez et al., (2014). Depth values are extracted and combined from the USGS and Perez et al., (2014) which range from 5 to 25 km. This approach uses the average depth for each band: 15 km for the western band and 5 km for the eastern. For Cuesta de Chada Fault (N°37), located in the Pirque area, average 25 km seismic depth its used due to the presence of the Santa Rosa Cluster (Barrientos et al., 2004; Perez et al., 2014).

The used Wells and Coppersmith (1994) equation is:

$M = a + b*\log(RA)$; $a=4.07$; $b=0.98$

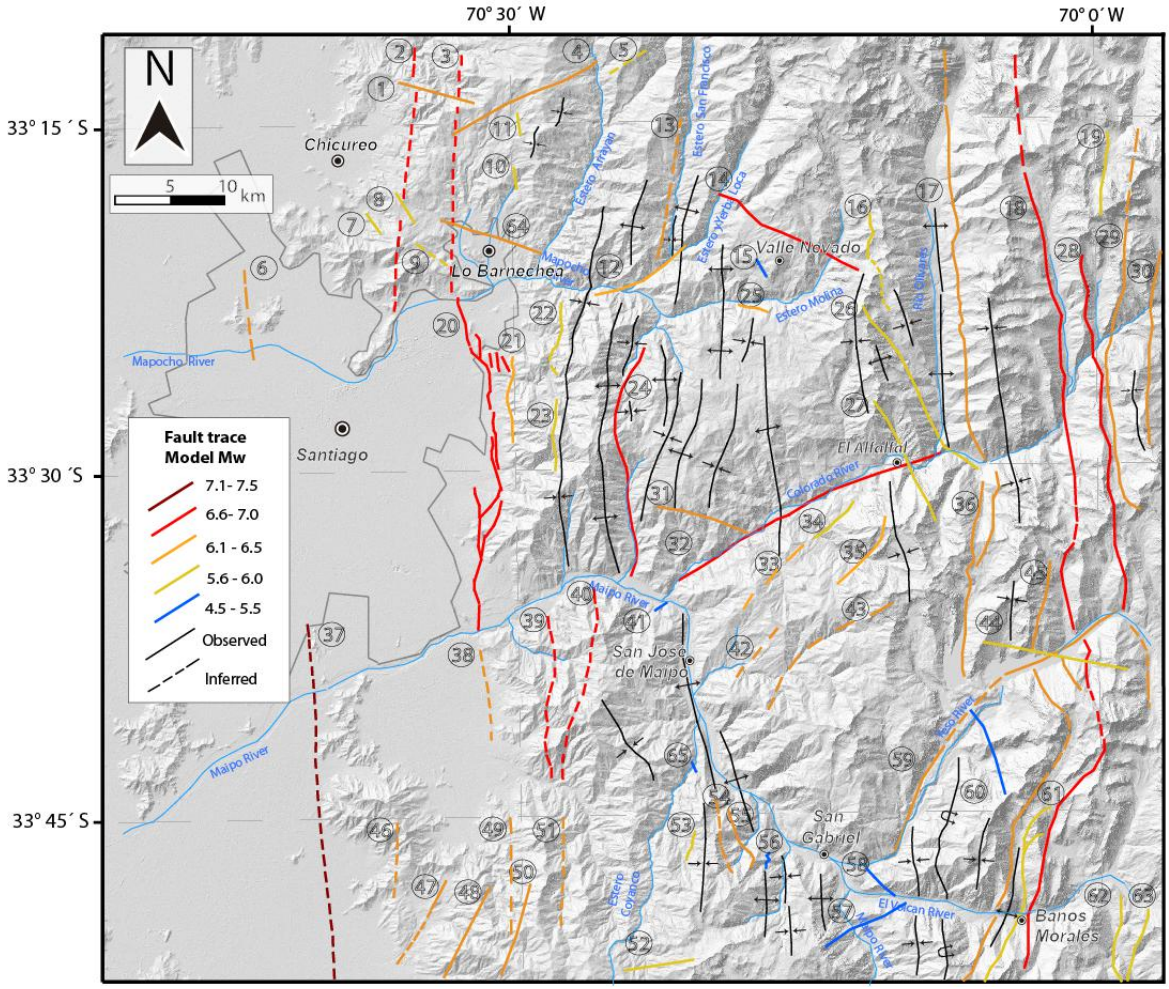


Figure 6.4 Structural map showing faults color coded which are assigned in base of expected Moment Magnitude (Mw) based of Wells and Coppersmith (1994). Faults are considered as composed by only one segment and "rupture area" (calculated in base of average seismogenic depth) as a key parameter. Numbers and colors are the same for the Table 6.1.

### 6.2.5 All faults no-segmentation / Rupture area as a key parameter / Maximum seismogenic depth

Every fault is considered as composed by only one segment. Faults composed by observed and inferred segment will count as only one fault with a length value as the sum of every segment. This scenario allows us to calculate a full length rupture scenario for each fault. The fault parameter used to estimate Mw is the "Rupture area (RA)" in $km^2$. The used equation is for all type of faults (ie, normal, reverse, strike slip), because Wells and Coppersmith (1994) indicates that the regression for all slip type is appropriate. Legend is the same for the Figure 6.1. Kinematics are omitted to highlight the fault extend and the seismic potential. Figure 6.5 shows the calculated Mw for each fault.

The geometric parameters for the fault are extracted from the author´s work, like fault length, but fault dip is rarely reported in the text or in the maps used to make this compilation. The mapped fault trace intrinsically contain the dip of the fault, but unfortunately for scaling problems and simplified mapping, there is no good degree of certainty for the extracted data, thus when dip data are no directly expressed, average 30° dip are assigned for reverse faults, 60° for normal faults, 80° for strike-slip faults and 45° for no-kinematics faults. Field work in the Rio Volcan, the El Diablo Fault (N°18), Chacalles-Yesillo Fault (N°45), the Baños Morales Fault (N°61), Punta Zanzi Fault (N°62) and the Baños Colina Fault (N°63, allow us to have solid dip data, which are all nearly vertical faults. The San Ramon Fault (N°22) also has dip of 50° (Perez et al., 2014). Two seismic depths are used for each seismicity band defined by Perez et al., (2014). The depths values are extracted and combined from the USGS and Perez et al., (2014). This approach uses the maximum depth for each band: 25 km for the western Band and 15 km for the eastern. For Cuesta de Chada Fault (N°37), located in the Pirque area, maximum 30 km seismic depth its used due to the presence of the Santa Rosa Cluster (Barrientos et al., 2004; Perez et al., 2014)

The used Wells and Coppersmith (1994) equation is:

$M = a + b*\log(RA)$; $a=4.07$; $b=0.98$

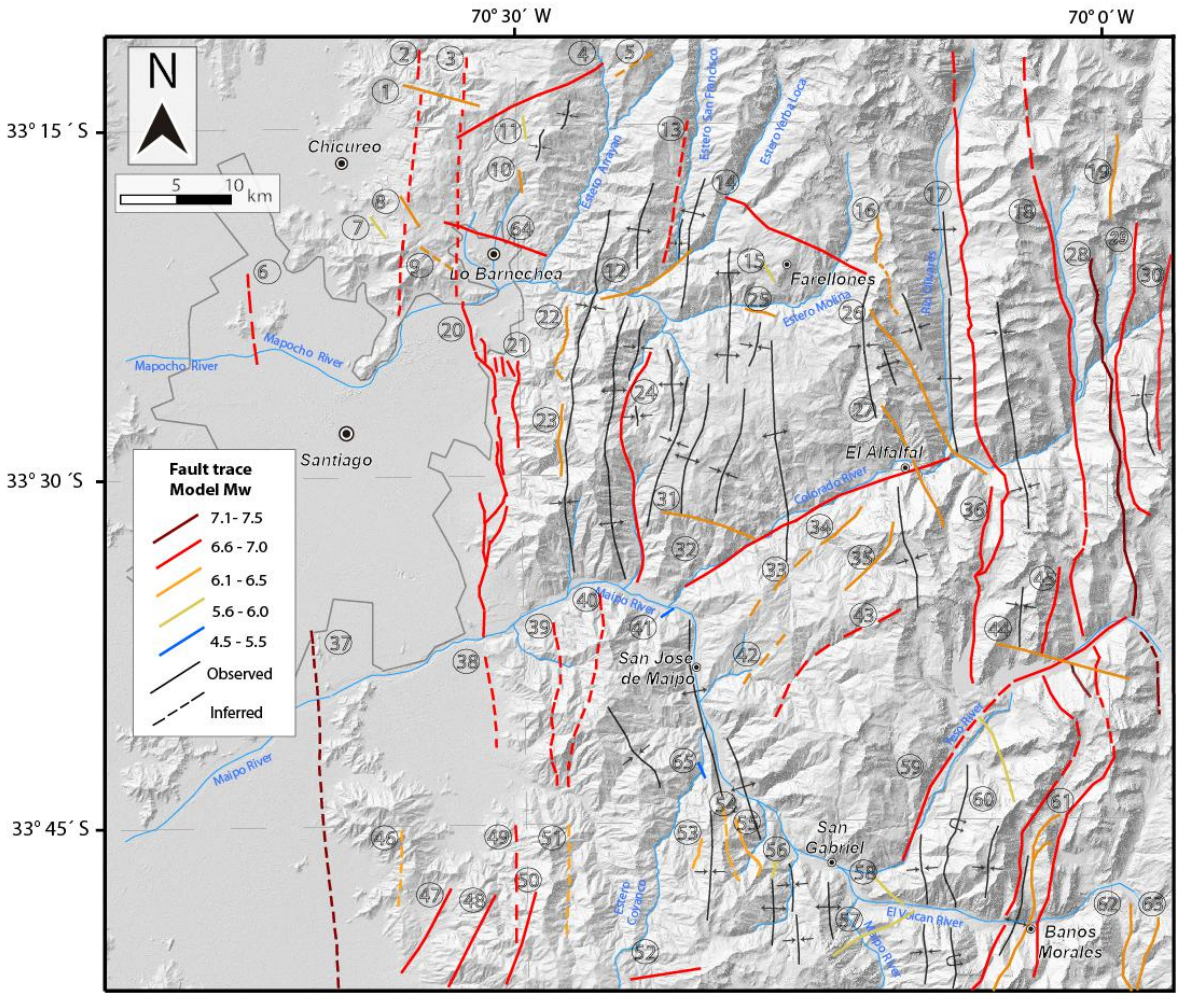


Figure 6.5 Structural map showing faults color coded which are assigned in base of expected Moment Magnitude (Mw) based of Wells and Coppersmith (1994). Fault are considered as composed by only one segment and "rupture area" (calculated in base of maximum seismogenic depth) as a key parameter. Numbers and colors are the same for the Table 6.1.

## 6.3 Moment Magnitude Potential of Potentially Active Faults near Santiago, Chile summary

The different analyses show us the variable spectrum of expected Mw for each fault in the Metropolitan region at Cordilleran area, for different rupture scenario and different earthquake fault parameters. Considering all the rupture scenarios the estimated Mw range from 4.1 to 7.2

The result shows that, independently of the fault segmentation and the seismic depth, the faults capable for produce a seismic event with Mw>6.5 are located mainly in the western flank of the Principal Cordillera and in high Range less than 15 km to the west from the Chile-Argentina border. The central part of the Principal Cordillera, where NW and NE striking fault dominates, ruptures from Mw: 5.6 – 6.5 are expected.

At the western flank of the Principal Cordillera, the faults with higher potential Mw (>6.5) are N°2, N°3, N°20, N°24, N°37 and N°40. However, just the fault N°20 (San Ramon Fault) and the fault N°24 (Covarrubias-Manzano fault) are observed fault, the others are only inferred faults. In the eastern side of the Principal Cordillera, near the Chile-Argentina border, the most hazardous structures are the faults N°18, N°28, N°29, N°36, N°45, N°59. All of these faults are mainly observed.

If we star to analyze and compare the different scenarios the following statement are derived:

(1) Using Surface rupture length (SRL) as a key parameter, when fault are separated in segment, the fault N°18 (El Diablo Fault), N°20 (San Ramon Fault) and N°45 (Chacayes-Yesillo) reduce their expected Mw. However, the N°18 and N°45 are still able to produce seismic events with Mw 6.5 - 7.0 ruptures; however, minor segments of these fault are capable to produce ruptures with Mw: 6.1 - 6.5 around the Yeso river dam. The N°20 reduces it expected Mw 6.6 – 7.0 to Mw 6.1 - 6.5. The other faults doesn´t change in a significate way.

(2) Using average Rupture area (RA) as a key parameter, we can notice that the western flank of the Principal Cordillera remains as a hazardous zone (Mw>6.5). In fact, this area increase the expected Mw, as we can see in faults N°37 (Mw 7.0 – 7.5), N°39 (Mw 6.6 – 7.0) and N°46° (Mw 6.0 – 6.5). At the eastern side of the Principal Cordillera near the Chile-Argentina border, fault reduces their hazard compared to the estimation using Surface Rupture length, been only the fault N°18 and N°28, the ones expected to produce ruptures with Mw 6.6 – 7.0. The other fault, in general are expected to produce seismic events with Mw 6.1 - 6.5. This is because at the eastern side of the Principal Cordillera, shallower seismic depth (5 km) is used, thus implying minor Rupture area and lower Mw are obtained.

(3) Using maximum Rupture area as a key parameter, the most hazardous scenario is shown. This scenario indicates that only eight faults are expected to produce ruptures with Mw < 6.1. The faults with expected ruptures with Mw 6.5-7.0 are twenty-six, and mostly located in the western and eastern sides of the Principal Cordillera, however the central part of the Principal Cordillera also present at least 5 structures with expected Mw 6.5-7.0, more than in any other scenario.

(4) The seismic potential of individual faults, using different Wells and Coppersmith (1994) empirical relations, indicates for the whole fault population in the cordilleran area of the Metropolitan region, that the structures capable to produce the higher rupture Mw locates mainly at the western and eastern flanks of the Principal Cordillera where mainly N-S trending structures are located. This is primary because here the faults were continued and prolonged along different E-W river valleys, and therefore, a longer fault trace length is observed yielding higher SRL and RA affecting directly the Mw calculus. Nevertheless, at the western flank most of the structures are inferred, thus, the analysis in this area has a lower degree of certainty compared with the mostly N-S trending faults locate near the Chile-Argentina border where numerous authors (see Table 6.1) had observed and mapped this faults. This higher expected Mw are well spatially correlated with the shallow seismicity (Barrientos et al., 2004; Pérez et al., 2014); which also suggest these areas as the most hazardous zones.

(5) The central part of the Principal Cordillera presents mainly NW and NE trending faults with shorter fault trace length, which is reflected in lower SRL and RA, and thus, lower expected magnitude ranging in general Mw 5.6-6.5. Disperse seismicity is present in this area, which combined with the lower Mw expected let us establish this area as the less hazardous zone.

(6) The segmentation of fault traces reduces the hazard directly at the San Ramon fault and also in the high range where long continued faults are mapped, although, the rupture Mw expected are 6.5 – 7.0 for the structures near the Chile-Argentina border. The lower Mw expected near the Yeso River dam could be attributable to the inferred fault segment near the dam, probably caused by more erosion and/or poor accessibility in the area.

(7) The most variable results are produced when I use the RA as a key fault parameter. The variable seismic depth used shows us the impact for the Mw estimations, in which changes in the seismic depth affect directly the RA, and therefore, the expected Mw. The Figure 6.4 show us the lowest expected Mw (most conservative scenario) for most of the faults, using average seismic depth, meanwhile Figure 6.5 shows us the maximum expected Mw (worst case scenario) using maximum seismic depth. It worth to notice that this Mw estimation in base of RA also takes into account the SFL; in this case we only use no-segmentation fault, because of the low change of Mw estimation using segmented faults (see Table 6.1 and Fig.6.2 and 6.3). For the

estimation with the average RA (Fig. 6.4), even though the lowest Mw are expected, the shallower hypocenters implies higher expected shaking, therefore still been a dangerous scenario.

Analyzing the two newly mapped structures in this thesis, the El Arrayan fault (N°64), and the Estero Coyanco fault (N°65), I can say:

The El Arrayan Fault (N°64) can produce variable Mw depending on the rupture scenario. When I use the maximum RA as a key fault parameter, the El Arrayan Fault can produce seismic event with Mw 6.6-7.0, but when I use the SRL as a key fault parameter and the fault separated in segments, the fault can produce seismic events with Mw 5.6 -6.0. Independently of the estimated Mw, as the El Arrayan fault runs though populated area of Santiago (similar as N°20 San Ramon fault) it presents an important seismic hazard, making this structure a very hazardous fault.

On the other hand, the Estero Coyanco Fault (N°65), due to the poorly constrained fault trace, and therefore, short fault trace length, the estimations yield Mw<5.5 in every case, moreover estimations yield Mw<4.8 for all the rupture scenarios. But, using Maximum displacement as a key fault parameter, Mw 6.7-6.9 are expected (see Table 6.2). This fault locates less than 15 km from San José de Maipo, the most populated locality in the Maipo Valley, and with seismic depth of average 15 km, thus it can have important social and economic impact. More analysis should be done regarding the Estero Coyanco fault extend to better constrain the related seismic hazard.

Other faults that runs through populated areas or built environments areas are faults N°6 (Cerro de Renca fault) and N°37 (Portezuelo de Chada fault). These faults pass through Renca and Pirque areas of urban Santiago. The Portezuelo de Chada fault, in any case is expected to produce seismic events with Mw > 6.6, thus this is a very hazardous structure. The Cerro de Renca fault is expected to produce ruptures with Mw between 6.1 - 7.0, and runs directly through an urban area of Santiago, thus can produce important social impact. This fault should be focus of more neotectonic studies because of the Mw>6.1 and the location of the fault trace in populated areas.

Inside Maipo Valley, the most hazardous zone is Baños Morales locality, because in here, faults N°18, N°45 and N°61 pass less than 3 km from the locality, and this fault in most of the scenarios can produce seismic events with Mw 6.1 – 6.5, and in the worst case scenario these three fault are expected to produce ruptures with Mw 6.6 -7.0, moreover the fault N°18 (El Diablo fault) can produce ruptures with Mw> 7.0. Therefore this is a key area for seismic hazard. Considering the location of faults near others localities like San Gabriel, or the El Ingenio, no mayor fault pass through them, and the nearest faults are expected to produce ruptures with Mw 4.5-6.5. However less than 10 km SE of San Gabriel, the Mw 6.3 1958 Las Melosas earthquake occurred at 8 km depth (Alvarado et al., 2009), causing

important damage. This shows that even though the expected Mw are not higher than 6.5, the shallow hypocenter implies important seismic hazard.

The limitation of the analysis lies in the fact that most of the dips data for the faults are assigned in a general manner and not by detailed structural analysis. As I mentioned before, a change in the RA reflects important calculus variations, that´s why more detailed structural analysis should be done for each mapped fault to get a more precise geometrical constrains.

Second, we assume all the faults are "potentially active", but there is only evidence of recent motion for two of them due to a lack of investigation in this topic. Thus, we know where the potentially more hazardous structures are, and future neotectonic studies can focus on prove the recent motion for these faults, and in that way, complete and strengthen this seismic hazard analysis.

I suggest that the fault that should be studied in the future, with the goal to characterize their behavior, and evaluate their Quaternary motion, should be numbers: 2, 3, 4, 6, 13, 14, 21, 17, 18, 21, 24, 30, 32, 36, 37, 38, 39, 40, 45, 59, 61, 62, and 63, because this are the ones with higher expected in general Mw > 6.6 and/or they pass directly or less than 5 km from populated areas.

## 6.4 Relationship with potentially active faults and landslides

The spatial relation between crustal faults and landslides is very important because seismic events produced by rupture in crustal fault can be an important triggered for landslides.

For this analysis I will use the Antinao & Gosse (2009) landsilde inventory, the compiled structural data base of this work and the potentially moment of magnitude (Mw) derived from the rupture scenario using no-segmented faults, and Surface rupture length as a key parameter because it is the most representative scenario showing not the most conservative neither the worst case scenario. Figure 6.6 shows the previous mentioned features.

Most of landslides are located in the western flank of the Principal Cordillera, from Rio Maipo to the north, and more densely located north Mapocho River. Also, along river valley as Colorado River, Olivares River and Yeso River, numerous landslides are observed. Less landslides are located in the eastern side of the Principal Cordillera near the Chile-Argentina border. These landslides are very close located to important crustal faults similar as Antinao & Gosse (2009) affirmed.

Biggest landslides (10-25 $km^2$) are located mainly along river valley, and north of Lo Barnechea. Long length faults (>25 km) are reported along Colorado and Yeso River (N°32 and N°59), but for Lo Barnechea only 12 km long fault (N°64) is reported. The area with bigger (in length) faults is in the eastern side of the Principal Cordillera, where scarce landslides are reported, except for the El Volcan River, where landslides up to 10 $km^2$ are presented. This could be a consequence of the higher altitudes of the mountain chain, where high erosion can remove the landslides deposits.

North of Rio Mapocho, between Lo Barnechea and Estero Yerba Loca, landslides clustered trending NW-SE whit sizes of 10-25 $km^2$ an even more than 25 $km^2$ are located. In this area fault N°14 has the same orientation of the cluster, locates in the SE prolongation of it, and is capable to produce Mw 6.1-6.5. Thus, this fault can be a potentially trigger for this landslide, unfortunately there is no evidence for recent motions of this fault. Another fault that can potentially trigger these landslide is the Fault N°64, because it presents the same orientation of the cluster, the clusters locates at the fault hangingwall and the fault is capable to produce ruptures of MW 6.1-6.5. Additionally, recent motion (Early-Middle Pleistocene) was reported for this fault (See Chapter 3 this work), defining it as "active" and therefore, more likely to been responsible for the needed shaking to trigger the landslide. Other faults in the area, like faults N° 1, N°2 and N°3 can also produce Mw 6.1 – 6.5, but unfortunately this faults are inferred (N°3 and N°2), have no kinematic reported (N°1) and have been not reported as active. The other faults in the area presents orientations not compatible with the landslide or are expected to produce Mw < 6.1.

In the San Ramon Range the landslides present N-S trending, which is well in agreement with the N-S orientated faults in the area (N°20, N°22, N°23 and N°24). Only fault N°20 (San Ramon fault) was reported as active, and the landslide locates at the hangingwall, thus this is a potentially trigger structure for the landslides. The faults (N°22, N°23 and N°24 are closely located to the landslides and capable to produce ruptures of Mw 5.6-7.0, but as they are not "active" there is less probably for been the triggers.

Along Colorado River valley, Olivares River valley and Yeso River valley numerous landslides are located, ranging their size from >1.5 $km^2$ to 10-25 $km^2$. Fault with length more than 25 km long (faults N° 17, N°32 and N°59) and capable to produce ruptures with Mw 6.6-7-0 are also located along this rivers, been closely related to the landslides and thus potentially triggers for them. Unfortunately these faults are not reported as active. In Colorado River, faults N°33 and N°34 are located along landslides, but as this faults have no kinematics and one of them (N°33) is just inferred, there is less probability of been the trigger of the landslides.

In the Maipo River, near San Gabriel and El Ingenio, landslides along river valley are also reported. This landslides appear to be spatially related only to minor faults capable to produce ruptures of Mw 4.5-6.0. Additonally this faults are not reported as active (N°53-56). But in the Estero Coyanco, fault N°65 (Estero Coyanco fault) was recently reported as active (Chapter 4 this thesis), the length of the fault is very short and capable to produce Mw < 4.8 in base of Surface rupture length (SRL) but Mw 6.7 – 6.9 in base of Maximum displacement (MD) (See Table 6.2). The prolongation of this fault trace to the SE coincides with the location of the landslides. If this fault can be prolonged to the SE by more detailed mapping, it could be a very good candidate as a trigger for the landslides.

In the El Volcan river valley, landslides up to 10 $km^2$ are reported, here at least three faults are capable to produce ruptures with Mw 6.5-7.0 and one (N°18 El Diablo fault) capable to produce Mw > 7.0. The fault N°18 by kinematic analysis (Chapter 5 this work) is inferred to be potentially active, and thus the most probably trigger for this landslides.

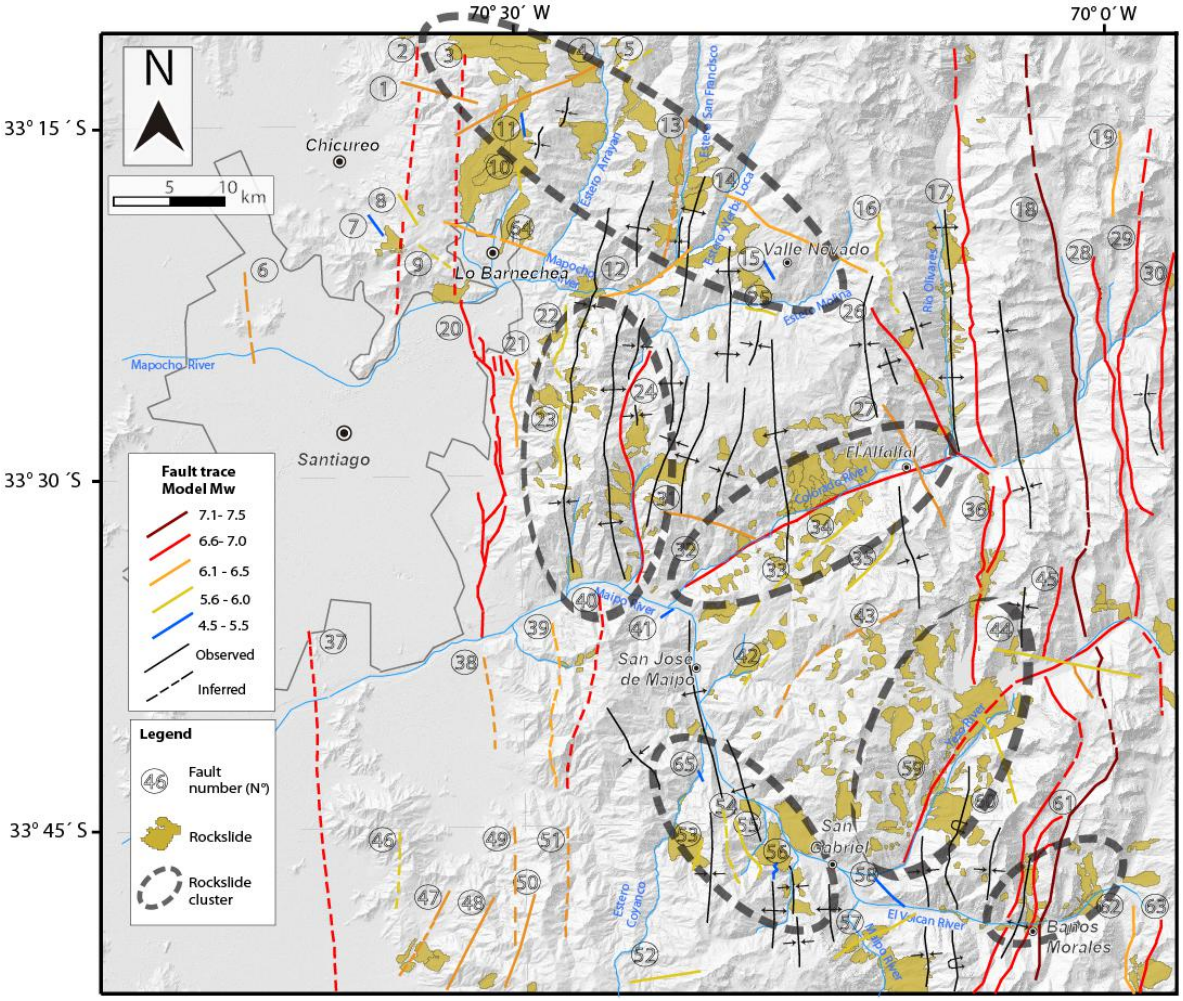


Figure 6.6 Structural map showing faults color coded which are assigned in base of expected Moment Magnitude (Mw) based on Wells and Coppersmith (1994). Faults are considered as composed by only one segment and "surface fault length" as a key parameter. Numbers and colors are the same for the Table 6.1. Rockslide inventory from Antinao & Gosse (2009) is shown in orange-yellow polygons. Clusters of rockslides are indicated by dashed ellipses.

As summary, important landslides locates along regional-scale faults, suggesting a close relationship between both parameters as well as the Antinao & Gosse (2009) hypothesis. The estimated Mw of the faults are in agreement with these faults as a trigger mechanism for the landslides clusters. Actives faults, as N°20 San Ramon fault, N°64 El Arrayan fault, N°65 Estero Coyanco fault, and potentially active N°18 El Diablo fault, locates very close to important landslide clusters, supporting the idea of co-seismic landslides. However there is still an important number of long length faults with potentially high Mw (>6.0) that are not related to landslides, this could be because this faults are not active or because erosion have remove the coseismic landslides at the eastern side of Principal Cordillera.

## 6.5 PGA Estimation for EAF

Based on the length of characteristic earthquake rupture and fault geometry, we estimate the seismic hazard by calculating the corresponding peak ground acceleration (PGA). Commonly spectral shape, moment of magnitude , distance, depth, style of faulting, directivity effects, shear-wave velocity ($VS_{30}$), basin depth variations and hanging-wall effects, are usually used to estimate the attenuation (Chiou and Youngs 2014).

In this work we used the attenuation model from Sadigh et al., (1997) which is appropriated for crustal earthquake. We use a grid of 500 m spacing, we will consider as input parameter moment of magnitud, shortest distance to fault at surface and style of faulting. Site effects are not considered because the focus of this work its to provide a first order seismic hazard scenario.

In this study we will consider the rupture scenario based on the surface geometry of the EAF, i.e. we will consider each segment to rupture individually because we don´t have evidence to asume them to rupture together, that way we use a Mw. 6.4 (See Chapter 3). PGA estimations for each grid point correspond to the maximum PGA among all probable rupture scenarios.

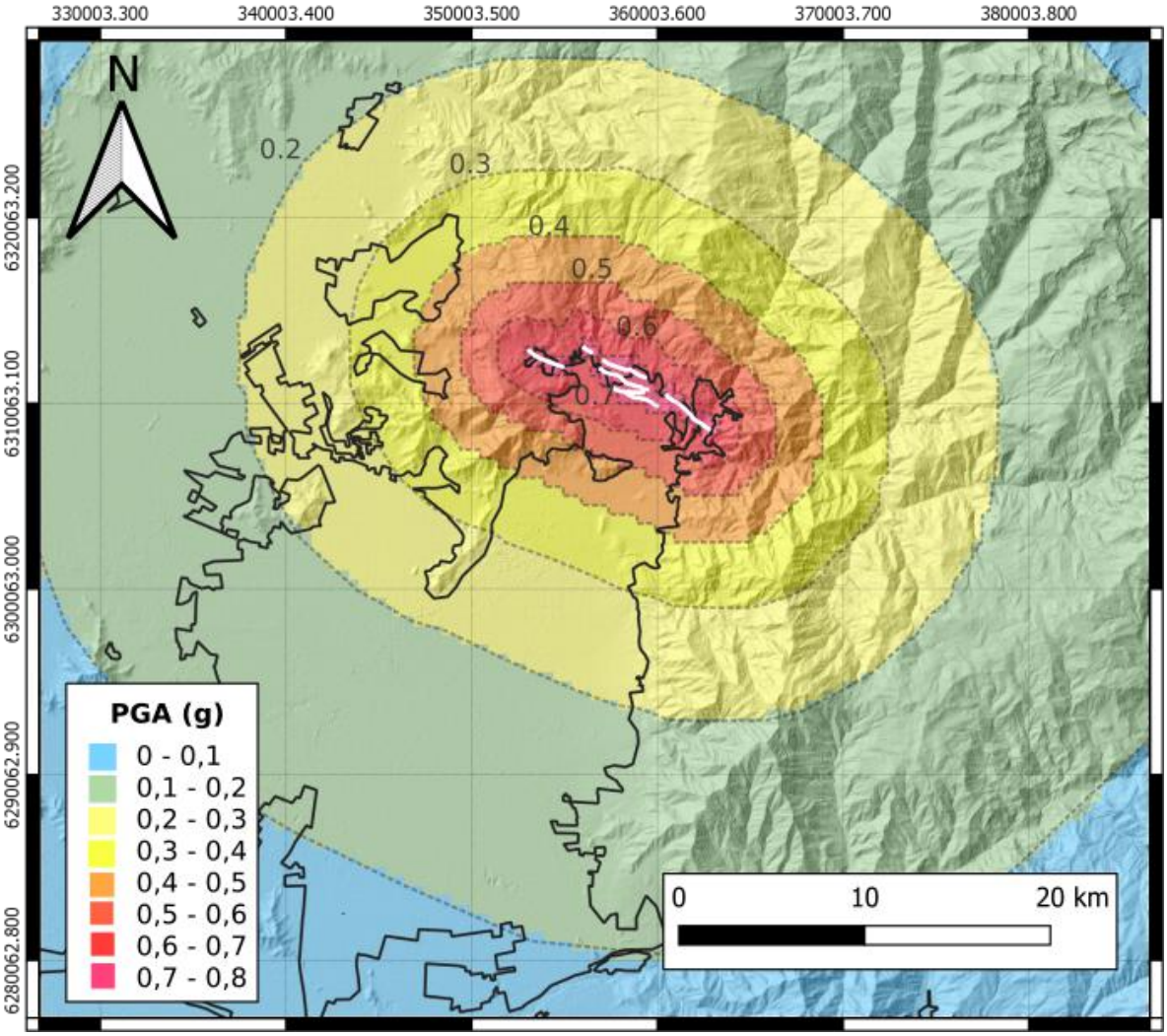


Figure 6.7 Peak ground acceleration (PGA) estimations corresponding to our rupture scenario for the EAF calculated from the Sadigh et al., (1997) model. Solid white line shows the EAF trace. Solid black line shows urban Santiago.

The results of the empirical model of Sadigh et al., (1997) are shown in Figure 6.7, representing the maximum expected PGA in the study area. The largest acceleration are observed above and immediately around the fault traces with PGA > 0.7 less than 0.5 km away from the fault trace at surface, reaching maximum PGA of 0.73. We also notice that PGA > 0.5 and PGA > 0.3 are less than 3.5 km and 10 km away from the EAF at surface respectably.

Previous works had estimated the seismic hazard of the Santiago city for a seismic scenario of crustal fault ruptures, but for the better constrained SRF. Pérez et al., (2014) and Estay et al., (2016) estimated peak ground accelerations of 0.2-0.3 (g) at 10 km from the SRF, and Ammirati et al., (2019) estimate PGA pf 0.4-0.5 (g) also at 10 km from the SRF. Meanwhile for our rupture scenario, we found PGA of 0.3 (g) at 10 km from the EAF at surface. Even though all of the previous studies and this work uses different

attenuation equations, they all shows similar estimations at distances greater than 10 km, except for the Ammirati et al., (2019) results estimating higher PGA. This can be attributed to the fact that Ammirati et al., (2019) uses a greater Mw of 7.5 for the characteristic earthaquake, compared to the other analysis that goes from Mw = 6.4 (this work), Mw = 6.6-6.7 (Estay et al., 2016) to Mw = 6.9(Perez et al., 2014).

Estay et al., 2016 and Ammirati et al., (2019) consider site effect in their works, identifying that PGA are intensified by deep soil and also are greater in the hanginwall rather than the footwall in general terms, indicating that areas that are in the hanginwall of the fault and filled with sediments, are the ones to expect greater accelerations. In this work we do not consider the site effects, however we can notice that in the proximity of the fault trace we can see that the greatest PGA estimated (>0.7 g) are around 500 m away from the fault, which is closer than expected for other studies for this same PGA. This can be attributed to the lack of site effects in the estimations and also to the fact that this study uses the smallest earthquake Mw = 6.4 of the comparison. Considering that the EAF is located in Lo Barnechea, an area cover mostly by sedimentary fill, and there is a considerable area of sedimentary fill above the hanginwall, we can say that our estimations are conservative, and future work should be focused on improve the estimations.

Despite the differences in the maximum earthquake, Mw = 6.9 in the case of Pérez et al. (2014), Mw = 6.6– 6.7 in the case of Estay et al., (2019) and Mw = 7.5 in the case of Ammirati et al., (2019), the different attenuation equations considering or not considering site effect of directivity, the range of PGA values are similar for crustal seismic sources in the Region Metropolitana. In addition, the largest PGA expected in this study reaches up to 0.7-0.8 g, a large number that confirms the potential hazards in the near-field of the EAF.

## Chapter 7: Conclusions

This chapter summarize and discuss the new information resulted from the researches related to the previous chapters, the ones aims to answer the research questions mentioned at Chapter 1. Implications derived from the new data and recommendations for future works are also included.

### 7.1 Main research questions and answers

| | |
|---|---|
| Are there other active crustal faults near Santiago that are possible seismic sources, besides San Ramon Fault and San Jose de Maipo Fault ? | In the carried out research, in base of geomorphological and structural analysis, two newly- discovered faults presents evidence of Quaternary activity; the El Arrayan fault and the Estero Coyanco fault. One previously known fault presents evidence of been potentially active (El Diablo fault) |
| What´s the seismic hazard related to these faults? | To provide an approximation of the fault related seismic hazard, potentially expected Mw were estimated, not only for the faults studied in this thesis, but also to every regional-scale mapped structure in the study area. This methodology indicated that the most hazardous zone (higher expected Mw) is the eastern flank of the Principal Cordillera, where N-S striking fault with length of tens of km and seismic depths between 5-15 km are located and capable to produce seismic events with Mw 6.5-7.2. The western flank of the Principal Cordillera present structures capable to produce seismic events with Mw 6.1-6.5 and in some scenarios Mw 6.5-7.0 for the San Ramon fault. Most of the structures in the western flank are "inferred" so there is less degree of certainty there, however there are closer to populated centers than the structures at the eastern flank, so they remain high-risk fault because of the direct impact in the population. The studied faults presents important seismic hazard, the El Arrayan fault is located beneath Lo Barnechea urban area and an expected future rupture Mw up to 6.4 in base of fault trace length, can affect directly not only the Lo Barnechea population, but also whole Santiago population. The Estero Coyanco is |

| | |
|---|---|
| | located less than 10 km to the south of San Jose de Maipo, the most populated locality at the Maipo Valley, and a rupture with Mw up to 6.9 can be expected in base of fault displacement, so important hazard is related. Finally for the EDF, a potentially rupture with Mw up to 7,1 can be expected for the worst case scenario in base of the tens of km of length of this structure.<br>The three fault studied in this thesis present direct relations with large (>0.1 $km^2$). El Arrayan fault locates less than 12 km from landslides, The Estero Coyanco fault is between 5-10 km from a landslide cluster trending in the same orientation of the fault strike, and the El Diablo fault is less than 5 km from numerous landslides. Besides the spatial relation of this fault with landslides, the active and potentially active character of these faults let me suggest that these faults are good candidates as triggers for coseismic landslides.<br>Deterministic PGA estimation was develop for the EAF. PGA up to 0.7 g are estimated 500 m away from the fault trace and up to 0.3 g 10 km away from the fault trace. |
| What is the relation of these faults to first order Andean structural system? | In base of the previously reported structures and the seismicity in the study area, the first order structural system indicates mayor deformation at the flanks of the Principal cordillera, being the western flank of the Principal cordillera characterized by shallow (10-15 km depth) seismicity compressive focal mechanism and N-S striking west-vergent reverse faults, and the eastern flank of the principal cordillera characterized shallow (5-10 km depth) seismicity, mostly strike-slip focal mechanism and subvertical east-vergent reverse faults.<br><br>The San Ramon fault, a N-S to NNW-SSE striking west-vergent reverse fault is compatible with a nearly E-W to ENE-WSW shortening direction, which coincides with the N°72-78 orientation of Tectonic Plates convergence vector (DeMets, 1994; Gripp & Gordon, 2002).<br><br>The El Arrayan fault is located in the western flank of the Principal Cordillera, at the foothill of the mountain range similar as the San Ramon Fault, but presents WNW-ESE orientation, mainly siniestral strike-slip and minor reverse kinematics (north side of the fault upwards). Fault plate kinematic analysis yields a shortening direction of 062°/03°, which is partly similar to the San Ramon fault.<br><br>The Estero Coyanco is also located at the western flank of |

| | |
|---|---|
| | the Principal Cordillera, not at foothills of the mountain range, but almost 10 km inside mountainous region, this is a NNW-SSE striking fault with east-vergent reverse mechanism, that can be produced by a ENE-WSW shortening direction, and which is compatible with the focal mechanism presented by Pérez et al., (2014) in the area. This shortening direction is also similar to the ones of the San Ramon fault and El Arrayan fault.<br><br>For the El Diablo fault, in this thesis we document for first time detail information about the kinematics of the fault, in which the most recent motion were inferred as mainly dextral-strike slip, derived from a NE-SW shortening direction, and consistent with focal mechanism previously reported for the El Fierro Fault system. This shortening direction is also similar to the shortening direction of the San Ramon fault, El Arrayan fault and Estero Coyanco fault. The Lavenu & Cembrano (1999) stress state for the Quaternary, derived from kinematic analysis of fault slip data, yield compressional NNE-SSW shortening direction, in agreement with the previously San Ramon fault, and the fault presented and analyzed in this work. Nevertheless, the N338°E compressional stress direction of the San José de Maipo fault (Lavenu & Cembrano, 2008) is the only one not compatible shortening direction.<br><br>Thus, the Quaternary deformation of Principal Cordillera responses to a homogeneous E-W to NE-SW shortening direction, coincident with the Plate tectonic convergence direction. Although, the western flank of the Principal Cordillera presents structures with N-S (ECF) and WNW-ESE (EAF) orientation accommodating mainly E-W margin perpendicular shortening, but also the WNW-ESE fault (EAF) accommodating N-S margin parallel shortening. On the other hand, the N-S striking EDF located at the eastern side of the Principal Cordillera would accommodate N-S margin perpendicular shortening. |

## 7.2 Implications

The newly gathered information obtained in this thesis strongly reinforces the statement that the Principal Cordillera it's an active mountain range which accommodates part of the stress transferred by the first-order subduction context of the Andean orogeny.

Previously researches has focused on the mountain front of the western flank of the Principal Cordillera, in which the San Ramon Fault highlights as the most hazardous structure near the most populated city in Chile (Rauld 2002, Armijo et al., 2010; Rauld 2011; Vargas et al., 2014). However, this is not the only regional-scale active structure in the Principal Cordillera, the location of Estero Coyanco fault, and El Diablo fault, indicated that the whole wide of the Principal Cordillera presents active deformation. Because the newly discovered El Arrayan fault is also located at the foothills of the mountain front and most of the fault trace is covered by urban development it implies very hazardous scenarios, thus society should be aware of the risk that they are exposed. This is essential information that political authorities should considerer at the moment of design urban areas where building can be located. In this way, the Chilean populations should consider that not only the historical mayor subduction earthquakes are the most dangerous seismic events; moreover, this work present 3 seismic sources capable to produce ruptures of considerable (Moment of Magnitudes) Mw 5.6-6.4 at very shallow depth very close to populated centers, being possibly very dangerous and catastrophic seismic events.

Strong shaking and building collapse in populated cities are not the only damage that seismic events can cause. At scarce populated area, inside the mountainous regions, important industrial development has been carried out, like drinking water supply, electrical supply and agriculture growth. These activities can be drastically affected by the main shaking of a seismic event which can destroy industrial facilities or by secondary coseimic hazards like landslides that can obstruct rivers and roads, similar as the consequences derived from the Las Melosas 1958 seismic event (Sepulveda et al. 2008). These consequences can affect directly the populations that lives and works near this industrial development, but also to an important percentage of Santiago population. The Estero Coyanco fault and the El Diablo fault are seismic sources capable to produce seismic events with Mw 6.7-6.9 and Mw 6.5-7.1, and are spatially related to large landslides, suggesting a possible causative relationship between them. Thus, these faults are important sources of seismic hazard that could directly affect population by strong shaking, but also by triggering landslides that can affect indirectly the population by creating damage on water or electric industry or obstructing important vehicle roads.

The variable orientation and kinematics reported for the studied fault in this thesis but the consistent stress state of them, indicated that Quaternary

deformation in the Principal Cordillera responses to a homogeneous E-W to NE-SW shortening direction, coincident with the Plate tectonic convergence direction. Although, the western flank of the Principal Cordillera presents structures with N-S (ECF) and WNW-ESE (EAF) orientation accommodating mainly E-W margin perpendicular shortening, but also the WNW-ESE fault (EAF) accommodating N-S margin parallel shortening. On the other hand, the N-S striking EDF located at the eastern side of the Principal Cordillera would accommodate mainly N-S margin perpendicular shortening.

## 7.3 Suggestions for future work

In this work, lot of effort was focused on the identification of potentially active fault by classical geomorphological and structural analysis, kinematic and slip data were collected. However, detail age constrain about fault rupture wasn´t develop, thus slip-rates presented in this thesis are first-order approximation. In this context, detail dating of the faulted and deformed Quaternary deposit can be an important input to better constrain the faults behavior. Radiocarbon dating in organic matter trapped in Quaternary deposits or OSL dating on minerals trapped in Quaternary deposits. Trenching and subsurface borehole data of the faults also can provide important information on-fault earthquake records, identifying the number of earthquake recorded and exposing datable deposits. Slip measurements, identification of earthquakes registered event, combined with deformed landform age constrains, should be done for the different fault segments that composed every active fault around Santiago Metropolitan region. This could provide a complete and solid slip rate and recurrence interval for each fault segment. That way a better fault rupture behavior knowledge can be acquire to be able to mitigate future damages caused by seismic events. Geophysical studies as gravity profiles along possible fault traces to identify basement density variations, high-resolution seismic tomography to interpret impedance changes associated with the deformed sedimentary cover, 2-D seismic reflection to identify offset Quaternary levels, or multi-electrode resistivity that allows to identify resistivity contrast related to faulting, are very useful to reveals fault behavior information.

The two clear faults with Quaternary activity (EAF and ECF) and the potentially active fault (EDF) reported in this thesis, duplicates the number of known active structures near Santiago in the Principal Cordillera. The scarce number of active structures previous to this work could represent the lack of geologist focused on neotectonics. Thus, more work should focused on identify structures that have experience Quaternary activity. This is of extreme importance because apart from inducing earthquake, active faults are the source of heavy damage to pavements, utilities, homes, businesses, factories and other manmade structures.

## Chapter 8: Bibliography


Angelier, J. T., & Mechler, P. (1977). Sur une methode graphique de recherche des contraintes principales egalement utilisables en tectonique et en seismologie: la methode des diedres droits. Bulletin de la Société géologique de France, 7(6), 1309-1318.

Aubouin, J. (1973). Des tectoniques superposees et de leur signification par rapport aux modeles geophysiques; l'exemple des Dinarides; paleotectonique, tectonique, tarditectonique, neotectonique. Bulletin de la Société géologique de France, 7(5-6), 426-460.

Aguirre, L. (1957). Perfil geológico entre la Cuesta de Chacabuco y el límite con la República Argentina. Memoria de Prueba, Escuela de Ingeniería, Universidad de Chile, 440 p.

Aguirre, L., (1960). Geología de los Andes de Chile Central, provincia de Aconcagua. Instituto de Investigaciones Geológicas, Santiago, Chile, Boletín Nº 9, 70 p.

Ahumada, E. A., & Costa, C. H. (2009). Antithetic linkage between oblique Quaternary thrusts at the Andean front, Argentine Precordillera. Journal of South American Earth Sciences, 28(3), 207-216.

Allmendinger, R. W. (1986). Tectonic development, southeastern border of the Puna Plateau, northwestern Argentine Andes. Geological Society of America Bulletin, 97(9), 1070-1082.

Allmendinger, R. W.; Cardozo, N.; Fisher, D. M. (2012). Structural geology algorithms: Vectors and tensors. Cambridge University Press: 286 p. Cambridge.

Alvarado, P., Barrientos, S., Saez, M., Astroza, M., & Beck, S. (2009). Source study and tectonic implications of the historic 1958 Las Melosas crustal earthquake, Chile, compared to earthquake damage. Physics of the Earth and Planetary Interiors, 175(1-2), 26-36.

Ammirati, J. B., Vargas, G., Rebolledo, S., Abrahami, R., Potin, B., Leyton, F., & Ruiz, S. (2019). The Crustal Seismicity of the Western Andean Thrust (Central Chile, 33°–34° S): Implications for Regional Tectonics and Seismic Hazard in the Santiago Area. Bulletin of the Seismological Society of America, 109(5), 1985-1999.

Angermann, D., Klotz, J., & Reigber, C. (1999). Space-geodetic estimation

of the Nazca-South America Euler vector. Earth and Planetary Science Letters, 171(3), 329-334.

Antinao, J. L., & Gosse, J. (2009). Large rockslides in the Southern Central Andes of Chile (32–34.5 S): Tectonic control and significance for Quaternary landscape evolution. Geomorphology, 104(3), 117-133.

Assinovskaya, B. A., & Ovsov, M. K. (2014). Seismotectonic zoning of the Finnish-Bothnia region based on the structural analysis method. Russian journal of Earth sciences, 14(2).

Astaburuaga, D., Farías, M., Charrier, R., & Tapia, F. (2012). Geología y estructuras del límite Mesozoico-Cenozoico de la Cordillera Principal entre 35º30'y 36ºS, Región del Maule, Chile. In Congreso Geológico Chileno (No. 13, pp. 250-252).

Astroza, M., Sandoval, M., & Kausel, E. (2005). Estudio comparativo de los efectos de los sismos chilenos de subducción del tipo intraplaca de profundidad intermedia. Jornadas de Sismología e ingeniería Antisísmica, (9).

Armijo, R., Rauld, R., Thiele, R., Vargas, G., Campos, J., Lacassin, R., & Kausel, E. (2010). The West Andean thrust, the San Ramon fault, and the seismic hazard for Santiago, Chile. Tectonics, 29(2).

Armijo, R., & Thiele, R. (1990). Active faulting in northern Chile: ramp stacking and lateral decoupling along a subduction plate boundary?. Earth and Planetary Science Letters, 98(1), 40-61.

Arriagada, C., Ferrando, R., Córdova, L., Morata, D., & Roperch, P. (2013). The Maipo Orocline: a first scale structural feature in the Miocene to Recent geodynamic evolution in the central Chilean Andes. Andean Geology, 40(3), 419-437.

Audin, L., Herail, G., Riquelme, R., Darrozes, J., Martinod, J., & Font, E. (2003). Geomorphological markers of faulting and neotectonic activity along the western Andean margin, northern Chile. Journal of Quaternary Science, 18(8), 681-694.

Baeza, O., (1999). Análisis de litofacies, evolución depositacional y análisis estructural de la Formación Abanico en el área comprendida entre los ríos Yeso y Volcán, Región Metropolitana. Memoria, Departamento de Geología, Universidad de Chile, Santiago, 119 p.

Barazangi, M., & Isacks, B. L. (1976). Spatial distribution of earthquakes and subduction of the Nazca plate beneath South America. Geology, 4(11), 686-692.

Barazangi, M., & Isacks, B. L. (1979). Subduction of the Nazca plate beneath Peru: evidence from spatial distribution of earthquakes. Geophysical Journal of the Royal Astronomical Society, 57(3), 537-555.

Barrientos, S., Eisenberg, A., (1988). Secuencia sísmica en la zona cordillerana al interiorde Rancagua. V Congreso Geológico Chileno, Santiago, Chile, F121–F132.

Barrientos, S., Vera, E., Alvarado, P., & Monfret, T. (2004). Crustal seismicity in central Chile. Journal of South American Earth Sciences, 16(8), 759-768.

Beck, S., Barrientos, S., Kausel, E., & Reyes, M. (1998). Source characteristics of historic earthquakes along the central Chile subduction Askew et Alzone. Journal of South American Earth Sciences, 11(2), 115-129.

Bell, T. H., & Etheridge, M. A. (1973). Microstructure of mylonites and their descriptive terminology. Lithos, 6(4), 337-348.

Brooks, B. A., Bevis, M., Smalley Jr, R., Kendrick, E., Manceda, R., Lauría, E., Maturana, R. & Araujo, M. (2003). Crustal motion in the Southern Andes (26°–36° S): Do the Andes behave like a microplate?. Geochemistry, Geophysics, Geosystems, 4(10).

Burbank, D. W., & Anderson, R. S. (2012). Tectonic Geomorphology, 2nd edition,. Blackwell Publishing Ltd.: 454 p. Oxford.

Brüggen, M. J. (1950). Fundamentos de la Geología de Chile. Instituto Geográfico Militar.

Borde, J. (1966) "Las incidencias cataclísmicas en la morfología de los Andes de Santiago," Informaciones Geográficas, XX, 7–25.

Bustamante, M. A., (2001). El contacto entre la Formación Abanico y las unidades mesozoicas, valle del río Volcán, Región Metropolitana. Memoria, Departamento de Geología, Universidad de Chile, Santiago, 54 p.

Cahill, T., & Isacks, B. L. (1992). Seismicity and shape of the subducted Nazca plate. Journal of Geophysical Research: Solid Earth, 97(B12), 17503-17529.

Caine, J. S., Evans, J. P., & Forster, C. B. (1996). Fault zone architecture and permeability structure. Geology, 24(11), 1025-1028.

Caine, J. S., Minor, S. A., Grauch, V. J. S., Budahn, J. R., & Keren, T. T. (2017). A comprehensive survey of faults, breccias, and fractures in and flanking the eastern Española Basin, Rio Grande rift, New Mexico. Geosphere, 13(5), 1566-1609.

Campbell, D., (2005). Termocronología del sector comprendido entre los ríos Rocín y Aconcagua: Implicancias en la evolución Meso- Cenozoica de la Zona. Memoria, Departamento de Geología, Universidad de Chile, Santiago, 113 p.

Candia, G., de Pascale, G. P., Montalva, G., & Ledezma, C. (2017). Geotechnical aspects of the 2015 Mw 8.3 Illapel megathrust earthquake sequence in Chile. Earthquake Spectra, 33(2): 709-728.

Carrizo, D., González, G., & Dunai, T. (2008). Constricción neógena en la Cordillera de la Costa, norte de Chile: neotectónica y datación de superficies con 21Ne cosmogónico. Revista geológica de Chile, 35(1), 01-38.

Carter, W.; Aguirre, L. (1965). Structural Geology of Aconcagua province and its relationship to the central Valley Graben, Chile. Geological Society of America, Bulletin 76: 651-664.

Casa, A. L., Yamin, M. G., Cegarra, M. I., Coppolecchia, M., & Costa, C. H. (2010). Deformación cuaternaria asociada al frente de levantamiento oriental de las sierras de Velasco y Ambato, Sierras Pampeanas occidentales. Revista de la Asociación Geológica Argentina, 67(4), 425-438.

Casas, E.A., Sepúlveda, S.A., Campos, J., Rebolledo, S., (2005). Estudio del terremoto de Las Melosas de 1958 mediante caracterización de deslizamientos cosísmicos, IX Jornadas Chilenas de Sismología e Ingeniería Antisísmica, Article A01-06, 8 pp., 16–19 de Noviembre de 2005, Concepción–Chile.

Castro Rivas, J. (2012).Estilo estructural en los depósitos mesozoicos y

genozoicos en el valle del río Colorado - Maipo, región Metropolitana, Chile (~33° 30' S). Memoria, Departamento de Geología, Universidad de Chile, Santiago, 79 p.

Charrier, R., Wyss, A., Flynn, J. J., Swisher III, C. C., Norell, M. A., Zapatta, F., ... & Novacek, M. J. (1996). New evidence for late Mesozoic-early Cenozoic evolution of the Chilean Andes in the upper Tinguiririca valley (35 S), central Chile. Journal of South American Earth Sciences, 9(5-6): 393-422.

Charrier, R., Baeza, O., Elgueta, S., Flynn, J. J., Gans, P., Kay, S. M., ... & Zurita, E. (2002). Evidence for Cenozoic extensional basin development and tectonic inversion south of the flat-slab segment, southern Central Andes, Chile (33–36 SL). Journal of South American Earth Sciences, 15(1), 117-139.

Charrier, R., M. Bustamante, D. Comte, S. Elgueta, J. J. Flynn, N. Iturra, N. Muñoz, M. Pardo, R. Thiele, and A. R. Wyss (2005), The Abanico Extensional Basin: Regional extension, chronology of tectonic inversion, and relation to shallow seismic activity and Andean uplift, Neues Jahrb. Geol. Palaeontol. Abh., 236, 43–47.

Charrier, R., Farías, M., & Maksaev, V. (2009). Evolución tectónica, paleogeográfica y metalogénica durante el Cenozoico en los Andes de Chile norte y central e implicaciones para las regiones adyacentes de Bolivia y Argentina. Revista de la Asociación Geológica Argentina, 65(1), 05-35.

Charrier, R., Pinto, L., & Rodríguez, M. P. (2007). Tectonostratigraphic evolution of the Andean Orogen in Chile. In The geology of Chile.

Childs, C., Manzocchi, T., Walsh, J. J., Bonson, C. G., Nicol, A., & Schöpfer, M. P. (2009). A geometric model of fault zone and fault rock thickness variations. Journal of Structural Geology, 31(2), 117-127.

Chester, F. M., & Chester, J. S. (1998). Ultracataclasite structure and friction processes of the Punchbowl fault, San Andreas system, California. Tectonophysics, 295(1-2), 199-221.

Chester, F. M., Evans, J. P., & Biegel, R. L. (1993). Internal structure and weakening mechanisms of the San Andreas fault. Journal of Geophysical Research: Solid Earth, 98(B1), 771-786.

Chester, F. M., Friedman, M., & Logan, J. M. (1985). Foliated cataclasites.

Tectonophysics, 111(1-2), 139-146.

Chester, F. M., & Logan, J. M. (1986). Implications for mechanical properties of brittle faults from observations of the Punchbowl fault zone, California. Pure and Applied Geophysics, 124(1-2), 79-106.

Chiou, B. S. J., & Youngs, R. R. (2014). Update of the Chiou and Youngs NGA model for the average horizontal component of peak ground motion and response spectra. Earthquake Spectra, 30(3), 1117-1153.

Cisternas, M. (2012). El terremoto de 1647 de Chile central como un evento intraplaca:¿ otra amenaza para Chile metropolitano?. Revista de Geografía Norte Grande, (53), 23-33.

Coira, B., Davidson, J., Mpodozis, C., & Ramos, V. (1982). Tectonic and magmatic evolution of the Andes of northern Argentina and Chile. Earth-Science Reviews, 18(3-4), 303-332.

Cortés, J. M., Casa, A., Pasini, M., Yamín, M., & Terrizano, C. (2006). Fajas oblicuas de deformación neotectónica en Precordillera y Cordillera Frontal (31° 30´-33° 30´ LS): controles paleotectónicos. Revista de la Asociación Geológica Argentina, 61(4), 639-646.

Cortés, J., Franchi, M., & Nullo, F. (1987). Evidencias de neotectónica en Las Sierras de Aguilar y del Tanque. In Cordillera Oriental y Puna Jujeñas, Argentina: X Congreso Geologico Argentino Actas (Vol. 1, pp. 239-242).

Costa, C. H., Giaccardi, A. D., & Díaz, E. F. G. (1999). Palaeolandsurfaces and neotectonic analysis in the southern Sierras Pampeanas, Argentina. Geological Society, London, Special Publications, 162(1), 229-238.

Costa, C., Machette, M. N., Dart, R. L., Bastías, H., Paredes, J. D., Perucca, L. P., ... & Haller, K. (2000). Map and database of Quaternary faults and folds in Argentina. US Geological Survey Open-File Report, 108, 75.

Davidson, J. (1971). Geología del area de las Nacientes del Teno, provincial de Curicó. Universidad de Chile, Departamento de Geología. Santiago. 135 p.

Davidson, J., Vicente, J. (1973). Características paleogeográficas y estructurales del área fronteriza de las nacientes del Teno-Chile- y

Santa Elena-Argentina, Cordillera Principal, 35º a 35º15’ de latitud sur. In Congreso Geológico Argentino, No. 5, Actas 5: 11-55.

Davis, G. H., Bump, A. P., Garćia, P. E., & Ahlgren, S. G. (2000). Conjugate Riedel deformation band shear zones. Journal of Structural Geology, 22(2), 169-190.

Deckart, K., Pinochet, K., Sepúlveda, S. A., Pinto, L., & Moreiras, S. M. (2014). New insights on the origin of the Mesón Alto deposit, Yeso Valley, central Chile: A composite deposit of glacial and landslide processes. Andean Geology, 41(1).

DeMets, C., Gordon, R. G., Argus, D. F., & Stein, S. (1994). Effect of recent revisions to the geomagnetic reversal time scale on estimates of current plate motions. Geophysical research letters, 21(20), 2191-2194.

Díaz, D., Maksymowicz, A., Vargas, G., Vera, E., Contreras-Reyes, E., & Rebolledo, S. (2014). Exploring the shallow structure of the San Ramón thrust fault in Santiago, Chile (~ 33.5 S), using active seismic and electric methods. Solid Earth, 5(2): 837-849.

Doblas, M. (1998). Slickenside kinematic indicators. Tectonophysics, 295(1-2), 187-197.

Dooley, T. P., & Schreurs, G. (2012). Analogue modelling of intraplate strike-slip tectonics: A review and new experimental results. Tectonophysics, 574: 1-71.

Dura, T., Cisternas, M., Horton, B. P., Ely, L. L., Nelson, A. R., Wesson, R. L., & Pilarczyk, J. E. (2015). Coastal evidence for Holocene subduction-zone earthquakes and tsunamis in central Chile. Quaternary Science Reviews, 113: 93-111.

Estay, N. P., Yáñez, G., Carretier, S., Lira, E., & Maringue, J. (2016). Seismic hazard in low slip rate crustal faults, estimating the characteristic event and the most hazardous zone: study case San Ramón Fault, in southern Andes. Natural Hazards & Earth System Sciences, 16(12).

Fagereng, Å., & Toy, V. G. (2011). Geology of the earthquake source: an introduction. Geological Society, London, Special Publications, 359(1), 1-16.

Farías, M., Charrier, R., Carretier, S., Martinod, J., Fock, A., Campbell, D., ... & Comte, D. (2008). Late Miocene high and rapid surface uplift and its erosional response in the Andes of central Chile (33–35 S). Tectonics, 27 (1).

Farías, M.; Comte, D.; Charrier, R. (2006). Sismicidad superficial en Chile central: Implicancias para el estado cortical y crecimiento de los Andes Centrales australes. In Congreso Geológico Chileno, No. 11, Actas 1: 403-406. Antofagasta.

Farías, M., Comte, D., Charrier, R., Martinod, J., David, C., Tassara, A., ... & Fock, A. (2010). Crustal-scale structural architecture in central Chile based on seismicity and surface geology: Implications for Andean mountain building. Tectonics, 29(3).

Faulkner, D. R., Lewis, A. C., & Rutter, E. H. (2003). On the internal structure and mechanics of large strike-slip fault zones: field observations of the Carboneras fault in southeastern Spain. Tectonophysics, 367(3-4), 235-251.

Flores, R., Arias, S., Jenshke, V., and Rosemberg, L. A. (1960). "Engineering aspect of the earthquakes in the Maipo Valley, Chile, in 1958." Proceedings of 2nd World Conference in Earthquake Engineering, Japan, 1, pp. 409–431.

Fock, A. (2005). Cronología y tectónica de la exhumación en el Neógeno de los Andes de Chile central entre los 33 y los 34 S. Memoria de Título (Inédito), Universidad de Chile, Departamento de Geología.

Folguera, A., Ramos, V. A., Hermanns, R. L., & Naranjo, J. (2004). Neotectonics in the foothills of the southernmost central Andes (37°–38° S): Evidence of strike-slip displacement along the Antiñir-Copahue fault zone. Tectonics, 23(5).

Förstner, W., & Pertl, A. (1986). Photogrammetric standard methods and digital image matching techniques for high precision surface measurements. In Pattern Recognition in Practice: 57-72.

Fuentes, F., Vergara, M., Aguirre, L., & Féraud, G. (2002). Relaciones de contacto de unidades volcánicas terciarias de los Andes de Chile central (33 S): una reinterpretación sobre la base de dataciones 40Ar/39Ar. Revista geológica de Chile, 29(2), 207-225.

Gana, P., & Wall, R. (1997). Evidencias geocronologicas 40Ar/39Ar y K-Ar

de un hiatus cretacico superior-eoceno en Chile central (33-33° 30'S). Andean Geology, 24(2), 145-163.

Giambiagi, L. B., Ramos, V. A., Godoy, E., Alvarez, P. P., & Orts, S. (2003). Cenozoic deformation and tectonic style of the Andes, between 33 and 34 south latitude. Tectonics, 22(4).

Godoy, E., & Lara, L. (1994). Segmentación estructural andina a los 33-34: nuevos datos en la Cordillera Principal. In Congreso Geológico Chileno (No. 7, pp. 1344-1348).

Godoy, E., Yáñez, G., & Vera, E. (1999). Inversion of an Oligocene volcano-tectonic basin and uplifting of its superimposed Miocene magmatic arc in the Chilean Central Andes: first seismic and gravity evidences. Tectonophysics, 306(2), 217-236.

González, G., Cembrano, J., Carrizo, D., Macci, A., & Schneider, H. (2003). The link between forearc tectonics and Pliocene–Quaternary deformation of the Coastal Cordillera, northern Chile. Journal of South American Earth Sciences, 16(5), 321-342.

Gregori, S. D., & Christiansen, R. (2018). Seismic hazard analysis for central-western Argentina. Geodesy and Geodynamics, 9(1), 25-33.

Gripp, A. E., & Gordon, R. G. (2002). Young tracks of hotspots and current plate velocities. Geophysical Journal International, 150(2), 321-361.

Gutscher, M. A., Spakman, W., Bijwaard, H., & Engdahl, E. R. (2000). Geodynamics of flat subduction: Seismicity and tomographic constraints from the Andean margin. Tectonics, 19(5), 814-833.

Harris, C.; Stephens, M. (1988). A combined corner and edge detector. In Alvey vision conference 15 (50): 147-151 p.

Hermanns, R. L., Niedermann, S., Garcia, A. V., Gomez, J. S., & Strecker, M. R. (2001). Neotectonics and catastrophic failure of mountain fronts in the southern intra-Andean Puna Plateau, Argentina. Geology, 29(7), 619-622.

Hills, E. S., (1963). Elements of Structural Geology. London, Methuen and Co. Ltd., 483 p.

Hull, J. (1988). Thickness-displacement relationships for deformation zones. Journal of Structural Geology, 10(4), 431-435.

Isacks, B. L. (1988). Uplift of the central Andean plateau and bending of the Bolivian orocline. Journal of Geophysical Research: Solid Earth, 93(B4), 3211-3231.

Jara, P. (2013). Tectónica mezo-cenozoica en la Cordillera Principal de Chile central entre 32° y 33°S. Análisis a partir de nuevos antecedentes de campo y modelamiento analógico. Tesis de grado para optar al grado de doctor en ciencias mención geología. Universidad de Chile, Departamento de Geología, Santiago, 331p.

Jara, P., & Charrier, R. (2014). Nuevos antecedentes estratigráficos y geocronológicos para el Meso-Cenozoico de la Cordillera Principal de Chile entre 32° y 32° 30'S: Implicancias estructurales y paleogeográficas. Andean geology, 41(1), 174-209.

Jordán, T. E., Isacks, B. L., Allmendinger, R. W., Brewer, J. A., Ramos, V. A., & Ando, C. J. (1983). Andean tectonics related to geometry of subducted Nazca plate. Geological Society of America Bulletin, 94(3), 341-361.

Kay, S. M., Godoy, E., & Kurtz, A. (2005). Episodic arc migration, crustal thickening, subduction erosion, and magmatism in the south-central Andes. Geological Society of America Bulletin, 117(1-2), 67-88.

Kebede, F., & Van Eck, T. (1997). Probabilistic seismic hazard assessment for the Horn of Africa based on seismotectonic regionalisation. Tectonophysics, 270(3-4), 221-237.

Lara, M., & Sepúlveda, S. A. (2010). Landslide susceptibility and hazard assessment in San Ramón Ravine, Santiago de Chile, from an engineering geological approach. Environmental Earth Sciences, 60(6), 1227-1243.

Lavenu, A. (2006). Neotectónica de los Andes entre 1 N y 47 S (Ecuador, Bolivia y Chile): una revisión. Revista de la Asociación Geológica Argentina, 61(4), 504-524.

Lavenu, A., & Cembrano, J. (1999). Compressional-and transpressional-stress pattern for Pliocene and Quaternary brittle deformation in fore arc and intra-arc zones (Andes of Central and Southern Chile). Journal of Structural Geology, 21(12), 1669-1691.

Lavenu, A., & Cembrano, J. (2008). Deformación compresiva cuaternaria

en la Cordillera Principal de Chile central (Cajón del Maipo, este de Santiago). Revista geológica de Chile, 35(2), 233-252.

Lavenu, A., Thiele, R., & Cembrano, J. (1994). Neotectónica compresiva plio-cuaternaria en la Depresión central de Chile. In Congreso Geológico Chileno (No. 7, pp. 324-328).

Lavenu, A.; Thiele, R.; Machette, M.; Dart, R.; Bradley, L-A.; Haller, K. (2000). Maps and Database of Quaternary Faults in Bolivia and Chile. United States of Geological Survey, Open-File Report 00-283: 50 p.

Leyton, F., Ruiz, S., & Sepúlveda, S. A. (2010). Reevaluación del peligro sísmico probabilístico en Chile central. Andean geology, 37(2), 455-472.

Li, Y. G., De Pascale, G. P., Quigley, M. C., & Gravley, D. M. (2014). Fault damage zones of the M7. 1 Darfield and M6. 3 Christchurch earthquakes characterized by fault-zone trapped waves. Tectonophysics, 618: 79-101.

Little, T. A. (1995). Brittle deformation adjacent to the Awatere strike-slip fault in New Zealand: Faulting patterns, scaling relationships, and displacement partitioning. Geological Society of America Bulletin, 107(11), 1255-1271.

Lomnitz, C. (1961). Los terremotos del 4 de septiembre de 1958 en Cajón del Maipo. In Anales de la Facultad de Ciencias Físicas y Matemáticas (Vol. 18, No. 18, pp. ág-275).

Lomnitz, C. (2004). Major earthquakes of Chile: a historical survey, 1535-1960. Seismological Research Letters, 75(3), 368-378.

Marrett, R., & Allmendinger, R. W. (1990). Kinematic analysis of fault-slip data. Journal of structural geology, 12(8), 973-986.

Marrett, R. A., Allmendinger, R. W., Alonso, R. N., & Drake, R. E. (1994). Late Cenozoic tectonic evolution of the Puna Plateau and adjacent foreland, northwestern Argentine Andes. Journal of South American Earth Sciences, 7(2), 179-207.

Marquardt, C., Lavenu, A., Ortlieb, L., Godoy, E., & Comte, D. (2004). Coastal neotectonics in Southern Central Andes: uplift and deformation of marine terraces in Northern Chile (27 S). Tectonophysics, 394(3-4), 193-219.

Massabie, A., Sanguinetti, A., Lo Forte, G., & Cegarra, M. (2003). La actividad neotectónica en la sierra Baja de San Marcos-Cruz del Eje, flanco occidental de las Sierras Pampeanas Orientales. Revista de la Asociación Geológica Argentina, 58(4), 653-663.

Mateo, M. L., Lenzano, L. E., & Moreiras, S. M. (2009). Aconcagua peak geodynamics from GPS observations, Mendoza, Argentina: preliminary results. Advances in Geosciences, 22, 169-172.

McGill, S. F., & Sieh, K. (1991). Surficial offsets on the central and eastern Garlock fault associated with prehistoric earthquakes. Journal of Geophysical Research: Solid Earth, 96 (B13): 21597-21621.

Moreiras, S. M., & Sepúlveda, S. A. (2014). Megalandslides in the Andes of central Chile and Argentina (32°–34° S) and potential hazards. Geological Society, London, Special Publications, 399, SP399-18.

Mosolf, J. G., Gans, P. B., Wyss, A. R., Cottle, J. M., & Flynn, J. J. (2019). Late Cretaceous to Miocene volcanism, sedimentation, and upper-crustal faulting and folding in the Principal Cordillera, central Chile: field and geochronological evidence for protracted arc volcanism and transpressive deformation. Bulletin, 131(1-2): 252-273.

Mirzaei, N., Mengtan, G., & Yuntai, C. (1998). Seismic source regionalization for seismic zoning of Iran: major seismotectonic provinces. Journal of earthquake prediction research, 7, 465-495.

Mpodozis, C; Ramos,V. (1989). The Andes of Chile and Argentina, in: Geology of the Andes and its relation to hydrocarbon and mineral resources; Ericksen, G.E., Cañas M.T. and Reinemund, J.A. (Editores), Houston, Texas, Circum-Pacific Council for Energy and Mineral Resources, Earth Science Series, Vol. 11, p.59-90

Muñoz, M., Deckart, K., Charrier, R., & Fanning, M. (2009). New geochronological data on Neogene-Quaternary intrusive rocks from the high Andes of central Chile (33º15'-34º00'S). In Congreso Geológico Chileno (No. 12, pp. 8-008).

Naranjo JA, Varela J (1996) Flujos de detritos y barro que afectaron el sector oriente de Santiago el 3 de mayo de 1993. (Debris and mud flows that affected the Santiago eastern zone on May 3rd 1993). Servicio Nacional de Geología y Minería, Boletín No. 47, Santiago

Naylor, M. A., Mandl, G. T., & Supesteijn, C. H. K. (1986). Fault geometries in basement-induced wrench faulting under different initial stress states. Journal of Structural Geology, 8(7), 737-752.

Nystrӧm, J. O., Vergara, M., Morata, D., & Levi, B. (2003). Tertiary volcanism during extension in the Andean foothills of central Chile (33 15’–33 45’ S). Geological Society of America Bulletin, 115(12), 1523-1537.

Pappalardo, R. T., & Greeley, R. (1995). A review of the origins of subparallel ridges and troughs: Generalized morphological predictions from terrestrial models. Journal of Geophysical Research: Planets, 100(E9), 18985-19007.

Pardo-Casas, F., & Molnar, P. (1987). Relative motion of the Nazca (Farallon) and South American plates since Late Cretaceous time. Tectonics, 6(3), 233-248.

Pardo, M., & Acevedo, P. (1984). Mecanismos de foco en la zona de Chile Central. Tralka, 2(3), 279-293.

Pérez, A., Ruiz, J. A., Vargas, G., Rauld, R., Rebolledo, S., & Campos, J. (2014). Improving seismotectonics and seismic hazard assessment along the San Ramón Fault at the eastern border of Santiago city, Chile. Natural Hazards, 71(1), 243-274.

Perucca, L., Audemard, F., Pantano, A., Vargas, H., Avila, C., Onorato, M., ... & Esper, M. (2013). Fallas cuaternarias con vergencias opuestas entre precordillera central y oriental, provincia de San Juan. Revista de la Asociación Geológica Argentina, 70(2), 291-302.

Perucca, L. P., & Onorato, R. (2011). Fallas con actividad cuaternaria en el corredor tectonico Matagusanos-Maradona-Acequion entre los rios de La Flecha y del Agua, provincia de San Juan. Revista de la Asociación Geológica Argentina, 68(1), 39-52.

Pfiffner, O. A., & Burkhard, M. (1987). Determination of paleostress axis orientations from fault, twin and earthquake data. In Annales Tectonicae (Vol. 1, pp. 48-57). Editrice Il Sedicesimo.

Phuong, N. H. (2001). Probabilistic seismic hazard assessment along the Southeastern coast of Vietnam. Natural hazards, 24(1), 53-74.

Piderit, E. (1961). "Estudios de los sismos del Cajón del Maipo en el año 1958," Thesis, Civil Engineering Dept., University of Chile, Santiago, Chile.

Piquer, J., Berry, R. F., Scott, R. J., & Cooke, D. R. (2016). Arc-oblique fault systems: Their role in the Cenozoic structural evolution and metallogenesis of the Andes of central Chile. Journal of Structural Geology, 89, 101-117.

Piquer, J., Hollings, P., Rivera, O., Cooke, D. R., Baker, M., & Testa, F. 2017. Along-strike segmentation of the Abanico Basin, central Chile: New chronological, geochemical and structural constraints. Lithos, 268: 174-197.

Piquer, J., Skarmeta, J., & Cooke, D. R. (2015). Structural evolution of the Rio Blanco-Los Bronces District, Andes of Central Chile: controls on stratigraphy, magmatism, and mineralization. Economic Geology, 110(8): 1995-2023.

Pollard, D. D., Segall, P., & Delaney, P. T. (1982). Formation and interpretation of dilatant echelon cracks. Geological Society of America Bulletin, 93(12), 1291-1303.

Quiroga, R. (2013). Análisis estructural de los depósitos cenozoicos de la Cordillera Principal entre el cerro Provincia y el cordón El Quempo, Región Metropolitana, Chile (33° 18' a 33° 25' S). Memoria de título, Departamento de Geología, Universidad de Chile. 128 p.

Ramos, V.A., Godoy, E., Lo Forte, G., Aguirre-Urreta, M.B., (1991). La Franja Plegada y Corrida del Norte del Río Colorado, Región Metropolitana, Chile Central. Actas VI Congreso Geológico Chileno, Santiago, pág. 323-327.

Ramos, V. A., Cegarra, M., & Cristallini, E. (1996). Cenozoic tectonics of the High Andes of west-central Argentina (30–36 S latitude). Tectonophysics, 259(1-3), 185-200.

Ramos, V. A., Cristallini, E. O., & Pérez, D. J. (2002). The Pampean flat-slab of the Central Andes. Journal of South American earth sciences, 15(1), 59-78.

Rauld, R. (2002). Análisis morfoestructural del frente cordillerano de Santiago oriente, entre el Río Mapocho y la Quebrada de Macul. Memoria de Título (Inédito), Universidad de Chile, Departamento de

Geología: 57 p.

Rauld, R. (2011). Deformación cortical y peligro sísmico asociado a la falla San Ramón en el frente cordillerano de Santiago, Chile Central (33° S). Santiago, Chile: PhD. thesis in Science of Geology, Universidad de Chile.

Riedel, W. (1929). Zur Mechanik geologischer Brucherscheinungen ein Beitrag zum Problem der Fiederspatten. Zentbl. Miner. Geol. Palaont. Abt., 354-368.

Riesner, M., Lacassin, R., Simoes, M., Armijo, R., Rauld, R., & Vargas, G. (2017). Kinematics of the active West Andean fold-and-thrust belt (central Chile): Structure and long-term shortening rate. Tectonics, 36 (2): 287-303.

Riquelme, R., Martinod, J., Hérail, G., Darrozes, J., & Charrier, R. (2003). A geomorphological approach to determining the Neogene to Recent tectonic deformation in the Coastal Cordillera of northern Chile (Atacama). Tectonophysics, 361(3-4), 255-275.

Rivano, S., Sepúlveda, P., (1986). Hoja Illapel (1:250,000 scalemap), IV Región de Coquimbo. Carta geológica de Chile, vol. 69. Servicio Nacional de Geología y Minería, Santiago.

Robertson, E. G. (1983). Relationship of fault displacement to gouge and breccia thickness. American Institute of Mining Engineering Transactions, 274, 1426-1432.

Scholz, C. H. (1988). The brittle-plastic transition and the depth of seismic faulting. Geologische Rundschau, 77(1), 319-328.

Scholz, C. H. (2002). The mechanics of earthquakes and faulting. Cambridge university press.

Schwartz, D. P., & Coppersmith, K. J. (1984). Fault behavior and characteristic earthquakes: Examples from the Wasatch and San Andreas fault zones. Journal of Geophysical Research: Solid Earth, 89(B7): 5681-5698.

Sellés, D., (1999). La Formación Abanico en el Cuadrángulo Santiago (33º 15’-33º 30’S; 70º30’-70º45’O), Chile Central. Estratigrafía y geoquímica. Tesis, Departamento de Geología, Universidad de Chile, Santiago, 154 p.

Sellés, D., Gana, P., (2001). Geología del área Talagante-San Francisco de Mostazal: Regiones Metropolitana y del Libertador General Bernardo O'Higgins, Escala 1:100.000. SERNAGEOMIN, Carta Geológica de Chile, Serie Geología Básica, Nº 74.

Sepúlveda, S. A., Astroza, M., Kausel, E., Campos, J., Casas, E. A., Rebolledo, S., & Verdugo, R. (2008). New findings on the 1958 Las Melosas earthquake sequence, central Chile: implications for seismic hazard related to shallow crustal earthquakes in subduction zones. Journal of Earthquake Engineering, 12(3), 432-455.

Sepúlveda, S. A., & Moreiras, S. M. (2013). Large volume Landslides in the central Andes of Chile and Argentina (32º-34ºS) and related hazards. Italian Journal of Engineering Geology and Environment - Book Series (6).

Sepúlveda, S. A., Moreiras, S. M., Lara, M., & Alfaro, A. (2015). Debris flows in the Andean ranges of central Chile and Argentina triggered by 2013 summer storms: characteristics and consequences. Landslides, 12(1), 115-133.

Serey A; Sepúlveda, SA; Murphy, W; Petley DN; De Pascale, G. (2020). Developing conceptual models for the recognition of coseismic landslides hazard for shallow crustal and megathrust earthquakes in different mountain environments – an example from the Chilean Andes. Quarterly Journal of Engineering Geology and Hydrogeology, https://doi.org/10.1144/qjegh2020-023

SERNAGEOMIN (Servicio Nacional de Geología y Minería). (2003). Mapa Geológico de Chile, Versión Digital. Santiago, Chile, Servicio Nacional de Geología y Minería, scale 1: 1,000,000.

Sibson, R. H. (1977). Fault rocks and fault mechanisms. Journal of the Geological Society, 133(3), 191-213.

Sibson, R. H. (1983). Continental fault structure and the shallow earthquake source. Journal of the Geological Society, 140(5), 741-767.

Skempton, A. W. (1966). Some observations on tectonic shear zones. In 1st ISRM Congress. International Society for Rock Mechanics.

Sylvester, A. G. (1988). Strike-slip faults. Geological Society of America

Bulletin, 100(11): 1666-1703.

Tchalenko, J. S., & Ambraseys, N. N. (1970). Structural analysis of the Dasht-e Bayaz (Iran) earthquake fractures. Geological Society of America Bulletin, 81(1), 41-60.

Thiele, R., & Cubillos, E. (1980). Hoja Santiago: región metropolitana: carta geológica de Chile escala 1: 250.000. Instituto de Investigaciones Geológicas.

Thomas, H. (1958). Geología de la Cordillera de la Costa entre el valle de La Ligua y la cuesta de Barriga. Inst. Invest. Geol. (Chile), Bol., No. 2, 86 p.

Thompson Jobe, J. A., Philibosian, B., Chupik, C., Dawson, T., K. Bennett, S. E., Gold, R., ... & Pierce, I. (2020). Evidence of previous faulting along the 2019 Ridgecrest, California, earthquake ruptures. Bulletin of the Seismological Society of America, 110 (4), 1427-1456.

Troncoso Castro, M. (2014). Evidencia geomorfológica de neotectónica en el borde oriental de la depresión Los Andes - San Felipe, Provincia de Los Andes, Región de Valparaíso.

Udías, A., Madariaga, R., Buforn, E., Muñoz, D., & Ros, M. (2012). The large Chilean historical earthquakes of 1647, 1657, 1730, and 1751 from contemporary documents. Bulletin of the Seismological Society of America, 102(4), 1639-1653.

Vargas, G., Klinger, Y., Rockwell, T. K., Forman, S. L., Rebolledo, S., Baize, S., ... & Armijo, R. (2014). Probing large intraplate earthquakes at the west flank of the Andes. Geology, 42(12), 1083-1086.

Villela Olavarría, D. (2015). Desarrollo estructural de la cordillera principal al suroeste del Río Maipo, sector de El Ingenio, Región Metropolitana,Chile (33°40'-33°50'S).

Wall, R., Sellés, D., & Gana, P. (1999). Área Tiltil-Santiago, Región Metropolitana. Servicio nacional de geología y minería.

Wells, D. L., & Coppersmith, K. J. (1994). New empirical relationships among magnitude, rupture length, rupture width, rupture area, and surface displacement. Bulletin of the seismological Society of America, 84(4), 974-1002.

White, S. (1973). Syntectonic recrystallization and texture development in quartz. Nature, 244(5414), 276.

Wilcox, R. E., Harding, T. T., & Seely, D. R. (1973). Basic wrench tectonics. Aapg Bulletin, 57(1), 74-96.

Woodcock, N. H., & Fischer, M. (1986). Strike-slip duplexes. Journal of structural geology, 8(7), 725-735.

Yáñez, G., Cembrano, J., Pardo, M., Ranero, C., & Selles, D. (2002). The Challenger–Juan Fernández–Maipo major tectonic transition of the Nazca–Andean subduction system at 33–34 S: geodynamic evidence and implications. Journal of South American Earth Sciences, 15(1), 23-38.

# Chapter 9: Appendant

## 9.1 Conference participation

### 9.1.1 PATA DAYS 2017: 8th International Workshop on Peloseismology, Avtive Tectonics and Archeoseismology, 13th-16th November.

Poster presentation:

*"New evidence of active faulting in the western flank of the central Chilean High Andes, Metropolitan Region."*

**INQUA Focus Group Earthquake Geology and Seismic Hazards**

paleoseismicity.org

**New evidence of active faulting in the Western flank of the Central Chilean High Andes, Metropolitan Region.**

*J. Araya (1), G. De Pascale (1), M. Persico (1), F.Sandoval (1), A. Serey (1), S. Sepulveda (1) M. Froude (2), D. Petley (2), W. Murphy (3)*

(1) Department of Geology, University of Chile, Santiago, Chile
(2) Department of Geography, University of Sheffield, Sheffield, UK
(3) School of Earth and Environment, University of Leeds, Leeds, UK

***Abstract:*** *The Chilean Central High Andes between 33° and 34°S is an active mountain range. At the continental intraplate zone, crustal faults are partially responsible for recent and current uplift of this orogen. These crustal structures are potential seismic sources that threaten nearby populated cities. The objective of this work is to identify active crustal faults using remote sensing and field work to further determine the potential seismic hazard for Santiago. Fault rocks such as gouge, cataclasite and breccia, as well as geomorphic features, like fault scarps and lineament have revealed previously un-identified active crustal faults in the western flank of the central Andes and also extend some previous fault traces.*

***Key words****: Crustal faults, seismic hazard, Santiago de Chile, landslides.*

# NEW EVIDENCE OF ACTIVE FAULTING IN THE WESTERN FLANK OF THE CENTRAL CHILEAN HIGH ANDES, METROPOLITAN REGION

**José Araya *(1),** G. De Pascale (1), M. Persico (1), F.Sandoval (1), A. Serey (1), S. Sepulveda (1) M. Froude (2), D. Petley (2), W. Murphy (3) (*email: joaraya@ing.uchile.cl)
(1) Department of Geology, University of Chile, Santiago, Chile
(2) Department of Geography, University of Sheffield, Sheffield, UK
(3) School of Earth and Environment, University of Leeds, Leeds, UK

## 1) INTRODUCTION

Numerous crustal faults are located near Santiago and important shallow seismicity characterized the cordilleran area. However only a few structures were proven as active (Lavenu and Cembrano 2008; Vargas et al., 2014; Troncoso 2015).

**What other faults may be active here?**

This work shows the preliminary results of a neotectonic study.

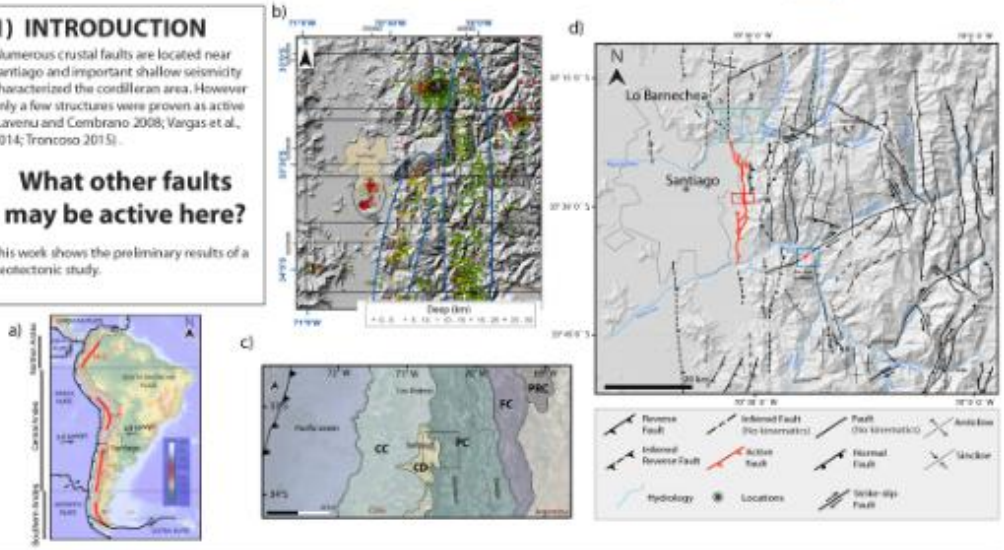


## 2) PRELIMINARY RESUTLTS

**Fault rocks and fault scarp evidence an unpreviously mapped active fault "El Arrayan Fault" in the NE corner of Santiago de Chile**
**The fault outcrop as well as the fault scarp located to the north of the northern end of the Cariño Botado Fault proposed by Troncoso (2015), suggests that the fault trace of this quaternary structure continuous to the north of the Estero San Francisco at least 1 km**

## El Arrayan Fault

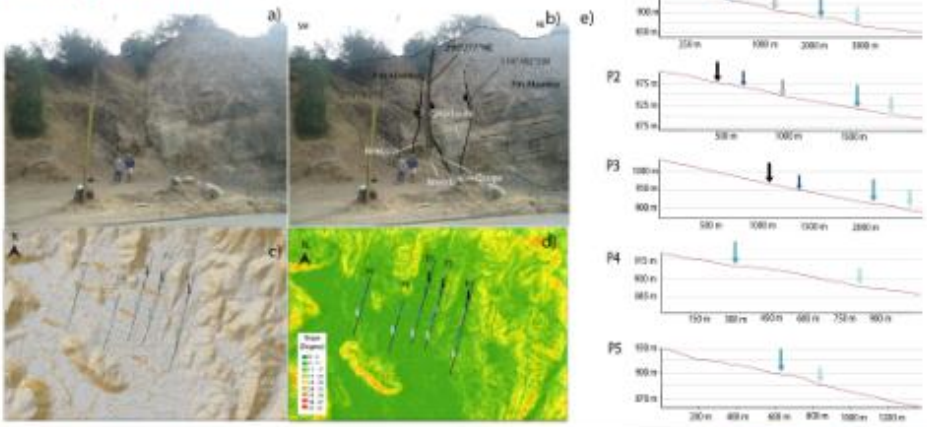


## Cariño Botado Fault

### 9.1.2 XV Congreso Geológico Chileno, Concepcion 18th - 23th November, 2018.

Oral presentation 22/11/2018:

*"New evidence of Quaternary deformation and seismic hazard along active faults, Chile´s capital Santiago."*

**New evidence of Quaternary deformation and seismic hazard along active faults, Chile´s capital Santiago.**

J. Araya (1), G. De Pascale (1), M. Persico (1), F.Sandoval (1), A., S. Sepulveda (1)(2), M. Froude (3), D. Petley (3), W. Murphy (4)

(1) Department of Geology, University of Chile, Santiago, Chile
(2) Department of Engineering, O'Higgins University, Rancagua, Chile
(3) Department of Geography, University of Sheffield, Sheffield, UK
(4) School of Earth and Environment, University of Leeds, Leeds, UK

Key words: Active tectonics, Crustal faults, Seismic hazard, Santiago de Chile.

The western flank of the central high Chilean Andes between 33° and 34°S is an active mountain range, where important shallow seismicity and quaternary faulting was recently identified. Some of the crustal structures are, such as the San Ramon fault, part of the West Andean Thrust System (WATS), and thought to be potential seismic sources that threaten Chile´s most populated region. Field work and remote sensing techniques provides new evidence for two newly discovered crustal structures. First, the El Arrayan fault, a WNW-ESE striking fault located in Lo Barnechea area, in the NE corner of Santiago. Topographic analysis shows fault scarps, revealing the recent activity of this structure. Kinematic indicators in fault rocks indicate variable styles of deformation. A deflected water stream coincident with fault scarp supports a left lateral motion. Second, the Estero Coyanco Fault, a NW-SE striking fault located in the Maipo Valley. Field characterization shows a 60 m-wide fault zone, with evidence for faulting of Quaternary deposits. Kinematic indicators as well as topographic expression, suggest a reverse mechanism for this fault. Fault scarps measurements in addition to fault length estimations for these 2 faults, when combined with fault scaling parameters, suggest the possibility of generating earthquakes with moment magnitudes (Mw's) up to 6.9, emphasizing that other faults besides the San Ramon fault may be important players for the seismic hazard of Chile´s capital. The close spatial relationship between El Arrayan Fault and rockslides highlights the possibility of coseismic landslides as an important geological hazard. This work presents the results of a new neotectonic study that reports two previously unrecognized and potentially active faults that contributes to the knowledge of crustal seismic sources near Chile´s capital city, Santiago, which is fundamental to developing better crustal seismic hazard analysis.

## 9.2 Argisoft digital elevation model reports:

### 9.2.1 Drone model July 10 flight 2018 Araya Sfm

**Survay Data**

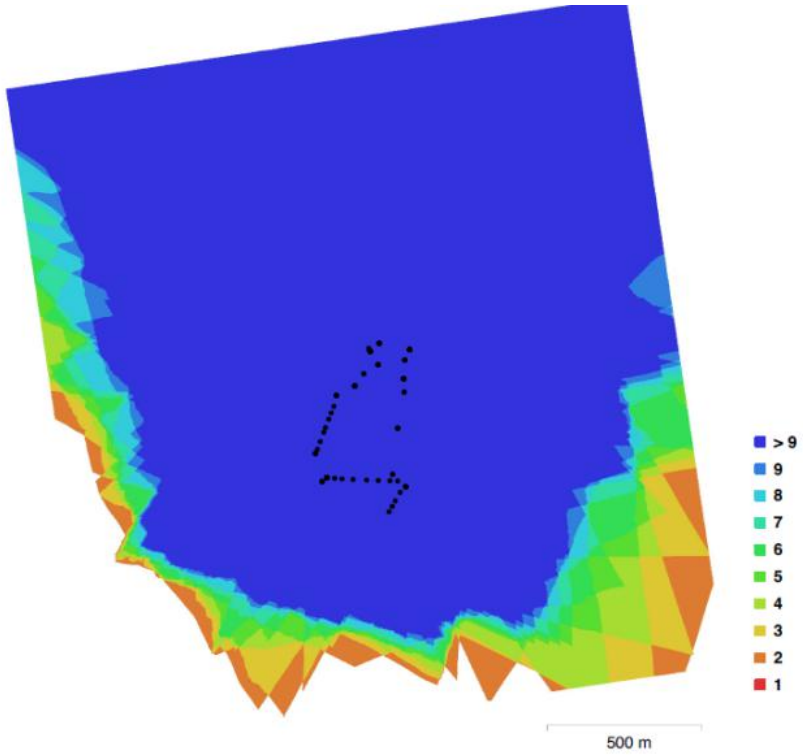


Figure 9.1 Camera locations and image overlap.

Table 9.1 Cameras.

| Camera Model | Resolution | Focal Length | Pixel Size | Precalibrated |
|---|---|---|---|---|
| FC330 (3.61 mm) | 4000 x 3000 | 3.61 mm | 1.56 x 1.56 µm | No |

Number of images: 125
Flying altitude: 502 m
Ground resolution: 19.8 cm/pix
Coverage area: 4.03 km²
Camera stations: 125
Tie points: 34,959
Projections: 460,926
Reprojection error: 1.33 pix

## Camera calibration

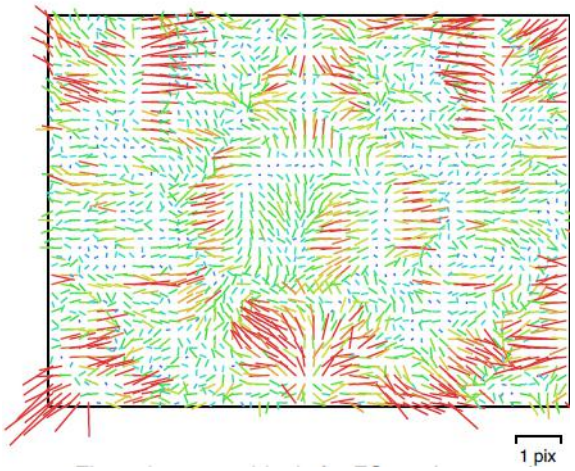


Figure 9.2 Image residual for FC330 (3.61mm)

**FC330 (3.61 mm)**
125 images

| Type | Resolution | Focal Length | Pixel Size |
|---|---|---|---|
| **Frame** | **4000 x 3000** | **3.61 mm** | **1.56 x 1.56 µm** |

| | Value | Error | F | Cx | Cy | B1 | B2 | K1 | K2 | P1 | P2 |
|---|---|---|---|---|---|---|---|---|---|---|---|
| F | **2339.38** | 0.048 | 1.00 | 0.02 | -0.72 | 0.34 | 0.03 | 0.07 | 0.12 | 0.00 | -0.37 |
| Cx | **-36.5726** | 0.052 | | 1.00 | 0.01 | -0.01 | 0.52 | 0.05 | -0.03 | 0.89 | -0.02 |
| Cy | **54.4006** | 0.081 | | | 1.00 | -0.76 | -0.01 | -0.26 | 0.05 | 0.04 | 0.63 |
| B1 | **-1.22622** | 0.02 | | | | 1.00 | -0.00 | 0.04 | -0.00 | -0.03 | -0.17 |
| B2 | **0.201172** | 0.015 | | | | | 1.00 | 0.00 | -0.01 | 0.16 | 0.01 |
| K1 | **-0.000795912** | 2e-05 | | | | | | 1.00 | -0.88 | 0.05 | -0.38 |
| K2 | **-0.00216895** | 1.8e-05 | | | | | | | 1.00 | -0.03 | 0.06 |
| P1 | **-0.000333813** | 5.9e-06 | | | | | | | | 1.00 | -0.00 |
| P2 | **0.000148309** | 6.1e-06 | | | | | | | | | 1.00 |

Table 9.2 Calibration coefficients and correlation matrix.

**Camera Locations**

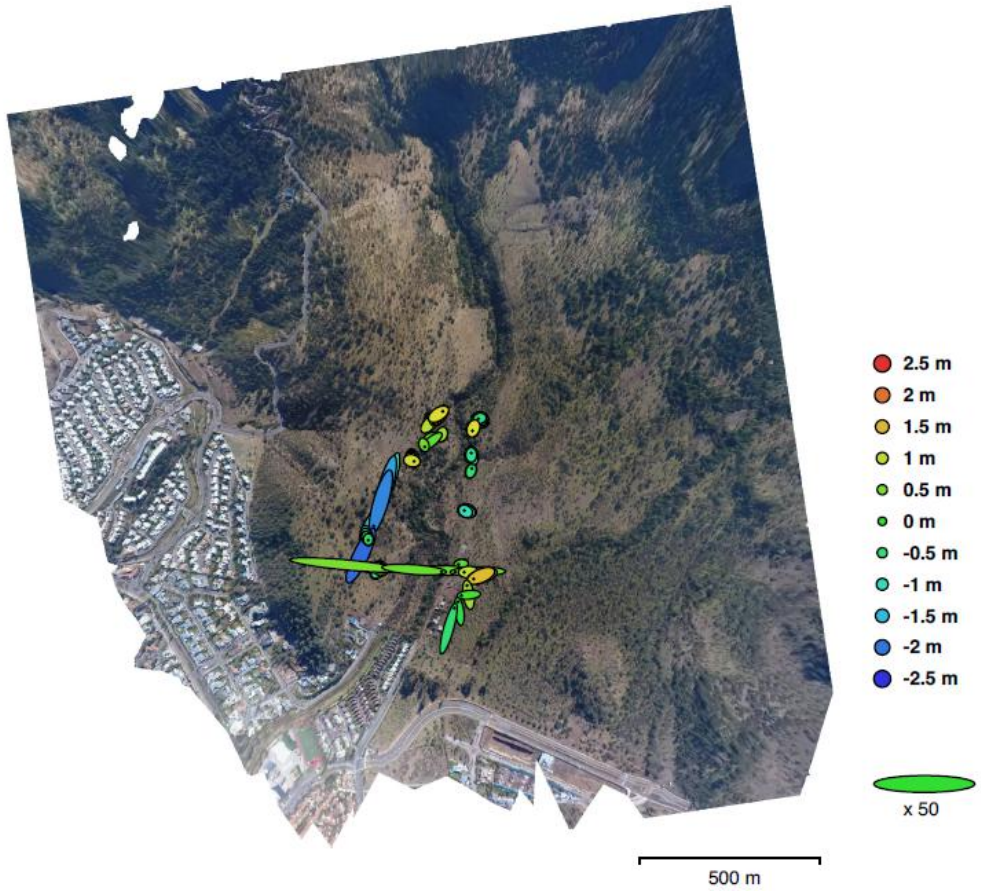


Figure 9.3 Camera locations and error estimates. Z error is represented by ellipse color. X, Y error are represented by ellipse shape. Estimated camera locations are marked whit a black dot.

Table 9.3 Average camera location error. X: Longitude, Y: Latitude, Z: Altitude

| X error (m) | Y error (m) | Z error (m) | XY error (m) | Total error (m) |
|---|---|---|---|---|
| 0.773087 | 0.590845 | 0.849114 | 0.973016 | 1.29142 |

## Digital elevation model

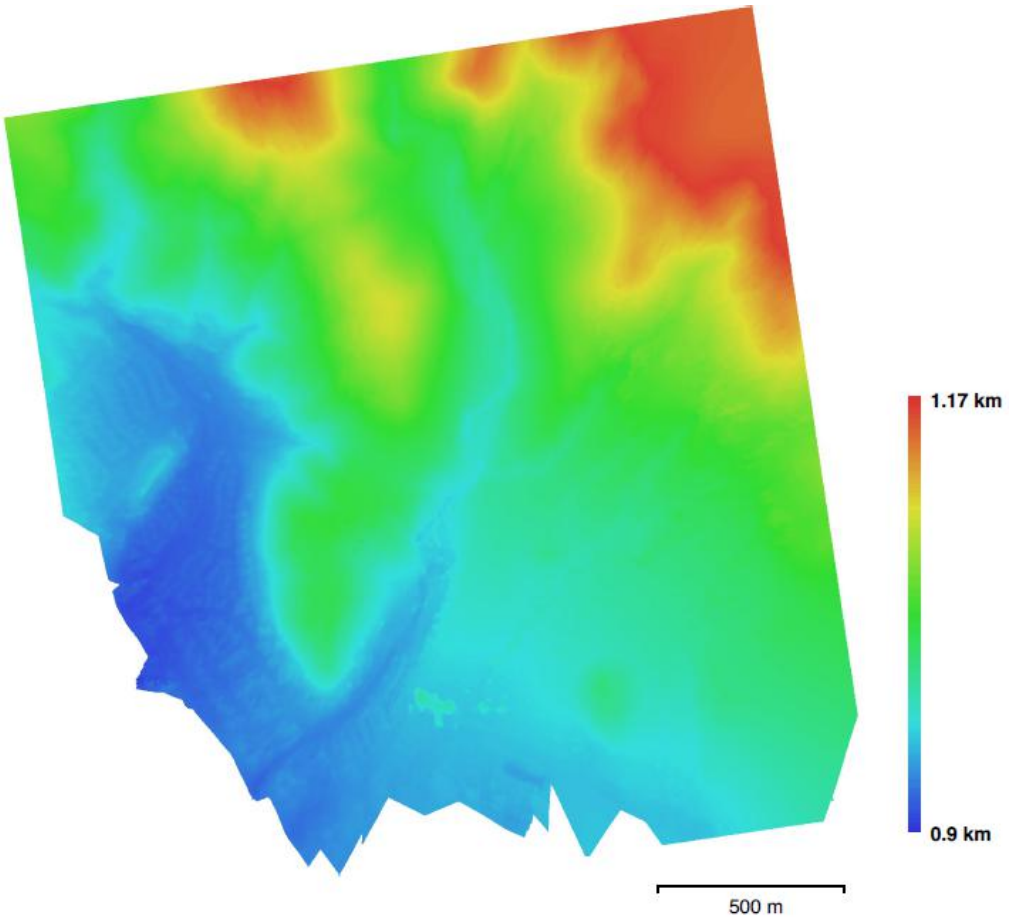


Figure 9.4 Reconstructed digital elevation model.

Resolution: 79.3 cm/pix

Point density: 1.59 points/m²

## Processing parameters

General
Cameras 125
Aligned cameras 125
Coordinate system WGS 84 (EPSG::4326)
Rotation angles Yaw, Pitch, Roll
Point Cloud
Points 34,959 of 49,490
RMS reprojection error 0.186654 (1.32658 pix)
Max reprojection error 0.563135 (24.6939 pix)
Mean key point size 6.71435 pix
Effective overlap 13.5779
Alignment parameters
Accuracy Medium
Generic preselection Yes
Reference preselection Yes
Key point limit 40,000
Tie point limit 4,000
Adaptive camera model fitting Yes
Matching time 17 minutes 3 seconds
Alignment time 2 minutes 53 seconds
Dense Point Cloud
Points 6,228,674
Reconstruction parameters
Quality Medium
Depth filtering Moderate
Depth maps generation time 19 hours 48 minutes
Dense cloud generation time 13 hours 19 minutes
Model
Faces 409,862
Vertices 205,642
Texture 4,096 x 4,096, uint8
Reconstruction parameters
Surface type Height field
Source data Dense
Interpolation Enabled
Quality Medium
Depth filtering Moderate
Face count 415,232
Processing time 14 seconds
Texturing parameters
Mapping mode Generic
Blending mode Mosaic
Texture size 4,096 x 4,096

Enable color correction No
Enable hole filling Yes
UV mapping time 1 minutes 32 seconds
Blending time 5 minutes 31 seconds
Tiled Model
Reconstruction parameters
Source data Dense cloud
Tile size 256
Processing time 2 hours 44 minutes
DEM
Size 2,942 x 3,113
Coordinate system WGS 84
(EPSG::4326)
Reconstruction parameters
Source data Dense cloud
Interpolation Enabled
Processing time 8 seconds
Orthomosaic
Size 11,572 x 11,768
Coordinate system WGS 84
(EPSG::4326)
Channels 3, uint8
Reconstruction parameters
Blending mode Mosaic
Surface DEM
Enable color correction No
Enable hole filling Yes
Processing time 7 minutes 52 seconds
Software
Version 1.3.2 build 4205
Platform Mac OS 64

### 9.2.2 Drone model April 9 flight 2018 Araya Sfm

### Survay Data

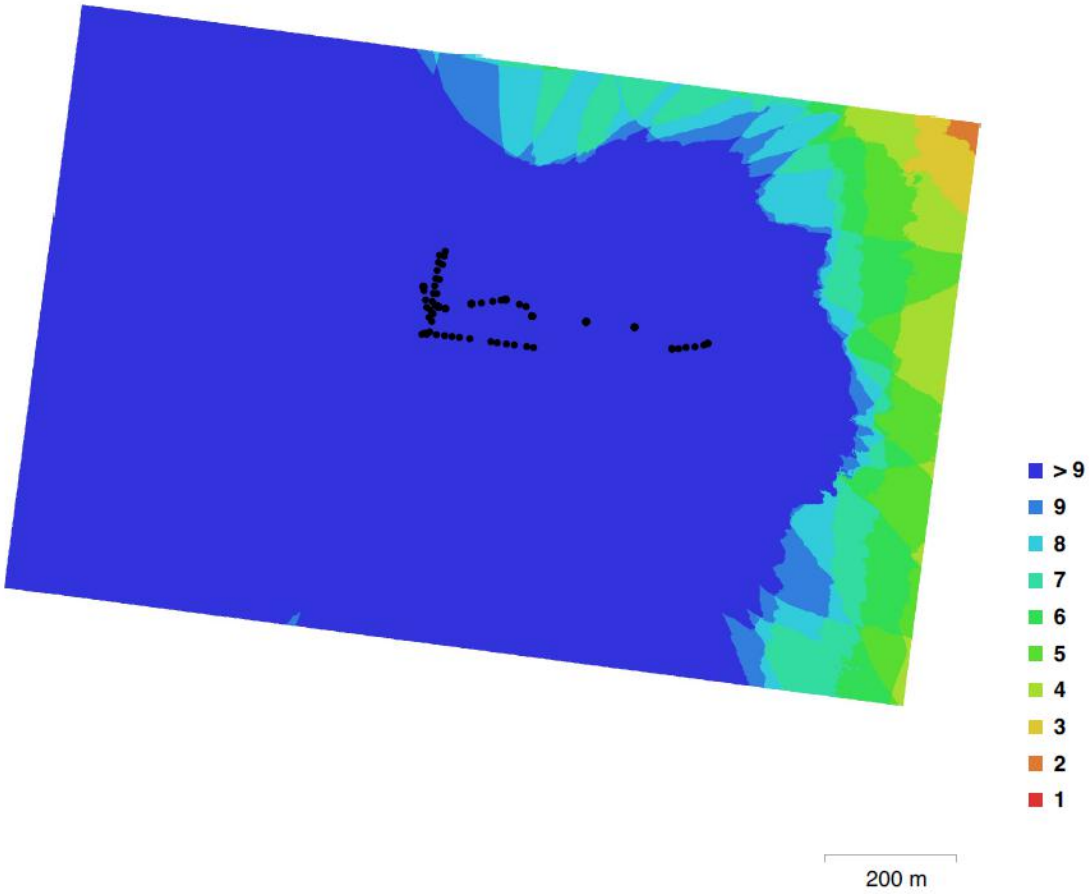


Figure 9.5 Camera locations and image overlap.

Table 9.4 Cameras.

| Camera Model | Resolution | Focal Length | Pixel Size | Precalibrated |
|---|---|---|---|---|
| FC330 (3.61 mm) | 4000 x 3000 | 3.61 mm | 1.56 x 1.56 µm | No |

Number of images: 136
Flying altitude: 348 m
Ground resolution: 13.1 cm/pix
Coverage area: 1.24 km²
Camera stations: 136
Tie points: 26,545
Projections: 373,698
Reprojection error: 1.46 pix

## Camera calibration

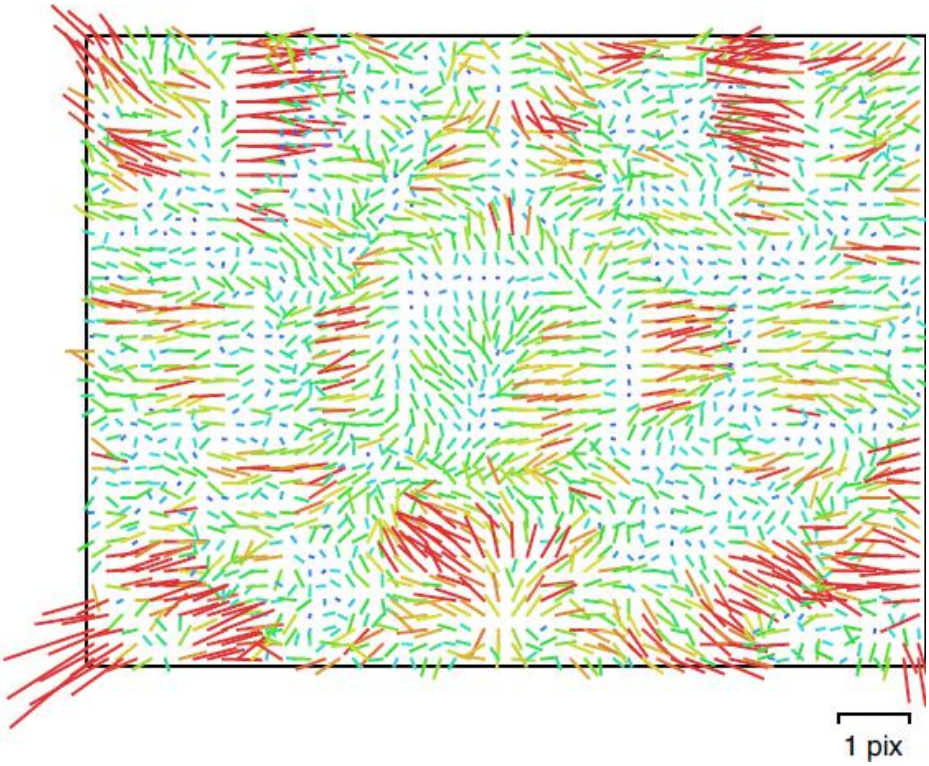


Figure 9.6 Image residual for FC330 (3.61 mm).

Table 9.5 Calibration coefficients and correlation matrix.

**FC330 (3.61 mm)**
136 images

| Type | Resolution | Focal Length | Pixel Size |
|---|---|---|---|
| **Frame** | **4000 x 3000** | **3.61 mm** | **1.56 x 1.56 µm** |

| | Value | Error | F | Cx | Cy | B1 | B2 | K1 | K2 | K3 | P1 | P2 |
|---|---|---|---|---|---|---|---|---|---|---|---|---|
| F | **2338.34** | 0.045 | 1.00 | -0.02 | -0.72 | -0.20 | 0.03 | -0.12 | 0.22 | -0.19 | 0.00 | -0.46 |
| Cx | **-37.8475** | 0.038 | | 1.00 | 0.04 | -0.02 | 0.22 | -0.02 | 0.01 | -0.01 | 0.89 | 0.02 |
| Cy | **53.4003** | 0.037 | | | 1.00 | -0.14 | 0.00 | -0.16 | 0.05 | -0.04 | 0.03 | 0.66 |
| B1 | **-1.77391** | 0.0091 | | | | 1.00 | -0.05 | -0.04 | -0.02 | 0.02 | -0.02 | 0.22 |
| B2 | **0.0814304** | 0.0092 | | | | | 1.00 | 0.01 | -0.00 | 0.00 | -0.06 | -0.09 |
| K1 | **0.00207291** | 4.5e-05 | | | | | | 1.00 | -0.95 | 0.89 | -0.03 | -0.21 |
| K2 | **-0.00751398** | 9.2e-05 | | | | | | | 1.00 | -0.98 | 0.02 | 0.04 |
| K3 | **0.00298016** | 5.9e-05 | | | | | | | | 1.00 | -0.01 | -0.03 |
| P1 | **-0.000431863** | 4.9e-06 | | | | | | | | | 1.00 | 0.04 |
| P2 | **-1.18826e-05** | 4.4e-06 | | | | | | | | | | 1.00 |

**Camera locations**

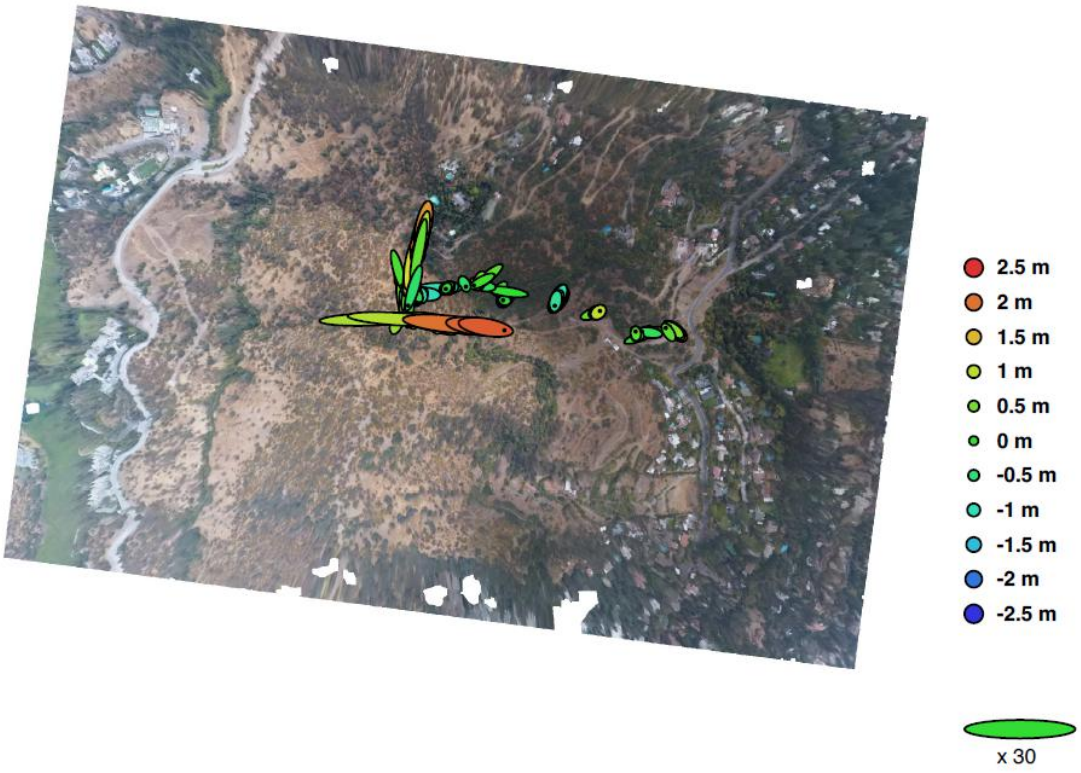


Figure 9.7 Camera locations and error estimates. Z error is represented by ellipse color. X, Y error are represented by ellipse shape. Estimated camera locations are marked whit a black dot.

Table 9.6 Average camera location error. X: Longitude, Y: Latitude, Z: Altitude

| X error (m) | Y error (m) | Z error (m) | XY error (m) | Total error (m) |
|---|---|---|---|---|
| 0.896626 | 0.751239 | 0.785092 | 1.16974 | 1.40878 |

**Digital elevation model**

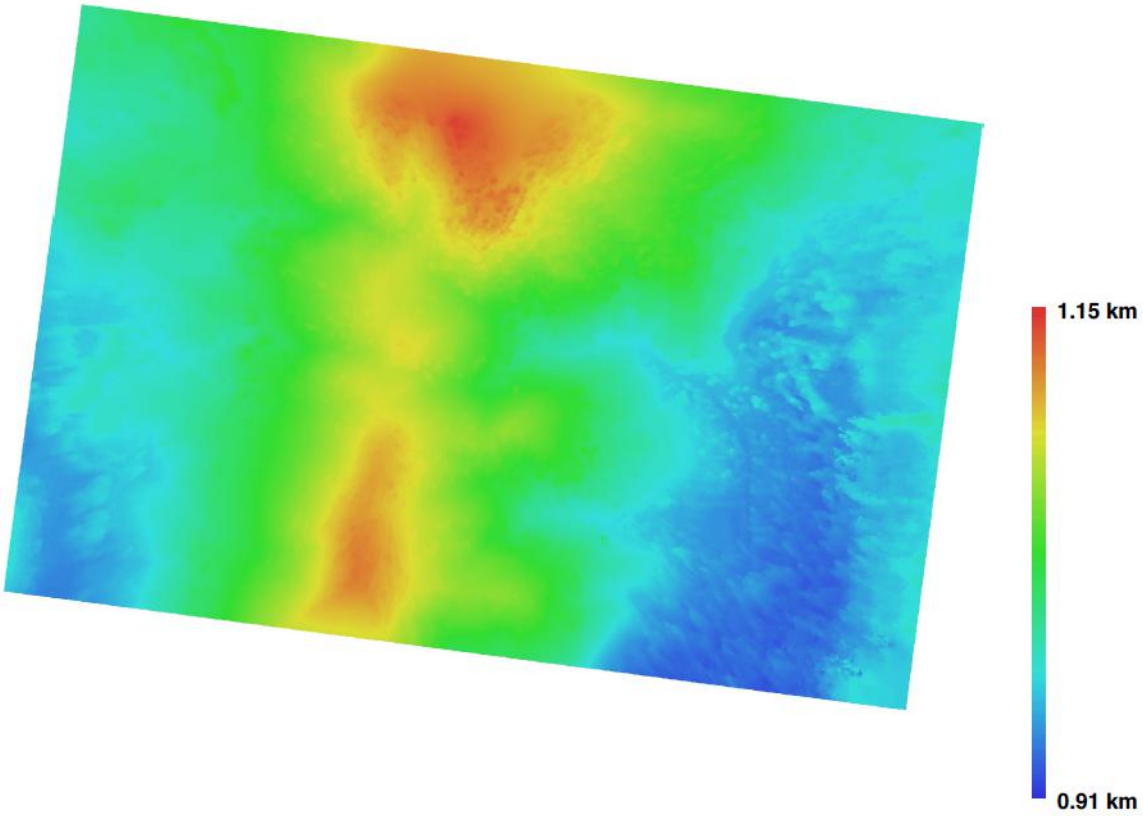


Figure 9.8 Reconstructed digital elevation model

Resolution: 26.3 cm/pix
Point density: 14.5 points/m²

## Processing parameters

General
Cameras 136
Aligned cameras 136
Coordinate system WGS 84 (EPSG::4326)
Rotation angles Yaw, Pitch, Roll
Point Cloud
Points 26,545 of 46,995
RMS reprojection error 0.232789 (1.45998 pix)
Max reprojection error 0.704729 (32.0563 pix)
Mean key point size 5.85694 pix
Effective overlap 14.4269
Alignment parameters
Accuracy Highest
Generic preselection Yes
Reference preselection Yes
Key point limit 40,000
Tie point limit 4,000
Adaptive camera model fitting Yes
Matching time 53 minutes 50 seconds
Alignment time 10 minutes 3 seconds
Dense Point Cloud
Points 19,387,466
Reconstruction parameters
Quality High
Depth filtering Moderate
Depth maps generation time 1 days 19 hours
Dense cloud generation time 8 hours 30 minutes
Model
Faces 1,291,960
Vertices 646,242
Texture 4,096 x 4,096, uint8
Reconstruction parameters
Surface type Height field
Source data Dense
Interpolation Enabled
Quality High
Depth filtering Moderate
Face count 1,292,484
Processing time 53 seconds
Texturing parameters
Mapping mode Generic
Blending mode Mosaic
Texture size 4,096 x 4,096
Enable color correction No
Enable hole filling Yes

UV mapping time 1 minutes 16 seconds
Blending time 4 minutes 3 seconds
Tiled Model
Reconstruction parameters
Source data Dense cloud
Tile size 256
Processing time 1 hours 7 minutes
DEM
Size 5,662 x 4,069
Coordinate system WGS 84 (EPSG::4326)
Reconstruction parameters
Source data Dense cloud
Interpolation Enabled
Processing time 24 seconds
OrthomosaicSize 11,324 x 8,138
Coordinate system WGS 84 (EPSG::4326)
Channels 3, uint8
Reconstruction parameters
Blending mode Mosaic
Surface DEM
Enable color correction No
Enable hole filling Yes
Processing time 7 minutes 26 seconds
Software
Version 1.3.2 build 4205
Platform Mac OS 64